UNIVERSITY OF SOUTHAMPTON

Finite Element Analysis of Ankle Foot Orthoses

Mark Andrew Arnold

Submitted for the degree of Doctor of Philosophy

Department of Mechanical Engineering

July 1999

UNIVERSITY OF SOUTHAMPTON

ABSTRACT

FACULTY OF ENGINEERING AND APPLIED SCIENCE
DEPARTMENT OF MECHANICAL ENGINEERING

Doctor of Philosophy

FINITE ELEMENT ANALYSIS OF ANKLE FOOT ORTHOSES

Mark Andrew Arnold

An Ankle Foot Orthosis (AFO) is a support prescribed for patients with disorders of the lower limb to improve gait. The mechanical characteristics of plastic AFOs are difficult to predict, therefore their design evaluation is currently based on a trial and error approach. This thesis contributes to the development of a more rational method of AFO selection based on the finite element method (FEM). A versatile FE analysis procedure was developed for customising a solid model of an asymmetric AFO and predicting its behaviour prior to manufacture. Accurate prediction of stress concentrations was achieved through iterative mesh refinement. Linear static analyses were performed to assess the effect of geometry, loading and constraint on the AFO's structural behaviour. The magnitude of the maximum stress, ankle moment and heel rotation were all found to depend on the distribution of imposed displacement at the foot region simulating rotation about the ankle joint axis. In all cases, the critical stresses were located around the ankle trimline. Relaxing the constraint at the heel was found to significantly reduce the maximum stress and moment required to produce a given rotation about the ankle axis.

By incorporating large deformation effects and the non-linear elastic behaviour of polypropylene into the finite element model, the analytical results became more consistent with experimental measurements. Thus, a difference in behaviour between dorsiflexion and plantar flexion motion was predicted. Deformation in the frontal and transverse planes was predicted from linear and non-linear analysis, and both constant and variable thickness has been modelled. Through simulation of published experimental results, the dependence of ankle moment on ankle trimline radius was numerically demonstrated. Reliable predictions of varying stiffness over large rotations were obtained. The FEM was thus shown to be an effective tool for a thorough and accurate mechanical evaluation of a customised plastic AFO.

Contents

Appendices

List of Tables

List of Figures

Preface

The author is indebted to Clare Harding for her support and encouragement throughout this work. The author wishes to thank Dr Stavros Syngellakis, Senior Lecturer in Solid Mechanics from the Department of Mechanical Engineering for supervising this research, and Dr Hamid Rassoulian, Senior Bioengineer from the Department of Medical Physics and Bioengineering at Southampton General Hospital for additional supervision, the manufacture of the testing apparatus and assistance during the experimental work. The author would also like to thank Paul Keeping, then Head Orthotist from the Department of Orthotics and Prosthetics at St. Mary's Hospital (Isle of Wight), for the manufacture of an orthosis, supply of materials and invitation to visit the hospital, and Dr Richard Downes, Engineering and Graphical Software Specialist at Computing Services, for help with the finite element analysis software and other computing resources. The author is also grateful to Tadashi Sumiya, MD, from the Rehabilitation Engineering Centre for Employment Injuries, Japan, for additional geometric data on their published work, and Professor Andy Keane, Head of the Department of Mechanical Engineering, for access to additional computing facilities.

Abbreviations

AFMA	Automated Fabrication of Mobility Aids
AFO	Ankle Foot Orthosis
APDL	ANSYS Parametric Design Language
CAD	Computer Aided Design
CAM	Computer Aided Manufacture
CG	Centre of Gravity
DLFC	Dundee Limb Fitting Centre
DOF	Degree(s) Of Freedom
FEA	Finite Element Analysis
FEM	Finite Element Method
GRF	Ground Reaction Force
HKAFO	Hip Knee Ankle Foot Orthosis
JCG	Jacobi Conjugate Gradient (solver)
KAFO	Knee Ankle Foot Orthosis
MPJ	Metatarsophalangeal joint
NSP	North Sea Plastics Ltd.
NYU	New York University
PCG	Preconditioned Conjugate Gradient (solver)
PLS	Posterior Leaf Spring
SASI	Swanson Analysis Systems, Incorporated
SRSS	Square Root of the Sum of the Squares
TIRR	Texas Institute of Rehabilitation and Research
UC-BL	University of California Biomechanics Laboratory

Notation

α, β, β_1, γ	Numerical factors depending on the ratio of a plate
δl	Elongation at failure
δ_{max}	Maximum displacement of a node
δ_x, δ_y	Nodal displacements in nodal x and y directions
δ_z	Medial/lateral displacement of node at middle of distal trimline
ϵ	Total strain
ϵ_p	Primary creep strain
ϵ_0	Elastic strain
$\dot{\epsilon}_c$	Creep strain rate
$\dot{\epsilon}_s$	Secondary creep rate
η	Percent energy error
θ	Applied angle of rotation about ankle joint axis
θ_f	Rotation of node at distal trimline about ankle joint axis
θ_h	Rotation of node at heel region about ankle joint axis
ν	Poisson's ratio
σ	Stress
σ_{eqv}	Equivalent stress
σ_u	Ultimate tensile strength
σ_x, σ_y	Normal stresses parallel to x and y axes
σ_Y	Yield stress
σ_1, σ_2, σ_3	Principal stresses
A, B, C	Material creep constants
C_1 to C_{10}	ANSYS creep constants

D	Flexural rigidity of a plate or shell
E	Young's modulus
F	Resultant reaction force at nodes with imposed displacement
F_x	Reaction force at a node in nodal x direction
F_y	Reaction force at a node in nodal y direction
G	Shear modulus
J, K	Material creep constants
M	Total moment about ankle joint axis
M_e	Experimental moment about ankle joint axis
M_{foot}	Moment contribution from nodes at the foot
M_{heel}	Moment contribution from nodes near the heel
M_x, M_y	Bending moments per unit length in rectangular plate
N_x	Magnitude of the lateral load per unit length
R	Perpendicular distance of node from ankle joint axis
S	Number of load steps
T	Temperature
X, Y, Z	Global Cartesian coordinate system directions
a, b	Plate dimensions parallel to x and y axes
c	Material creep parameter
h	Thickness of a plate or shell
n	Material creep constant
q	Applied pressure on rectangular plate
r	Material creep parameter
t	Time
w_{max}	Maximum deflection at the centre of a rectangular plate.
x, y, z	Nodal coordinate system directions

Chapter 1

Introduction

1.1 Purpose of Orthoses

An *orthosis* is a device used in the rehabilitation of patients with impaired function of some movable part of the body [World Book Inc., 1988]. It acts as an artificial support whose aim is to relieve pain, align, prevent or correct deformities and thus improve or restore the lost function. The most common type of orthosis prescribed for disorders of the lower limb is the *Ankle Foot Orthosis (AFO)* [Halar & Cardenas, 1987]. Its purpose is to improve the gait pattern, decrease energy expenditure, ensure safe ambulation, stabilise the ankle, and possibly prevent or reduce the progress of deformities [Leonard *et al.*, 1989].

Modern designs of AFO are worn inside the shoe (see Figure 1.1). They are manufactured by vacuum forming a sheet of thermoplastic material of the desired thickness over a positive cast of the patient's lower limb and then the material is trimmed to the desired shape. This trimming stage is important as it affects the resistance of the AFO to deformations caused by motion of the foot, which must be set according to the patient's disability. AFOs also form the base component to which other components are added to form more extensive orthotic systems for the

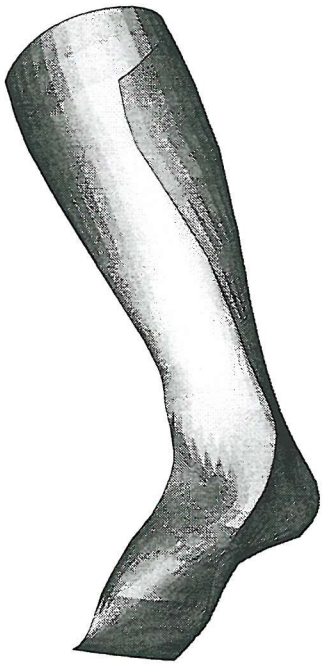

Figure 1.1. A plastic ankle foot orthosis

lower limb, such as a Knee Ankle Foot Orthosis (KAFO) and a Hip Knee Ankle Foot Orthosis (HKAFO).

1.2 Conditions Requiring an Orthosis

An AFO can be prescribed for the management of a wide range of disorders, each having different characteristics. These characteristics also vary between patients with the same abnormality and with a particular patient over time, making the prescription of an AFO all the more difficult. Spastic muscle problems can be controlled by an orthosis, although structural problems must first be surgically corrected [Rosenthal, 1984]. Orthoses can be used in rheumatic diseases to restrict motion and support the joints in their optimum functional positions [Hicks *et al.*, 1989]. This type of disorder will compromise the musculoskeletal system by altering the structure and function of the joints, resulting in an abnormal posture and movement pattern with increased energy expenditure. Orthoses are also used

for burn patients, to maintain optimal positioning and immobilisation of the affected body part. A dorsiflexion assisting AFO may be used in drop-foot gait.

Another example is lower limb spasticity, which is characterised by increased muscle tone where the muscles are in a constant state of contraction. This may be as a result of cerebral palsy or head (brain) injury, and orthoses may be prescribed to correct the joint position. Cerebral palsy is a non-progressive disorder of the brain affecting movement and posture, and classifications include hemiplegia and bilateral hemiplegia (quadriplegia) [Anderson & Meadows, 1979]. The majority of spastic cerebral palsy patients exhibit high tone in some muscles, such as the plantar flexors, causing an equinovarus deformity [Middleton *et al.*, 1988]. AFOs may be used to resist plantar flexion, dorsiflexion and varus/valgus deformities due to external forces or uncontrolled muscle activity. Hemiplegic gait is characterised by slow speed and poorly coordinated movements [Lehmann *et al.*, 1987]. The gait pattern is very different from that of an able-bodied person as a result of the inability to control movement. Weakness in groups of muscles, including the dorsiflexors, results in an equinovarus position of the foot.

1.3 AFO Prescription

The techniques used at present for the prescription of an AFO for an individual patient involve performing a clinical examination of the patient to obtain qualitative information regarding their disability [Halar & Cardenas, 1987]. The first stage of this involves a physical examination to establish the range of motion of the joints, the tone and strength of the muscles, joint stability, sensory determination and coordination. Secondly, a visual assessment of the patient's gait pattern is carried out to check the phases of gait for abnormalities to determine what could be corrected by an AFO. An AFO is then manufactured and its rigidity and hence trimline assessed by manually flexing the AFO. The flexibility of an AFO to dorsiflexion and plantar flexion also has the most significant effect on a patient's gait [Yamamoto *et al.*, 1993b]. The AFO is subsequently checked to

evaluate its fitting and effect on ambulation via further gait studies.

These current methods of prescription have the disadvantage of being subjective in nature, as the assessment depends on the personal impressions and experience of the fitter [Chowaniec *et al.*, 1979]. Although this form of assessment requires no special apparatus and is relatively quick to perform, it does not provide any quantitative information about the patient's disability. Also, to avoid toe clearance problems associated with an AFO that is too flexible, orthotists will sometimes prescribe an orthosis that is too stiff. This overbracing causes higher energy expenditure during gait [Leone, 1987]. Therefore, orthotic prescription should additionally involve such things as a quantitative assessment of the patient's residual muscle function about the ankle, and gait analysis with and without the AFO to obtain kinematic and kinetic data. It should be noted that such data would only be useful in the design of an AFO if combined with an analytical assessment of its behaviour.

The main objective when prescribing an orthosis is to match the modes of control available with a particular design to the functional deficits of the patient, to restore a normal walking pattern [McCollough, 1975]. An ideal orthosis should therefore correct only those motions that are considered abnormal or undesirable, while permitting motion where normal function can occur. This can be achieved by ensuring the orthosis directs joint motions similar to those of a normal limb [Lehneis, 1974]. To fulfil their purpose, AFOs must also be designed to fit properly, as poorly fitted orthoses can result in discomfort, skin abrasion and restriction of function [Hicks *et al.*, 1989]. When prescribing an AFO for a young child, it is also important to recognise the unusual demands that their daily activities can put on an orthosis, as it must not interfere with the normal crawling action of the child [Anderson & Meadows, 1979].

One useful advantage of modern, plastic AFOs is the ability to alter their characteristics by modifying the material thickness or the shape of the trimlines. Condie & Meadows [1977], Lehmann *et al.* [1983] and Sumiya *et al.* [1996b] have shown how it is possible to utilise a single design of plastic AFO for patients with

varying degrees of impairment using this principle. This keeps the number of designs of AFO to a minimum, which is of benefit to orthotists as they only have to be familiar with the characteristics of a single type of orthosis, and hence understand its behaviour to a greater degree. Reducing the range of products will also benefit prescription services, as less of their money will be tied up in stock. However, plastic AFOs also make the task of customisation very difficult because, in spite of their apparent simplicity, the mechanical characteristics are much more difficult to establish. This is largely due to their complex shape and the non-linearity of the material.

1.4 Analytical Studies of Plastic AFO Characteristics

1.4.1 Review

In order to make effective use of a particular design of plastic AFO, it is important to understand its behaviour during use. It is generally accepted that testing and analysis can lead to improved AFO designs. Lam *et al.* [1986a] developed a two-dimensional finite element model of the lower part of a polypropylene AFO and a simplified normal foot, consisting of bones, soft tissue and ligaments, to study motion in the sagittal plane when subjected to several static loading conditions. Two-dimensional, four noded quadrilateral elements were used to model the bone, soft tissue and AFO, and one dimensional truss elements were used for the ligaments.

For the first loading condition, the muscle force in the Achilles tendon was represented by a concentrated nodal force, and a gravitational load was applied to represent the weight of the foot. Next, a nodal force was applied to the heel region to represent an average person's weight. Then, a nodal force of the same magnitude was applied to the toe region, and finally the load was uniformly distributed over

the sole of the foot. The nodes at the upper boundary of the foot and AFO were fully constrained to simulate the foot rotating about a fixed leg and calf strap respectively. Material properties for the model were assumed to be linear elastic.

The responses for each of the four loading conditions were obtained for the foot without an AFO, with an AFO closely fitted to the contours of the foot, and with a modified AFO that had a flattened sole and calf region. The results showed that the rotation of the foot (calculated as the rotation of a node towards the toe region about a node at the ankle) decreased with an AFO in all load cases, and that the modified AFO further reduced this rotation. Peak stresses in the AFO occurred either at the upper boundary, or at the heel region. The stresses were also higher in the closely fitted AFO than the modified one, emphasising the effect of slight geometry modifications. Extending the length of the sole of the AFO was also found to have little effect on results. To study the response of the model due to both static and dynamic loading conditions, Lam *et al.* [1986b] continued their work by applying a dynamic load in the form of an initial velocity to represent an average walking motion. The peak stresses for the dynamic analysis were found to be slightly higher than those obtained from a static analysis, although not significantly.

Leone [1987] has studied the structural response of a PLS type AFO during the swing phase of gait with a simple theoretical model using beam equations. The AFO geometry was broken down into three simplified sections modelled as one dimensional structural beam elements. The calf region was subjected to bending and torsional loads, the sole region subjected only to bending loads, and the heel region was assumed relatively stiff and to undergo displacement without deformation (rigid body motion). The calf region was assumed to be a circular sector channel section of constant thickness. The sole region was assumed to be a 'U' shaped channel section from the heel to a specified distance, and a flat plate from the end of this section to the toe. The section properties were calculated at intervals along each region, and a computer program was written to perform the calculations.

Three concentrated forces were applied individually at the toe. A vertical force was applied to represent the weight of the foot and the forces involved in positioning the foot distributed over a small contact area. Horizontal forces were applied in the direction of motion, and perpendicular to this, to represent surface traction. The AFO was assumed to be constrained against all translations and rotations at the calf strap location to represent its restraining action against movement. Excellent agreement was found between the values of bending and torsional deformation of the AFO predicted from the model and values obtained from a finite element analysis incorporating space frame members. Good agreement was also found between theoretical values and those obtained from experimental tests, where an AFO was supported and loaded in the same manner assumed in the analysis. It was concluded that this simple model was computationally easy to utilise for predicting the characteristics of AFOs.

Leone *et al.* [1988] extended this work to include an analysis of a three dimensional finite element model of a solid ankle AFO. The model geometry was assumed the same as in the previous analysis, except that in this case the ankle trimlines covered the malleoli. The model was constructed of plate bending elements, and was assumed symmetric about the midsagittal plane to simplify model generation. The model was fully constrained at all the nodes along the proximal calf trimline, and a constant displacement was applied at the metatarsal head area causing dorsiflexion. To validate the results from the analysis, experimental data was obtained from the actual AFO modelled using an Instron testing machine. The calf section of the inverted AFO was bolted to the base of the test apparatus using angle brackets, loads were incrementally applied directly to the metatarsal region of the AFO causing dorsiflexion, and dial gauges were placed at key locations on the AFO to monitor normal displacements.

Analysis and test results averaged from a number of runs were plotted in the form of flexibility (displacement divided by load) versus applied loading. Also included on these graphs were values calculated using beam equations, as used in the previous paper. The data obtained at the position of applied loading revealed that

the two sets of analytical data bounded the experimental test results up to the onset of buckling instability, at which point the flexibility of the experimental AFO increased until complete failure. Experimental test results obtained from the dial gauge measuring normal deflection at the malleoli protrusion revealed these same trends, and it was concluded that local buckling in this region was the mechanism for failure. Stress contours obtained from the finite element analysis revealed that the largest compressive stresses were also located at the malleoli protrusion, and they also concluded that finite element analysis could give more information than that obtainable from the simpler beam analysis.

Leone *et al.* [1991] further explored the behaviour of solid ankle AFOs during dorsiflexion with a comparison of instability loads obtained from testing and those predicted by finite element analysis. The experimental testing procedure was identical to that of the previous paper, and results revealed the same local buckling at the malleoli protrusion. A dial gauge positioned at this location recorded a nearly linear variation of normal deflection as the load was increased from zero to a certain limit. Above this point, the rate of deformation started to increase rapidly due to the onset of buckling, and shortly after the AFO had failed. The finite element model was constructed in the same manner as in the previous work, although this time thick shell elements were used.

An initial linear analysis was performed to obtain the Euler buckling load, which is an upper limit on the actual buckling load. Due to the large deflections encountered in the experimental tests, a geometric non-linear analysis was then performed, where the loading is incrementally applied and an iterative solution technique is used. The resulting load versus deflection plot revealed a similar trend to the experimental results, that is the curve became non-linear after a certain point showing decreasing stiffness, although the magnitude of loading was substantially greater for a set deflection. It was concluded that refinements in the model, including the use of non-linear material properties and modelling the entire AFO geometry, could bring these results in line with the experimental data, although at a cost of increased processing time.

Chu *et al.* [1995] expanded on the work carried out by Lam *et al.* [1986a] by developing an asymmetric three-dimensional finite element model of a polypropylene AFO and a lower limb. An AFO was manufactured to fit a normal subject, and the geometry of this was then digitised. A total of 313 three-dimensional solid elements were used to represent the AFO (128 elements), the bones and the soft tissue, and truss elements were used for the ligaments. The upper boundary of the AFO model was constrained in all directions to simulate the calf strap, and the leg was also constrained at its upper boundary in this manner to simulate a fixed leg. No space was assumed to exist between the bones and the soft tissue of the foot, or between the soft tissue and the orthosis. Slip was also not considered in these parts of the model, although vertical slip was allowed between the soft tissue and tibia. The ground reaction forces at heel strike and toe off were simulated by concentrated nodal forces, and the weight of the foot was also simulated.

The material properties for the soft tissue, bones, ligaments and AFO were assumed to be linear, perfectly elastic and isotropic. Static analyses were conducted for dorsiflexion, plantar flexion, eversion, inversion, adduction and abduction motions during swing, and heel strike and toe off conditions were simulated during stance. The results revealed that the peak compressive stress (1.6 MPa) occurred at a stress concentration in the heel region of the AFO during heel strike, and the peak tensile stress (0.8 MPa) occurred on the lateral calf trimline during toe-off. It was found that the asymmetric stress distribution in the AFO varied significantly with a change of ground contact point during heel strike, but was not significantly altered during toe-off. Parametric studies revealed that the model was sensitive to changes in the elastic modulus of the AFO. They concluded that, for a more realistic model, non-linear and viscoelastic properties of the AFO material should be incorporated into the analysis, and that the stress distribution in an AFO during stance is the key characteristic in designing an AFO.

A recent investigation by Abu-Hasaballah *et al.* [1997] initially involved the real-time measurement of contact pressures between a custom-made AFO, lower

limb and shoe during gait of four able-bodied subjects. A resistance pad system was used to collect maximum and average pressures over the entire inner surface of the AFO, the foot enclosure exterior surface and at the calf strap. The largest pressures were found to occur during the mid-stance phase of gait at the AFO/shoe interface. An AFO was then digitised and the data used to generate a mesh of 8-node solid elements. The measured contact pressures were used as applied loading for a number of analyses. The maximum equivalent stress (11.8 MPa) was predicted to occur at the medial ankle trimline during stair climbing. As the measured contact pressures and predicted stresses were negligible at the calf region of the AFO during all activities, this region was trimmed to reduce weight. Approximately 30 % of the material was removed, although the maximum stress predicted from the corresponding finite element model was increased.

1.4.2 Discussion

A number of analytical studies of the mechanical characteristics of AFOs have been undertaken in the past, although certain assumptions were made in most cases to simplify the analyses producing less realistic results. For example, all previous analyses assumed linearly elastic material behaviour, whilst only one analysis included large deformation effects. All finite element models also appeared to adopt a constant thickness distribution, and no assessment of the sensitivity of predicted results to discretisation error was reported.

Analyses performed by Lam *et al.* [1986a] and Lam *et al.* [1986b] consisted of a two-dimensional finite element model of the lower part of an AFO. This model only approximated the structural behaviour of an actual AFO, although the analyses were simplified considerably. The foot was also modelled with the aim of studying its effect on the behaviour of the AFO, although the elements of the AFO and foot were actually connected together at the nodes. The results would therefore have been unrealistic as contact elements should have been used to model such a situation, although this is a geometric non-linearity and increases solution

time. As only the lower part of the AFO was modelled, constraints were applied in an unrealistic manner such that no deformation was assumed to take place in the upper part of the AFO. This was the only work to include a dynamic loading.

Leone [1987] simplified the geometry considerably by modelling the AFO, which in reality is a three-dimensional structure, using beam theory. The constraints applied at the calf strap region were not realistic in that the model was constrained against all translations and rotations, whereas an AFO has some freedom of movement during gait. The heel region of the model was also assumed to be rigid, although this is not entirely unrealistic. The loading was also simplified to concentrated forces applied at the toe region, and some contradictions were evident as the swing phase of gait was being studied and yet horizontal forces were applied to represent surface traction. The study was also confined to swing, as it was considered that the primary design condition of a PLS type AFO is to control drop foot during this phase of gait. The results therefore gave no indication of the behaviour of such a device during the stance phase, where higher loading would obviously be applied to the device. No constraint was applied at the heel region, which was considered unrealistic.

The analyses performed by Leone *et al.* [1988] and Leone *et al.* [1991] were an improvement on previous work, as a three-dimensional finite element model was considered, although the model was assumed symmetric about the midsagittal plane for simplification. The constraints applied at the calf band region were again unrealistic, although they allowed comparison of results with the previous analysis to be made. The mesh appeared too coarse to accurately predict the location and magnitude of peak stresses, although this was probably to reduce solution time. The results did reveal that a geometric non-linear analysis was necessary to predict the buckling behaviour of an AFO during dorsifiexion, and it was suggested that, for more accurate results, material non-linearity must also be taken into account.

Chu *et al.* [1995] constructed a more realistic three-dimensional asymmetric model of an AFO, including the lower limb. Again the mesh appeared too coarse to obtain reasonably accurate stress results. The choice of element type was also not

the most appropriate for modelling a thin solid, as three-dimensional structural solid elements are computationally more expensive than other suitable elements due to the additional degrees of freedom. The loading conditions were represented by concentrated nodal forces, which are unrealistic and introduce localised stress concentrations. The constraints at the calf strap region were again inappropriate, and contact elements were not used to model the interaction between the AFO and the lower limb, but a perfect connection was assumed. Nonetheless, some constraint would have existed at the heel region of the AFO. Results revealed that the stress distribution in an AFO is asymmetric, emphasising the need for an asymmetric model if reliable results are to be obtained. Note that the magnitude of the predicted stresses were lower than those reported by Abu-Hasaballah *et al.* [1997] because Chu *et al.* [1995] had modelled the middle calf region as a flat plate.

1.5 Objectives

From previous work [Arnold, 1995] and from reviewing the literature, it was clear that there was a need for a systematic method of customisation of an AFO to meet the needs of an individual patient. Previous analyses have all concentrated on studying the behaviour of an existing AFO, but little attention has been given to developing a process for customising and evaluating an AFO before manufacture. Various assumptions have also been made to simplify the analyses, which included constructing the geometry of the model as either two dimensional or symmetric, using a coarse finite element mesh, applying the loads and constraints in an unrealistic manner, ignoring the geometric and material non-linearities and also assuming static loading conditions.

The aim of this present research was therefore to develop an analytical procedure for the evaluation of AFO designs using finite element analysis. This would enable better biomechanical matching of the orthosis to the patient in a multi-disciplinary environment, by replacing the current trial and error approach with a reliable numerical model, and hopefully lead to new, more effective designs, enhanced

patient treatment and reduced manpower requirements. The specific objectives for this work were firstly to construct a flexible modelling routine that generates a realistic, three dimensional, asymmetric finite element model of an AFO to fit a particular patient according to a number of user defined design parameters. The effect of variations in the density of the finite element mesh on results would be investigated to see whether the model is sensitive to the number of elements.

Using this modelling routine, a number of analyses would then be performed on a model of a particular AFO to investigate its behaviour under load and advance current understanding. This should include both linear and non-linear static analyses to see whether the more accurate non-linear analyses predict results significantly differently from those obtained from the linear analyses. Both geometric and material non-linearities would also be considered to assess their combined effect on AFO behaviour. Once the results from these analyses have been understood in relation to one particular design of orthosis, similar analyses should then be performed on models of a number of different AFO designs to assess the effects that varying design parameters has on AFO behaviour. If time and resources permit, consideration should be given to the design and manufacture of a test rig for experimentally validating the response of the finite element model when subjected to known loading conditions.

1.6 Organisation of Thesis

This research is presented in a logical sequence of chapters to complement each of the main objectives. Chapter 2 includes background material, detailing the basic concepts of human gait, the biomechanics of the foot and ankle, and AFO designs. It also reviews previous experimental studies of plastic AFO characteristics. Chapter 3 describes the modelling of an AFO in detail, discussing the construction of the solid model of a leg, the solid model of an AFO and meshing the model. It also includes background information on the properties of plastics and more specific details on polypropylene modelling. Chapter 4 considers the AFO when

subjected to static loading conditions. After describing a technique for kinematic loading and constraint, a series of linear analyses are detailed which assess the effect of varying the distribution of imposed displacement, symmetry and constraint. Mesh refinement is then discussed, including the sensitivity of the model to element density and element type. Analyses including geometric, material and then combined non-linearities are then detailed.

Chapter 5 firstly describes analyses performed to assess the sensitivity of the model to elastic properties and variation in thickness. Analyses simulating published experimental results as a means of validation are then detailed, including the sensitivity of the model to ankle trimline radius and the analysis of large ankle rotations. Experiments performed for further validation and the corresponding analysis are then described. Finally, Chapter 6 consists of the conclusions and recommendations for future work. Appendix A describes a number of test problems that were analysed to assess element accuracy, and Appendix B includes additional figures that were not considered essential to the understanding of the main text. If more detailed information is required on the actual analyses performed, Appendix C includes analysis details specific to ANSYS, and Appendix D includes listings of the more important ANSYS routines developed.

Chapter 2

Background

2.1 Basic Concepts of Human Gait

Human locomotion, or *gait*, is highly complex in nature, and a sound understanding of normal and abnormal gait is extremely important for the design of orthotic devices [Peizer & Wright, 1969]. The walking pattern of any individual represents a solution to the problem of moving about while maintaining acceptable appearance, minimum effort and adequate stability [Bowker & Hall, 1975]. It is the product of interactions between forces generated within the body and those forces acting upon it, which must be coordinated with every step. An observable irregularity can be produced by even the most minor alteration to normal gait. Locomotion can therefore be analysed on two levels, the subjective, observable factors of gait and the objective, biomechanics of gait.

For the purpose of analysis, the lower limb can be simplified to a structure of articulated sticks resembling the limb segments. When viewed from the side, the movement of a single limb repeats with every step, passing through a sequence of standing on the ground followed by swinging in the air. This is known as the *gait cycle* and, by convention, starts the instant that the heel of the swinging limb

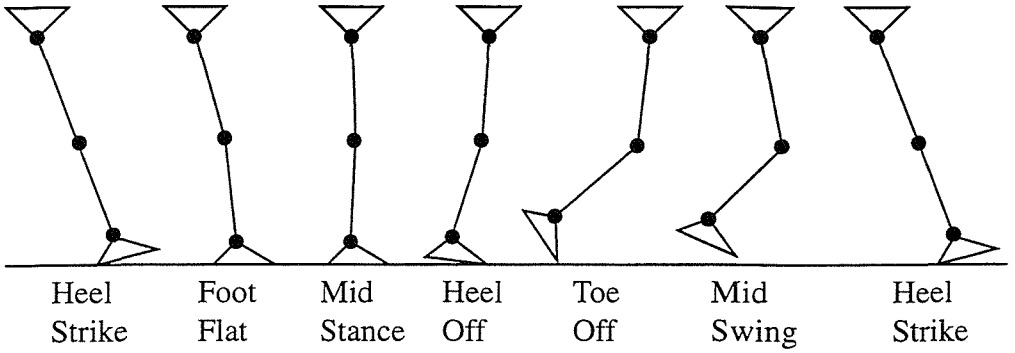

Figure 2.1. The gait cycle

strikes the ground and ends when that same heel next contacts the ground (see Figure 2.1). This period can be divided into two phases, the *stance phase* occupying approximately 60 % of the gait cycle followed by the *swing phase* occupying the remaining 40 %, and these two phases can be further characterised by key events. This sequence is observed with normal subjects when walking over level surfaces, and any other situations, such as uneven ground, inclines or running, will alter these observations.

The stance phase begins at *heel strike*, the instant that the heel of the shoe contacts the floor and the transfer of body weight begins. Shortly after comes *foot flat*, when the sole of the shoe comes into contact with the ground. This is followed by *mid stance*, where the body moves forward over the supporting leg and the person is balanced on the stance limb. Next comes *heel off*, where the heel lifts off the ground, and shortly after this comes *push off*, where the body is propelled forward by primarily the calf muscles. The stance phase ends at *toe off*, when the foot leaves the ground. The swing phase represents the period between toe off and the next heel contact. It consists of a period of *acceleration*, *mid swing* and a period of *deceleration*, where the leg is swung forward in preparation for the next heel contact. *Double support* is the resulting overlap of the stance phases of each leg, where both feet are in contact with the ground. It occurs as a person alternates from the swing phase to the stance phase on each leg, between push off and toe off on one foot, and between heel strike and foot flat on the other.

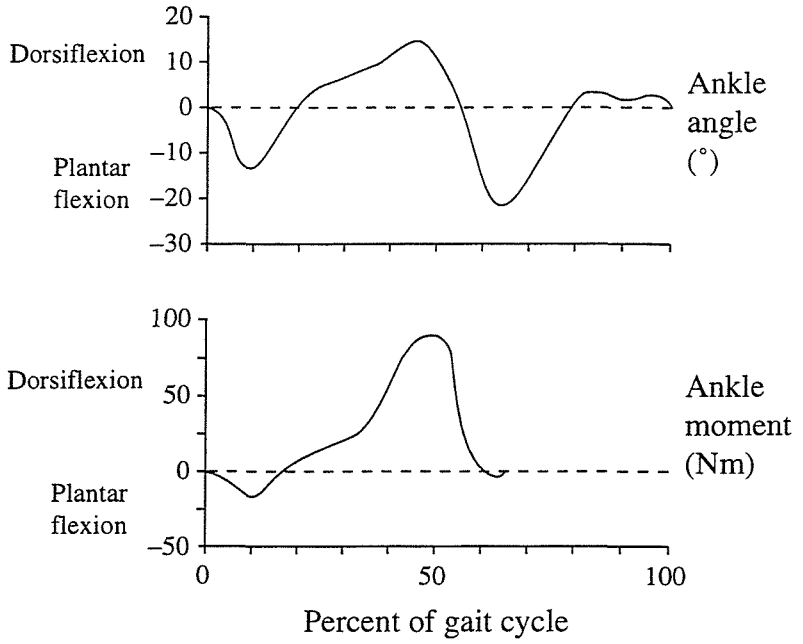

Figure 2.2. Ankle joint kinematics and kinetics (adapted from Peizer & Wright [1969])

The biomechanics of gait considers the motion of and forces on limb segments that produce gait. In the sagittal plane, the ankle angle and moment can be plotted over one complete cycle, leading to a number of conclusions (see Figure 2.2). At heel strike the foot is in an approximately neutral position, and as the body weight is transferred to the stance limb the ground reaction force creates a moment tending to cause plantar flexion of the foot. This moment reaches its peak of about 26 Nm (19 ft lb) just before foot flat, and coincides with a peak ankle angle of 15 ° to 20 ° plantar flexion. The motion at this stage is governed by contraction of the ankle dorsiflexors, which absorb the moment while allowing the ankle to move into plantar flexion to control foot slap.

The anterior progression of the tibia relative to the foot after foot flat causes the ankle joint to move from plantar flexion to a maximum dorsiflexion angle of 15 ° just prior to heel off. This coincides with a large dorsiflexion moment generated about the ankle joint, which reaches a peak of about 95 Nm (70 ft lb) shortly after heel off, due to the ground reaction force being in front of the ankle joint. The rate of motion is controlled at this stage by contraction of the plantar flexors to limit

dorsiflexion. The dorsiflexion moment then falls rapidly up to toe off, and is accompanied by a reversal in the direction of ankle motion to a maximum plantar flexion angle of 15 °. This is due to contraction of the plantar flexors to provide push off. During swing, the ankle returns to its neutral position in preparation for the next heel contact, although the dorsiflexors are active to provide toe clearance.

Rotation in the frontal plane is of less magnitude than that in the sagittal plane. Between heel strike and foot flat, the subtalar joint moves in the direction of eversion about 6 ° from its initial position of inversion to approximately a neutral position. With a large amount of body weight applied at foot flat, an inversion moment reaching a peak of about 20 Nm (15 ft lb) is generated, although the foot remains in the same position due to the activity of the evertors. The inversion moment steadily decreases up to toe off, and the subtalar joint inverts from mid stance to a peak of about 6 ° just before toe off. Considering rotation in the transverse plane, the tibia rotates internally by 9 ° from its initial position of external rotation at heel strike until it reaches a peak shortly after foot flat. The tibia then rotates in the opposite direction by 17 ° until toe off, passing through its initial position just after heel off. The torque about the tibia during this rotation reaches a peak of about 7 Nm (5 ft lb) directed internally just prior to heel off.

The reaction forces between the foot and the floor can be measured with a force plate, a device upon which a subject may stand or walk. This can measure the magnitude and direction of the vertical force, the anterior/posterior shear force, the medial/lateral shear force, and also the internal/external moment about the long axis of the tibia. The vertical Ground Reaction Force (GRF) for a normal subject walking barefoot is characterised by a curve with three peaks (see Figure 2.3) [Czerniecki, 1988]. The first transient, which is termed step shock, reaches a peak of 0.85 body weight (BW) immediately following heel strike, although this can be diminished and even eliminated when impact absorbing footwear is worn. The centre of pressure (and ground contact point) of the foot at this instant is positioned at the posterior and lateral part of the heel. The second peak, due to the maximum deceleration of the CG, reaches 0.8 to 1.1 body weight during the

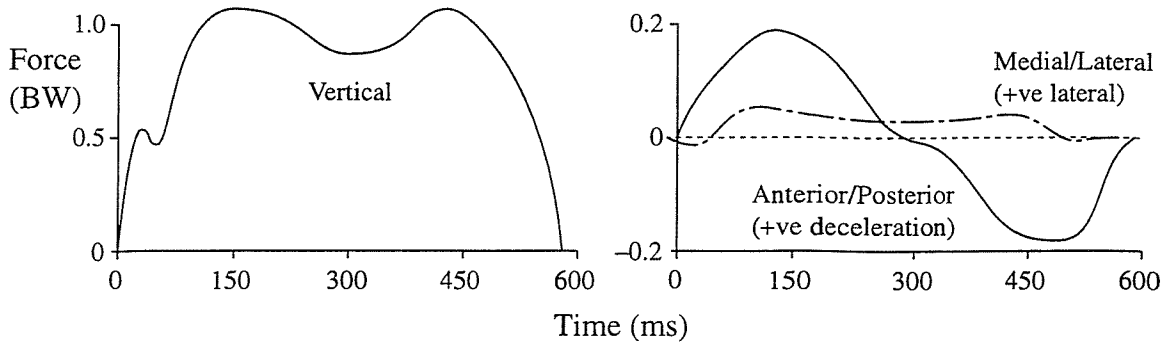

Figure 2.3. Ground reaction forces during walking

first 20 % of stance.

The magnitude of the vertical GRF decreases between foot flat and heel off to 0.8 body weight at 50 % stance phase, and the centre of pressure moves forward rapidly towards the metatarsal area. The highest forces occur in the period between heel off and toe off, although they are applied at a lower rate than before, and the thrust peak of the vertical GRF due to maximum acceleration of the CG is 1.3 body weight. The anterior/posterior (braking and propulsive) and medial/lateral GRFs are much smaller in magnitude than the vertical GRF, reaching only 0.15 to 0.2 body weight and 0.05 body weight respectively. The GRFs and loading rates are also a lot higher during running than those experienced in walking.

2.2 Biomechanics of the Foot and Ankle

The biomechanics of the foot and ankle is a complex, integral part of the biomechanics of the lower limb [Mann, 1975]. The articulation of the talus with the tibia and fibula is known as the ankle joint (see Figure 2.4). The axis of rotation about this joint passes distal to the tips of the medial and lateral malleoli, the bony protrusions at the distal end of the tibia and fibula respectively, and can be estimated as the line joining each malleolus. The projection of this axis onto the transverse plane is directed laterally and posteriorly and is at an angle of

approximately 84 ° to the longitudinal axis of the foot, which passes between the second and third toe.

The ankle joint axis is directed laterally and distally (downward) in the frontal plane, and the angle between this axis and the long (vertical) axis of the tibia is approximately 80 °. The inclined orientation of this axis is of functional significance, as motion of the foot about the ankle in the sagittal plane is accompanied by rotation in the transverse plane, and also rotation of the foot about its longitudinal axis [Czerniecki, 1988]. Alignment of the ankle joint axis is the most important factor to consider when designing orthoses. The motion that occurs about the ankle joint is dorsiflexion and plantar flexion.

The subtalar joint is the articulation between the talus and the calcaneus, and its axis is directed laterally and posteriorly in the transverse plane, at an angle of approximately 23 ° to the long axis of the foot. In the sagittal plane the axis is directed posteriorly and distally, at an angle of approximately 41 ° to the ground. Motion occurring at the subtalar joint is inversion and eversion, where the calcaneus moves toward and away from the midline of the body respectively. The subtalar axis acts as an oblique hinge, where external (outward) rotation of the leg about the tibia produces inversion of the calcaneus, and internal (inward) rotation causes eversion. Therefore, rotation in the subtalar joint is coupled to the rotation of the lower segment, and this motion is passed through the talus and calcaneus to the navicular and cuboid bones respectively.

The transverse tarsal joint is composed of the articulation between the talus and navicular (talonavicular joint) and the articulation between the calcaneus and cuboid (calcaneocuboid joint), and any combination of motion in the talus and calcaneus affects its stability. With the hindfoot everted, the axes of these two joints are parallel and relatively free motion can occur about them. However, with the hindfoot inverted, these axes are divergent and some degree of restriction in the joint is present. The motion that occurs at this joint is primarily in the plane of abduction/adduction, where the fore part of the foot moves outward and inward in the plane of the sole. The navicular articulates with the three cuneiforms, which

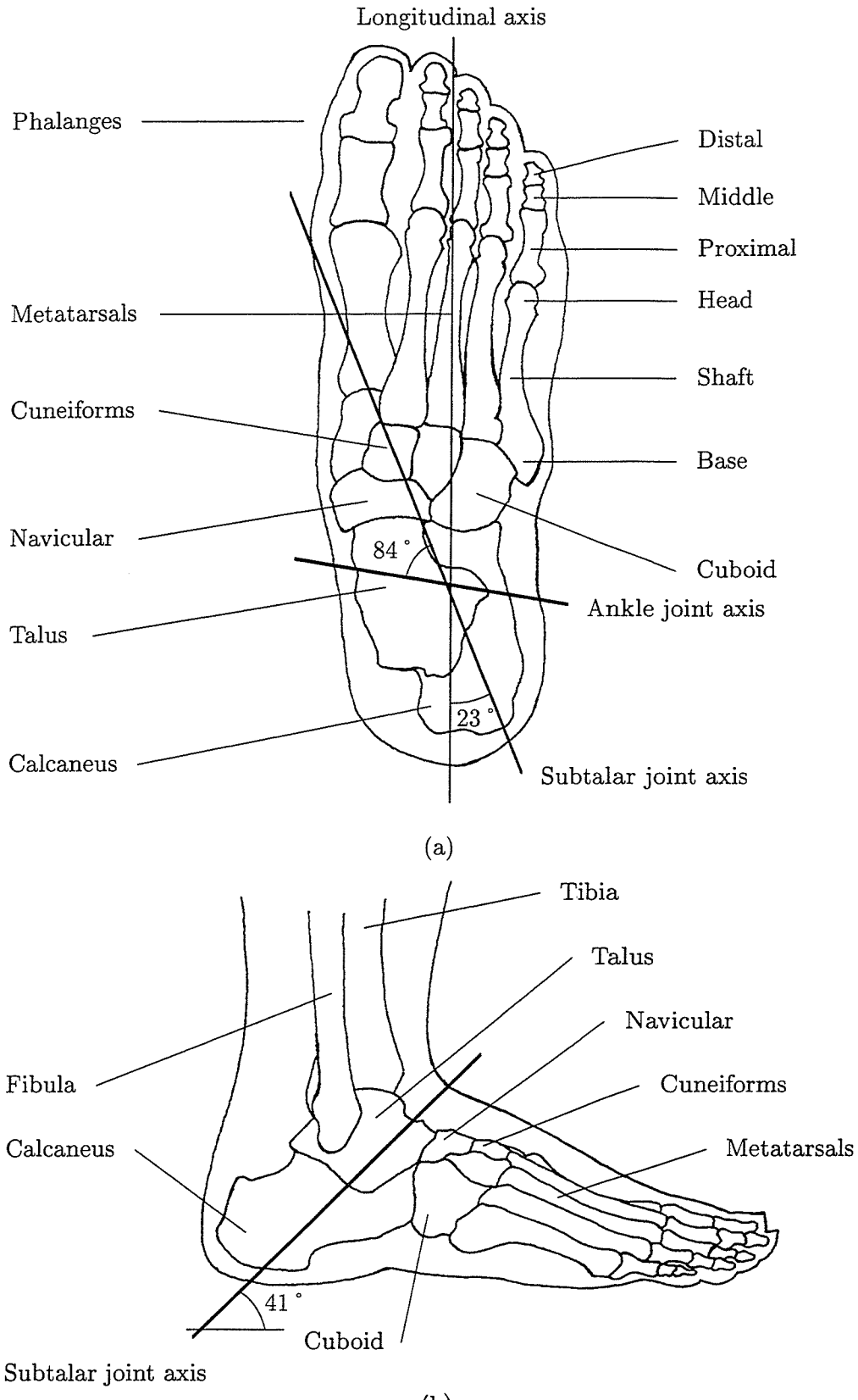

Figure 2.4. Bones of the foot. (a) superior view. (b) lateral view.

themselves articulate with the three medial metatarsals, and the cuboid articulates with the two lateral metatarsals. The articulation between the metatarsals and the phalanges (metatarsophalangeal joints) is called the metatarsal break. In the transverse plane, this axis passes from the head of the second (most distal) metatarsal to the head of the fifth (most proximal) metatarsal, at an angle of approximately 62 ° to the long axis of the foot.

During normal locomotion, each lower segment of the skeleton (consisting of part of the pelvis, femur, tibia and fibula) undergoes rotation in the transverse plane, and this acts on the talus, which transmits this rotation through the subtalar joint to the foot. The lower limb rotates internally during swing and early stance, causing the hindfoot to become everted. This results in a relatively flexible longitudinal arch of the foot, allowing the foot to easily adapt to uneven terrain. The lower limb then rotates externally until just after toe off, causing the hindfoot to become inverted and producing a more stable longitudinal arch of the foot to enable push off. The transverse tarsal joint and joints distal to this therefore cause a conversion of the flexible foot into a rigid arch system. Any abnormality in the function of one of the segments will therefore cause the gait pattern to be altered.

2.3 Conventional AFO Designs

The double upright, metal AFO consists of two metal uprights attached to a metal stirrup at their lower ends with hinged ankle joints (see Figure 2.5) [Halar & Cardenas, 1987]. This stirrup is built into the layers of the sole of the shoe, and it includes a sole plate of a certain length extending anteriorly. The metal uprights are also connected proximally with a rigid posterior calf band and a soft anterior closure (usually Velcro). One or two adjustable stops may be incorporated into each upright to restrict motion at the ankle joint, an anterior stop limiting dorsiflexion and a posterior stop limiting plantar flexion. Metal springs may also be used to assist motion in either direction if desirable. This type of AFO requires an 'orthopaedic' shoe of sturdy design and construction, usually having leather

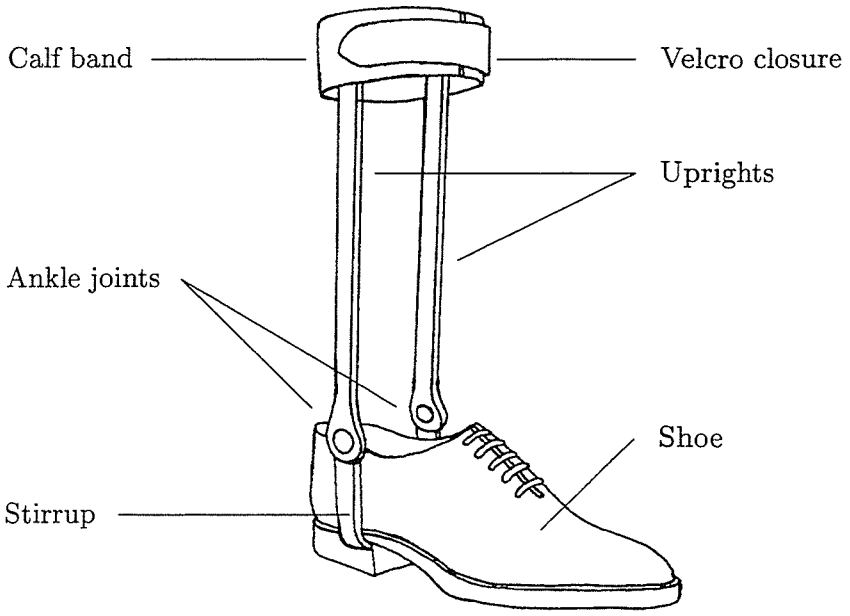

Figure 2.5. Conventional double upright, metal AFO

soles, hard rubber heels and a special opening and lacing suitable for one-handed closure. With the proper shoe accurately attached to the AFO, the best possible force transmission between the ground and the patient's leg will result.

A plantar flexion stop can be used to simulate the dorsiflexors in picking up the toe during swing, and also decelerating the foot at heel strike to prevent foot slap [Lehmann, 1979]. At heel strike, the ground reaction force is located at the posterior part of the heel and creates a flexion moment at the knee joint, making the knee unstable and prone to buckling in patients with weak knee extensors. This flexion moment will become smaller in magnitude and duration as the posterior stop is set in a more plantar flexed position, as the ground reaction force is located more anteriorly. Therefore, the amount of plantar flexion allowed by the stop is a compromise between providing enough toe pickup, which improves as the position of the posterior stop becomes more dorsiflexed, and knee stability, which increases as the stop becomes more plantar flexed. In some cases, providing enough toe clearance may still cause an uncontrollable flexion moment at the knee.

Therefore, a heel cut-off can be used to relocate the ground reaction force more anteriorly to minimise the moment.

A dorsiflexion stop can be used with a sole plate extending to the metatarsal heads to simulate the plantar flexors at push-off. At this instant, the ground reaction force is located at the metatarsal head area and is directed ahead of the knee, creating an extension moment about it which causes stability and effectively locks the knee in position. Although the knee will not buckle, if this extension moment is too great and applied over a long duration it can damage the knee, resulting in 'back-knee'. This extension moment about the knee will become larger in magnitude and duration as the anterior stop is set in a more plantar flexed position. Using both stops simultaneously, maximum stability of the knee during stance and minimum instability at heel strike can be obtained by setting the ankle in a more plantar flexed position, however this results in the least toe clearance during swing. Therefore, a compromise must be reached whereby the least amount of assistance required to provide adequate toe clearance is used.

Improvements can be made in the function of this type of device by incorporating plastic components into its design. One such design is the NYU (New York University) Insert Orthosis [LeBlanc, 1972]. This consists of a double upright, metal AFO with the stirrup laminated into a custom-made shoe insert at manufacture, rather than being fixed within the shoe. This type of orthosis has been found to provide pain relief, proper support of the foot, good control of the foot and ankle, better cosmesis, and to make possible the interchange of shoes, although it would be difficult to manufacture and would usually require wider shoes. Another such design, the patellar-tendon-bearing AFO, consists of a double upright, metal AFO with the calf band replaced by a custom-made, plastic calf enclosure. This can provide a wider contact area with parts of the leg, helping to reduce the loading at the ankle by bearing part of the body weight at the patellar tendon. One disadvantage of both these types of AFO is weakness at the interface between the plastic and metal parts, limiting their applications.

Another conventional type of AFO is the single upright AFO, which may be

prescribed for minor disorders of the lower limb. It consists of a calf band attached to an upright, a single ankle joint and a stirrup built into a shoe or plastic insert. The upright may be permanently attached to the back or side of the shoe, or alternatively it may clip on allowing easy transfer between shoes. An example is the UC-BL (University of California Biomechanics Laboratory) Dual-Axis Ankle Orthosis, which consists of a single metal upright positioned on the lateral side of the leg and attached to a calf band. Two joints are located at the other end of this upright, the lower of which attaches to the shoe, to duplicate the combined motion of the ankle and subtalar joints. It has been found that this design of AFO was light, cosmetic and gave freedom of movement, although it was difficult to fabricate and required special alignment jigs.

The advantage of conventional orthoses is that their mechanical characteristics are relatively simple to predict, and they can be idealised as a pivoted, rigid lever which can be either free to rotate, locked or spring assisted [Condie & Meadows, 1977]. The disadvantages of these types of orthosis are that they are generally over designed to prevent breakage, which could be caused by poor fit or alignment, and they were therefore heavier than necessary [Lehneis, 1974]. In some cases they applied more control than was required, which could result in the wasting away of near normal muscles that were not permitted to be active [Engen, 1972]. They were also unhygienic, had poor cosmesis, and they could only be used with one pair of shoes.

2.4 The All-Plastic AFO

A modern, plastic AFO is worn inside a normal shoe and exerts corrective forces directly onto the patient's limb, rather than through the shoe [Jebsen *et al.*, 1968]. It can be identified by three basic regions, the posterior calf enclosure, the posterior ankle enclosure and the foot enclosure, and its boundary is defined by a number of trimlines (see Figure 2.6) [Halar & Cardenas, 1987]. During manufacture, the proximal trimline should be positioned just below the head of the

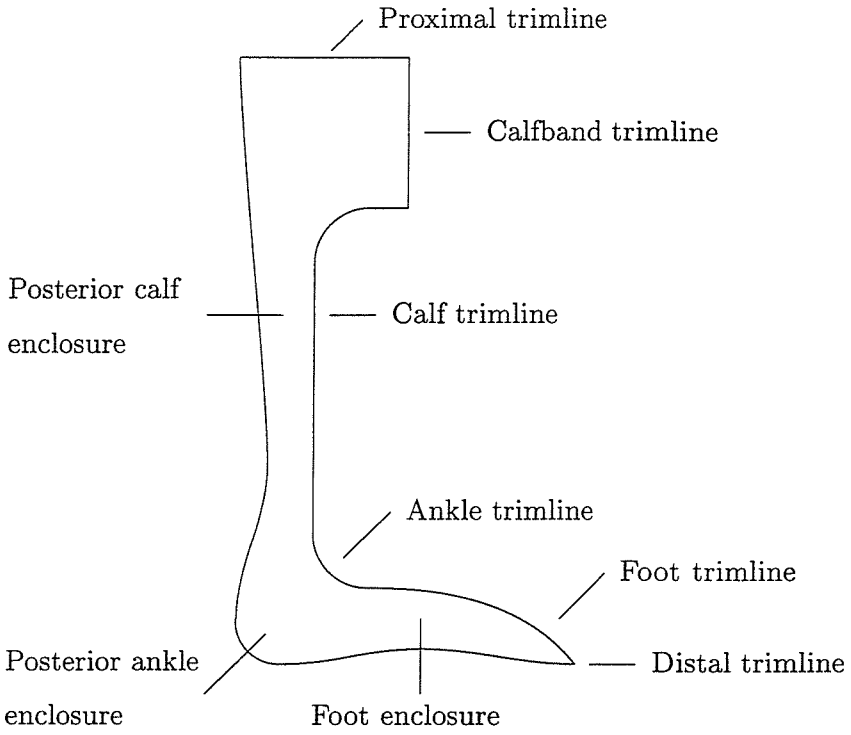

Figure 2.6. Regions and trimlines of a plastic AFO

fibula, encircling 3/4 of the calf circumference. The calf trimline (anterior trimline) connects the proximal trimline to the ankle trimline, and generally curves posteriorly as it moves distally. The ankle trimline location is the most important factor affecting AFO rigidity, and the more anterior it is located, the greater the resistance to rotation about the ankle [Stills, 1975]. Therefore, when flexibility is required the ankle trimlines should be posterior to both malleoli, whereas they may surround the malleoli when motion about the ankle is not desirable. The distal trimline should extend to the metatarsal heads. Care must be taken to ensure the trimlines do not lie close to a bony prominence, as pressure areas can occur causing discomfort.

The mechanical characteristics of a particular AFO are evaluated based on its resistance to rotation of the foot about the ankle joint. The corrective forces that need to be applied by an AFO to the patient's limb during gait are generated from deformation of the ankle region of the AFO [Yamamoto *et al.*, 1993a]. Since the device is vacuum formed over a mould of the patient's leg, its geometry depends on

the particular patient. Therefore, the rigidity can only be adjusted by altering the material thickness and location of the trimlines, although corrugations can be incorporated into the device during manufacture to provide local reinforcement. The orientation of the foot region with respect to the calf region will also affect the functioning of the device, and should be considered during casting.

There are several stages in the manufacture of a custom-made, plastic AFO. The patient's lower limb is firstly wrapped with plaster of Paris bandage and the attitude of the foot relative to the calf is adjusted to give the required amount of dorsiflexion, ensuring that correct ankle alignment is maintained while hardening [Murray & Greenfield, 1970]. The cast is then removed from the patient, by cutting it open and sealing with bandage, and a positive, plaster of Paris cast is then obtained from this negative cast. When hardened and removed from the negative cast, the surface of the positive cast is then smoothed and, if necessary, modified by either building up the surface to provide relief in sensitive areas, or by removing material to incorporate control areas in the AFO for applying corrective forces. Problems can be encountered during casting due to spasm produced by various stimuli (including heat emitted from the plaster) resulting in a misshapen cast [Anderson & Meadows, 1979]. An awareness of tonic reflexes is therefore essential in orthotic management, as this problem can be reduced by careful positioning of the body in a relaxed position during casting, reducing muscle tone.

The remaining stages of manufacture involve heating the thermoplastic material in an oven and then applying it to the positive cast through vacuum forming and manual draw of the material. Some methods involve lowering the thermoplastic material onto the cast, which is placed on the flat bed of the machine, and then generating a vacuum between the material and this surface to induce the material to form closely to the contours of the cast. An alternative technique adopted by St. Mary's Hospital (Isle of Wight) involves wrapping the material around the positive cast and then generating a vacuum between the cast and a porous stockinet placed over the cast before manufacture. After the material has cooled, the AFO is trimmed to the desired shape. Prefabricated AFOs are also available

mass produced in a range of sizes, and they can be modified to suit a specific patient by trimming and localised heating and reforming [Staros & LeBlanc, 1975]. However, for permanent use, custom-made ones are preferred.

The principles applied to conventional orthoses with regard to plantar flexion and dorsiflexion stops are equally valid for plastic AFOs [Lehmann, 1979]. As plastic AFOs cannot be adjusted after manufacture to the same degree as conventional orthoses, the ankle angle at casting is very important. The foot must be cast at an ankle angle sufficient to provide toe clearance during swing and yet minimise the flexion moment about the knee at heel strike. The extension moment during late stance, which stabilises the knee, can be set when trimming around the ankle. The length and rigidity of the foot enclosure, the equivalent of the sole plate in a conventional orthosis, can also be adjusted.

The main advantages of modern, plastic designs of AFO are that they are more cosmetic and hygienic, lightweight, easily applied or removed, and as they require no shoe attachments can be used with different shoes. They are also worn inside the shoe, providing the positioning and support of the foot, and this change in function has allowed the use of more cosmetic and readily available commercial shoes, rather than special orthopaedic shoes [Hicks *et al.*, 1989].

The disadvantages with plastic AFOs are that they can break at the junction between the foot and ankle trimlines, the edges can cause skin breakdown, and prefabricated AFOs cannot control severe deformities in some cases. Some designs have a tendency to buckle at the ankle region during the stance phase of gait, and subtle factors such as excessive heat or forming forces can cause a significant difference in wall thickness [Golay *et al.*, 1989]. Unlike conventional orthoses, plastic AFOs have no discrete ankle joint axis and so their behaviour is unpredictable [Condie & Meadows, 1977]. Therefore, as plastic AFOs cannot be set to provide a specific corrective force as easily as conventional AFOs, a trial and error policy has been the method adopted by orthotists in the past for assessing the advantages of new designs.

2.4.1 Alternative Designs

Jebsen *et al.* [1968] devised a plastic AFO (the Seattle orthosis) whereby the positive cast is modified with a build-up of plaster over both malleoli and, if necessary, removal of plaster around the calf to control varus or valgus deformity of the foot. Four layers of nylon stockinet are then placed over this cast, including fibreglass reinforcement at the ankle, and then polyester resin is applied over them. When the material has hardened, the AFO is trimmed to the desired shape and an anterior Velcro strap closure is attached. To control varus deformities, the ankle trimlines completely cover the lateral malleolus and partially cover the medial malleolus, and for valgus deformity this is reversed. This design was found to provide plantar flexion control and medial/lateral stability for patients with flaccid and spastic lower limbs, and the device could be used with normal size shoes, usually worn over a thin stocking, although if tight around the heel a wider shoe was necessary. The disadvantage with this design is that it is more expensive and time consuming to manufacture than other types of plastic AFO.

Murray & Greenfield [1970] also developed a plastic AFO (the Rancho orthosis) of similar shape to the previous device, but this design was moulded from polypropylene. Firstly, the surface of the positive cast is built up over each malleolus with felt. Polypropylene sheet is heated in an oven until clear, placed around the cast and then brought together along two edges. To avoid marking the surface, the plastic is only finally moulded to the contours of the cast when the surface has cooled, and after cooling the AFO is cut to the desired shape and the edges are smoothed. They found that it cost the same as a conventional device to manufacture and that pressure areas could be relieved by locally heating and stretching the material during fitting, but a wider fitting shoe could be required.

Engen [1972] developed a new design of plastic AFO with the Texas Institute of Rehabilitation and Research (TIRR). Initial designs manufactured from polypropylene were found to be too flexible to provide sufficient assistance, but further experimentation showed that corrugations could be integrated into the

walls of the design and provided sufficient strength without compromising the weight. Circular section nylon rods were secured to the positive cast to produce the corrugations. After heating the polypropylene sheet, it was folded over the posterior region of the cast, stretched over the heel portion and then pinched together to form a seam at the anterior surface. The material was then shaped around the corrugations and, after hardening, the AFO was removed from the cast, trimmed to the desired shape and the edges smoothed.

A padded insert was then fixed to the inside of the calf region, and a Velcro calf strap fastening was attached. The trimline included two cut-outs, one at the heel region and another above this. The device was found to provide dorsiflexion assistance, medial/lateral stability and its rigidity could be customised for an individual by adjusting the width of the trimline above the heel cut-out, enabling the device to meet a range of requirements, although a more careful fitting process was required as the contours were critical to its functional characteristics. Rubin & Dixon [1973] found that the device could be adjusted to provide a high resistance to motion by also closing the heel opening.

The spiral AFO was designed by Lehneis [1974] to control motions in every plane, and is manufactured from an acrylic-nylon thermoplastic material. The spiral region starts from the medial side of the foot, passes posteriorly around the leg for 360 $^{\circ}$, and ends at the medial side of the leg below the knee with a calf band. It allows controlled plantar flexion through the spiral unwinding, and rewinding of the spiral provides dorsiflexion. The pre-cut calf band is heated and formed over the positive cast such that the opening is on the lateral side of the calf just below the neck of the fibula. When cooled, the pre-cut spiral part is heated and then wrapped around the foot and leg such that it overlaps the medial part of the calf band.

After cooling, the two pieces are drilled and, upon removal, riveted together. The edges are smoothed, and any adjustments are made during fitting with a heat gun. A similar design, the hemispiral AFO, starts from the lateral side of the foot, passes around the back of the leg 180 $^{\circ}$, and ends at the medial side of the leg,

resulting in greater stiffness than the full spiral. It was found that both designs resulted in a reduction in energy expenditure, and polypropylene could be used as a replacement material for the spiral AFO with patients experiencing early breakages. Rubin & Dixon [1973] found that the spiral AFO is more expensive and suffered from a higher frequency of breakages than other designs of AFO.

Other designs of plastic AFO include the Teufel AFO, which is manufactured from Ortholen and commercially available in a range of preformed sizes [Rubin & Dixon, 1973]. The design is trimmed well posterior to the malleoli, causing a posterior leaf spring (PLS) effect which permits dorsiflexion, resists plantar flexion, but provides no medial/lateral stability [Halar & Cardenas, 1987]. Stills [1975] developed a plastic AFO similar to the laminated Seattle orthosis, but this was vacuum-formed from a sheet of heated thermoplastic, usually polypropylene due to its light weight, low cost and high fatigue resistance. The Hartshill orthosis is manufactured from polypropylene, and the ankle trimline extends forward to the medial malleoli resulting in a rigid device [Condie & Meadows, 1977].

Italiano *et al.* [1986] utilised the results from both experimental and analytical analyses to develop a lightweight plastic orthosis with a uniform stress distribution. By reducing the thickness of the device in low stress regions using a milling machine, a weight reduction of 27 % was achieved. An anterior leaf spring AFO has been designed by Wong *et al.* [1992] for indoor barefoot walking, although they found no significant difference between this design and a posterior trimmed AFO. Breakages also occurred in patients with strong spastic reflexes after only four weeks of gait training, although they concluded that this was due to the weakness of the thermoplastic material.

2.4.2 Materials

There are a number of different sheet plastics available for use in manufacturing AFOs, and although several different materials might be suitable for a particular device, the choice may be subjectively based on the orthotists prior experience

[Showers & Strunck, 1985]. The choice of material will also govern to some extent the fabrication techniques used. Polypropylene is the most commonly used material for AFOs and is available in a range of grades. Standard grade is the most common but it can become brittle and discolour with age, copolymer is slightly more flexible than standard grade, and Orthopaedic grade is similar to standard grade but with additives making it the most flexible of the three.

North Sea Plastics Ltd., who are specialists in plastic materials for prosthetics and orthotics, supply a range of thermoplastics for use with AFOs [NSP, 1995]. Homopolymer polypropylene provides good chemical resistance and moulding properties, although it has a low impact resistance and is 'notch' sensitive. It is available stress-relieved in a range of thicknesses, all in a natural colouring. A less rigid copolymer polypropylene is also available in a wide range of colours, and its advantages over homopolymer include a higher impact resistance. High density polyethylene is also a popular material and, like copolymer polypropylene, offers good impact resistance and flexural strength. It is available in a range of colours and thicknesses, but it shrinks when heated. Ortholen, an ultra high molecular weight polyethylene, has excellent impact properties, is very tough and has good flexural strength, although it is difficult to mould. Sub-Ortholen, a high molecular weight polyethylene, is similar to Ortholen but is more easily moulded.

2.5 Experimental Studies of Plastic AFO Characteristics

2.5.1 Review

Condie & Meadows [1977] utilised equipment developed at the Dundee Limb Fitting Centre (DLFC) to measure the characteristics of a number of designs of plastic AFOs, which were all quoted as being for flaccid conditions of the foot. The 'characteristic' of an AFO was defined as the resistive moment generated when the

foot region of the device is rotated about the ankle joint. This moment would increase with increasing deflection of the AFO in the sagittal plane, and this relationship could be plotted in the form of a graph. The AFO tested was clamped to the apparatus at the calf band and foot regions, and it was deflected through its normal range of motion by motion of the foot region relative to the calf. The moment/angle characteristics about the ankle joint were plotted directly by the apparatus, allowing comparisons between different orthoses and also analysis of the effects of varying the trimlines of an individual orthosis.

The designs of AFO examined included the Teufel orthosis, the Hartshill orthosis and the TIRR orthosis. Results showed that the TIRR and the Teufel orthoses had relatively low stiffness compared to the Hartshill orthosis, and were assumed to be more appropriate for patients with isolated weakness of the dorsiflexor muscles (drop foot) as they provided the least resistance to movement controlled by unaffected muscles. Also evident from the results was that the stiffness of the Hartshill orthosis in dorsiflexion reduced with increasing moment, indicating some form of non-linear behaviour, although it was stated that this device was normally forced into extreme dorsiflexion at fitting to reduce its resistance to motion in that direction.

For more general ankle-foot disorders including spasticity, the DLFC customise the Hartshill design by moving the ankle trimlines forward, rather than using the spiral orthosis which, in their experience, had fracture problems. The increase in the stiffness characteristics of such a device were shown through testing. With more severe cases, rather than using the hemispiral, which they found effective when correctly fitted but difficult to manufacture and awkward to don, the DLFC further adapted the Hartshill AFO to impose forces to the patient's limb to correct varus or valgus deformity. This is achieved by applying such forces by hand, while the plaster bandage sets, and also by further modifying the positive cast if desired. This modified design was found to be only slightly more difficult to manufacture and don than the standard Hartshill design.

Chowaniec *et al.* [1979] have described a test rig designed to measure the

mechanical characteristics of plastic AFOs by trying to simulate realistic loading conditions, although no results were presented in this work. An AFO was clamped at the foot region, and the calf band region was also clamped in such a way as to constrain anterior/posterior and medial/lateral translations, but allow vertical translation and rotations about all three axes. Deformation was then applied by moving the foot region relative to the calf band region, although exact details were not given. A load transducer was used to measure plantar flexion/dorsiflexion and inversion/eversion moments, and four potentiometers were used to measure the rotations and vertical translation.

Lehmann *et al.* [1983] have examined the amount of plantar flexion and dorsiflexion resistance provided by a number of designs of plastic AFO during gait. These included the commercially available TIRR and Teufel orthoses, both of which are trimmed posterior to the malleoli, and also a custom-made design of orthosis. This is based on the more expensive and slightly more rigid laminated plastic Seattle orthosis, which is trimmed anterior to the malleoli, but is vacuum-formed from high density polypropylene. They also studied the effects of trimming the custom-made orthosis to two additional configurations, to make it comparable to the TIRR and Teufel orthoses. From the initial trim, these subsequent trims were formed by cutting away at the AFO to produce a more posterior trimline about the ankle.

For the above experiments, both hemiplegic and normal subjects walked with each orthosis while a device measured ankle angle. A gait event marker system was also used to record occurrences of gait events for left and right limbs. Comparisons between measurements showed that the initial trim of the custom-made orthosis was the least flexible, providing the greatest resistance to both plantar flexion and dorsiflexion, and differences in gait were evident between hemiplegic and normal subjects. Progressive trimming of this orthosis posterior to the malleoli made it more flexible at the ankle and comparable in function to the TIRR and Teufel orthoses. They also found that setting the orthosis in slight dorsiflexion when forming provided additional dorsiflexion lift during swing, and concluded that it is

desirable to have a single design of AFO such that this resistance can be modified to suit a range of requirements.

Golay *et al.* [1989] investigated the effect that malleoli prominence had on the rigidity of plastic AFOs during dorsiflexion. Rigidity was defined as the relationship between applied load and sagittal plane rotation of the foot region relative to the calf. The testing apparatus consisted of a below knee prosthetic leg with a hinged ankle joint, onto which an AFO was fixed via a calf strap, and the foot part of this assembly was mounted to the apparatus. A tensiometer was attached to this calf strap to measure force, which was applied perpendicular to the tibial axis of the prosthesis using a winch mounted to the apparatus. Positive casts of the artificial leg were obtained and modified with no plaster build-up over the malleoli, 6.35 mm (1/4″) build-up, 12.7 mm (1/2″) build-up, and 19.05 mm (3/4″) build-up. Three identically trimmed polypropylene AFOs were then vacuum formed over each of these positive casts, and the medial and lateral sagittal wall thickness at the malleoli regions were compared to ensure minimum variations due to manufacture.

Before testing, the malleoli apex diameter for each AFO was measured for calculation purposes. Each AFO was then deformed into 16 ° dorsiflexion in increments of 2 °, using an angular scale to set the angle from a reference point on the proximal edge of the AFO. At each interval, the applied force was read off the tensiometer and the malleoli diameter was measured with a vernier calliper. Plots of applied load versus ankle angle for each build-up revealed that AFO rigidity decreased with increasing malleoli build-up, and the AFOs with no build-up were significantly more rigid than those with build-up. There was also a significant difference in rigidity between AFOs with 6.35 mm build-up and those with a greater build-up, although not significantly between AFOs with 12.7 mm build-up and 19.05 mm build-up. These plots also indicated a linear variation up to a certain load level, after which the curves became non-linear with decreasing rigidity.

Plots of 'diametrical strain', the percent increase in malleoli diameter, versus ankle

angle revealed that the diametrical strain decreased with increasing malleoli build-up. There was a significant difference between all of the AFO categories, except those with 6.35 mm and 12.7 mm build-ups, although at small angles the results were scattered. The investigators concluded that when designing an AFO to restrain motion about the ankle, a compromise must be reached between providing maximum rigidity, which requires minimal malleoli build-up, and avoiding excessive pressure areas, which requires maximal malleoli build-up. They also stated that malleoli build-up effectively 'pre-buckles' an AFO, whereby it losses a significant amount of rigidity although its diametrical strain remains low when under load.

Yamamoto *et al.* [1993a] adapted a muscle training machine to measure the flexibility characteristics of various types of plastic AFO when fitted to a patient's limb. The flexibility was defined as the relationship between ankle or subtalar joint angle and resistive moment, depending on which of the two axes was being studied. After donning an AFO, the patient's foot was secured to a foot plate, which in turn was fixed to a pulley whose rotational axis was aligned parallel to either the ankle or subtalar joint axis. Then, with the patient sitting with completely relaxed limb muscles, the pulley rotated at a constant velocity through the normal range of motion. The resistive moment measured in this manner indicated the sum of the resistive moments of the AFO and passive components of the ankle or subtalar joint. These two tests were performed on a number of AFOs, including three posterior spring type AFOs with different trimlines at the ankle joint, three anterior spring type AFOs, and two spiral type AFOs. Both tests were repeated for the patient without AFO to give the resistive moment of the passive components of their ankle and subtalar joints, and the difference between these results and the previous represented the resistive moment of the AFO.

Plots of ankle joint and subtalar joint angle versus resistive moment for each AFO showed a hysteresis loop when the direction of motion was reversed. The posterior spring type AFOs were found to be the most rigid of the orthoses on test. They were very rigid in dorsiflexion but had even greater rigidity in plantar flexion, and

they also had relatively high rigidity in inversion and eversion. Flexibility in plantar flexion was found to depend on the width of the ankle region of the AFO, while the height of the trimline in this region affected the flexibility in dorsiflexion. The anterior spring type AFOs were found to be less flexible in dorsiflexion than plantar flexion, and they had relatively low rigidity in all directions. The hemispiral AFO was quite rigid in plantar flexion, inversion and eversion, but flexible in dorsiflexion, whereas the full spiral AFO was flexible in both dorsiflexion and plantar flexion. To examine the viscous properties of the AFO materials, all measurements were carried out at three different loading rates, 5, 10 and 50 ° per second, although results showed that the flexibility of the AFOs was not affected by the velocity of applied loading.

Lunsford *et al.* [1994] have examined the viscoelastic behaviour of paediatric, solid ankle (Rancho) AFOs under cyclic loading conditions. The test apparatus consisted of a steel frame, an electric motor, a crank with push rod, and a child's artificial leg hinged at the ankle. Three identical AFOs were manufactured from polypropylene sheet, vacuum formed over a positive cast of the artificial leg, and measurements of the wall thickness at specific locations revealed minimal variations between each AFO. After the AFO had been attached to the artificial leg via a calf strap, the assembly was mounted to the testing apparatus by clamping the foot region. It was then deformed into 10 ° dorsiflexion by manually applying a force via the push rod attached to the calf strap region of the artificial leg. The ankle angle was confirmed with a protractor, and a mean force was calculated from values measured using a force gauge from three successive tests.

The push rod was then attached to the crank and a continuous cyclic loading was applied to the assembly from 10 ° dorsiflexion to 15 ° plantar flexion. At intervals of 24, 48 and 72 hours, the loading was stopped and a force value recorded in the same manner as before. After 72 hours of cyclic loading had ceased, force values were also obtained at 15, 30, 45, 60, 240 and 540 minutes of recovery. At the same time intervals that the force measurements were obtained, the AFO malleoli diameter was also measured in the 10 ° dorsiflexion position using a dial calliper.

This allowed the diametrical strain to be calculated, which represents buckling in the malleoli region, and in this case was expressed as the percentage change in malleoli diameter with respect to the pre-cycling, unstressed diameter.

The mean and standard deviations of the applied force revealed that the AFO stiffness decreased significantly over the first 24 hours of loading, although not significantly over the remaining two 24 hour periods. During recovery, the stiffness increased significantly during the first 15 minute period, and after 60 minutes the AFO had fully recovered. The variations in diametrical strain of the AFO were not as large as the stiffness, but followed similar trends. Note that diametrical strain had increased following cyclic loading. During cyclic loading of each AFO, crazing (microfracturing) of the material was evident on all three specimens just above the ankle trimline as a discoloured area. This indicated that the stresses in this region had caused permanent plastic deformation of the AFO, although it was stated that this would not affect its ability to resist dorsifiexion. It was concluded that, although the AFO would loose its stiffness while a patient walked while wearing it, during periods of little activity the AFO would regain its original stiffness.

In a test programme intended for validation of analytical results (see page 26), Chu [1995] obtained measurements from two strain gauges bonded to the outer surface of a polypropylene AFO. The use of strain gauges for measuring AFO deformation had been inhibited in the past due to the difficulty of attaching them onto this type of thermoplastic material. The two strain gauges were located along the lateral calf trimline at different heights. The AFO was worn by an able-bodied person and subjected to various loading conditions. Although the author concluded that the maximum strain and hence stress was located at the lower strain gauge, consistent with analytical predictions, this could not actually be confirmed unless additional strain gauges were used to obtain a more detailed strain distribution.

Sumiya *et al.* [1996a] developed a device capable of measuring the ankle moment in plastic AFOs under deformation. It consisted of a moulded plaster artificial foot, which was attached to a metal pipe representing the tibia with a hinged joint positioned at the ankle axis. This pipe also formed a sliding joint through the

centre of a moulded plaster artificial calf, and it was clamped at its free end. The AFO was secured to the artificial calf by the calf strap, and the sole region of the AFO was bolted to the artificial foot just anterior to the heel. A tensiometer was attached at some distance along and perpendicular to a metal bar, which was hinged at the ankle joint to act as a lever arm. The ankle moment applied to the bar in this manner was transferred to the AFO by a pin connecting the bar to the artificial foot, and a protractor was centred at the ankle axis to measure the ankle angle. To apply a set deflection, the tensiometer was manually pulled at a slow angular velocity to approximate static loading conditions. They concluded that realistic measurements could be obtained from this simple device, although errors could arise from the manual application of forces and friction between the pipe and artificial leg.

Sumiya *et al.* [1996b] utilised this device to analyse the effect of consistently adjusting the ankle trimline and hence the posterior calf enclosure width on the stiffness of posterior spring type AFOs. An AFO was manufactured from polypropylene for each of the 30 subjects to be studied. The ankle axis was assumed at lateral malleolus height, perpendicular to the midline of the foot at its intersection with the anatomical ankle axis. The ankle trimline for each device consisted of a circular arc centred at the ankle axis, and the radius was varied from 20 % to 60 % of the lateral malleolus height to represent each trimline stage. The remaining trimlines were obtained from tangents to the ankle trimline and straight lines according to the AFO dimensions. After setting up each AFO in the device, the artificial foot was dorsiflexed and plantar flexed 15 ° at intervals of 2.5 ° and the ankle moment was calculated. Results of the measurements obtained for each of the nine different trimline stages showed that the resistive ankle moment to motion in both directions was roughly inversely proportional to the trimline stage, and for each angle and trimline stage the resistance to plantar flexion motion was greater than dorsiflexion. The plaster calf was also found to slide along the pipe proximally under plantar flexion and distally under dorsiflexion.

The aim of an experimental study by Nagaya [1997] was to correlate the flexibility

of a shoehorn-type AFO with various key dimensions. Thirty-two AFOs prescribed for hemiplegic patients were tested. The foot region of each AFO was clamped to the testing apparatus and deflected into dorsiflexion and plantar flexion through a constant horizontal force acting at the calfband region. The magnitude of this force was selected to avoid collapse due to buckling at the ankle under dorsiflexion. The angle of rotation was measured between a horizontal plane and a line connecting the posterior regions of the heel and calf. It was recognised that the axis of rotation did not correspond to the anatomical ankle joint and also moved during deflection of the AFO. The study concluded that the width of the ankle joint area was a major factor influencing the flexibility in both directions of rotation. The plastic sheet thickness was also a factor in dorsiflexion and the height of the lateral foot trimline in plantar flexion.

The focus of a recent experimental investigation by Klasson *et al.* [1998] was the measurement of the flexibility of a 'stiff' polypropylene AFO in all planes under an applied moment in a single plane. This behaviour has been termed cross-coupled deformation. The calf region of an AFO was attached via upper and lower straps to a rigid foam calf structure terminating at its distal end at approximately ankle joint height. The AFO was then subjected independently to moments in the sagittal, frontal and transverse planes through coupled forces applied to the dummy calf, whilst the sole region of the AFO was clamped to the apparatus. All translational and rotational degrees of freedom of the dummy calf were measured except its proximal/distal translation. The test did not account for the compliance of the soft tissue and shoe or the function of the ankle joint, so the applied moments and resulting rotations occurred about instantaneous axes.

Under dorsiflexion and plantar flexion moments of equal magnitude, the AFO's proximal trimline rotated internally and externally, respectively, relative to the sole. The magnitude of these rotations in the transverse plane were approximately half of those applied in the sagittal plane, whilst the rotation in the frontal plane was minimal. The AFO also translated medially at ankle joint level under dorsiflexion and laterally under plantar flexion. An eversion moment caused the

proximal trimline to rotate externally by half the magnitude of the rotation measured in the frontal plane, whereas an inversion moment caused internal rotation of similar magnitude to the frontal plane rotation. The rotations in the sagittal plane were minimal under inversion and eversion moments, but it was noted that the flexibility of the AFO in the frontal plane was greater under eversion than inversion moments. Under internal and external moments, the coupled rotations in the frontal and sagittal planes were minimal compared to those rotations measured in the transverse plane.

2.5.2 Discussion

The experiments carried out by Condie & Meadows [1977] have shown that it is possible to measure one characteristic of an AFO by performing a simple flexibility test and measuring the stiffness of the device. This approach gave meaningful results, but the method of loading and constraints was not realistic when considering how an AFO deforms during gait. The mechanical test rig described by Chowaniec *et al.* [1979] for measuring the characteristics of an AFO applied loads and constraints that simulate walking conditions more closely, allowing the AFO freedom of movement in certain directions relative to the lower limb, although it did not take into account the interaction between them.

The test apparatus used by Golay *et al.* [1989], Lunsford *et al.* [1994] and Sumiya *et al.* [1996a] consisted of an artificial leg with a hinged ankle joint to simulate the interaction between the AFO and the foot. This allowed the loading to be more realistically applied to the AFO than in the above experiments, so the results were more realistic. Yamamoto *et al.* [1993a] utilised testing apparatus to obtain the characteristics of an AFO while a subject was actually wearing the device, as opposed to simulating the loading and constraints. The results obtained from using this apparatus would therefore be more realistic than the results from the previous experiments, as the loading would be distributed over the AFO in a far more realistic manner than that possible with a solid artificial limb.

Chapter 3

Modelling the AFO

3.1 The Finite Element Method

3.1.1 Background

The *Finite Element Method* is an advanced and versatile numerical procedure for routinely analysing problems too complicated to be solved by classical analytical methods [Cook *et al.*, 1989]. It originated as a method of stress analysis in the 1950s, but today is an extremely valuable tool used in all fields of engineering, for example heat transfer, fluid flow and magnetic fields. The basic idea of the method is to replace a relatively complex analytical problem by a simpler numerical one, thus recreating mathematically physical behaviour. A typical analysis produces a large number of simultaneous algebraic equations that would be tedious to generate and solve by hand, hence many computer software packages are commercially available for performing such calculations. The results are never exact, as the solution is based on simplifying assumptions and is therefore an approximation, but results can be obtained that are accurate enough for engineering purposes.

For the purpose of analysis, the continuum is considered as an assembly of small

parts known as *elements*, each having a simple geometry whose behaviour is much easier to model than that of the complete structure. Elements are connected to one another at *nodes*, usually located at the corners and mid-sides of each element, and the assembly of elements is known as a *mesh*. It is important to note that discretisation is not simply a matter of cutting the continuum into a number of pieces and then pinning them back together again at the nodes, as such a model would not behave like a continuum. The elements are assembled so that the nodal displacements are continuous across element interfaces, although there may be jumps in the derivatives on which strains and hence the stresses depend. Accuracy improves as more elements are used to model the structure, although this results in more equations to process.

The advantages of the finite element method over exact analytical solutions are that the structure to be analysed can have arbitrary shape, loading and support conditions, the finite element model closely resembles the actual structure physically, and the mesh can be constructed from elements of different type and shape. The disadvantages are that it requires reliable software and powerful computer hardware to implement the method. Commercially available software requires an experienced user with knowledge of the underlying principles to define an effective model and interpret the results. Even though finite element programs are very powerful, the computed answer may still be wrong. Important aspects of physical behaviour, such as yielding or buckling, may have been overlooked by the user. A poor mesh or an inappropriate element type may have been used, the support conditions may have been applied unrealistically, or the user might have ignored the program's limitations. Computed results should therefore be compared with results obtained by some other means, such as an alternative program that relies on a different method, a simplified model suitable for hand calculations, or from experiments performed on the actual structure.

3.1.2 Analysis Procedure

A typical finite element analysis will involve three main stages, two of which involve user interaction and the other which is carried out automatically by the computer program. Firstly, a *preprocessor* is used to develop the finite element mesh, define the material properties, and specify the known loads and constraints to be applied to the model. There are two different methods for generating the element mesh, although it is possible to use both methods to define different parts of a model [Fagan, 1992]. The first method is by direct user input, also known as *direct generation*, where the user must define the location of every node, as well as the size, shape and connectivity of every element directly. Although this method is ideal for small, simple problems, it soon becomes tedious and prone to error when analysing larger problems and prohibits mesh refinement. Previous work appeared to have used digitised points on an AFO's surface for the direct generation of nodes and elements, limiting their investigations.

The alternative method is to use *automatic mesh generation*, which is preceded by *solid (geometric) modelling*, whereby the user firstly defines the geometrical boundaries of the structure using computer-aided drawing techniques. The lowest order solid modelling entities are points, also known as keypoints, and higher order entities are lines (edges), areas (surfaces) and volumes. The user must then specify mesh controls to establish the size and desired shape of elements at every location in the structure, and finally instruct the program to perform the mesh generation and therefore define all the nodes and elements automatically.

There is no advantage to be gained from using automatic mesh generation for small models having simple geometry, but for large, complex models it is the faster and most effective method. It enables the user to easily modify the geometry and allows operations such as dragging and rotating, including Boolean operations which provide the means of constructing a model using logical operators such as add, subtract and intersect. Other advantages over direct generation are that mesh refinement and design optimisation can be directly carried out. The only

disadvantage with this method is that it can require larger amounts of CPU time to build-up the model.

Depending on the modelling technique used, loads and constraints can either be applied directly to the nodes and elements of the model, or alternatively, they can be applied to the points, lines, areas and volumes of the solid model if present. If the latter method is used, the program will transfer the loads and constraints from the solid model to its nodes and elements during solution. The main advantage with the second method is that the loads are independent of the finite element mesh, allowing the mesh density to be modified without affecting the loading.

The second stage is to use a *solver* contained within the analysis package to perform the actual analysis from the input file generated by the preprocessor. After initiating the solution, the package will automatically formulate the properties of each element, combine these properties to obtain the finite element model of the structure, solve the resulting simultaneous equations to determine the nodal displacements, which are considered the primary unknowns calculated in a structural analysis, and finally calculate other quantities such as strains and stresses, which are derived from the nodal displacements.

Finally, when the analysis is complete, a *postprocessor* is used to list and plot the results from the output file (results file) generated by the analysis package for interpretation. For large models the amount of data output from the analysis package can be vast, so some form of graphical output is essential. With some software the analysis portion is accompanied by built-in pre- and postprocessors, forming a complete package suitable for general-purpose analyses. Stand-alone preprocessors and postprocessors are also available for use as alternatives to those contained within a complete package, or alternatively for use with dedicated analysis software.

3.1.3 Available Resources

The *Finite Element Analysis (FEA)* software that was utilised for this research was ANSYS. This program was initially released in 1970 by Swanson Analysis Systems, Incorporated (SASI), and since then it has evolved into a general-purpose package suitable for analysing problems from various disciplines, including structural, electrical, thermal and fluids, and on many different types of computer [SASI, 1994a]. The majority of the work was carried out using ANSYS Revision 5.1, although the previous version, Revision 5.0A, was also used during the initial model development. ANSYS Revision 5.3 became available after a period of approximately 18 months into this work. This version included several new features that were considered useful, such as improved meshing and enhanced graphical capabilities. However, problems were encountered with the preprocessor, which delayed its use by a further 6 months until an update was available.

Due to the large processing requirements with these types of analysis, high performance computers are required to run software packages such as ANSYS. The computer hardware available for this work were Silicon Graphics Indigo R3000 workstations equipped with 33 MHz processors, 32 MB RAM and approximately 180 MB of temporary local disk storage. Also available were a limited number of more powerful Silicon Graphics Indigo R4000 workstations equipped with 100 MHz processors, either 32 MB or 48 MB RAM, and approximately 800 MB of temporary local storage. The server used for this Data Visualisation service was a Silicon Graphics Crimson R4000 equipped with a single 100 MHz processor and 128 MB RAM. This hardware was a few years old at the start of this work and could no longer be considered as state-of-the-art.

ABAQUS, another well known finite element analysis package, also became available approximately 18 months into this work on an IBM SP2 supercomputer with parallel processing capabilities. Unlike ANSYS, during a typical analysis the preprocessing and postprocessing stages are performed using separate packages to the main ABAQUS/Standard solver. From the documentation supplied [HKS,

1996], ABAQUS/Standard appeared to be a more powerful and flexible package than ANSYS with regard to the handling of such things as material properties and element types. Because of its potential advantages and in order to obtain additional results for comparison purposes, it was considered desirable to become familiar with this alternative software package.

Unfortunately, initial attempts at modelling an AFO with available versions of the preprocessor, ABAQUS/Pre, were unsuccessful because the trimming process could not be performed without software errors. MSC/PATRAN, a pre- and postprocessor which could also be used with both ANSYS and ABAQUS, became available in the final year of this project. This provided the advantage that the same model could be analysed using both solvers with little extra effort. As ABAQUS/Pre was in fact a cut-down version of this preprocessor, similar problems were experienced when generating the model in the version of MSC/PATRAN available. Although most of these problems were eventually overcome, due to time constraints it was decided to concentrate on ANSYS.

3.2 Modelling Orthoses and Prostheses

3.2.1 Background

The first step towards an analysis of an AFO is to generate the finite element model comprised of a mesh of nodes and elements. More specifically, as automatic mesh generation was to be used to permit modification of both trimline and mesh density, the geometry of the physical AFO had to be defined within the software as a solid model suitable for meshing. This process is identical to that performed within Computer Aided Design (CAD) software, but small features such as fillet radii are usually suppressed to simplify meshing. Indeed, it is possible to export geometry descriptions from CAD software and import into a preprocessor for subsequent meshing using the *IGES (Initial Graphics Exchange Specification)* data format.

Boone *et al.* [1994] have reviewed the use of CAD and Computer Aided Manufacture (CAM) in the manufacture of custom-made prosthetic and orthotic devices, a new development which was termed the Automated Fabrication of Mobility Aids (AFMA). The aims of such technology were an improvement in the prescription service, by increasing production efficiency and thereby reducing the time and cost of the manufacturing process, as well as providing numerical accuracy and reproducibility by allowing control over the variables inherent in the design of such devices.

The three main stages in the design of a prosthetic or orthotic device using the AFMA process were the *input* of the anatomical form, the *design* of the device and finally *output* of the finished design to a manufacturing system. The first stage in prosthesis design, to which that work aimed to contribute, involved taking a negative plaster cast of the patient's residual limb and digitally measuring (digitising) the three-dimensional coordinates of a series of points along a number of horizontal profiles of the inner surface of this cast, as well as any additional anatomical landmarks. Finally, a computer was used to translate the numerical measurements of the geometry into an accurate graphical representation of the limb on screen.

The second stage involved sculpting the residual limb geometry into an acceptable prosthetic socket, and one software package developed for this purpose was named ShapeMaker. As modifications to the shape may be necessary to design a comfortable socket, this program adopted a process of interactively altering the contours that mimics traditional sculpting practices. This allowed shape rectification in the form of depression and relief to be made, and different levels of control were available, each requiring more interaction with the software but yielding finer control over the finished socket. The third stage involved translating the socket design into a physical object, by computer-controlled carving of a positive cast of the socket geometry and then forming the thermoplastic material over this cast.

Lord & Jones [1988] have discussed the problems of designing a custom-made

component to support and interact with a uniquely shaped body segment using a CAD/CAM system. One of the problems that can be encountered during shape measurement is that the body segment does not have a unique shape, even in a fixed orientation, and is heavily dependent on the tissue loading at the time of measurement. For example, when taking a cast of the foot, differences in geometry can occur depending on whether the foot is unloaded, partially loaded or fully loaded. Therefore, the shape of the support surface is not just a model of the body contours, but factors such as the effect of body orientation on surface geometry, cosmesis and the method of securing the device to the patient will affect the final design and it will ultimately be a distortion of these body contours.

During modelling, the shape of any body segment can be represented by the coordinates of a number of points on its surface relative to a three-dimensional frame of reference. The actual surface generated from this data can either consist of a number of small facets (triangular or quadrilateral shaped polygons) with the data points at their vertices, or alternatively the surface can be generated by some form of interpolation between the data points using Bézier or B-spline surfaces [Foley *et al.*, 1990]. These are types of parametric surface, where the x, y and z coordinates of a point are defined using polynomials of two independent parameters.

The advantage of the second method is that the surface can be interactively adjusted, the amount of data and therefore storage space is reduced, and the surface representation is smooth and continuous and may be subdivided. It should be noted that the surface must still be tessellated into polygons for displaying. Problems can arise using a parametric representation of a surface when mapping a rectangular grid of data points onto a complicated surface. As an example, a grid will wrap over a cylindrical surface such as the calf region of a lower limb, but will distort when wrapped around a hemispherical surface such as the distal end of the residual lower limb.

3.2.2 Application to AFO Modelling

Some of the techniques discussed above may be adapted to the problem of generating a finite element model of an arbitrary AFO for analysis. The modelling approach chosen will not depend on whether the AFO is a prefabricated or custom-made design, since they are both vacuum formed over a cast of the lower limb. However, unlike prefabricated AFOs, the cast geometry for custom-made AFOs does not conform to any standard pattern. It is also believed that analysis would be most beneficial for the latter type of AFO as they are preferred for permanent use. Modelling will therefore be focused on custom-made AFOs during this work, although the procedures developed could easily be applied to the analysis of prefabricated AFOs. A procedure was initially developed for generating a AFO model based on 23 user-defined dimensions, including the height, width and radius of a number of circular cross-sections through the calf region, but this approach was considered too restrictive.

Two different approaches were therefore considered for generating the solid model of a custom-made AFO. The geometry of the AFO could either be digitised *after* trimming, in which case the model would be generated within the software directly, or alternatively the vacuum-formed sheet could be digitised *before* final trimming. The disadvantage with the former approach is that, to assess the behaviour of different trimlines, a new AFO may have to be manufactured and then digitised for each design. Using the latter approach, as the trimming stage would be performed within the software, only the geometry of each new trimline would need defining. The untrimmed AFO would therefore need manufacturing and digitising only once, and design optimisation could be more easily implemented. For this reason the latter approach was adopted.

As custom-made AFOs are initially vacuum-formed over a positive cast of the patient's leg, the interior surface geometry of the untrimmed AFO closely matches the surface geometry of the plaster cast and hence that of the leg. If the numerical model of an AFO is to be realistic, its untrimmed geometry must also match this

same surface. Therefore, the first stage of the modelling routine must be to construct a geometric model (solid model) of the leg's surface to represent the untrimmed AFO using a preprocessor. This stage coincides with the input of the anatomical form.

The next stage in the manufacturing process of a custom-made AFO involves trimming the initial vacuum-formed thermoplastic material to obtain the final design of AFO with the required trimlines. This physical process can be duplicated in the preprocessor by firstly defining the required trimlines for a particular design, and then by using Boolean operations such as intersection and subtraction to sculpt the solid model of the leg (representing the untrimmed AFO) to obtain the solid model of the trimmed AFO. This stage therefore coincided with the design of the device, although it was not possible to interactively alter the surface geometry with the available software. This research did not concentrate on the final stage, that is the manufacture of the device, but transferring the trimline from the physical cast to the solid model and vice versa is discussed.

3.3 Solid Model of Leg

The first stage of the modelling routine was to generate the solid model of the leg to represent the untrimmed AFO. The geometry of a leg is an asymmetric surface in three-dimensional space and can be modelled in the preprocessor as an area. As the leg surface is of arbitrary shape, the area must be defined using keypoints and lines that represent the contours of the leg. In order to define the necessary keypoints, the coordinates of a series of points located on the surface of the leg must first be obtained.

3.3.1 Leg Surface Data

There are optical methods under development that can almost instantaneously capture the coordinates of thousands of points directly from the surface of a subject's foot, but the points will generally be unstructured and require conversion into a structured form before generating a parametric representation [Lord *et al.*, 1991]. Alternatively, a method of digitising these coordinates from a cast of the subject's lower limb using a hand-held stylus can be used. Although this approach is more time-consuming, it is possible to directly obtain a structured set of points suitable for surfacing. Other methods for obtaining contours include silhouetting, where the limb is imaged around its circumference and captured on video, but the surface geometry must have no re-entrants [Lord & Jones, 1988].

For this initial model, the lateral and anterior profiles of a normal person's right lower limb, as well as the transverse profile of the foot, were traced onto paper. This process, a basic form of silhouetting, allowed the coordinates of a number of points to be digitised from manual measurements taken from these drawings, rather than using artificial (computer generated) data. For a later model developed in Section 5.5.2, this manual approach was replaced with a more accurate coordinate measurement machine.

All measurements were taken relative to a global Cartesian coordinate system, XYZ. The origin of this system was located at the intersection of a vertical plane positioned along the midline of the foot and a line connecting the medial and lateral malleoli, all of which were estimated from the drawings. This placed the origin approximately midway between the two malleoli. The X axis pointed anteriorly and was coincident with the midplane of the foot, the Y axis pointed proximally and passed through the approximate centre of the calf band region, and hence the Z axis pointed rightward. This definition was consistent with the standard proposed by the International Society of Biomechanics for an absolute reference system for the reporting of kinematics data, although this standard is not unique [Wu, 1979].

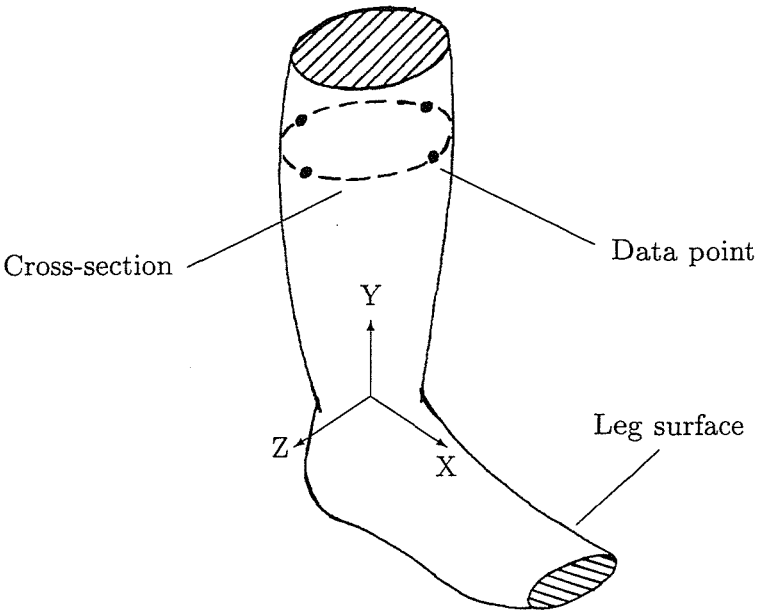

Figure 3.1. Points representing leg surface

As shown in Figure 3.1, the coordinates of 4 points located on the surface of the lower limb and distributed around the circumference of each of 17 planar cross-sections through the leg/foot were obtained, making a total of 68 data points. These cross-sections were not all parallel to the global Cartesian X-Z plane, as implied by Figure 3.1. This coordinate data was then manually entered into a text file and stored on disk for subsequent input. The format of this data consisted of a table, with the columns representing the X, Y and Z coordinates and the rows corresponding to each data point (see Appendix, Section D.1).

The number of points required to accurately represent the leg profile will depend on what part of the limb is being modelled. In regions where there is a sharp variation in the surface contours, such as the heel and ankle regions, a greater concentration of points is required. However, in flatter regions where the variation is more gradual, such as the calf region, the points can be more spaced out. Although the number of points used for generating this model was not sufficient to accurately represent the subject's leg profile, due to the limited number of profiles (or silhouettes) obtainable, a reasonably realistic model could be constructed. In

addition, it was considered important to develop a versatile method that could be easily adapted to model any individual's leg profile, irrespective of the amount of coordinate data available or the method used to capture it. In later modelling, certain sections were refined to include more points (see Section 5.5.2).

3.3.2 Defining Keypoints and Lines

The next stage involved reading the leg surface data into the preprocessor and defining the keypoints representing the surface from these coordinates (see Appendix, Section C.1). After defining the keypoints, they were then used to generate lines representing the cross-sections. As the leg surface is curved, 17 curved lines were generated around the circumference of the limb using splines fitted through the series of keypoints at each individual cross-section. Problems were encountered when using the same keypoint to define both the start and end point of each of these splines, due to a restriction within the ANSYS preprocessor. Therefore, two separate keypoints were defined for the ends of each line using the same coordinate data, making 5 keypoints per cross-section and a total of 85. To enable visual differentiation between each of these two keypoints on the display, they were actually defined a small distance apart.

Due to the limited number of points, the slopes at the two ends of each spline were forced to be parallel for additional control over the shape of each curve and to ensure continuity in gradient. The cross-sections therefore appeared elliptical in shape, with the keypoints actually defining their major and minor diameters. Rather than connecting the keypoints together with splines around the circumference of the limb (the shortest distance), an alternative approach considered was to connect them along the length of the limb (the longest distance). This resulted in fewer lines from which to generate the leg surface and a less accurate representation of the geometry, due to the loss of control over the end slopes of each cross-section.

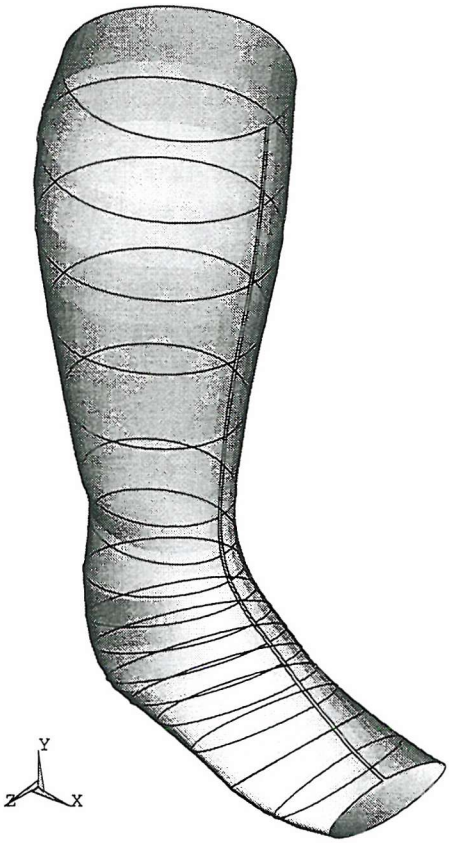

Figure 3.2. Plot of leg surface showing contour lines

3.3.3 Defining Areas

To complete the asymmetric solid model of the leg, these splined contour lines were then used to construct the surface area of the leg. One method would be to simply generate a series of areas between each adjacent pair of lines, although this would result in areas with curvature in only a single direction and also slope discontinuities between adjoining areas. Therefore a single, continuous area (see Figure 3.2) was generated by 'skinning' a surface through the set of contour lines (also shown on plot), which effectively acted as ribs over which the surface was stretched. For presentation purposes, the XYZ triad representing the global Cartesian coordinate system origin is not displayed in its true location in Figure 3.2 and some subsequent figures.

The first and last contour lines became effectively two opposite edges of the skinned area, while the remaining two edges were automatically generated as splines through the end keypoints of the contour lines (see Appendix, Section C.2). As the skinning operation produced an open-ended surface, it was clearly not possible to define all the contour lines parallel to the global Cartesian X-Z plane and still produce an area encompassing the sole of the foot. Instead, the orientation of the cross-sections altered from being parallel to the X-Z plane at the calf, to being approximately parallel to the Y-Z plane at the toes.

3.4 Solid Model of AFO

3.4.1 Preliminaries

The next stage of the modelling routine was to trim the solid model of the leg representing the untrimmed AFO to generate the solid model of the trimmed AFO. As the material used to manufacture AFOs is relatively thin compared to the other dimensions, it can be realistically modelled using shell elements, rather than using 3D solid elements which are less efficient for analysing shell-type solids. This choice of element type also simplified the modelling process at this stage as the AFO could be represented by areas, with the thickness of the material assigned as a constant associated with the shell elements, rather than actually having to construct the model using volumes.

One method of defining the trimline of a particular design of AFO is to digitise the coordinates of a series of data points located on a preliminary trimline sketched onto a positive cast of the patient's leg. This coordinate data would then have to be input into the preprocessor in a similar manner as the leg coordinate data. The advantage with this method is that the user can more easily visualise the AFO geometry in three dimensions while sketching the trimline on a cast. A major problem encountered with this method, due to the limitations of the software, was

that of transferring these data points onto the interpolated leg area. Although the trimline data could be manually combined with the leg surface data to model the trimmed AFO directly, automating this process would be complicated. The AFO would also be restricted to having a smooth trimline, as the skinning process could not produce corners or even fillets with small radii of curvature.

Initial attempts to define the geometry involved drawing a realistic trimline onto the hand-prepared lateral view of the leg. The coordinates of a number of points on this trimline were then measured and read into the preprocessor. Then, either a single, continuous spline line was fitted through all the keypoints defined from the data points to represent the trimline, or alternatively a combination of straight, splined, tangent and filleted lines was used to connect the keypoints together. Since the measurements of point coordinates were obtained from a lateral view, only their X and Y values in the sagittal plane were known. Therefore, to extend the constructed trimline into three dimensions, it had to be projected parallel to the Z axis so that it intersected the leg surface. The disadvantage with this approach was that there was too much data to input when defining the trimline, and for design optimisation it would be more convenient to have as few variables as possible.

The final approach adopted involved representing a typical AFO by a minimal set of physical dimensions sufficient to define the trimline in the sagittal plane relative to the global Cartesian origin at the ankle joint (see Figure 3.3). These consisted of the height of the proximal trimline (shown as PROXIMAL in Figure 3.3), the location of the distal trimline (DISTAL), the length and overlap of the calfband trimline (CALFBAND and OVERLAP respectively), the radius of the ankle and calf trimline arcs (RADIUS) centred on the Y axis, and finally the ankle joint vertical clearance (ANKLE). This whole trimline would also have to be projected onto the leg surface. For this leg geometry, the horizontal distance from the heel to the origin was 55 mm and the vertical distance 83 mm. A realistic set of measurements was then selected for the trimline of this initial design of AFO based on the dimensions of the solid model of the leg (see Table 3.1). The small fillet

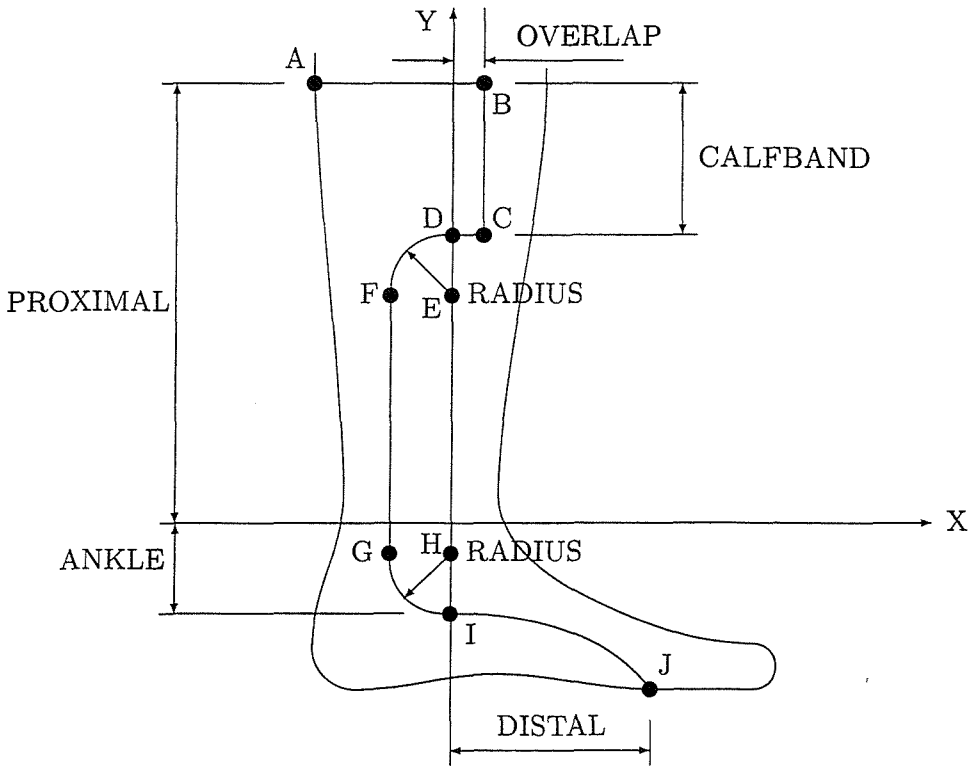

Figure 3.3. Dimensions for construction of trimline

radii that would typically exist at the corners 'B' and 'C' of the calf band region were ignored, as they would have minimal effect on the results but would introduce complications when meshing.

The advantage with this method of trimline definition was that it would be simple to alter the AFO design by simply changing its dimensions, rather than having to obtain the trimline coordinate data again. The disadvantage with this approach compared to digitising a trimline from the positive cast was that the final design of trimline must subsequently be transferred to the physical vacuum-formed sheet accurately at manufacture. There are usually variations between the trimlines on the medial and lateral edges of an AFO when viewed in the sagittal plane, because the orthotist applies different trimlines to each side. The distal trimline may also be slanted when viewed in the transverse plane to follow the contours of the toes. Although it was possible to duplicate this form of trimline with ANSYS, the anticipated slope discontinuities at the transition between the distal trimline and the medial and lateral foot trimlines were considered unrealistic. A single trimline

Dimension	Magnitude (mm)
PROXIMAL	260
DISTAL	110
CALFBAND	80
OVERLAP	30
RADIUS	30
ANKLE	30

Table 3.1. Dimensions for initial trimline

defined on the X-Y plane was therefore projected onto both medial and lateral aspects of the model, but because of the asymmetric geometry of the leg surface, the medial and lateral edges were in fact different.

3.4.2 Defining Keypoints and Trimline

Keypoints necessary for constructing the trimline, labelled from 'A' to 'J' in Figure 3.3, were first defined on a plane parallel to, and at a certain distance from, the X-Y (sagittal) plane in terms of the dimensions in Table 3.1. Since the X coordinate of point 'A' was not known, but would depend on the leg geometry, another point was defined having the same Y coordinate as 'A' and an arbitrary X coordinate of magnitude ensuring the proximal trimline would extend far enough in the negative X direction. Similarly, the Y coordinate of point 'J' was also unknown, but as this trimline was orientated at an oblique angle, the same procedure could not be used. A technique for finding the Y coordinate of this point on an actual physical cast of the leg would be to position a straight edge aligned parallel to the Z axis at the required X coordinate so that it was tangent to the cast surface. Therefore, this same procedure was carried out in the preprocessor by defining a plane, performing a Boolean intersection and constructing a tangent line (see Appendix, Section C.3).

The proximal trimline was defined as a straight line between keypoints 'A' and 'B',

and the calfband trimline as a straight line between keypoints 'B' and 'C'. The calf trimline was represented by straight lines between keypoints 'C' and 'D' and keypoints 'F' and 'G', and also a circular arc from keypoints 'D' to 'F' with the centre of curvature at keypoint 'E'. The ankle trimline was defined as another circular arc of the same radius from keypoints 'G' to 'I' with the centre at keypoint 'H'. The line between keypoints 'F' and 'G' was tangent to the two circular arcs. Finally, the foot and distal trimlines were defined as a single, curved line which was tangent to the ankle trimline at keypoint 'I' and also passed through keypoint 'J' at its opposite end.

The next stage was to project these lines onto the leg area to give the true location of the trimline, rather than its projection onto the X-Y plane that had been constructed. This was performed by using a dragging operation, which generated areas and their corresponding lower order entities (keypoints and lines) by sweeping the specified pattern of lines parallel to a predefined drag path (see Figure 3.4). Although it was possible to define this path by one or more lines forming a smooth, continuous curve, in this case it was simply defined as a straight line parallel to the Z axis between two keypoints located either side of the X-Y plane.

3.4.3 Boolean Operations

To cut the leg area at the true trimlines, a Boolean subtraction operation (see Appendix, Section C.4) was performed to divide the leg area at its intersection with the dragged trimline areas (see Figure 3.5). The unwanted part of the leg area which remained after the Boolean operation was then deleted. One problem with the current solid model of the AFO was that the complicated geometry would be difficult to mesh, as controls for automatic mesh generation could only be specified at keypoints and lines on solid model boundaries, and there were only a limited number of these entities located around the area boundary. Meshing is also better controlled with areas of simple shape, rather than complicated areas. It was therefore decided to divide the area into a number of separate (but connected)

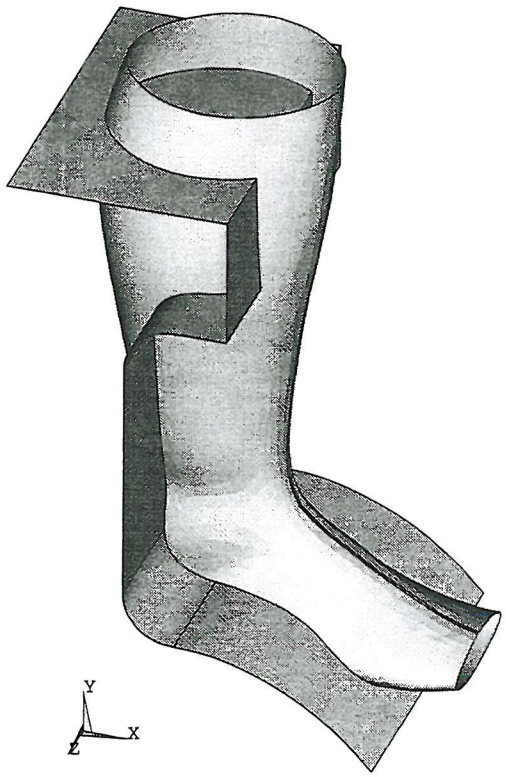

Figure 3.4. Area plot of dragged trimline

areas of simpler shape using further Boolean operations. ANSYS 5.3 additionally provided interior mesh controls, which allowed the element size at the interior of an area to expand or contract relative to the size on that area's boundary according to specified criteria.

It was considered advantageous to divide the AFO area into medial and lateral halves on either side of the global Cartesian X-Y plane, as this would allow the model to be easily modified to investigate the behaviour of a symmetrical AFO based on half of the geometry of the asymmetric AFO modelled. Symmetry could also be used to reduce the cost and size of an analysis by modelling only half of the AFO. It was also decided to divide the AFO into areas corresponding to the foot, heel, calf and calfband regions of the AFO, as this would facilitate the application of loads and constraints which tend to be concentrated over one or more of these

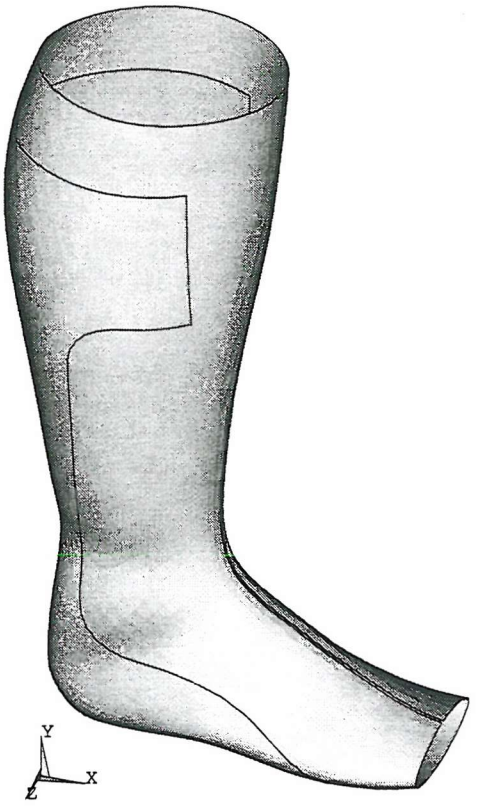

Figure 3.5. Plot of cut leg surface

particular regions. This process was carried out by first defining rectangular areas on the X-Y plane and on planes perpendicular to this at the locations where the AFO area was to be divided (see Figure 3.6). Then, to bisect the AFO area by these planes, the Boolean subtract operation was again used (see Figure 3.7).

3.5 Model Meshing

3.5.1 Element Selection

The final stage of the modelling routine was to mesh the solid model of the AFO and thus generate the corresponding finite element model. The first step was to select the type of element to be used, as there are several structural element types

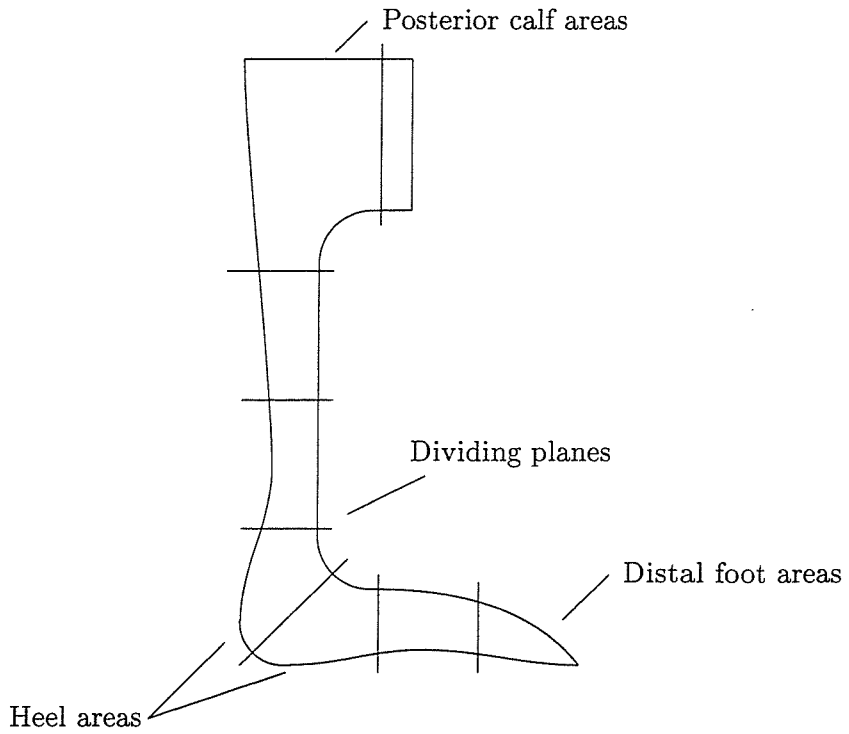

Figure 3.6. Dividing planes to simplify model

available within analysis packages including spar, beam, 2D solid, 3D solid, shell and contact elements. Due to the thin, shell like structure of plastic AFOs, it had already been decided that a shell element would be the most appropriate type of element to use. When meshing an area with shell elements, the mid-surface of each element will lie on that area. In the current model the areas were generated from data points corresponding to the outer surface of the leg, or alternatively the inner surface of an AFO manufactured to fit that leg. Therefore, the model is not strictly correct as the areas are out of position by half the shell thickness, which may affect results.

Elements can also be broadly classified as either linear or quadratic, depending on the degree of the polynomial used to describe the element's displacement field (see Figure 3.8). *Linear elements* (no midside nodes) can yield an accurate answer in a reasonable amount of computer time for structural analysis as long as degenerate forms are avoided at high stress gradient regions [SASI, 1994a]. Degenerate area elements are those whose characteristic shape is quadrilateral, but are generated as

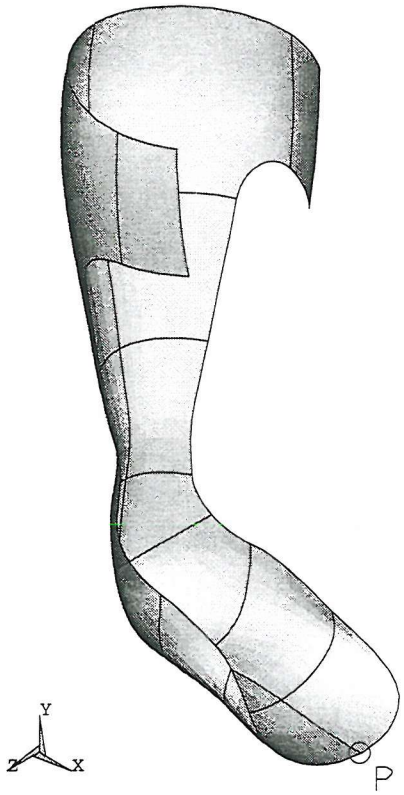

Figure 3.7. Area plot of sub-divided AFO

triangular. They are generally used for modelling a transition from a finely meshed region to a coarser mesh, and for modelling irregular or warped surfaces (where the nodes of a quadrilateral element would not lie on the same plane).

Degenerate elements formed from quadrilateral shaped linear elements are much less accurate than those formed from quadratic elements, and should be used with caution. Linear elements usually give better accuracy at less expense if a fine mesh is used for non-linear structural analyses involving plasticity, rather than a 'comparable' mesh of quadratic elements (see Figure 3.9). The reason for this is that the mesh must be fine enough in regions undergoing plastic deformation to provide an adequate integration point density, and as linear and quadratic elements each have the same number of integration points, linear elements are generally preferred. Most curved shell structures can also be analysed with a high

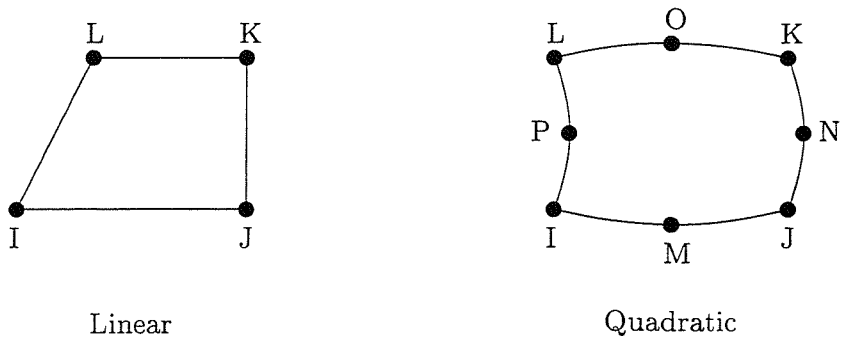

Figure 3.8. Basic types of area element

degree of accuracy in a minimum amount of time with these flat elements, so long as each element does not extend over more than a 15 ° arc.

Quadratic elements, which have midside nodes, are usually more efficient than linear elements for linear structural analyses with mixed element shapes. These elements exhibit a few peculiar traits that one must be aware of in order to use them correctly. The most important of these are that, firstly, distributed loads and reaction forces are not allocated to element nodes according to 'common sense', as midside nodes are allocated a greater proportion of the load and the loads assigned to corner nodes may act in the opposite direction. The corner node of an element should only be connected to the corner node of an adjacent element, not to any of its midside nodes, and adjacent elements should have connected midside nodes. Connecting elements should also have the same number of nodes along the

Figure 3.9. Comparable meshes of linear and quadratic elements

common edge, so when mixing element types it is necessary to remove the midside node from the common edge.

These elements should have straight edges except when modelling a curved boundary, in which case no single element edge should subtend more than 15 ° and the remaining edges should be straight. If the angle subtended by a curved element edge exceeds this amount, there will probably be localised inaccuracy in the results, although if the angle becomes too great, global inaccuracies may arise. A midside node should be positioned at the exact midpoint of the element edge, or within a distance of one tenth of the edge length. The user rarely has to worry about these points, as automatic mesh generation ensures that the elements are formulated accordingly.

Comparing the features, assumptions and restrictions of the shell elements available for structural analysis within ANSYS, the most suitable for this particular problem were a 4-node elastic shell, a 4-node plastic shell and an 8-node shell [SASI, 1994c]. As shells, all three elements had bending and membrane capabilities, 6 degrees of freedom (DOF) at each node (translations in the nodal coordinate system x, y and z directions and rotations about the nodal x, y and z axes) and both in-plane and normal loads were permitted. The nodes of each 4-node elastic shell element had to lie on a flat plane (although a slightly warped shape was permitted), whereas the plastic shell and 8-node shell elements were well suited to modelling warped and curved shell structures respectively.

The *nodal coordinate system, xyz,* defines the DOF directions at each node. By default, the nodal coordinate system at each node is parallel to the global Cartesian coordinate system, but each node may have its nodal coordinate system rotated to any orientation. Input data interpreted in this coordinate system include forces and constraints applied at nodes, and results data include the DOF solution and nodal reaction forces. Every element has its own *element coordinate system* to determine the direction of orthotropic material properties, applied pressures and some stress results. For a large deflection analysis, each element coordinate system rotates from its initial orientation by the amount of the rigid body rotation of that

element. However, the nodal coordinate systems *do not* rotate in this manner.

Transverse shear deformation can be significant in thick plates, where the thickness is greater than roughly one-tenth the plate width [Cook, 1995]. The 4 node elastic element was essentially a thin shell element as shear deformations were not included, whereas the other two elements both supported this feature allowing moderately thick shells to be modelled. These models are analogous to Kirchhoff and Mindlin plate theories, where transverse shear deformation is neglected in the former but allowed to develop in the latter. Transverse shear stresses were calculated for all elements and assumed to be constant through the thickness, whereas the out-of-plane (normal) stress varied linearly through the thickness. In reality, transverse shear stresses vary quadratically through the thickness, although this approximation would have little effect on results. Although all three elements had stress stiffening and large deflection capabilities, the latter two elements also supported large strain features and non-linear stress-strain materials.

Due to the doubly curved surface of the AFO, the possibility of triangular shaped elements being generated at critical regions and the perceived need to incorporate material non-linearities (but not plasticity) into the model, it was decided that the 8-node element would be the most suitable choice for the initial linear and non-linear analyses. It might have been necessary to revert to the plastic shell element at a later date for certain non-linear analyses, as it supported creep capabilities. Although this element also supported shear deformations, this was of secondary importance when selecting an element because these effects would be minimal, as the AFO could be categorised as a thin shell.

After the element type had been defined, it was also necessary to specify the set of geometric constants, also known as real constants or element physical properties, associated with that element type. The constants required for the element type chosen consisted of the thickness of the element at each corner node, if the thickness is assumed to vary linearly over the area of the element. The thickness of each element must have been less than twice its radius of curvature, although it should ideally have been less than one-fifth of the radius of curvature. The initial

model of the AFO was assumed to have a constant thickness of 2 mm, so only a single value had to be specified for all elements.

In reality, the thickness of an AFO tends to vary over the geometry due to its non-developable surface, so when vacuum-forming a sheet of plastic material over the positive cast, it stretches in a non-uniform manner. This causes thinning of the material at high curvature regions proportional to the length of draw of the material. Also, the thickness will vary between manufactured specimens due to the manual application of the plastic sheet to the positive cast prior to vacuum forming. Therefore, a constant thickness is not realistic but, at this early stage, it was a reasonable assumption to make in order to simplify the model (see Section 5.2).

3.5.2 Automatic Mesh Generation

The art of finite element analysis lies in the ability to select the correct mesh density to solve a problem accurately and in the shortest time. A coarse mesh may be adequate where stress is close to uniform, but for high stress gradients a finer mesh is required [Cook *et al.*, 1989]. If only deflections need to be assessed during a small deformation analysis a comparatively coarse mesh will suffice, as displacements are usually calculated more accurately than stresses. It is therefore up to the user to decide how fine the element mesh should be in order to obtain good results, but there are a number of techniques that can be used to help with this decision.

Firstly, the results of a preliminary finite element analysis could be compared with known accurate experimental or analytical results, and the mesh subsequently refined in regions where the discrepancy is great [SASI, 1994a]. Secondly, an initial analysis could be performed using a reasonable mesh and then the problem could be re-analysed using twice as many elements in critical regions. If the results are nearly identical, the mesh is adequate, whereas if they are substantially different, further mesh refinement is necessary until convergence is obtained. The final

technique is to use *adaptive meshing*, which is where the analysis software automatically refines the mesh in an iterative manner until it meets acceptable error estimation criteria (see Section 4.2).

The last step before meshing the solid model of the AFO was to specify meshing controls. The user must firstly establish the shape of the elements that are to be generated, as some element types can take on more than one shape. For example, shell elements can be triangular or quadrilateral, and solid elements can be tetrahedral or hexahedral. In general, it is easier for a mesh generator to use triangular shaped elements than quadrilateral elements [Fagan, 1992]. Although early mesh generators restricted the use of quadrilateral shaped elements to simple geometry only, more sophisticated meshing algorithms have essentially removed most of the limitations associated with this element shape.

Free meshing is where no special requirements restrict the element shapes, and an area can be meshed with either a mixture of triangular and quadrilateral element shapes, or else only triangular shaped elements. *Mapped meshing* is where the mesh generator is forced to use all quadrilateral elements to generate the mesh within an area, regardless of corner angles, although certain conditions must be satisfied for this to work and the resulting mesh may be distorted. If a mapped area mesh was to be generated with ANSYS, each area had to be bounded by either three or four lines, have an equal number of element divisions on opposite sides, and the number of element divisions had to be even if the area was bounded by only 3 lines. Free meshing may still have resulted in an all quadrilateral mesh being generated, provided that the corner angles were reasonable and the above conditions were satisfied.

An individual element will perform best if its shape is compact and regular, as elements tend to stiffen and lose accuracy as their shape distorts from a square or equilateral triangle. Element shapes must therefore be controlled to minimise the degree of distortion, as there are limits depending on which element is used. The types of distortion an element can undergo include aspect ratio distortion where the element becomes elongated, angular distortion where the element becomes

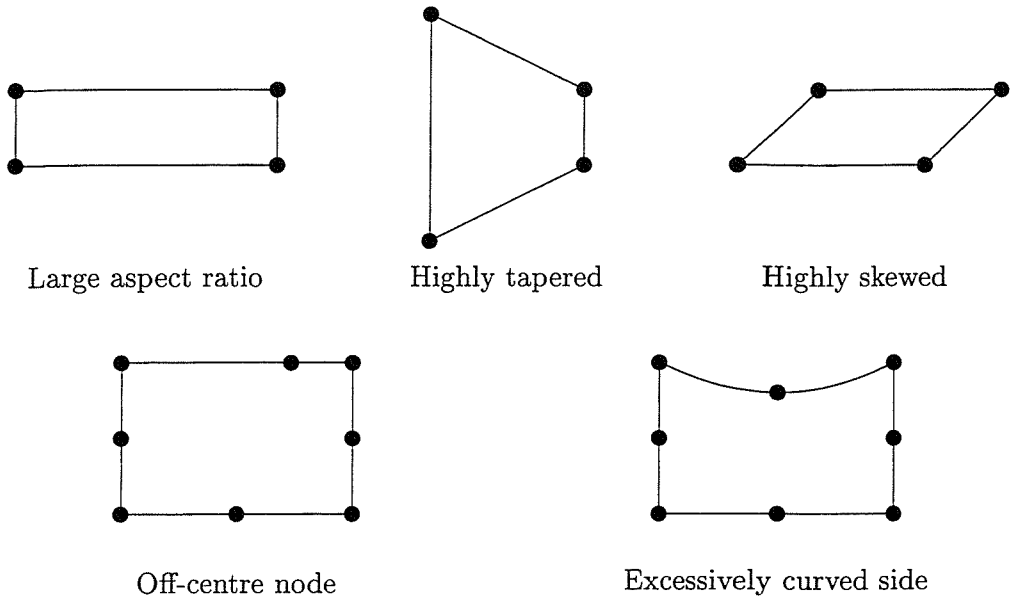

Figure 3.10. Types of element shape distortion

skewed or tapered, distortion due to the sides of an element becoming too curved, and midside node position distortion where the midside nodes (if any) are too far off centre (see Figure 3.10). If the mesh surrounding a distorted element is satisfactory, the error usually only has a local effect on results, although if these poorly shaped elements are located at a critical region their effect will be more severe.

Errors can also occur where element stiffness changes abruptly across element boundaries, but this can be minimised by using a uniform mesh where there are no large discrepancies in the size of adjacent elements. Poorly shaped quadratic elements will usually produce better results than linear elements of similar shape, and the latter should be avoided if excessively distorted. Preprocessors generally perform shape checking to ensure that element distortion is within acceptable limits. For example, the angle between any two sides of a quadrilateral shaped element should be within 45 ° and 135 ° for linear elements, and within 30 ° and 150 ° for quadratic elements [SASI, 1994c]. If problems arise a warning may be given, although as the criteria are not universally applicable to every situation, it is up to the user to make the final decision as to whether the mesh is acceptable.

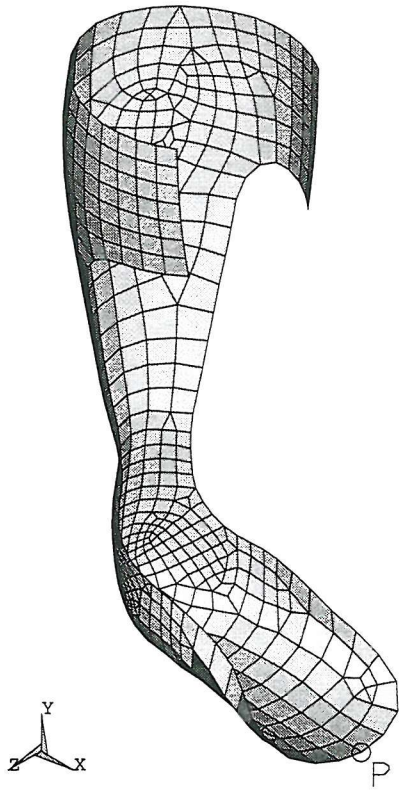

Figure 3.11. Plot of element mesh

For the initial mesh the element shapes were not restricted, so the elements could be a mixture of triangular and quadrilateral shapes. Since there was no prior knowledge of the stress distribution over the AFO, only a global element size specification was defined such that the number of element divisions per line was between 3 and 15, the maximum spanned angle per element was 30 °, and the maximum element edge length was 15 mm (see Appendix, Section C.5). The final step was to instruct the preprocessor to automatically generate the nodes and elements in the areas comprising the solid model of the AFO, and when complete the mesh consisted of 1848 nodes and 597 elements (see Figure 3.11). Note that, although the element selected was capable of having curved edges, these edges are plotted straight and so the model appears cruder than it actually is.

During the meshing operation, the ANSYS preprocessor reported a warning

message stating that a number of elements at the foot region of the model had midside nodes improperly located, due to excessive curvature. This could have been subsequently remedied by mesh refinement in this region of the model, but for this initial mesh it was decided to wait until results from an analysis were available so that the stress gradients in this region were known. Listings of the ANSYS command log files for generating the solid model of the leg, the solid model of the AFO and finally the mesh are included in the Appendix, Section D.1.

The mapped meshing capabilities of ANSYS were also tested, but a number of drawbacks with this approach were found. As the number of element divisions had to match on opposite lines, it had to remain constant from the distal trimline to the line at the top of the calf region in order to mesh the whole AFO with quadrilateral elements. Therefore, the mesh ended up being uniform along the length of the model, which was not efficient and would prohibit selective mesh refinement in critical regions. The program also had difficulties performing mapped meshing of the two distal areas of the foot region, which were only bounded by three lines. Although the two proximal calf areas were both bounded by five lines, this would not cause a problem for mapped meshing as it was possible to 'concatenate' two lines together to form a single line for meshing purposes only. Most of these shortcomings were removed with ANSYS 5.3, which allowed transition mapped meshing of 4 sided areas if the line divisions matched certain patterns. This was found to produce satisfactory mapped meshes having varying density.

3.6 Properties of Plastics

Before discussing polypropylene models for finite element analysis, it was thought useful to give a brief account of the general characteristics of polymers. Polymers can be classified according to the degree of crystallinity [Callister, 1991]. A *crystalline* polymer has an ordered arrangement of the molecular chains such that a periodic and repeating atomic arrangement is achieved, whereas an *amorphous*

polymer has a non-crystalline structure. A *semi-crystalline* polymer exhibits only partial crystallinity. The deformation behaviour of plastics, as with other materials, may be obtained experimentally under uniaxial tension at a constant strain rate. The stress-strain curves of polymers obtained from a uniaxial tensile test are complex and exhibit distinct types of behaviour, while temperature also has a significant influence on their behaviour.

The *glass transition temperature* is the temperature at which amorphous and semicrystalline polymers change state from a rubbery solid (supercooled liquid) to a rigid (glassy) solid upon cooling. Above this temperature the short term behaviour of polymers approach that of an elastomer, or rubber, where the relationship between stress and strain is non-linear, the strain is nearly completely and instantaneously recoverable, and the material can experience large strains at relatively low stress levels [Williams, 1973]. The behaviour of elastomers can therefore be assumed as perfectly elastic and independent of time and load history, but these observations would apply to plastics only to a certain extent as time-dependent and irreversible deformation would also occur.

Although not an exact description of polymers, linear elasticity theory does describe many aspects of their low strain, short-term behaviour. As the theory is well understood for crystalline solids such as metals, it is therefore a good first approximation from which models of viscoelastic behaviour may be developed. The theory of plasticity, which assumes permanent, irreversible deformation, does not generally approximate the behaviour of plastics, as deformation may be recovered over time. Nonetheless, many glassy polymers undergo a process which may be equated to yielding. As the behaviour of polymers is time-dependent the yield point of such materials is difficult to define due to the problem of recognising irrecoverable deformations. Therefore, it is often based on rapid changes in the slope of the stress-strain curve.

As with metals, yielding of polymers is usually unaffected by hydrostatic (mean normal) stress, a quantity which produces only change in volume and whose magnitude equals the octahedral normal stress (octahedral planes make equal

angles with respect to the three principal directions). It may therefore be described in terms of the deviatoric stresses, which are a measure of the deviation of the actual stress state from the hydrostatic stress state and which produce only change in shape (distortion). Therefore, the von Mises yield criterion is applicable, which states that yielding begins when the maximum octahedral shear stress in the solid reaches a critical value which is proportional to the yield stress in uniaxial tension. The Tresca yield criterion, which states that yielding begins when the maximum shear stress in the solid equals the yield stress in pure shear, generally offers an inferior interpretation to the von Mises criterion of the physical phenomenon associated with yielding of polymers.

When designing a load-bearing structure, it is important to consider both the stiffness characteristics of the material so that the component does not deform beyond functional or aesthetic limits, and the strength so that it does not fail within its life cycle [Ogorkiewicz, 1977]. With plastics, the deformation behaviour is more important than with metals since the stiffness of plastics is relatively low. Therefore, rather than employing the traditional approach to stress analysis where the failure stress (yield or rupture) is used to derive the allowable stress for the design, an alternative approach may be used that limits the maximum strain.

Creep is a rate-dependent material non-linearity whereby a material subjected to a constant load will experience an increase in deformation with time [Benham & Crawford, 1987]. Creep data is traditionally obtained experimentally from uniaxial tensile tests and plotted as strain versus time (or log time) for a particular stress and temperature. When presented as a family of creep curves for different values of stress, a constant strain section through them gives an isometric curve, where stress is plotted against time. This curve is often used as an approximation to *stress relaxation*, which is a phenomenon related to creep where the stress or load required to maintain a constant displacement or strain reduces with time. Alternatively, a constant time section through the creep curves results in an isochronous curve, where stress is plotted against strain. Additionally, a curve of relaxation modulus against time may be derived from the isometric curve.

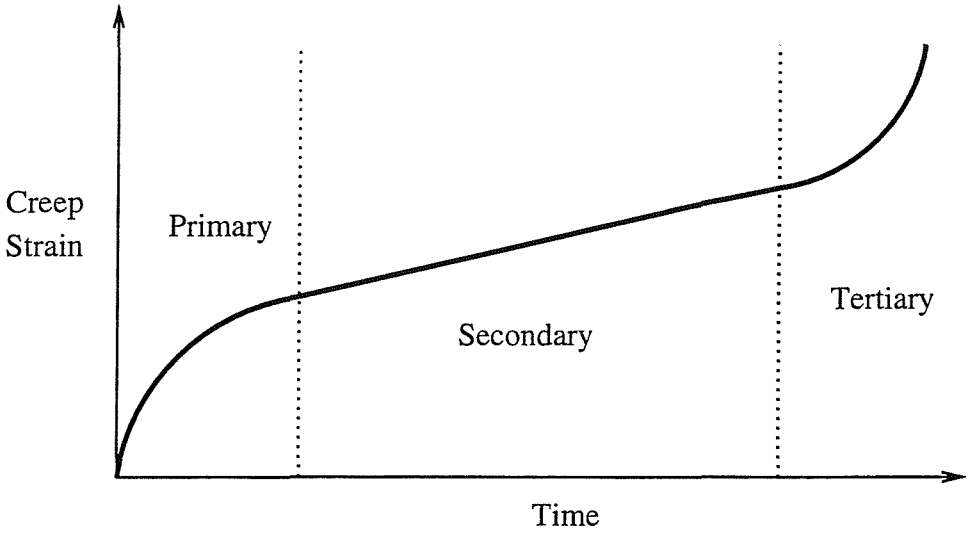

Figure 3.12. Phases of creep due to constant applied stress

Three stages of creep may be evident from a typical creep curve (see Figure 3.12). The primary stage is where the creep strain rate is decreasing with respect to time, and usually occurs over a relatively short period. The secondary stage is where the strain rate remains constant, so that the creep strain increases at a constant rate. Finally, in the tertiary stage the strain rate increases with time until failure. According to Callister [1991], this type of behaviour can be significant in many polymers at room temperatures and stress levels below yield, due to their molecular structure, and should therefore be considered a primary design criterion.

Polymers have similar creep curves to metals except they generally exhibit considerable recovery of creep strain upon removal of the load and have a memory, such that the stress and strain are dependent on the loading history. The stress-strain relationships of such materials are also non-linear and dependent on strain rate, so the modulus of elasticity cannot be assumed constant. This sensitivity to loading history and interdependence of stress and strain with time is termed *viscoelasticity*, and incorporates both elastic and viscous components.

The mechanical characteristics of polymers are also sensitive to temperature and nature of the environment, and are much more sensitive to temperature changes within the vicinity of room temperature [Callister, 1991]. Temperature effects can

be shown as a family of isometric or isochronous curves for several temperatures, and increasing the temperature will result in an increase in creep rate and ductility such that the stiffness and strength of the material is reduced. Therefore, temperature, time and preparation conditions must be taken into account to ensure that the testing conditions for obtaining material properties are similar to those experienced during service.

Plastics will exhibit failure when subjected to a constant load due to creep deformation, a phenomenon named creep rupture. Although fracture of thermoplastic materials will usually be ductile in nature, some plastics have a tendency to embrittlement, that is brittle fracture of a ductile material can occur, when subjected to constant loads over an extended time period, at reduced temperatures, under increased strain rates or in the location of sharp notches (stress concentrations). Brittle fracture is an unstable failure mode occurring due to rapid crack propagation with little or no accompanying plastic deformation. This type of failure could have serious consequences in relation to an AFO design, as no prior warning of failure would be evident.

Another visible phenomenon in the form of local inhomogeneous deformation may occur in plastics before rupture that may be considered as unacceptable and hence signify failure. Crazing is a crack-like phenomenon associated with the fracture of some glassy thermoplastics which indicates regions of very localised yielding. Crazes form at highly stressed regions of the material and will propagate perpendicular to the tensile direction, influencing long-term durability. Cracks result from flaws in the material where two new surfaces are created. Unlike crazes, cracks can cause local rupture in the material as they cannot support any loading [Gotham, 1974]. Stress whitening indicates local changes in the refractive index of the material, and can be due to a concentration of microvoids, micro-crazes or micro-cracks.

3.7 Polypropylene Models

Polypropylene is classified as a semi-crystalline polymer. The maximum achievable crystallinity of polypropylene is generally limited to about 70 % in a carefully annealed specimen, although it will usually lie between 50 % and 60 % in normal mouldings [ICI, P1/1]. Polypropylene is one of the lightest thermoplastics, with a density of about 905 kg/m^3, but this depends on the crystallinity, as does creep. As the glass transition temperature for polypropylene has been reported as $-20\,^\circ$C [Callister, 1991], the short-term behaviour of an AFO at operating temperatures (20–30 $^\circ$C) would lie within the rubbery state. Therefore, the material would be non-linear. It should be noted that the melting temperature of polypropylene, where it changes state from a solid to a viscous fluid, is around 165 to 175 $^\circ$C. For crystalline and semicrystalline materials, this point is indicated by a discontinuity in specific volume when plotted against temperature. An amorphous material does not exhibit this phenomenon.

As polypropylene homopolymer is relatively brittle, having poor impact resistance, its toughness may be improved through the copolymerisation with ethylene. This allows a wider range of properties to be developed, although the stiffness is reduced. Random and 'block' copolymers of propylene and ethylene are the two most common types. *Random* copolymers are the simplest, whereby ethylene monomer of up to 5 % weight is randomly incorporated into the propylene. *Block* copolymers have alternating clusters of propylene and ethylene along the polymer chains. They have higher toughness than random copolymers, whilst retaining most of the stiffness and high temperature resistance of homopolymer, and are available in medium and high impact versions. All grades of polypropylene are capable of forming thin, hinge regions due to their high durability to flexing. Copolymer polypropylene creeps more than homopolymers, but both have good creep resistance compared to high density polyethylene.

3.7.1 Linear Elasticity

For the sake of simplicity and as a first approximation, the material was modelled as being linearly elastic for the initial analyses, although non-linear elasticity was considered at a later stage (see Section 4.3.2) so that more realistic results could be obtained. Moreover, neither anisotropic material properties nor the variation of material properties with temperature were accounted for in any analysis. It should be noted that orientation is induced in the material at manufacture in the direction of draw [Birley & Scott, 1982], which would remain in the finished AFO, so the elastic properties of the material would actually be orthotropic.

Table 3.2 lists the properties of polypropylene obtained from various sources, as well as those obtained from a tensile test performed by the author (see Section 3.7.2). For the values obtained from NSP [1995] and ICI [P1/1], the lower values in each range relate to copolymer polypropylene, while the higher values correspond to homopolymer. As the modulus obtained from a true, non-linear stress-strain curve decreases with increasing strain, the exact meaning of values quoted in material property literature is unclear. This is one explanation for the range of values given above, although the time dependency of the material is another reason.

The material property data required in linear elastic analyses were the Young's modulus and Poisson's ratio. The shear modulus, G, was not explicitly defined and so defaulted to a value obtained from the following equation:

$$G = \frac{E}{2(1+\nu)} \tag{3.1}$$

A value of 1000 MPa was selected for Young's modulus based on the tensile modulus measurement of the copolymer polypropylene supplied by North Sea Plastics Ltd., which quoted a range of 900 to 1100 MPa. This agreed with other reported findings (see Table 3.2). The tensile yield stress was also given in the literature as 20 MPa [NSP, 1995], so the yield strain, calculated from the quotient

Source	E (MPa)	σ_Y (MPa)	σ_u (MPa)	δl (%)	Remarks
NSP [1995]	900–1350	20–28	—	—	25 mm/min
Callister [1991]	1140–1550	—	31–41	100–600	Room Temperature
ICI [P1/1]	900–1750	24–37	—	—	50 mm/min, 50 % Relative Humidity, 23 ° C
Van Krevelen *et al.* [1976]	1400	32	33	400	—
Figure 3.13	1390	12	—	—	Room Temperature

E = Young's modulus; σ_Y = yield stress; σ_u = ultimate tensile strength; δl = elongation at failure.

Table 3.2. Reported properties of polypropylene

of yield stress and Young's modulus, was therefore 2 % and could be used as an alternative indication of yielding. This value agrees with Birley & Scott [1982], ICI [1980] and ICI [P1/1], who quote the limiting strain for polypropylene as being between 1 % and 3 %.

No exact data was available from suppliers about the Poisson's ratio of polypropylene, although different values of 0.43 and 0.34 (ambient pressure, room temperature) have been reported by Van Krevelen & Hoftyzer [1976] and Hartmann [1980] respectively. Most plastics have a Poisson's ratio between 0.35 and 0.45, and although the magnitude is not very easy to measure experimentally, the exact value is not so important [ICI, 1980]. The Poisson's ratio of most polymers below their glass transition temperature was between 0.35 and 0.4 according to Williams [1973]. Also, the time dependency of this parameter does not usually affect results significantly, so a constant value in the range 0.3 to 0.4 may be used in a time-dependent analysis [Williams, 1973; Benham & Crawford, 1987]. A value of 0.35 was therefore adopted in this work based on these remarks. The model's sensitivity to variations in Young's modulus and Poisson's ratio is reported in Section 5.1.

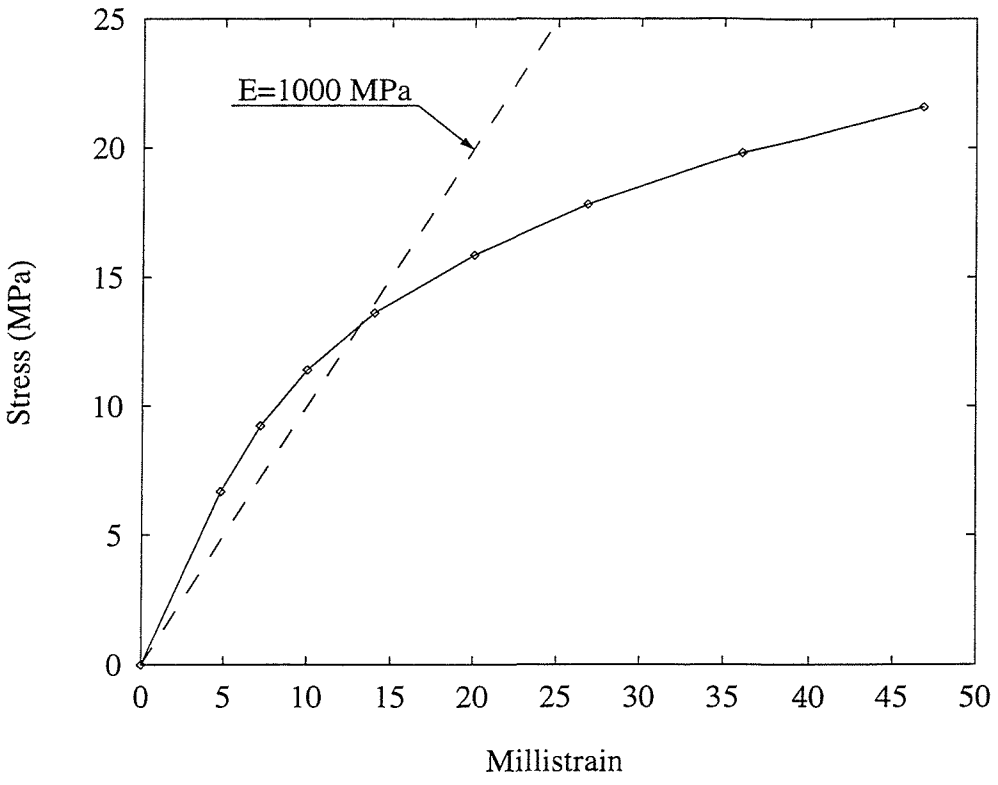

Figure 3.13. Non-linear response of copolymer polypropylene

3.7.2 Non-linear Elasticity

As with all thermoplastics, the tensile properties of polypropylene depend upon the strain rate and temperature. A simple uniaxial tensile test was performed on a copolymer polypropylene specimen, supplied by North Sea Plastics Ltd., at room temperature and at a constant strain rate. The load-extension graph and the stress-strain graph derived from this appeared to be non-linear with a decreasing stiffness as the load increased within the elastic region (see Figure 3.13). This result agreed with data presented by Ogorkiewicz [1977] for polypropylene at rates of elongation of between 0.21 and 0.42 mm/s, where strains of approximately 3.9 % and 3.4 % respectively were found at 20 MPa.

The Young's modulus calculated from the initial slope of the stress-strain graph was found to be 1390 MPa, which is higher than the value of 1000 MPa quoted by NSP [1995]. Because stress is not directly proportional to strain for polypropylene, the *tangent modulus* obtained from the slope of this stress-strain curve varies and

hence the material properties are deformation-dependent. A non-linear elasticity analysis is therefore required, where the load is applied incrementally and, after each step, the material property matrix and hence the stiffness matrix of the structure are updated based on the strains calculated in the previous step and the input stress-strain curve. Using the offset method, a 0.2 % proof stress of 12 MPa was obtained from Figure 3.13.

The stress-strain relationships obtained in this manner allow comparisons between materials to be made, but this data can be misleading because it conceals the time-dependent nature of the material. The stress versus strain curves of polypropylene vary depending on the strain rate, due to the entangled, long chain structure of all thermoplastics. As there is no definitive knowledge of the strain rates a component is subjected to during use, it is not clear which curve to introduce into the material model. Also, the short duration of these types of test cannot provide long term properties of plastics. Therefore, creep tests are considered more useful in characterising the behaviour of plastics for use in design.

3.7.3 Creep

Consideration was given to modelling the time-dependent behaviour of polypropylene, with the aim of providing a foundation upon which transient analyses with cyclic loading could be developed. ANSYS had the capabilities to model the time-dependence of stress and strain that is evident in viscoelastic materials [ANSYS, Inc., 1995], but as there were no shell elements available within the program that supported this feature, the possibility of using creep models was considered. To model creep, the user had to define an equation for the creep strain rate, $\dot{\epsilon}_c$, as a function of stress, strain and temperature from a library of predefined creep equations, also known as equations of state. These equations must be determined from experiments, usually uniaxial tensile tests, so that the model captures the key features of the material behaviour.

Equations of state imply that the creep strain rate at a particular time is

independent of the load history, which in general is not true. For multi-axial states of stress, the von Mises equations are used to calculate an equivalent stress and strain for use in the creep strain rate equation, which assumes isotropic behaviour. There were separate equations available for both the primary and secondary creep phases. When more than one type was selected the combined effects were used, though alternative equations that explicitly combined the two phases were also available. During calculation, ANSYS used a stepping function to calculate the change in creep strain within a time step, that is, it assumed that the creep strain rate remained constant over each time interval. This could cause the computed solution to drift from the exact solution, so to minimise this error a small time step was required when the creep strain rate changed rapidly.

A number of references were found that detailed results obtained from creep testing of polypropylene. Bucknall & Page [1982] discussed the effect that rubber particles had on the creep behaviour of polypropylene. Specimens of both homopolymer and rubber-toughened copolymer polypropylene were tested at 20 ° C under constant load. The creep strain rate was found to be continuously decreasing with time and strongly dependent on the applied stress. It was proposed that the data obtained could be represented by the Andrade creep equation of the form

$$\epsilon_c = \epsilon - \epsilon_0 = ct^{1/3} \tag{3.2}$$

where ϵ_c is creep strain, ϵ is the total strain, ϵ_0 is elastic strain, t is time and c is a material parameter (units of $s^{-1/3}$). This empirical equation was found to produce good correlation for strains between 3 and 5 %, but plots of strain versus the cube-root of time deviated from linearity at lower strains. As $\log c$ was found to be increasing linearly with applied stress, the relationship between creep strain rate and applied stress for both homopolymer and copolymer polypropylene could be defined by the following equation:

$$\dot{\epsilon}_c = \frac{1}{3}ct^{-2/3} = \frac{1}{3}AB^{\sigma}t^{-2/3} \tag{3.3}$$

Dixon-Stubbs [1981] performed creep experiments with a polypropylene specimen at 20 ° C. In contrast to the results of Bucknall & Page [1982], the graphs of strain versus time obtained exhibited all three stages of creep, since the time scale in this latter work was greater. Therefore the creep behaviour of polypropylene could not be represented by Equation (3.2), which predicts a continuously decreasing creep rate, as this would ignore the constant secondary creep rate. The following equation was therefore proposed as better suited to characterise polypropylene:

$$\epsilon = \epsilon_0 + \epsilon_p[1 - \exp(-K\dot{\epsilon}_s t)] + \dot{\epsilon}_s t \tag{3.4}$$

where ϵ_p is the maximum primary creep strain (0.0178 for polypropylene), $\dot{\epsilon}_s$ is secondary creep strain rate, and K is a dimensionless material constant (166 for polypropylene). Equation (3.4) could accurately describe the creep curves over the whole loading period except the initial 10 % to 20 % of the primary region of the creep curve, where the difference between calculated and experimental strain values increased progressively to over 100 % as time approached zero.

This deviation occurred because the experimental creep strain rate decreased more rapidly with increasing time than was predicted by Equation (3.4), and the computed initial creep rate was also considerably lower than that obtained experimentally. Therefore, the creep strain component $(\epsilon - \epsilon_0)$ predicted by this equation for any value of time was less than that obtained experimentally. This required a correction to be made to the computed value of the initial, elastic strain in Equation (3.4), such that its magnitude was larger than the value actually obtained. Although this corrected the computed total strain over most of the primary and secondary creep period, the strain in the initial region of primary creep was still an overestimate.

The creep properties of polypropylene over a range of stresses was also investigated, as these properties can vary significantly with stress. From tabulated data on the logarithm of secondary creep strain rate versus the logarithm of stress, the following equation could be derived:

$$\dot{\epsilon}_s = C\sigma^n \tag{3.5}$$

where the material constants C and n were calculated as 7.206×10^{-27} and 15.375 respectively. Therefore, substituting this relationship into Equation (3.4) and differentiating with respect to time, the creep strain rate could be represented by an equation of the form

$$\dot{\epsilon}_c = \epsilon_p[J\sigma^n \exp(-J\sigma^n t)] + C\sigma^n \tag{3.6}$$

where the material constant J was calculated from the product of constants K and C to be 1.196×10^{-24}. The numerical values quoted above for C, n and J are only valid in Equation (3.5) and Equation (3.6) when strain rate, time and stress are expressed in s^{-1}, s and MPa respectively.

In order to incorporate either of these empirical results into the AFO model, an appropriate creep equation must firstly be selected and the required material constants must be calculated. ANSYS did not supply a primary creep equation that could represent the relationship proposed by Bucknall & Page [1982], but Equation (3.6) proposed by Dixon-Stubbs [1981] could be defined by a combination of primary and secondary creep equations available within ANSYS. The primary creep equation was defined as follows:

$$\dot{\epsilon}_c = C_1\sigma^{C_2} r \exp(-rt) \qquad \text{where} \qquad r = C_5\sigma^{C_3} \exp(-C_4/T) \tag{3.7}$$

In this equation, C_1 to C_5 are material constants and T is temperature. The secondary creep equation was of the form

$$\dot{\epsilon}_c = C_7\sigma^{C_8} \exp(-C_{10}/T) \tag{3.8}$$

where C_7, C_8 and C_{10} are again material constants. Therefore, by substituting $C_1 = 0.0178$, $C_2 = 0$, $C_3 = 15.375$, $C_4 = 0$ and $C_5 = 1.196 \times 10^{-24}$ into Equation (3.7), and $C_7 = 7.206 \times 10^{-27}$, $C_8 = 15.375$ and $C_{10} = 0$ into Equation (3.8), the desired creep strain rate equation was obtained. As stated above, these numerical values are only valid when strain rate, time and stress are expressed in s^{-1}, s and MPa respectively. A static analysis was then performed to simulate the tensile tests reported by Dixon-Stubbs [1981], and the same creep strain history was obtained (see Figure 3.14).

Although it was possible to model creep behaviour, the error reported over the initial 10 % to 20 % of the primary creep stage was considered unacceptable. This was because the time to the onset of secondary creep was 21 ks with an applied stress of 20.69 MPa, so 10 % to 20 % of this period was of approximately 1 hour duration and was therefore of most interest for this research due to the time scale involved. As the elastic strain component had to be overestimated so that the deviation in creep strain was corrected, an artificially low Young's modulus had to be defined, calculated as a function of stress. Although this would not cause problems during analyses where the stress was constant over the model and static, the stress variation over an AFO would result in nonhomogeneous material properties.

Another limitation was that creep was modelled in ANSYS as an irreversible strain and, when simulating recovery upon removal of the load, only the elastic strain was recoverable. Although this would not be important when simulating a static load, it would not be possible to simulate the typical load reversals encountered during gait without reverting to a complicated method of superposition. Therefore, it was not feasible to realistically model viscoelastic behaviour in ANSYS. Due to the relatively short loading cycles plastic AFOs are subjected to in service, the magnitude of creep strain predicted by Equation (3.4) would be small relative to the elastic strain, so it was decided to consider only time independent behaviour in this work.

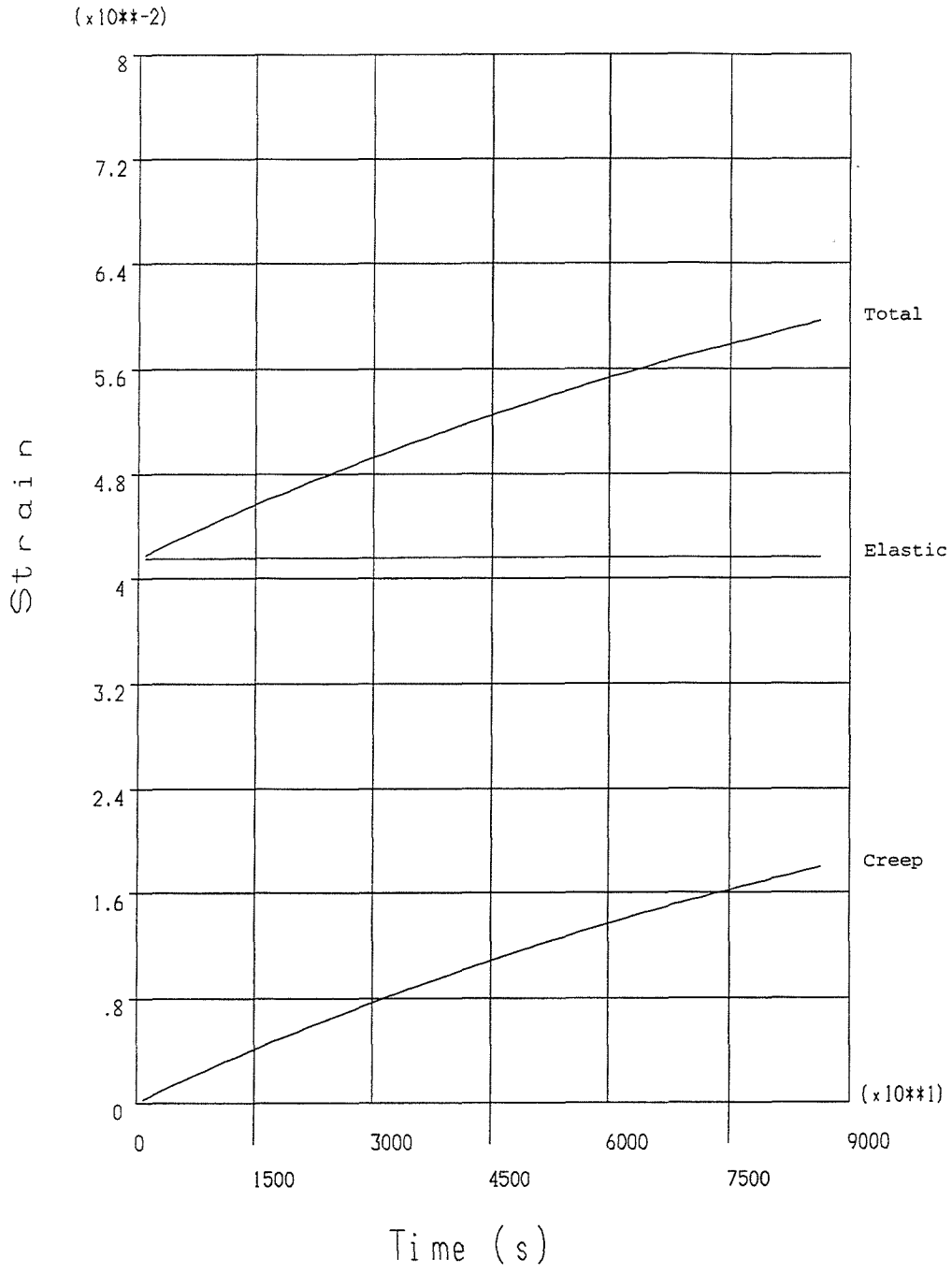

Figure 3.14. Creep curve for polypropylene at 17.24 MPa over 1 day

Chapter 4

Static Analyses

The loading conditions an AFO is subjected to during use are complex, due to interaction with both the lower limb and shoe. These loads vary with respect to time in a cyclic manner, so a dynamic analysis is necessary to determine an AFO's response to such conditions. The problem can also be classified as non-linear, due to non-linearities in the material properties, the changes in geometry and contact conditions. At this stage of the research, it was decided to consider the AFO in isolation and apply the loads to it directly, rather than additionally model the lower limb and shoe and loading the combined model. This would make the modelling process simpler and eliminate the contact non-linearity, reducing solution time. To accurately model the limb would necessitate a separate work.

4.1 Linear Static Analyses

4.1.1 Discussion

The simplest form of structural analysis is a static analysis, where the displacements, stresses and strains in a structure are determined under steady

loading conditions [SASI, 1994a]. This assumes that the loads and the structure's response vary slowly with respect to time, so that significant inertia and damping effects are not induced and can therefore be ignored. The types of loading allowed include externally applied forces and pressures, steady-state inertia loads such as gravity, and imposed (non-zero) displacements (see Appendix, Section C.6). Before attempting a dynamic analysis, it is also sensible to perform a more efficient linear static analysis of the same model to check for errors.

Although in reality every structure behaves in a non-linear manner, in some cases the problem may be approximated satisfactorily using linear theory [Cook *et al.*, 1989]. Also, a non-linear analysis will usually require more trial runs than a linear analysis, as the strategy is influenced by the outcome of previous analyses. Therefore, it is beneficial to start simply by performing a linear analysis of the problem and then add the non-linearities one by one, such that the effect of each is more apparent. As non-linear analyses tend to be computationally expensive, superfluous non-linearities should not be introduced.

The results from a linear static analysis are directly proportional to the magnitude of the applied loading. This is due to the assumptions that the material behaves in a linear elastic manner, where the stresses are proportional to the strains, the nodal displacements and element rotations are small, and finally that the loads remain in their original orientations during deformation. The simultaneous equations of equilibrium can therefore be constructed in terms of the original structure and solved in one step [Cook, 1995].

4.1.2 Static Simulation of Gait

When a normal person ambulates while wearing an AFO, a number of important events occur that are best highlighted by considering the pivoting motion of the foot relative to a fixed calf. Plantar flexion motion of the foot tends to plantar flex the AFO by applying a distributed load to the inner surface of the foot enclosure at the contact with the foot. Rigid body rotation of the *complete* AFO about the

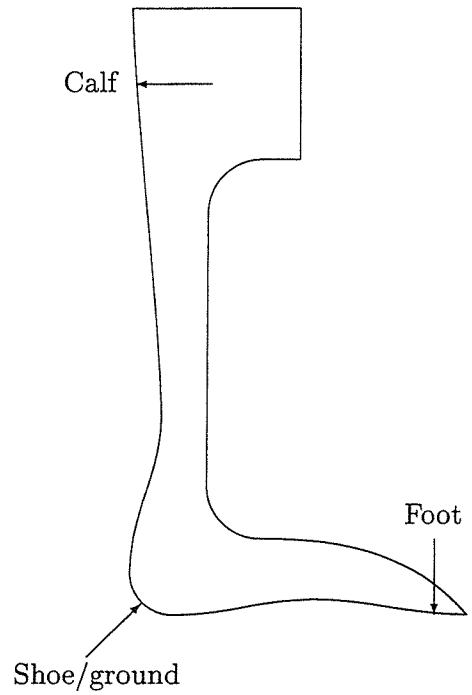

Figure 4.1. Three point system of forces during plantar flexion

ankle joint would cause the posterior calf enclosure of the AFO to move anteriorly, but this motion is resisted by the calf, which applies a distributed loading in a posterior direction.

With no shoe worn, the AFO would be insufficiently constrained due to the above conditions and would therefore separate from the heel to remain in an undeformed state. Thus, a further constraint is applied through the shoe (due to tension in the shoe laces) to the heel region of the AFO to resist relative rigid body motion of the AFO [Paul, 1996] and hold the AFO against the heel. This constraint generates a reaction in a superior and anterior direction which, in combination with the forces from the foot and calf, form a system of three forces (see Figure 4.1). This system of loading would occur during active plantar flexion of the foot during swing.

Although the above description appears unrealistic as it assumes the foot does not contact the ground, the reaction forces generated at the heel constraint could alternatively be considered as representing the distribution of ground reaction

force following heel strike. This ground reaction force would supplant the action of the shoe during swing by forcing the heel of the AFO to remain in contact with the foot. It would also generate a plantar flexion moment about the ankle and ultimately cause plantar flexion motion of the foot in the same manner as described above. Between heel off and toe off, plantar flexion of the foot caused by contraction of the calf muscles would also apply similar loading conditions to those described in the previous paragraph.

Dorsiflexion motion of the foot relative to a fixed calf does not directly dorsiflex the AFO, but instead a distributed loading is applied by the shoe to the underside of the AFO foot enclosure. Although this does not require significant tension in the shoe laces, the shoe clearly plays an important role. Without tension in the calf strap, the posterior calf enclosure of the AFO would lose contact with the posterior region of the calf, due to motion in the posterior direction arising from rigid body rotation of the AFO about the ankle. Therefore, the function of the calf strap is to resist this motion by applying a load to the calfband region of the AFO in an anterior direction. The calf strap therefore only functions during dorsiflexion, whereas the shoe is required during both directions.

With these two loads applied the AFO is again improperly constrained and can undergo rigid body motion relative to the lower limb. A less obvious distributed loading is applied by the heel to the inner surface of the posterior ankle enclosure of the AFO, which effectively constrains motion by applying a resistive load in a posterior and inferior direction (see Figure 4.2). The loading conditions described above accurately represent active dorsiflexion of the foot during swing, required to ensure adequate toe clearance. During the stance phase of gait between mid stance and heel off, dorsiflexion motion is due to the ground reaction force acting at the metatarsal region and generating a dorsiflexion ankle moment, but it causes a similar distributed loading to be applied through the shoe to the same foot region of the AFO. These regions of loading and constraint can therefore simulate the complete gait cycle.

During motion of the foot about the ankle joint axis, both the foot and heel

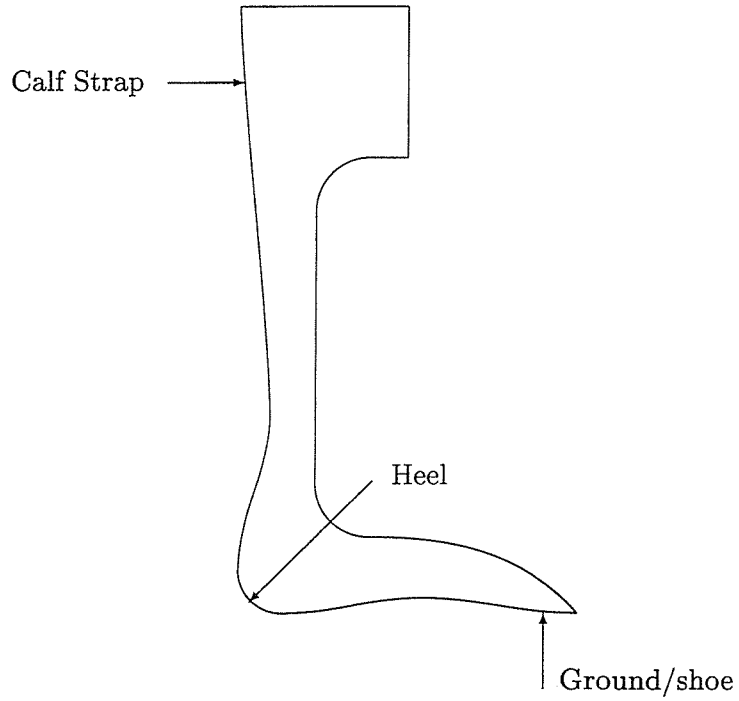

Figure 4.2. Three point system of forces during dorsiflexion

regions of the AFO are made to rotate about this same axis, assuming a rigid shoe is worn. This motion causes the calf band region of the AFO to translate parallel to the longitudinal axis of the tibia, in an inferior direction during dorsiflexion and a superior direction during plantar flexion [Sumiya *et al.*, 1996a]. In reality, there would be some resistance to this motion of the calfband region of the AFO, and also to internal and external rotations of this same region about the longitudinal axis of the tibia. This resistance would be due to friction against slip between the inner surface of the AFO and the skin as a result of tension in the calf strap, but even if no slip occurred, deformation of the underlying tissue would still be evident due to its softness. Because of lack of any data or evidence, it will be assumed that friction against this type of motion is negligible.

There will also be some motion of the calfband region of the AFO in the radial direction of the tibial axis for this same reason, but this would just result in a slight rigid body rotation of the whole AFO about the ankle joint axis during the initial rotation of the foot. Therefore, ignoring this rigid body rotation and assuming that

the calf band region is rigidly constrained in the radial direction was considered a valid assumption. Also, the heel region of the AFO is not rigidly constrained to rotate with the foot about the ankle joint axis due to the compliance of the shoe, but this effect should be minimal providing the shoe laces are tightly secured.

Because only the AFO had been modelled and not the lower limb and shoe, one difficulty that became apparent was that of applying the loading in a realistic manner. During gait, only a proportion of the ground reaction force applied to the lower limb is actually supported by the AFO, the rest being resisted by the leg muscles. This proportion is difficult to quantify as it depends on the severity of the patient's disorder. Therefore, the problem was initially considered from the alternative perspective of applying a realistic rotation to the foot region of the AFO about the ankle joint axis to find its resistance to rotation. The results obtained in this manner could not be considered in isolation when prescribing an AFO, but would have to be viewed with reference to data about the patient to understand its effect on ambulation. For example, the corrective forces required by a patient could be compared to the moment provided by an AFO.

4.1.3 Kinematic Loading

A number of analyses were performed on the AFO model using different deformation strategies, with the objective in each case being to induce 5 ° plantar flexion rotation of the foot region about the ankle joint axis. This small angle was selected because linear elasticity theory ignores large deformation effects which would be apparent under larger rotations of the foot region. The deformation strategies consisted of imposed nodal displacements on the distal foot region compatible with 5 ° rotation and applied as follows:

1. At a single node located at the intersection of the global Cartesian X-Y plane and the distal foot trimline, that is, at the centre of this distal trimline (point 'P' in Figure 3.7 and Figure 3.11).

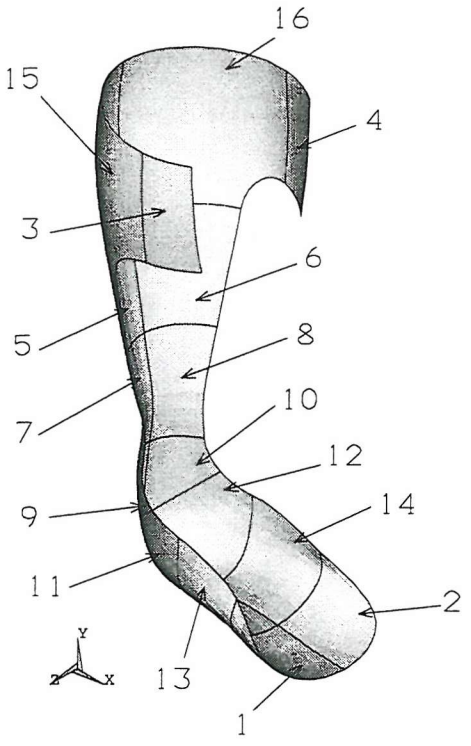

Figure 4.3. Area numbers of sub-divided AFO

2. At all the nodes located on the common line between the two distal areas of the foot region (area numbers 1 and 2 in Figure 4.3) which intersects the distal trimline at point 'P'.

3. As above, but with the line extended posteriorly to (but excluding) the node directly below the ankle axis and included in the heel constraint.

4. At a rectangular patch of nodes in the centre of the two distal areas of the foot region (those within a set distance from the X-Y plane).

5. At all nodes on the two distal areas of the foot region.

To simplify the model, the ankle joint axis was assumed coincident with the global Cartesian Z axis and all motion of the foot was assumed to occur about this axis, that is, rotation about the subtalar joint axis was ignored. The ankle joint axis could later be modelled in a more realistic manner by defining a local coordinate system in the correct orientation, but at this stage it was considered unnecessary.

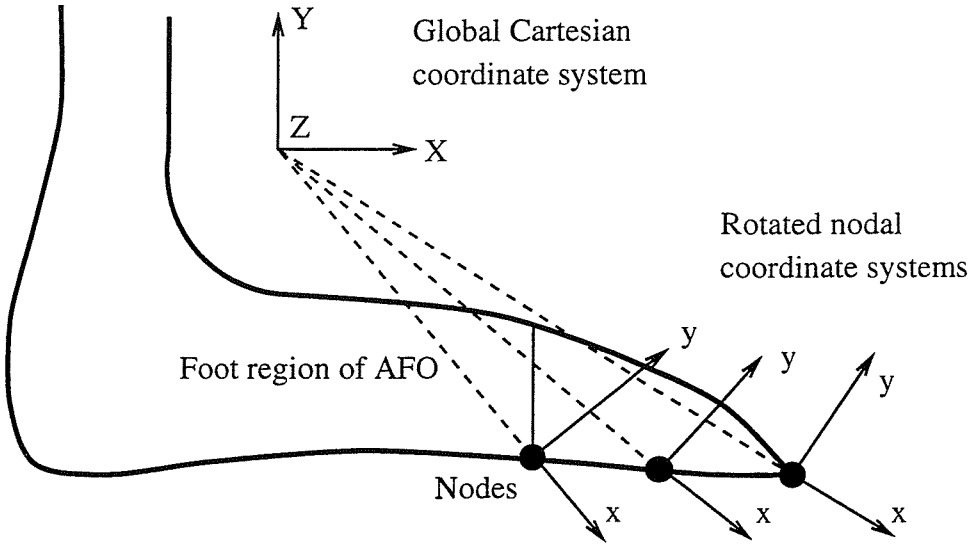

Figure 4.4. Nodal coordinate system orientations at the foot

The imposed displacements were applied at each node with respect to its rotated nodal coordinate system, xyz, as shown in Figure 4.4. This was achieved through the following three stages:

1. The nodes used to enforce the rotation of the foot about the ankle were selected (and grouped to simplify selection).

2. The nodal coordinate system of each selected node, initially aligned with the global XYZ axes, was rotated about its z axis such that its x axis intersected the global Z axis (see Figure 4.4).

3. A linear displacement was applied to each selected node in the nodal y direction of magnitude $R\theta$ (+ve dorsiflexion, $-$ve plantar flexion), where R is the perpendicular distance of the node to the global Z axis and θ is the angle to be applied (in radians). The magnitude of the nodal displacement calculated in this way was actually the arc length, but this was considered a valid approximation for small angles of rotation.

No other rotational or translational constraint was imposed on these nodes. It may be noted that the nodal coordinate systems were not manually rotated by user-specified amounts, but were rotated automatically such that the nodal y direction of each was aligned in the tangential direction of the global cylindrical coordinate system, which was located at the global Cartesian origin with its longitudinal axis coincident to the global Cartesian Z axis. As the position vectors of each of these nodes from the origin were not parallel, the directions of the corresponding imposed displacements were slightly inconsistent. Also, as each node could displace to any position on a plane normal to its nodal y coordinate direction, the actual rotation of each node about the ankle axis would depend on its displacement in the nodal x direction.

4.1.4 Constraints

As stated in Section 4.1.2, the calf effectively constrains motion of the calf band region of an AFO during plantar flexion in a radial direction relative to a cylindrical coordinate system, whose Z axis is parallel to the longitudinal axis of the tibia, but allows motion in the circumferential and longitudinal directions. To simplify the constraints during dorsiflexion, the calf strap was assumed to be of the type that wraps around the posterior calf region of the AFO, rather than the type riveted to the sides and causing localised stress concentrations. The calf band would therefore be constrained during dorsiflexion in a similar manner to plantar flexion, so the constraints could be distributed over the same region of the model.

These partial constraints were applied to all the nodes of the two posterior areas of the proximal calf region (area numbers 15 and 16 in Figure 4.3 on page 110) for both dorsiflexion and plantar flexion to simulate this radial constraint. This was achieved by rotating the default nodal coordinate system for each node about its y axis so that its x axis intersected the global Y axis (see Figure 4.5). The constraints were then applied in the nodal x directions of each of these nodes, while their remaining degrees of freedom remained unconstrained. The AFO was

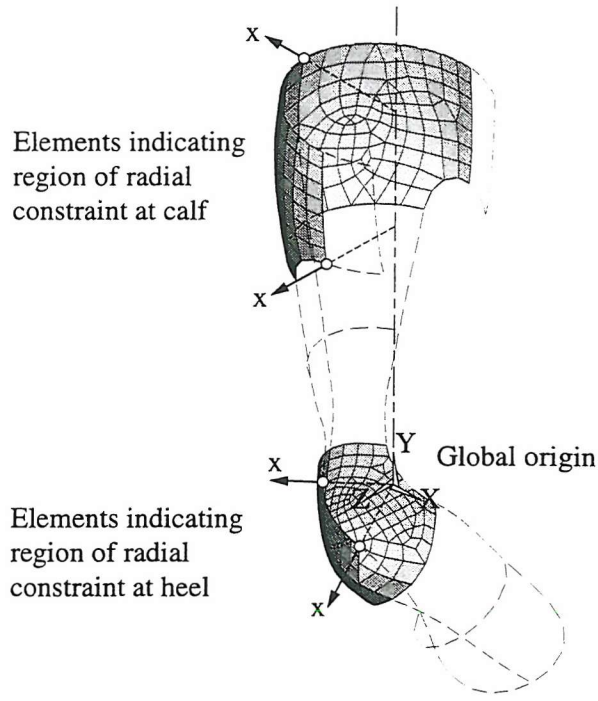

Figure 4.5. Distribution of radial constraint and nodal coordinate system orientations at the heel and calf

therefore free to translate up and down the calf, and to undergo internal and external rotations. As before, the nodal coordinate systems were automatically rotated using a local cylindrical coordinate system whose longitudinal axis was coincident to the global Cartesian Y axis and assumed to represent the tibia.

Constraints were also applied to all the nodes in the four areas comprising the heel region of the AFO (area numbers 9 to 12 in Figure 4.3 on page 110), where the shoe secures the orthosis to the heel of the foot. This region would also rotate around the ankle joint axis as the foot moved into plantar flexion or dorsiflexion. The nodal coordinate system of each node was first rotated so that its x axis passed through the global Cartesian origin (see Figure 4.5). Each of these nodes was then constrained in this direction, while remaining free to displace in all other directions. Rotation of the nodal coordinate systems was achieved using the global spherical coordinate system located at the global Cartesian origin (midway along the anatomical ankle joint axis), and the nodal x axes were effectively coincident to the radial direction of this spherical coordinate system after rotation.

Coupling and constraint equations may be used to model special relationships between different degrees of freedom that cannot be described with elements. *Coupling* is a technique which may be used to model rigid body regions, whereby one or more slave nodal degrees of freedom are constrained to have the same value as a master (prime) degree of freedom. This was found to be unsuitable for this work because the nodal coordinate systems of the coupled nodes had to be consistent. *Constraint equations* allow more general relationships to be defined, for example, between rotational and translational degrees of freedom. Although this technique may have proved suitable for these initial linear analyses, as these equations were based on small deflection theory, the solution process could not have been adopted for a large deformation analysis.

4.1.5 Solution Algorithm

The final part of preprocessing was to select the solver to be used, as there were a number of methods available within ANSYS (see Appendix, Section C.7). The default method, which was suitable for any type of analysis, was the *frontal solver*. This solver does not assemble the full global stiffness matrix, as in Gaussian elimination, but a triangularised matrix is assembled directly as the DOFs are eliminated, and the nodal DOFs are then calculated by back substitution. The term *wavefront* is often used with this type of solver to represent the number of DOFs that are currently retained during processing, and this quantity varies as each element is processed. The highest value of the wavefront is termed the *maximum wavefront*, and its size affects the memory required to perform an analysis.

A more important quantity is the root-mean-square value, termed the *RMS wavefront*. This will have an effect on the solution time, such that the smaller the RMS wavefront the quicker the CPU time required. The order in which elements are processed by the frontal solver affects the wavefront size, so the elements should ideally be numbered along the shortest dimension of a model to reduce the

maximum wavefront [SASI, 1994d]. ANSYS provided facilities to manually control the reordering of elements to minimise the wavefront size, but this was performed automatically at the start of the frontal solution process by default. This operation did not affect the element numbers used during pre- and postprocessing, but only the order that they were internally processed.

An estimate of the RMS wavefront prior to solving revealed that the default solver was the most appropriate for this model, as alternative methods only offered benefits for larger wavefront models. After solving, the actual RMS wavefront confirmed that the estimate and the choice of solver was valid. During the solution phase, a message appeared warning that the ratio of the radius of curvature to element thickness was less than 5 for a number of elements at the heel region of the model. This was not a result of the mesh being too coarse in this region, but was due to the high curvature in this region of the model. As this ratio was not lower than 4 in any of these elements, it was considered acceptable.

4.1.6 Summary of Results

Analyses were performed with displacements imposed at a single node located at the centre of the distal trimline, at all nodes located on the common line between the two distal areas of the foot, at all nodes on this line when extended posteriorly, at a patch of nodes (a sub-area) in the centre of the two distal areas of the foot, and finally at all nodes on these two distal areas. The key results obtained after solving these five analyses are listed in Table 4.1. This included the maximum displacement of any node in the model (labelled DMX in plot legends), δ_{max}, the magnitude of the medial/lateral displacement (+ve lateral) calculated at the node at the middle of the distal trimline (point 'P'), δ_z, the *actual* angle of rotation of this node about the ankle joint axis, θ_f, and the rotation of a node at the heel region, θ_h. Also tabulated is the resultant reaction force calculated at the nodes where displacement was imposed, F, the total moment generated about the ankle joint axis by the reaction forces at each of these nodes, M, and the maximum

Deformation Strategy	δ_{max} (mm)	δ_z (mm)	θ_f (°)	θ_h (°)	F (N)	M (Nm)	Max σ_{eqv} (MPa)	
							Inner	Outer
Point	12.4	−2.1	−4.9	−3.4	−23.7	−3.3	24.5	21.8
Line	12.3	−2.1	−5.0	−4.6	−46.6	−4.5	33.5	15.3
Extended Line	12.4	−2.6	−5.0	−4.9	−61.7	−4.8	36.2	16.5
Sub-area	12.3	−2.5	−5.0	−4.8	−50.4	−4.7	34.5	15.8
Area	12.0	−0.1	−5.0	−4.9	−61.4	−4.8	34.6	16.1

δ_{max} = maximum displacement of a node; δ_z = medial/lateral displacement of node at middle of distal trimline; θ_f = rotation of this node about ankle joint axis; θ_h = rotation of a node at heel region; F = resultant reaction force at nodes with imposed displacement; M = total moment about ankle joint axis; σ_{eqv} = equivalent stress.

Table 4.1. Summary of results for imposed displacement strategies

equivalent stress, σ_{eqv}, obtained on the AFO's inner and outer surfaces.

Referring to Figure 4.6, the rotations of the nodes at the foot and heel regions about the global Z axis were calculated from the vector (cross) product of vector **a**, the position vector from the global origin to the node considered in its undisplaced location, and vector **b**, the position vector of that same node in its displaced location. The components of vector **b** were calculated from the addition of vector **a** and the displacement vector of that node, **u**. The Z components of these vectors were set to zero such that the vector product was coincident to the global Z axis. The moment about the global Z axis was calculated from the summation of the individual moments of reaction forces (F_y) at each node where a displacement had been imposed. The moment arm for each node was calculated from the addition of the perpendicular distance of the undisplaced node from the global origin, $|\mathbf{a}|$, and the displacement of this node in the nodal x direction, δ_x. These calculations were performed within the ANSYS postprocessor using macros written in the *ANSYS Parametric Design Language* (see Appendix, Section D.3). It may be noted that these calculations were always performed with respect to the global Z axis, even if the ankle trimline arc was not centred on this axis.

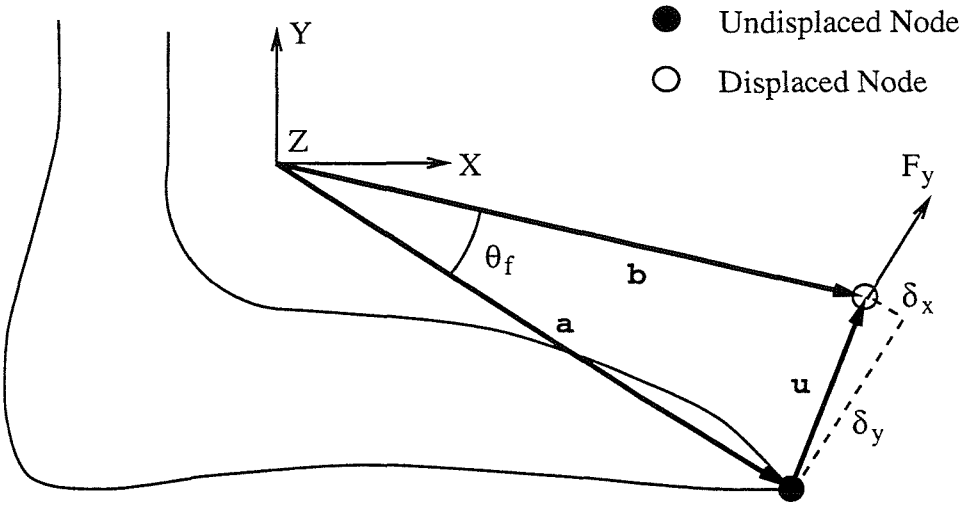

Figure 4.6. Calculation of ankle rotation and moment

Comparing the results from the five deformation strategies, the 5 ° rotation of the foot region about the ankle axis was achieved every time, although a slight variation was present due to approximations made in the calculation of the imposed displacement. Listings of the nodal displacements for the first deformation strategy revealed that the maximum displacement (the maximum calculated modulus of any displacement vector) occurred at the node where the imposed displacement had been applied. This was because the distance of this node from the ankle joint was greatest. For the subsequent analyses, the maximum displacement occurred either at this same node, or at a node near this point but still located on the distal trimline.

4.1.7 Deformation and Stresses due to Point Displacement

The most useful method of reviewing results from an analysis is through deformation and contour plots, although a tabular listing is the most appropriate method when the exact value cannot be obtained from a plot (see Appendix, Section C.8). A lateral view of the plantar flexed AFO for the first deformation strategy, the single node (point) displacement, revealed that the AFO had

deformed in an expected manner, with the foot and heel regions rotating into plantar flexion about the ankle joint axis (see Figure 4.7). This had caused the calf region to translate in a proximal direction as expected, remaining fixed in a radial direction. The ankle moment is therefore generated due to deformation at the ankle region of the AFO, as stated in Section 2.4. The undeformed geometry (wire mesh) of the AFO has been superimposed upon the deformed shape for clarity and, in this particular plot, the origin of the global Cartesian coordinate system is shown in its true location to help visualise the rotation. Also, the displacements have been scaled true to the model geometry.

Anterior and superior views of the deformed shape for this same analysis revealed that the model had deflected in a non-symmetric manner, with the foot region being displaced medially while undergoing plantar flexion (see Figure B.1 and Figure B.2). Because of this, the whole AFO had rotated internally about the global Y axis and so, assuming this AFO was being worn, an internal moment would be applied to the foot. This form of coupled motion was experimentally measured by Klasson *et al.* [1998], but no analytical work has reported this phenomenon. The distal trimline also appeared from the anterior view to have a region of high local deformation at the imposed displacement location in the form of a kink. Therefore, the foot region of the model would not have rotated about the ankle joint axis as a rigid body, but the nodes towards the heel region would have rotated by lesser amounts than those towards the distal trimline. This was evident from the angle of rotation calculated at the heel, which was found equal to 3.4°.

The reason for this medial displacement of the foot was the lack of symmetry in the AFO geometry, although the loading was symmetric about the midsagittal plane. The problem was therefore essentially one of asymmetric bending, where deformation does not occur in a single plane. This behaviour may also occur in bending of a symmetrical section about an axis which is not an axis of symmetry. Due to the lack of symmetry in the model geometry, applied forces may also cause twisting unless these forces act through a point termed the *shear centre*, which is a function of cross-section geometry [Benham & Crawford, 1987]. If the model and

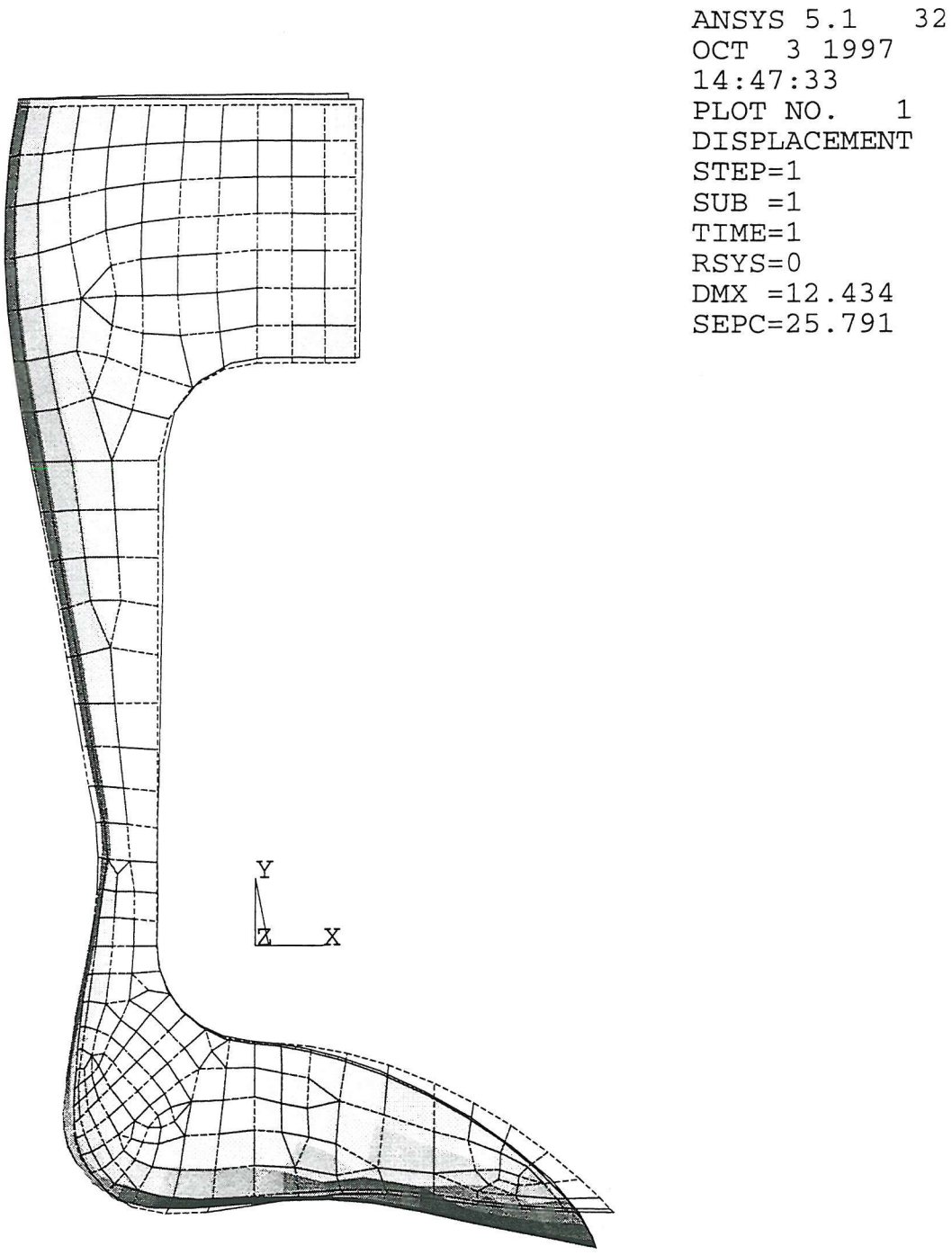

Figure 4.7. Lateral view of 5 ° plantar flexed AFO due to single node displacement

loading had both been symmetric about the midsagittal plane, this coupled motion would have been eliminated due to the fact that out-of-plane translation and in-plane rotations would have been indirectly constrained (see Section 4.1.9).

Contour displays can be plotted to show how results vary over the entire model. The normal and shear stress components in each element of the AFO could be displayed either in terms of the global Cartesian coordinate system directions, or alternatively relative to the individual element coordinate system directions. The disadvantage with the first approach was that these directions were not tangential or normal to the shell surface and so the results would be difficult to interpret. As the element coordinate system directions of adjacent elements were inconsistent, being orientated relative to each element's node coordinates (see Figure C.1), stress components plotted using the second approach could appear discontinuous.

In this situation it was considered more appropriate to plot the stresses in the AFO in terms of the *equivalent stress*, σ_{eqv}. Such a quantity is useful in that it is invariant, so it has the same numerical value in any coordinate system [Cook, 1995]. It is calculated according to the *von Mises yield criterion*, which replaces a complex, three-dimensional state of stress at a point in a structure with a single, positive quantity for comparison with the yield strength of the material. This criterion has been reported by Williams [1973] as being representative of the physical phenomenon associated with yielding of polymers. It may be obtained directly from the six stress components, or it can be calculated from the three principal stresses (the limiting values of the normal stress components upon which planes the shear stresses are zero), σ_1, σ_2 and σ_3, using the following equation:

$$\sigma_{eqv} = \frac{1}{\sqrt{2}}\left[(\sigma_1 - \sigma_2)^2 + (\sigma_2 - \sigma_3)^2 + (\sigma_3 - \sigma_1)^2\right]^{\frac{1}{2}} \tag{4.1}$$

As shells are subjected simultaneously to membrane and flexural deformation, stress results were available at both the inner and outer surfaces of the AFO. As the stresses are assumed to vary linearly through the thickness, the results at the middle surface could also be calculated from the average of the inner and outer

surface values. A plot of the (unaveraged) equivalent stress at the inner surface of the AFO for the first deformation strategy revealed that the maximum (indicated by the symbol MX) was located at a stress concentration close to the medial ankle trimline (see Figure 4.8). This agreed with previously reported analytical predictions by Abu-Hasaballah *et al.* [1997]. The location of the minimum stress (indicated by the symbol MN) was at the calfband region where the magnitude was negligible, and over the majority of the AFO the stresses were minimal. The element outlines have been removed on the interior of the AFO for clarity.

The magnitude of the maximum equivalent stress on the inner surface (given in the legend) was significantly higher than the value conventionally accepted as the tensile yield strength of the material, which was 20 MPa. Therefore, assuming that this yield criterion was applicable to polypropylene, some plastic deformation would remain in the AFO upon unloading. According to Figure 4.8, another visible stress concentration was located at the node where the imposed displacement had been applied. The high local deformation that was apparent in this region on the deformation plot was also evident in Figure 4.8, as contour plots are displayed relative to the deformed configuration. It may be noted that the location of this maximum was the same for the other four deformation strategies.

The maximum equivalent stress at the outer surface of the AFO was found to be slightly lower than at the inner surface, although still greater than the yield stress (see Figure 4.9). The location of this maximum stress was at the node where displacement was imposed, and there was a larger stress concentration in this region of the model than at the inner surface. The magnitude of the equivalent stress at the ankle/calf trimline intersection was not as large as that on the inner surface, although the magnitude of the minimum equivalent stress was again negligible. The magnitude of the equivalent stress at the middle surface revealed that the membrane stresses were considerable around the ankle trimline, where the maximum value (12.0 MPa) was located.

The total reaction forces in the global Cartesian X and Y directions at the foot, heel and calf, as well as the resultant reaction forces, are shown in Figure 4.10.

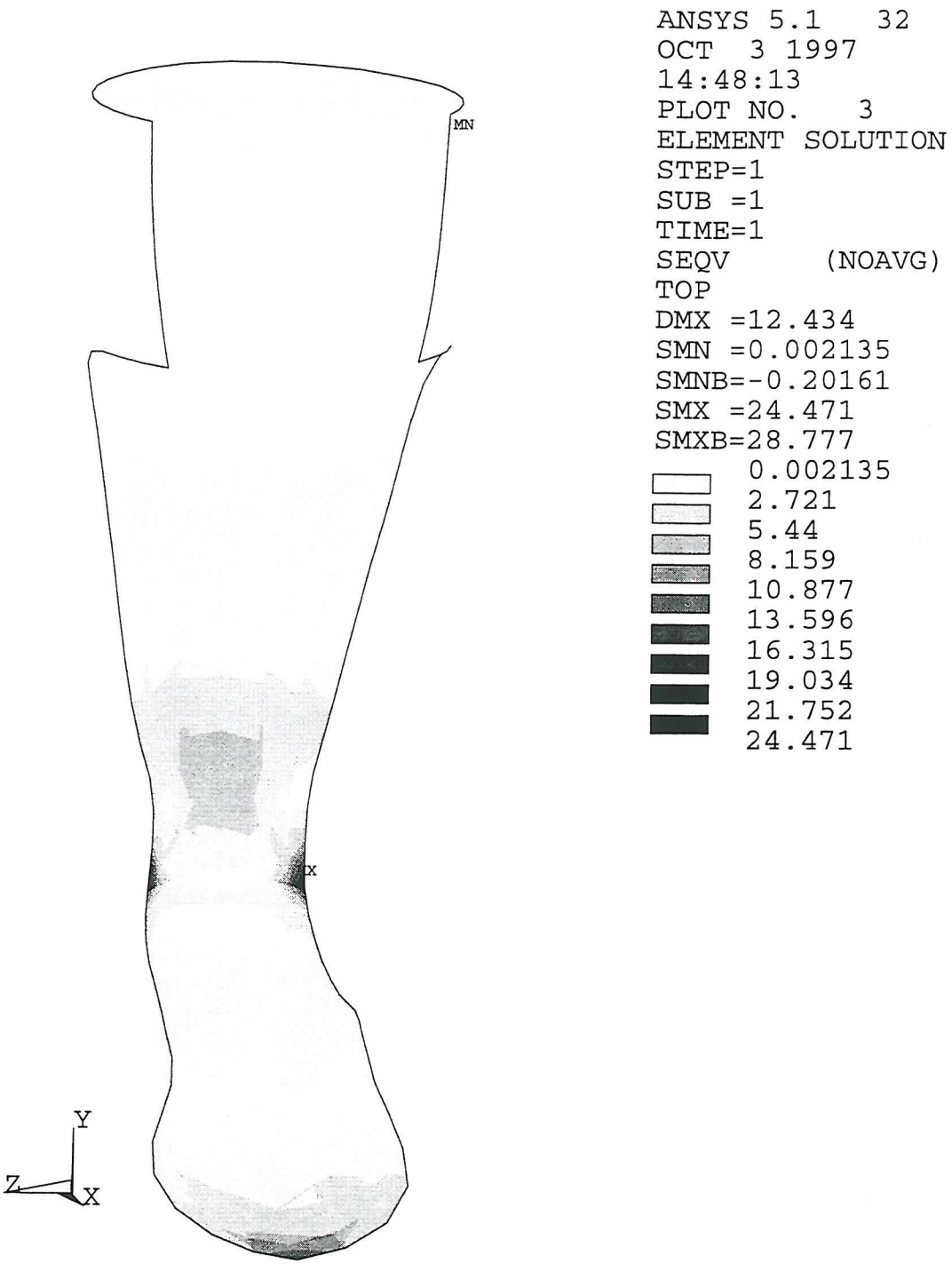

Figure 4.8. Equivalent stress at inner surface of 5 ° plantar flexed AFO due to single node displacement

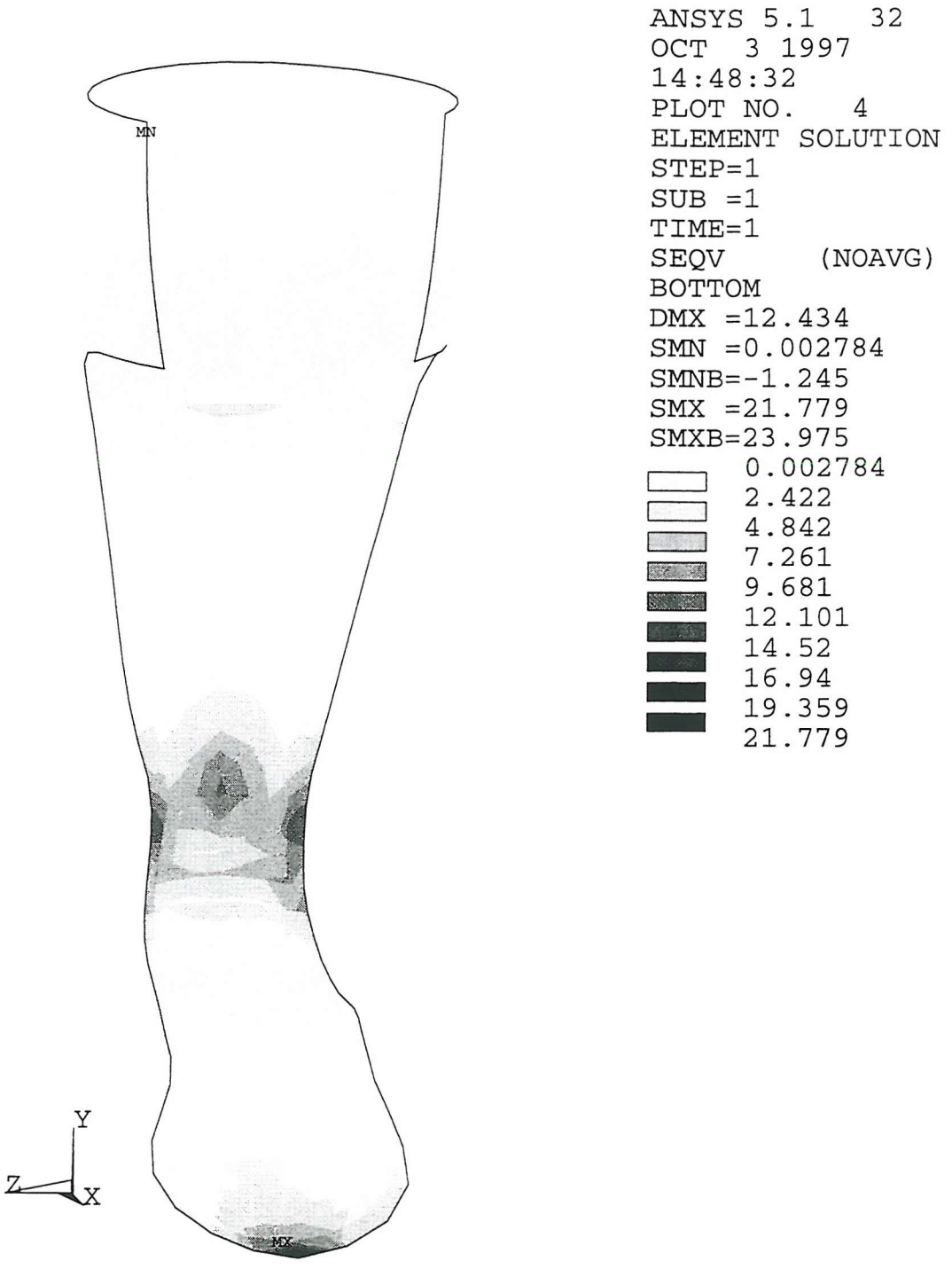

Figure 4.9. Equivalent stress at outer surface of 5 ° plantar flexed AFO due to single node displacement

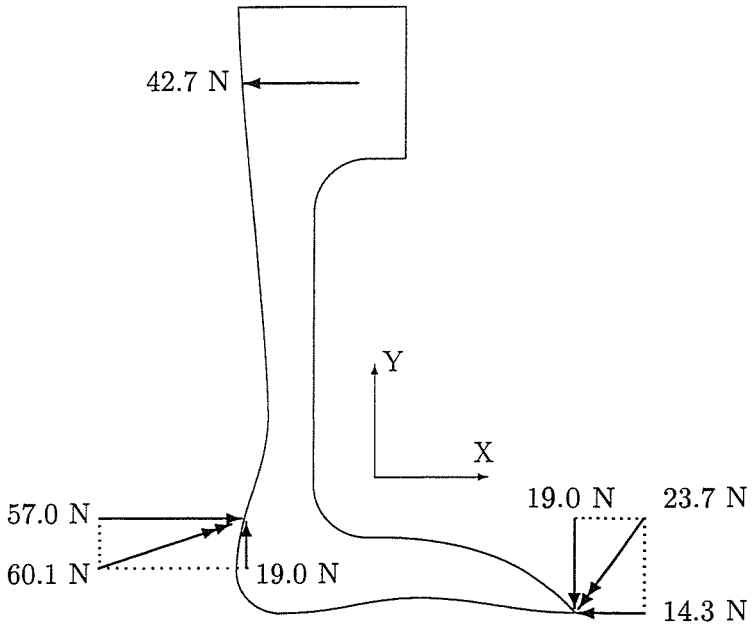

Figure 4.10. Reaction forces at foot, heel and calf due to single node displacement

Although not shown, the resultant forces at the foot and heel regions were orientated at 53.0 ° and 18.4 °, respectively, relative to the global X axis. It was noted that the individual reaction forces in the nodal x direction of those nodes constrained at the heel were concentrated towards the uppermost elements in this region. There was also a small total reaction force in the global Z direction at both the heel and calf regions of 0.2 N and -0.2 N, respectively, although equilibrium of forces existed.

4.1.8 Effect of Distributing Imposed Displacements

In reality, every load is applied over a finite region. It has been stated by Fagan [1992] that when a concentrated force is applied at a single node, the finite element method can yield unreliable results in the immediate vicinity of this load, although the stresses far from this node should be reliable. If the stresses close to this load are not important, but the distal effects are, representing the load as a single nodal force will suffice. However, when local stresses are also of interest, the load should

be distributed over that region of the model in a more realistic manner. As constraints applied to a finite element model generate reaction forces, a single nodal constraint can also lead to high localised stresses in that region, again producing misleading results. This problem can also be overcome by distributing the constraint in a similar manner.

According to the above statement, the stress concentration caused by the imposed displacement of a single node should be ignored, and the stresses in this region would be smaller in magnitude had the load been applied in a more realistic manner. One undesirable effect of a stress concentration due to a load or constraint being applied to a single node is that, if the maximum stress occurs at the same location (as in Figure 4.9), fewer contour bands are available to represent the stress variation over the rest of the model. Also, for reasons that will become apparent in the Section 4.2, mesh refinement becomes disrupted by the high stress gradients near concentrated loads. The main incentive for the different deformation strategies was therefore to reduce any stress concentration arising from the inadequate distribution of reaction forces.

Lateral and anterior views of the deformation for the second deformation strategy, the line displacement, revealed that less local distortion had occurred in the model around the location of imposed displacements than with the first deformation strategy. Because of this reduced local deformation, stress concentrations were also reduced in that region. The reason was that, by distributing the imposed displacement over a greater region, the whole of the foot region had rotated more rigidly about the ankle joint axis. This caused the heel rotation to increase by 35 %, the ankle moment to increase by 36 % and the resultant reaction to increase considerably by 96 %. The magnitude of the reaction forces at the displaced nodes were found to be irregularly distributed and their signs inconsistent from one node to the next, indicating that the resultant of the reaction was more useful than its distribution.

A plot of the equivalent stress at the inner surface of the model for the second deformation strategy showed the maximum stress at the ankle trimline to be

greater by 37 % when displacement was imposed along a line, rather than at a single node (see Figure B.3). The stress contours in the calf region also appeared identical to the previous distribution, indicating that the stresses throughout this region had increased by a similar percentage. Therefore, these additional imposed displacements had actually caused higher stresses to develop due to the more rigid rotation, which contradicts the statements by Fagan [1992] to some extent. Hence, the above statements regarding concentrated loads cannot be universally applied.

A plot of the equivalent stress at the outer surface for the second deformation strategy revealed that the maximum stress had decreased by 30 % relative to that obtained with a single node displacement, and was now located at the medial ankle trimline (see Figure B.4). It may be noted that the magnitude of the stress in this region had actually *increased* relative to Figure 4.9 due to the greater distribution of imposed displacements. Although the stress concentration at the imposed displacements had been decreased, it was still significant. This stress concentration indicated that these displacements were still not adequately distributed, but it could also have been due to the fact that imposed displacements must be specified with a high degree of accuracy, as even a small relative displacement between nodes can cause high stresses [Fagan, 1992]. The location of this maximum stress was the same for the remaining deformation strategies except the area displacement, where it was located at the lateral ankle trimline.

It appears from the results for the last three deformation strategies that the effects of further distributing the imposed displacements and hence the reaction forces were less significant, although the stress concentration that remained at the imposed line displacement region on both inner and outer surfaces was eliminated. The equivalent stresses for the third strategy were found to have increased by 8 % compared to the results obtained for the second strategy at both the inner and outer surfaces. This was due to the additional imposed displacements causing a more rigid rotation of the foot region about the ankle joint axis, which was evident from the 7 % increase in the rotation at the heel. Although the resultant reaction force had increased by 32 %, the ankle moment had increased by only 7 % because

a significant proportion of this reaction was distributed over a few nodes nearest the heel region (directly below the ankle), where the moment arm was smaller.

The results obtained from the fourth deformation strategy showed that the large reactions near the heel region in the previous analysis were more widely distributed by imposing displacements over a patch, as opposed to a line. The total nodal reaction force was found to have decreased by 17 % from the previous analysis, although the moment had only decreased by 2 %. The maximum equivalent stresses were also found to have decreased slightly. Comparing the results from the fifth deformation strategy to those obtained from the fourth, the maximum equivalent stresses only increased by 0.3 % and 2 % at the inner and outer surfaces, respectively. Rotation at the heel, as well as the ankle moment, both increased by 2 %, although the resultant reaction force increased by 22 % because a large proportion of this reaction was again distributed over the nodes nearest the heel region.

The most interesting observation from the fifth deformation strategy was that the medial displacement of the foot region and hence the rotation of the AFO about the global Y axis had been almost eliminated. This was due to the fact that, for the imposed displacements over the whole, curved distal foot areas to be compatible, twisting of the foot region of the AFO about the global X axis was eliminated and the nodes were effectively more constrained to deform in the X-Y plane. Medial/lateral displacement is coupled with some distortion of the cross-section, which is inhibited if all its points are forced to move by the same amount in one particular direction. As there was no medial displacement in the foot region of the model, the maximum displacement was smaller than previously obtained, even though the angle of rotation remained the same.

4.1.9 Effect of Symmetry

The first analysis was repeated with a symmetric AFO model consisting of 1709 nodes and 550 elements, which was generated by reflecting the lateral half of the

Geometry Type	δ_{max} (mm)	δ_z (mm)	θ_f ($^\circ$)	θ_h ($^\circ$)	F (N)	M (Nm)	Max σ_{eqv} (MPa)	
							Inner	Outer
Asymmetric	12.4	−2.1	−4.9	−3.4	−23.7	−3.3	24.5	21.8
Symmetric	12.3	0.0	−4.9	−3.2	−21.6	−3.0	20.6	20.1

Table 4.2. Summary of results for symmetric geometry

initial finite element mesh about the global Cartesian X-Y plane. The reasons for this were to confirm that the medial/lateral deformation would be eliminated, and also to investigate what other effects this might have on results. Although this model gave similar results to those obtained from the asymmetric model, a number of points were noted (see Table 4.2). The medial/lateral displacement of the node at the middle of the distal trimline was zero as expected. The reaction and ankle moment had both decreased by 9 %, indicating that the stiffness of the symmetric model was lower than that of the asymmetric model, but this behaviour may have been opposite had this model been generated from the medial half of the asymmetric AFO. The maximum equivalent stress at the inner surface was 16 % lower, although its location was the same and, due to the symmetry of geometry, the stress contours were also symmetric about the same plane.

4.1.10 Dorsiflexion Rotation

The first analysis was again re-run with a 5 $^\circ$ dorsiflexion rotation about the ankle joint axis, as opposed to plantar flexion. With a linear analysis the global stiffness matrix is based on the original, undeformed geometry and so the results would be the same in magnitude, although opposite in sign. However, the magnitude of the ankle angle and moment, which were not standard results but were calculated using macros, were both found to be slightly different due to the nodal x displacement of the node being opposite in direction (see Table 4.3). It is also noted that, during dorsiflexion, the foot region of the AFO deformed in a lateral direction and the calf region translated distally. This first analysis was also

Direction of Rotation	δ_{max} (mm)	δ_z (mm)	θ_f ($^\circ$)	θ_h ($^\circ$)	F (N)	M (Nm)	Max σ_{eqv} (MPa)	
							Inner	Outer
Plantar Flexion	12.4	−2.1	−4.9	−3.4	−23.7	−3.3	24.5	21.8
Dorsiflexion	12.4	2.1	5.1	3.4	23.7	3.2	24.5	21.8

Table 4.3. Comparison of results for dorsiflexion and plantar flexion

repeated by replacing the imposed displacement at the node with a concentrated force equal in magnitude to the reaction force and defined relative to the same rotated nodal coordinate system, and the results were found to be identical.

4.1.11 Uniform Pressure on Foot Region

One of the aims of this work was to investigate ways of reducing artificial stress concentrations due to point loading and yet the reactions obtained by imposed area displacement had an irregular distribution, not reflecting the rather smooth interaction expected between the AFO and foot. For this reason, an analysis was to be performed with the imposed area displacement replaced by a uniformly distributed pressure of approximately the same intensity and applied over the same area. However, the existing constraint at the foot and heel was found to provide insufficient resistance against a rigid body rotation of the AFO about the global Y axis. This was caused by an off-centre resultant of the pressure acting on the asymmetric foot region generating a small moment about the global Y axis.

An additional constraint was therefore applied in the global Z direction to a single node at the heel to eliminate this. For a meaningful comparison, the AFO was again analysed under imposed area displacement, but with this additional heel constraint, and the results were found to be virtually identical to those in Table 4.1. The total reaction force obtained from this analysis was divided by the total surface area to yield a reasonable estimate of the magnitude of the uniform pressure to be applied (11.4×10^{-3} MPa). As plantar flexion motion was being considered, this pressure was thus distributed over the inner surface of all the

Cause of Deformation	δ_{max} (mm)	δ_z (mm)	θ_f (°)	θ_h (°)	F (N)	M (Nm)	Max σ_{eqv} (MPa)	
							Inner	Outer
Displacement	12.0	0.0	−5.0	−4.9	−61.2	−4.8	34.6	16.2
Pressure	13.4	−5.8	−5.0	−4.4	−46.7	−4.3	32.8	14.9

Table 4.4. Summary of results for displacement versus pressure

elements in this region, and the results obtained are summarised in Table 4.4.

The ankle moment for this analysis was found to be 10 % lower than that obtained from the imposed area displacement due to a proportion of the pressure being applied on the medial and lateral walls of the AFO foot region. It is also seen that the medial/lateral displacement of the foot region had increased significantly from that obtained with the imposed displacements. The maximum equivalent stress at the inner surface was 5 % lower due to a smaller rotation at the heel of 10 %, but its location and the contour patterns on both surfaces appeared the same. It is worth noting that the rotation under uniform pressure had reduced at the heel but not at the distal trimline, indicating some flexibility of the foot region. This result indicates the possibility of replacing an area displacement with an equivalent area pressure.

4.1.12 Effect of Constraints on Model Behaviour

An analysis was performed with the distribution of constraints at the heel region relieved so that only those nodes on the cup of the heel were constrained, rather than all the nodes in the four areas comprising the heel region as in previous analyses (see Figure 4.11). The imposed displacements at the foot region were applied in the same manner as with the fourth deformation strategy (over a patch). This modified form of constraint was found to have a significant effect on results (see Table 4.5). The most noticeable was a 38 % reduction in the maximum equivalent stress on the inner surface at the ankle trimline, which was now located on the lateral edge. There was a smaller reduction of only 13 % in the value

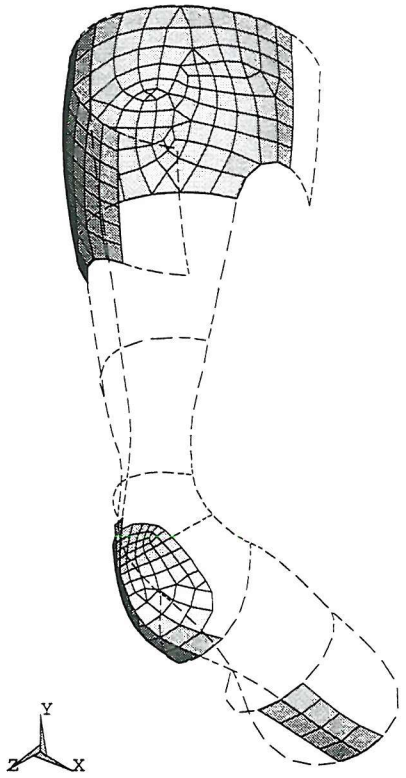

Figure 4.11. Elements indicating revised region of constraint at the heel

obtained at the outer surface, which was again located at the lateral ankle trimline. The reason for these reductions was that the stresses were more widely distributed over this region. The ankle moment was found to have decreased by 26 %, indicating the importance of the mode by which the heel is constrained.

A further simplified analysis was performed to highlight the shortcomings of previously reported analyses by again applying displacement over a patch, but with no heel constraint and the model rendered vertically stable by additionally constraining the calf at most of the nodes on the proximal trimline in the global Y direction. The results obtained are summarised in Table 4.5. A lateral view of the deformation revealed that the foot and heel regions of the AFO had not rotated about the ankle joint axis, but had *translated* posteriorly (see Figure B.5). The medial/lateral displacement of the distal foot trimline was found to have been

Heel Constraint	δ_{max} (mm)	δ_z (mm)	θ_f ($^\circ$)	θ_h ($^\circ$)	F (N)	M (Nm)	Max σ_{eqv} (MPa)	
							Inner	Outer
Full	12.3	−2.5	−5.0	−4.8	−50.4	−4.7	34.5	15.8
Reduced	12.2	−2.1	−5.0	−4.8	−37.8	−3.5	21.5	13.7
None	12.1	0.1	−4.9	−2.5	−6.2	−1.0	9.5	6.9

Table 4.5. Effects of varying region of heel constraint

eliminated by removing the heel constraint, when compared to the results obtained with the heel fully constrained. The resultant reaction force and moment were found to be, respectively, 12 % and 21 % of those obtained with the heel fully constrained.

Plots of the equivalent stress revealed that the maximum stress at the inner surface was located at the ankle trimline on the lateral edge, and was 28 % of that obtained with the heel fully constrained (see Figure B.6). The maximum equivalent stress on the outer surface was located in the same location as on the inner surface, and was 44 % of that obtained with the heel constrained (see Figure B.7). In both figures, the stresses appeared more widely distributed over the calf region and hence the stress concentrations at the ankle trimline were less severe. The reason for these differences was that, as the heel region was not forced to rotate about the ankle joint axis, most of the deformation was sustained by the calf region. This result showed that applying various, possibly unrealistic, constraints to the model could yield very different results, including an underestimate of the stresses in critical regions of the AFO and an incorrect estimation of the moment.

An alternative to the radial constraint at the heel with respect to a spherical coordinate system was to constrain the nodes in the radial direction of a cylindrical coordinate system located at the origin and whose longitudinal axis was coincident to the global Cartesian Z axis. Constraints were applied to the model as described in Section 4.1.4, except that the nodal coordinate system of each node at the heel (initially aligned with the global XYZ axes) was instead rotated about its z axis such that its x axis intersected the global Z axis. Displacement was

Heel Constraint	δ_{max} (mm)	δ_z (mm)	θ_f ($^\circ$)	θ_h ($^\circ$)	F (N)	M (Nm)	Max σ_{eqv} (MPa)	
							Inner	Outer
Spherical	12.4	−2.1	−4.9	−3.4	−23.7	−3.3	24.5	21.8
Cylindrical	12.3	0.2	−4.9	−3.3	−24.0	−3.4	24.6	22.2
Cylindrical ($\delta_z = 0$ at heel)	12.3	−0.1	−4.9	−3.3	−25.0	−3.5	24.1	22.9

Table 4.6. Effects of varying type of heel constraint

imposed at a single node on the distal trimline, as with the first analysis.

Two addition analyses were performed using this revised heel constraint, with and without constraints applied at these nodes at the heel in the global Z direction to prevent medial/lateral motion of this region. The results obtained (see Table 4.6) showed little difference to those obtained from the first analysis, except for the medial/lateral displacement of the foot region and hence rotation of the AFO about the global Y axis, which had been nearly eliminated. It may be noted that the heel displacements in the global Z direction for the first two analyses in Table 4.6 were −0.5 mm and 0.3 mm respectively. These different types of constraint therefore have a similar effect on the behaviour of the AFO, although with larger rotations of the foot region these differences would become more pronounced. Listings of the ANSYS command log files for performing some of these analyses are included in the Appendix, Section D.2.1. It should be noted that, for maximum versatility in these procedures, the loads and constraints were defined independent of the node/element numbering and hence the mesh, as there is no guarantee that these will remain the same upon modification of mesh density.

4.2 Mesh Refinement

4.2.1 Discretisation Error

When performing a finite element analysis of a physical structure, the problem is firstly represented by a mathematical model [Cook, 1995]. The difference between this model and the physical problem introduces a *modelling error.* Next, the mathematical model is discretised into a number of elements, thereby causing a *discretisation error.* This error is due to both the physical structure and mathematical model having an infinite number of points, each having 6 degrees of freedom, whereas the finite element model has a finite number of points. Finally, a *numerical error* is caused by the rounding of floating point numbers to a fixed number of decimal places by the computer, however this error is usually small.

Derived solution data, such as stress and strain, is typically discontinuous from element to element and can be plotted as contours that are discontinuous across element boundaries. The contours within each element are therefore unaffected by the results for surrounding elements, and the discontinuity between the stress contours of adjacent elements gives an indication of the stress gradient across these elements. Alternatively, derived data may be averaged (smoothed) at nodes where two or more elements are connected so that continuous contours are produced. However, an unaveraged contour plot with significant inter-element discontinuities indicates the need for a finer mesh [Cook *et al.*, 1989]. Therefore, contours based on continuous nodal average stresses are deprived of this useful information, and too much smoothing can make the results seem more accurate than they actually are.

As the equivalent stress contours are a measure of the entire state of stress, an unaveraged contour plot can be visually examined for discontinuities at inter-element boundaries to estimate the discretisation error. The amount of discontinuity can therefore be regarded as a simple, qualitative measure of whether the mesh is adequate. In an adequately refined mesh the stress bands are slightly discontinuous between element boundaries, but a global contour pattern is visible

[Cook *et al.*, 1989]. If no such pattern is evident then the mesh is too coarse, whereas if the contours are perfectly continuous the mesh is too fine. Note that, in cases where the model includes step changes in thickness or material, stress discontinuities are valid.

With reference to the equivalent stress contour plots from the previous analyses, there appeared to be no significant visual discontinuities in the stress bands between elements over both the inner and outer surfaces. However, upon closer inspection of the stress contours in the vicinity of the maximum stresses, it became apparent that there were quite large discontinuities indicating that the mesh may have needed refinement in these regions. Over the remaining region of the model the stress discontinuities were minimal, indicating that the mesh was too fine relative to the density at the critical regions and could possibly be made coarser. It may be noted that this approach to assessing discretisation is subjective, and a more objective estimate was possible within ANSYS for linear static analyses based on the Z^2 *error estimator*, as described by Cook [1995] and outlined below.

A solution from a finite element analysis contains sufficient information to allow a quantitative estimate of the discretisation error to be calculated and hence used to guide subsequent mesh refinement. During the solution phase, the *energy error* (units of Nm) is firstly calculated for every element and displayed, if necessary, as a contour plot. This quantity is a measure of the inter-element discontinuity in the stress field between elements which is similar in concept to strain energy. This error is based on the difference between the averaged and unaveraged nodal stress vectors within an element, that is the stress error vector, which is a consequence of the assumption made in the finite element method that only displacements are continuous at the nodes [SASI, 1994d].

This structural energy error is then summed over the entire model and used to calculate the overall *percent energy error*, η, relative to the total strain energy of the structure. This is a single, global quantity representing the error relative to that particular mesh discretisation, and is not an absolute measure of error. Also, the continuous stress field is considered the most accurate representation of the

exact stress field for the current discretisation. Interestingly, if the energy error is constant over the entire model, the current mesh discretisation is therefore the most efficient for that number of elements, a concept termed *error equilibration.*

Adaptive meshing is a process whereby the software monitors the discretisation error and automatically refines the mesh in an iterative manner until either the percent energy error equals a user-defined target value, or alternatively a specified limit on the maximum number of iterations is reached. This procedure was found to be too restrictive when using rotated nodal coordinate systems and required large amounts of disk storage, so it was decided to manually perform the mesh refinement using the same iterative approach. This involved firstly listing the percent energy error during postprocessing. If the magnitude of this quantity was too large, the mesh was then refined at the locations of high error on a contour plot of the energy error in order to obtain a more accurate solution.

4.2.2 Sensitivity to Element Density

To investigate the influence of mesh density on the results and thus try and reduce one possible source of error in the model, a series of analyses were performed with a pressure applied on the distal foot regions. The magnitude of this pressure (8.65×10^{-3} MPa) was taken lower than that used previously (to obtain the results of Table 4.4). The element sizes were manually refined in an iterative manner local to high error regions, which were generally concentrated where high stress gradients were located. Element sizes were also made coarser where the stress gradients were low. It may be noted that mesh refinement would have been hindered if a single nodal displacement was applied and if the software was responsible for automatically refining the mesh, as refinement would be concentrated at the misleading high energy errors surrounding this node. Although manual mesh refinement would not be hindered to the same extent, the concentrated error would nonetheless be detrimental.

Starting with the original solid model of the AFO, mesh refinement was actually

carried out using a number of techniques. The process was guided by a plot of energy error for the initial mesh, which revealed that the error was highly concentrated in the region where the ankle and calf trimlines met on both medial and lateral edges (see Figure B.8). The simplest method for locally refining a mesh at a particular location would be to define the desired element size at the nearest keypoint(s). However, it was difficult to assess the element size at the high error regions in the initial mesh because of the manner in which it had been generated. Therefore, to overcome this problem, the elements sizes at these keypoints were defined by applying scale factors to the sizes obtained from the initial mesh. The default element size specifications from the initial mesh were unaltered.

It was also decided that the size of the elements at the calf band region of the model were too fine, as the stress gradients in this region were minimal. The element sizes in these regions were therefore increased for all other meshes by forcing a specified number of divisions on the lines bounding these areas. It is noted that, due to limits on the curvature of individual elements, there was a limit on how coarse the mesh could be made. Another possible source of error was related to the elements located at the foot region of the model, where a number of distorted elements had been generated during the first meshing operation. As the stress gradients in this region of the model were minimal, the element distortions would have little effect on results. Subsequent analyses with different loading conditions could nonetheless result in larger stress gradients in this region, in which case this distortion would become more critical. Therefore, for the second mesh, the element sizes were also refined there.

The completed second mesh consisted of 1708 nodes and 549 elements (see Figure 4.12), which was surprisingly a reduction in number from the previous mesh. A plot of the energy error following an analysis revealed that this quantity was more distributed throughout the high stress regions for this second mesh, but its location remained the same (see Figure B.9). For the third mesh the elements were also slightly refined in the proximal calf region, as the error at this location had become relatively large, and the resulting mesh consisted of 2229 nodes and 724

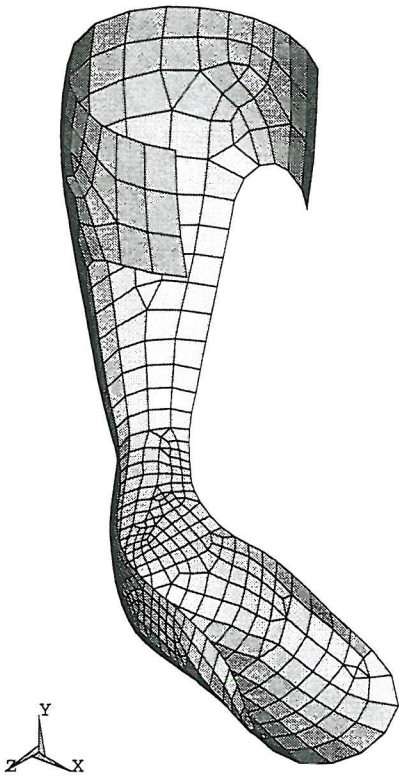

Figure 4.12. Element plot of second mesh

elements. The element sizes were refined over most of the calf region of the model for the fourth mesh, resulting in a mesh of 3691 nodes and 1224 elements. For the final mesh, the element sizes were refined over the whole of the model as a final attempt at reducing the discretisation error in the model, and the resulting mesh consisted of 5028 nodes and 1667 elements (see Figure 4.13).

A finite element model is usually stiffer than the physical structure, because the assumed displacement shapes effectively *constrain* the model to deform in an unrealistic manner. With an applied loading, the predicted displacements will therefore be less than results from the corresponding mathematical model in an overall sense, but will converge with mesh refinement [Cook, 1995]. Comparing the results from all five meshes, the maximum displacement and the distal trimline rotation appeared to be insensitive to mesh density over the finite element meshes

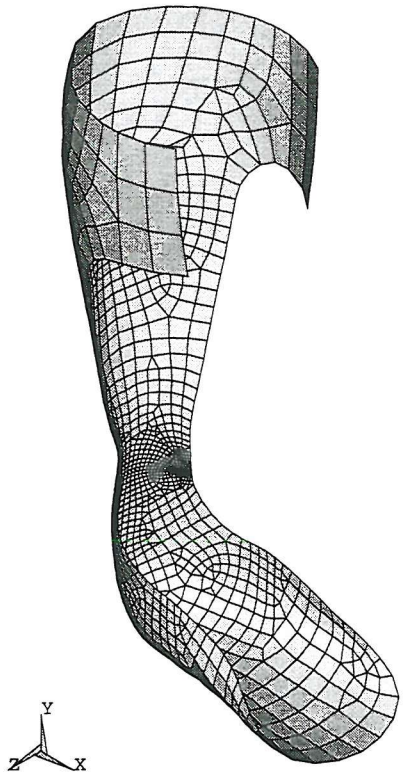

Figure 4.13. Element plot of fifth mesh

considered (see Table 4.7). The maximum equivalent stress at the inner surface appeared to be monotonically increasing towards a final value with each refinement, whereas the maximum equivalent stress at the outer surface appeared to be oscillating about its final value. This is because the displacements are usually calculated more accurately than stresses, since stresses are functions of the derivatives of the displacement field.

The magnitude of the percent energy error also decreased considerably, indicating a more reliable solution. However, the rate of convergence suggested that the elements corresponding to largest errors need to be decreased significantly in size before this value reduces to below the 5 % default target value for adaptive meshing. A larger reduction in the magnitude of the percent energy error was found following the second refinement. Reductions in percent energy error

No. of Nodes	No. of Elements	RMS Wavefront	δ_{max} (mm)	δ_z (mm)	θ_f (°)	η (%)	Max σ_{eqv} (MPa)	
							Inner	Outer
1848	597	238	10.2	−4.4	−3.8	22.9	24.9	11.3
1708	549	206	10.2	−4.4	−3.8	20.4	25.7	11.6
2229	724	224	10.2	−4.4	−3.8	15.9	26.3	12.0
3691	1224	337	10.2	−4.4	−3.8	12.6	26.8	11.3
5028	1667	400	10.2	−4.5	−3.8	10.6	27.2	11.5

Table 4.7. Summary of results from mesh refinement

following the third and fourth refinements were also lower. Comparing the results for the first and second meshes shows the number of nodes, elements and hence solution time reduced while the accuracy of the maximum equivalent stress increased and the percent energy error decreased. Therefore, by explicitly controlling the density of the mesh at high and low stress gradient regions using local mesh controls, it is possible to produce a more efficient mesh than could be obtained using global specifications alone.

For subsequent non-linear analyses, the RMS wavefront had a larger effect on the solution time due to the iterative manner in which this type of solution was obtained. Therefore, the second mesh appeared to be the most appropriate discretisation to adopt, as the RMS wavefront was minimal and the solution time was therefore kept to a minimum. Since the magnitude of the percent energy error was only a relative measure of error, the significance of these high values could not be ascertained until results had converged further. However, considering that the maximum equivalent stress at the inner surface only increased by about 5 % between the second and fifth meshes, it appeared that the magnitudes of percent energy error obtained were not so critical. This was verified during a number of test problems to assess element accuracy (see Appendix A). It may be noted that this approach to mesh refinement would not have produced the same mesh if the loads had been applied differently. Also, the ANSYS meshing algorithm is dependent on the order in which the areas were meshed, which was considered

Mesh Number	Max σ_{eqv} (MPa)			
	Averaged		Unaveraged	
	Inner	Outer	Inner	Outer
1	21.3	11.1	24.9	11.3
2	23.6	11.1	25.7	11.6
3	25.4	11.3	26.3	12.0
4	26.7	10.5	26.8	11.3
5	27.0	10.8	27.2	11.5

Table 4.8. Comparison between averaged and unaveraged equivalent stresses

undesirable. Listings of the ANSYS command log files for generating some of these meshes are included in the Appendix, Section D.2.2.

4.2.3 Effects of Averaging Stresses at Nodes

To show the effect of nodal averaging, the equivalent stresses obtained from analysing these five meshes were replotted with continuous contour bands. The maximum values obtained at the inner and outer surfaces of the AFO were found to be lower than those obtained from the discontinuous (unaveraged) contours, but the locations were the same and the difference between the averaged and unaveraged results decreased during mesh refinement (see Table 4.8). Although the average stresses at nodes that are interior to the boundary of the structure may be the most accurate available for the current discretisation and more reliable than the stress in any element at that node, only the unaveraged stress contours have been reported in this work because of the reasons stated earlier. Also, this averaging results in smeared values at nodes where elements of different material, thickness, element coordinate system orientation or other discontinuities meet, which should be avoided.

No. of Nodes	No. of Elements	RMS Wavefront	δ_{max} (mm)	δ_z (mm)	θ_f (°)	η (%)	Max σ_{eqv} (MPa)	
							Inner	Outer
929	903	118	9.8	−4.3	−3.6	32.2	20.3	13.0
1119	1095	123	10.1	−4.4	−3.7	21.1	24.5	11.6
1365	1354	153	10.1	−4.5	−3.8	19.8	25.7	11.5
2263	2262	198	10.2	−4.5	−3.8	16.3	26.5	11.7
3800	3809	263	10.2	−4.5	−3.8	13.7	26.6	11.5
5342	5388	368	10.2	−4.5	−3.8	12.1	26.9	11.5
7348	7405	425	10.3	−4.5	−3.8	11.0	27.0	11.3

Table 4.9. Results from mesh refinement with 4-noded elements

4.2.4 Alternative Element Type

As a comparative exercise, analyses were performed on an AFO modelled using the alternative 4-node plastic shell element and seven different mesh densities. The procedure for mesh refinement remained the same, but as these elements were not as accurate as the 8-node shells, a denser mesh was required to achieve similar accuracy. More specifically, a comparative mesh of 4-node elements would require approximately 4 times as many elements as the 8-node element mesh. The results obtained from these different meshes are summarised in Table 4.9 and, compared with the results from the previous element type, the sixth mesh in Table 4.9 (5342 nodes) appeared to be the closest match to the fifth mesh in Table 4.7 (5028 nodes).

The rotation and medial/lateral displacement of the distal trimline had both converged during refinement to the same values obtained with the 8-noded element. Although the rate of convergence was slower with respect to the number of elements, it was equivalent when comparing the number of nodes. Convergence of the equivalent stress results showed the same trends as in Table 4.7 and appeared to be converging to similar values. It was noted that the local discontinuities in the stress contours using the 4-noded elements were generally

more evident than with meshes using the 8-noded elements.

Although the RMS wavefront appeared to converge to approximately the same value for both element types, suggesting equivalent solution times, the CPU time required for the sixth mesh in Table 4.9 was actually 41 % greater than that required for the fifth mesh in Table 4.7. Since the number of DOF was approximately the same, this was attributed to the greater number of elements for which strains and stresses would be derived during solution, although the difference in element formulation would also have affected computational cost. Therefore, the 8-noded element type was more efficient for this problem, and a smaller number of elements was also found particularly advantageous during postprocessing.

4.3 Non-linear Static Analyses

A structure is considered to behave in a *non-linear* manner if it exhibits a change in stiffness during loading. A non-linear problem is therefore more complicated to solve than a linear problem because the stiffness matrix used to calculate the nodal displacements is actually a function of these unknowns [Cook, 1995]. As numerical methods cannot solve these non-linear equations explicitly, the solution is obtained as a series of linear approximations with corrections using a Newton-Raphson iterative procedure. Within each iteration, the solver evaluates a load imbalance corresponding to the difference between the applied load and the reaction force of the structure. It is this out-of-balance force that must converge so that the solution is in equilibrium.

There are three main causes of this type of structural behaviour. *Changing status non-linearities* include problems involving contact, where the stiffness of part of a structure changes suddenly depending on its status. These types of behaviour are modelled using special non-linear elements. *Geometric non-linearities* include problems where the stiffness of a structure changes due to a change in its geometric configuration, for example during large deformation. Finally, *material*

non-linearities include problems associated with changes in material properties, such as non-linear stress-strain relationships.

When discussing non-linear analyses, a particular loading configuration for which a solution is to be obtained is termed a *load step* [SASI, 1994a]. Its main use in transient analyses is to divide the load history curve into different sections. A load can be applied in an incremental manner by dividing each load step into a number of *substeps*, which are simply intermediate points where the results are calculated. They are usually necessary to apply the load gradually to aid convergence and ensure that accurate results are obtained. As the magnitude of the applied loads are ramped linearly within each load step, the number of substeps will affect the loading increments between each. At each substep, a number of *equilibrium iterations* are performed until either the solution has converged within tolerable limits, or the limit on the number of iterations has been reached.

The number of substeps suitable for a particular analysis is problem dependent. One approach is to specify a constant number of substeps such that the load increment remains constant throughout the load step. Although this may be suitable for problems where the behaviour is expected to remain non-linear during the complete load history, it is not economic for problems whose behaviour changes from linear to non-linear or where the behaviour is unknown. A more suitable approach in most situations is therefore to use a technique known as *automatic time stepping*, whereby the software estimates the optimum load increment between substeps based on the previous step so the solution can be obtained in the minimum number of iterations. Within ANSYS, this technique included a feature termed *bisection* that would automatically overcome a convergence failure (if possible) by halving the current load increment and restarting the analysis.

4.3.1 Geometric Non-linearity

The global stiffness matrix of a structure is dependent on the contributions of the stiffness of individual elements. This contribution can change when the nodes of an

element undergo displacement due to changes in both the *shape* of that element, which effects its individual stiffness matrix, and its *orientation*, which effects the transformation of the stiffness matrix of that element from local to global coordinates. By default, the displacements and hence the change in the global stiffness are assumed to be small, in which case a single iteration using the stiffness based on the original geometry is adequate. By activating *large deformation* effects, these stiffness changes will be taken into account and an iterative solution becomes necessary as the global stiffness is a function of the displacements.

Large deformation effects may be classified as either large strain or large deflection, depending on the type of element. Elements that support *large strain* effects will account for changes in both an element's shape and orientation, but the strain increment must be limited by dividing the applied load into substeps to maintain accuracy. For a large strain analysis, all stresses and strains are expressed in terms of true stress and true strain in the rotated element coordinate systems, but for regions where the strains are small, these quantities are no different to engineering stress and strain respectively. Poor element shapes will affect any iteration of a typical large strain analysis, as the initial mesh may become too distorted, so the deformed element shapes are just as important as the original, undeformed shapes. ANSYS does not perform element shape checking during the solution process, so the user must ensure that element shapes are satisfactory.

Large deflection effects are a limited form of large strain feature for elements that support large rotations but not large shape changes, in which case the strains are assumed to be small. Another form of geometric non-linearity is *stress stiffening*, where the in-plane (membrane) stresses in a structure affect its out-of-plane stiffness. This behaviour is most evident in thin, highly stressed membranes that are weak in bending. Stress stiffening effects can be incorporated into a small deflection analysis if required, but as the additional stress stiffness matrix changes during deformation the problem becomes non-linear. Stress stiffening may also be activated in a large deflection analysis to help convergence, although this does not affect the final converged solution.

Buckling analysis is used to calculate the critical buckling loads, at which point a structure becomes unstable, and the mode shapes associated with this response. There are two techniques for predicting this type of response. A linear, eigenvalue buckling analysis calculates the theoretical buckling strength of an ideal linear elastic structure. However, imperfections and non-linearities in a real structure prevent this load from being reached, so results are unconservative. This approach is therefore not recommended for the design of critical structures. A more accurate approach is non-linear buckling analysis, which utilises large deformation effects to find the load at which the solution begins to diverge and hence the buckling load. The accuracy of the result requires relatively fine load increments when approaching the buckling load. Using deflection-controlled loading, it is also possible to analyse snap-through structures after buckling.

The previous analyses were all based on small deflection and small strain theory, that is, large deformation effects had been ignored. However, as the rotations of the foot region of the AFO about the ankle joint axis can become quite large, the original stiffness matrix expressed in terms of the undeformed configuration will no longer adequately represent the stiffness of the structure corresponding to the deformed state [Cook, 1995]. It was therefore decided that a large deformation analysis might be necessary to obtain accurate results, so these effects were activated in the following analyses to investigate their significance. This type of non-linearity was simple to implement, as the preprocessing phase was essentially the same as a linear analysis. Because the element type had been selected with this capability in mind, different elements were not required, so the existing finite element model was adequate.

Sensitivity studies were performed to evaluate the benefits of various options available. Two identical analyses were performed, one with 5 evenly spaced substeps and the other with automatic time stepping activated such that the initial load increment was based on 5 substeps, but this could increase to a maximum of 10 substeps and decrease to a minimum of 3. The latter analysis required 20 % less cumulative equilibrium iterations over the entire load step to

Analysis Type	Direction of Rotation	δ_{max} (mm)	δ_z (mm)	θ_f (°)	Max σ_{eqv} (MPa)	
					Inner	Outer
Linear	N/A	10.2	−4.4	−3.8	25.7	11.6
Non-linear	Plantar Flexion	11.5	−5.3	−4.2	28.0	12.6
	Dorsiflexion	8.9	2.7	3.5	22.4	11.9

Table 4.10. Summary of results for geometric non-linearity

solve, but the results were identical. Stress stiffening was then activated to investigate its effect on convergence rate, but in this situation it was found to increase the number of equilibrium iterations and so it was deactivated. If the non-linear response is relatively smooth, convergence could also be accelerated using a *predictor* for the degree of freedom solution for the first equilibrium iteration of each substep. By activating this option, the cumulative number of iterations was found to decrease by a further 20 %.

To investigate the behaviour of the AFO in both plantar flexion and dorsiflexion motion with large deformation effects activated, two analyses were performed with the second mesh in Table 4.7 using the same loading and constraint conditions used during mesh refinement, that is, a pressure applied to two areas. The solution in each case converged quickly and was achieved in only 4 substeps. The key results obtained from these analyses for the last substep, where the pressure had increased to its maximum, are summarised in Table 4.10, along with results obtained from the linear analysis for comparison purposes.

As can be seen, the stiffness of the AFO appeared to be greater during dorsiflexion than plantar flexion when subjected to an identical pressure, as the magnitude of both the rotation and maximum displacement were lower. The linear analysis appeared to predict magnitudes for the maximum displacement, rotation and medial/lateral displacement somewhere between the results obtained from the two non-linear analyses. The maximum equivalent stresses at the inner and outer surfaces appeared to be greater in plantar flexion than dorsiflexion, although this was due to the greater displacement and hence rotation. The contours for both

directions of rotation appeared very similar and also matched those obtained from the linear analysis. These results showed that large deformations had a significant influence on the results, allowing the difference in behaviour of an AFO during plantar flexion and dorsiflexion to be predicted.

4.3.2 Material Non-linearity

This form of non-linearity includes non-linear stress-strain relationships such as plasticity and non-linear elasticity, where the structures stiffness depends on the load (and also temperature), as well as time-dependent non-linear behaviour such as creep and viscoelasticity, which may be dependent upon strain rate or temperature. As mentioned in Section 3.7, polypropylene exhibits a non-linear elastic behaviour, which can be modelled using a *multilinear elasticity* material model. This describes a conservative (path-independent) response where the loading and unloading follow the same stress-strain path. The load increments for this type of non-linearity may be relatively large compared to that required for plasticity, which is a non-conservative, path-dependent response where the load-response history must be closely followed for accurate results to be obtained [SASI, 1994a].

Two more analyses were performed with multilinear elasticity included to account for this material behaviour by defining a piece-wise linear stress-strain curve from 8 data points obtained from the experimental stress-strain curve (Figure 3.13) and starting at the origin. The slope of the curve after the final data point was assumed by ANSYS to be zero, such that strain would increase without an increase in stress. The Young's modulus was re-defined as 1390 MPa to match the slope of the first segment of this idealised stress-strain curve. Large deformation effects were disabled so that the effects of this material non-linearity could be viewed in isolation. These solutions were again quick to converge and required 5 substeps each. The main results for both plantar flexion and dorsiflexion motion are summarised in Table 4.11, along with the results from the linear analysis which

Analysis Type	Direction of Rotation	δ_{max} (mm)	δ_z (mm)	θ_f (°)	Max σ_{equ} (MPa)	
					Inner	Outer
Linear	N/A	7.4	−3.2	−2.7	25.7	11.6
Non-linear	Plantar Flexion	7.5	−3.3	−2.8	15.8	9.6
	Dorsiflexion	7.5	3.3	2.8	15.8	9.6

Table 4.11. Summary of results for material non-linearity

have been factored such that they correspond to a Young's modulus equal to that used during the non-linear analysis.

As expected, the results for both plantar flexion and dorsiflexion were the same, due to the fact that small deflection and small strain theory had been used. The magnitude of both the maximum displacement and rotation were only slightly higher than those obtained from the linear analysis due to the fact that, over most of the model, the stresses were small and so the modulus in these regions was similar to that from the linear analysis. The maximum equivalent stresses at both inner and outer surfaces were also lower than those obtained from the linear analysis, as the stiffness in these high stress regions was significantly lower than that over the majority of the model and so the load was effectively re-distributed over a larger area. These contour plots showed greater differences from the linear analysis plots than those obtained from the geometric non-linear analyses, although the differences were still small.

4.3.3 Combined Non-linearities

The geometric and material non-linearities from the previous analyses were combined to study the effects of both large deformation and multilinear elasticity. Although the non-linear material properties should have been re-defined in terms of true stress and strain as large deformation effects were being included, engineering stress and strain were used as the differences were calculated as only 4 % and 2 % respectively. As before, two analyses were performed to predict the

Analysis Type	Direction of Rotation	δ_{max} (mm)	δ_z (mm)	θ_f (°)	Max σ_{eqv} (MPa)	
					Inner	Outer
Linear	N/A	7.4	−3.2	−2.7	25.7	11.6
Non-linear	Plantar Flexion	8.3	−3.9	−3.0	16.2	9.9
	Dorsiflexion	6.7	2.3	2.6	15.1	9.7

Table 4.12. Summary of results for combined non-linearities

behaviour of the AFO during both plantar flexion and dorsiflexion. As with the previous non-linear analyses, the solution quickly converged in only 4 substeps. The results obtained from these analyses are summarised in Table 4.12, along with results from the linear analysis which have again been factored. Note that the tabulated values are different from those reported in Table 4.10 because the material model has changed from being linearly elastic with a Young's modulus of 1000 MPa to nonlinear elasticity with an initial tangent modulus of 1390 MPa.

The results for the maximum displacements during plantar flexion and dorsiflexion (see Figure B.10) were obtained from plots of the deformed shapes and lay either side of the value predicted by the linear analysis. The model again appears to have a greater stiffness in dorsiflexion than plantar flexion when comparing the rotations of the node on the distal trimline about the ankle joint axis, due to the geometric non-linearity. These results appeared to contradict the findings of previous experimental studies on AFO behaviour, where it has been found that posterior spring type AFOs have a greater resistance to plantar flexion than dorsiflexion [Yamamoto *et al.*, 1993a; Sumiya *et al.*, 1996b]. It seems therefore that the constraints over the heel and foot regions may have to be re-defined in order that non-linear responses be consistent with experimental observations.

Plots of the equivalent stress revealed that the maximum stresses at both inner and outer surfaces were slightly higher for plantar flexion than dorsiflexion, due to the geometric non-linearity, but these maxima were all substantially lower than those predicted by the linear analysis, due to the material non-linearity (see Figure B.11 and Figure B.12). The equivalent stresses obtained from the combined non-linear

No. of Nodes	No. of Elements	Direction of Rotation	δ_{max} (mm)	δ_z (mm)	θ_f (°)	Max σ_{eqv} (MPa)	
						Inner	Outer
1708	549	Plantar Flexion	8.3	−3.9	−3.0	16.2	9.9
		Dorsiflexion	6.7	2.3	2.6	15.1	9.7
2229	724	Plantar Flexion	8.3	−3.9	−3.0	17.1	10.1
		Dorsiflexion	6.7	2.3	2.6	15.6	9.5
3691	1224	Plantar Flexion	8.3	−3.9	−3.0	17.6	10.0
		Dorsiflexion	6.7	2.3	2.6	15.8	9.7

Table 4.13. Summary of results from non-linear mesh refinement

analyses were lower than the quoted yield strength of the material, assuming that it was possible to define a point on the non-linear elastic curve relating to yield.

Graphs of the displacement components in the global X, Y and Z directions of the node located at the intersection of the global Cartesian X-Y plane and the distal trimline (point 'P' in Figure 3.7) were plotted as a function of pressure for both directions. These displacement versus pressure histories revealed that the AFO behaviour was only slightly non-linear as the pressure was incrementally increased, and they appeared relatively smooth indicating that the time step size was not too great. Graphs of pressure versus rotation of this same node also displayed these same trends. However, the stiffness of some posterior spring type AFOs has been found to decrease during dorsiflexion [Condie & Meadows, 1977; Golay *et al.*, 1989; Leone *et al.*, 1991]. Therefore, it appears from these results that further analyses are needed to investigate the effect that different trimline locations and higher loading conditions have on AFO behaviour. A listing of the ANSYS command log file for performing either of the combined non-linear analyses is included in the Appendix, Section D.2.3.

4.3.4 Alternative Mesh Densities

Although it is not common practice to perform mesh refinement during a non-linear analysis due to the increased solution time, the previous non-linear analyses were repeated for both dorsiflexion and plantar flexion with the third and fourth meshes discussed in Section 4.2.2. The results, which are summarised in Table 4.13 together with those obtained from the previous mesh, showed the same trends as in linear mesh refinement. The maximum displacements and rotations were again not sensitive to mesh density, whereas the equivalent stresses showed convergence to final values. As the maximum variation in equivalent stress from the second mesh to the fourth mesh was about 9 %, it was clear that the results from a non-linear analysis were at least as sensitive to element density as those obtained from a linear analysis. Therefore, this source of error must not be ignored when evaluating the results.

Chapter 5

Investigating the Model's Sensitivities

5.1 Effect of Variation in Elastic Properties

Parametric studies were performed to assess the sensitivity of the model to variations in the material properties. This exercise was considered useful because manufacturers will usually quote a range of values to account for natural variations between specimens. Due to the uncertainty regarding the precise value of Poisson's ratio for polypropylene, the effect of the variation of this material constant was first investigated. An analysis was performed with the initial mesh and a pressure loading, as described in Section 4.2.2, but with a new Poisson's ratio of 0.385, a 10 % increase from the original value of 0.35. Postprocessing revealed that this relatively large increase in Poisson's ratio resulted in no change in the maximum displacement or the foot rotation, but caused a 2 % increase in medial/lateral deformation of the distal trimline, a 1 % decrease in the maximum equivalent stress at the inner surface, and no change in the maximum equivalent stress at the outer surface (see Table 5.1). These variations were considered insignificant, confirming that using the exact value of Poisson's ratio was not critical.

Young's Modulus (MPa)	Poisson's Ratio	δ_{max} (mm)	δ_z (mm)	θ_f (°)	Max σ_{eqv} (MPa)	
					Inner	Outer
1000	0.35	10.2	−4.4	−3.8	24.9	11.3
1000	0.385	10.2	−4.5	−3.8	24.6	11.3
1100	0.35	9.3	−4.0	−3.4	24.9	11.3

Table 5.1. Sensitivity of results to elastic material properties

To highlight the much lower significance of variations in Poisson's ratio compared to variations in Young's modulus, the above analysis was repeated with a new Young's modulus of 1100 MPa, a similar increase of 10 % from the original value of 1000 MPa, and with the Poisson's ratio reset to 0.35. Postprocessing revealed that this increase in Young's modulus resulted in decreases in the maximum displacement, the foot rotation and the medial/lateral foot displacement of 9 % each, while the maximum equivalent stresses at both inner and outer surfaces remained the same. These results were predictable as the displacement is inversely proportional to the stiffness, which is itself proportional to Young's modulus, while the stresses only depend on the distribution and magnitude of the applied loading. The results are therefore sensitive to variations in Young's modulus and so knowledge of its exact magnitude is critical. In both sensitivity studies described above, the stress contour patterns and the locations of maximum stress remained unchanged.

5.2 Effect of Variable Thickness

To study what effect a variation in thickness due to the vacuum forming process would have on results, a variable thickness model was developed. The geometry of a custom-made AFO, manufactured at St. Mary's Hospital (Isle of Wight) specifically for the purposes of this research, was examined and the thickness measured at a number of key locations using a micrometer. This revealed that the thickness of the material varied significantly over the AFO, particularly at the foot

region. The minimum thickness (2.2 mm), which was located at the heel region, was about 54 % of the maximum thickness (4.1 mm) located at the posterior calf region. The average thicknesses around the ankle trimline at the medial and lateral edges were 79 % and 78 % of the maximum thickness, respectively, which agreed with measurements made by Golay *et al.* [1989] who had found thickness ratios of 81 % and 77 % at the medial and lateral malleoli regions, respectively.

It was decided to amend the modelling routine to include elements of differing thickness to study the sensitivity of the results to such changes. As it would be impractical to assign a different thickness to the individual nodes of each element, the actual AFO was assumed as being divided into regions of constant thickness corresponding to the areas into which the previously described solid model had already been divided, although the geometry of the actual AFO was different from that of the model. Therefore, the variable thickness over each region of the actual AFO, corresponding to an area of the model, was averaged so that it could be approximated as being constant. The thickness values adopted are listed in Table 5.2 for both medial and lateral halves of the AFO. The values are ordered such that the first row corresponds to the calf band area and subsequent rows represent more distal areas, although area numbers can be identified from Figure 5.1.

The finite element model thicknesses given in Table 5.2 were calculated so that their ratio to maximum sheet thickness is the same as the local to maximum thickness ratio in the corresponding region of the actual AFO. They were based on a maximum sheet thickness of 2 mm, which was the uniform thickness used in all previous analyses. One shortcoming with this approach was that, in regions where the thickness varied significantly, it was not possible to capture both the maximum and minimum values. Therefore, as can be seen from the table, the minimum thickness ratio in the model was 70 % (corresponding to a minimum thickness of 1.4 mm) compared with 54 % given above for the actual AFO. This error could be reduced by dividing the AFO into a greater number of areas, but this would increase the complexity of the model. It may be noted that the thickness variations between each half arise due to a combination of the manual vacuum

Lateral Half			Medial Half		
Area Number	Thickness (mm)		Area Number	Thickness (mm)	
	Actual	FE Model		Actual	FE Model
3	3.5	1.75	4	3.6	1.8
15	3.8	1.9	16	3.8	1.9
5	3.9	1.95	6	3.9	1.95
7	4.0	2.0	8	4.0	2.0
9	3.6	1.8	10	3.6	1.8
11	2.8	1.4	12	2.8	1.4
13	3.0	1.5	14	3.3	1.65
1	3.4	1.7	2	3.5	1.75

Table 5.2. Thickness variation in custom-made AFO and FE model

forming process and the asymmetry of the positive cast.

A number of different analyses were performed on the variable thickness model with a uniform pressure and the second mesh density developed in Section 4.2.2 (see Figure 4.12) to allow comparison with previous linear and non-linear analyses to be made. The results obtained from a linear analysis are summarised in Table 5.3 along with the results obtained from the original model with a constant thickness of 2 mm. These results show that, by incorporating a variable reduction in thickness, the maximum displacement and rotation increased by 7 % and 8 %, respectively, due to a reduction in stiffness. The medial/lateral displacement of the distal trimline was also found to have increased by 5 %. Although the maximum equivalent stress in the inner surface increased only slightly, the value obtained at the outer surface had increased by 15 %.

The effect of variable thickness depends on whether the changes in thickness occur in regions of high or low stresses. For instance, if the thickness of the AFO is reduced in the high stress regions at the ankle trimline, its stiffness will reduce significantly. Results obtained from an analysis of this same model with a constant thickness of 1.4 mm, the minimum listed in Table 5.2 for the variable thickness

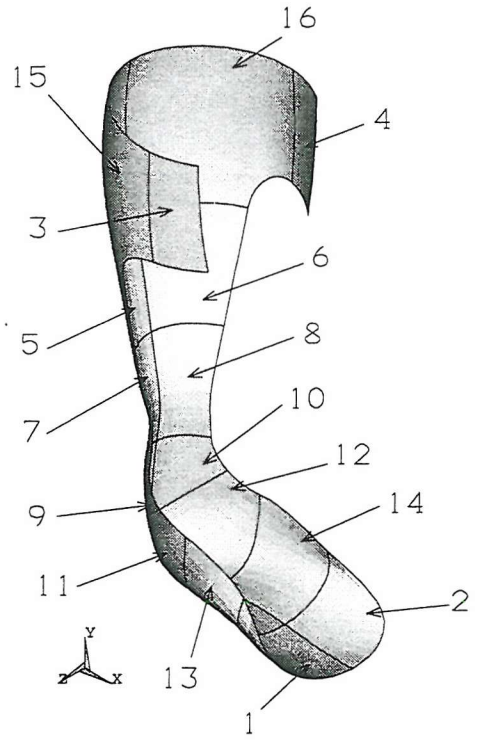

Figure 5.1. Area numbers of sub-divided AFO

model, showed increases in the maximum displacement and rotation of 102 % and 79 %, respectively (see Table 5.3). The maximum equivalent stresses at the inner and outer surfaces had increased by 82 % and 87 % respectively. The medial/lateral displacement had increased by 173 %. It may be noted that the maximum displacement at the centre of a uniformly loaded rectangular plate is indirectly proportional to the thickness-cubed (see Appendix A).

Thickness (mm)	δ_{max} (mm)	δ_z (mm)	θ_f ($^\circ$)	Max σ_{eqv} (MPa)	
				Inner	Outer
2	10.2	−4.4	−3.8	25.7	11.6
Variable	10.9	−4.6	−4.1	25.9	13.3
1.4	20.6	−12.0	−6.8	46.9	21.7

Table 5.3. Sensitivity of results to thickness variation under uniform pressure: linear analyses

Thickness	Direction of Rotation	δ_{max} (mm)	δ_z (mm)	θ_f (°)	Max σ_{eqv} (MPa)	
					Inner	Outer
Uniform	Plantar Flexion	8.3	−3.9	−3.0	16.2	9.9
	Dorsiflexion	6.7	2.3	2.6	15.1	9.7
Variable	Plantar Flexion	8.9	−4.1	−3.3	16.2	10.0
	Dorsiflexion	7.3	2.4	2.8	15.1	9.7

Table 5.4. Sensitivity of results to thickness variation under uniform pressure: non-linear analyses

Results obtained from applying the analysis which combined material and geometric non-linearity to the variable thickness model revealed that, firstly, the maximum displacements obtained during both plantar flexion and dorsiflexion increased by a similar percentage as for the linear analysis, that is, 7 % and 9 % respectively (see Table 5.4). The rotation increased by 10 % and 8 % during plantar flexion and dorsiflexion respectively. The changes in maximum equivalent stress obtained were less than 1 %, a different trend to those obtained from the linear analysis. Note that, for all the linear and non-linear analyses performed, the stress distributions did not appear to alter significantly. Overall, it has been shown that the thickness of the AFO can have a significant effect on results, so the variation in thickness should ideally be incorporated into the model if accurate results are to be obtained.

5.3 Model based on a Prefabricated AFO

An alternative model was developed based on a prefabricated AFO obtained from Southampton General Hospital in order to simulate buckling in the model, since such behaviour was evident in the physical device when manually forced into dorsiflexion. The leg surface geometry used for this model was that used for all previous models, but the dimensions for the trimline (see Table 5.5) were set to match those of the prefabricated AFO as closely as possible. Note that, as the

Dimension	Magnitude (mm)
PROXIMAL	250
DISTAL	115
CALFBAND	75
OVERLAP	20
RADIUS	35
ANKLE	53

Table 5.5. Dimensions for trimline of prefabricated AFO

dimensions RADIUS and ANKLE are not equal, the centre of the ankle trimline arc did not correspond to the ankle joint axis located at the global Cartesian origin. Again, the thickness of the real AFO was measured, averaged over the regions corresponding to the areas of the model and then defined as being constant in each area.

The variation in thickness measured in this case was more severe than for the previous custom-made AFO, with the maximum and minimum thickness being 3.5 mm and 1.3 mm, respectively, and therefore a thickness ratio of 37 % (see Table 5.6). However, the locations of these extreme values were the same as in the previous model. It may be noted that, for this model, the actual AFO thickness values were used for each area, rather than scaled values as in Section 5.2. The mesh density was defined as for the second mesh in Section 4.2.2 but, due to the fact that the geometry of the AFO had altered, the number of nodes and elements generated during meshing had changed to 1788 and 571 respectively (see Figure 5.2). An initial linear analysis revealed that this model had a lower stiffness than the original model due to a more posterior trimline.

To simulate realistic constraint at the heel, analyses combining geometric and material non-linearities were performed with the reduced constraint in this region described in Section 4.1.12. In search of buckling, the magnitude of the displacement imposed over the patch of nodes on the two distal areas of the foot was increased so that the maximum angle of rotation would reach 15 $^{\circ}$. As Table

Lateral Half		Medial Half	
Area Number	Thickness (mm)	Area Number	Thickness (mm)
3	2.0	4	1.7
15	2.3	16	2.3
5	3.5	6	3.4
7	3.5	8	3.3
9	3.2	10	2.8
11	1.7	12	1.3
13	1.7	14	1.7
1	2.3	2	2.3

Table 5.6. Thickness variation in prefabricated AFO and FE model

5.7 shows, the plantar flexion and dorsiflexion moment reactions about the ankle joint axis obtained with this heel support indicate that the stiffness was significantly greater in dorsiflexion than plantar flexion, which contradicted previous experiments as stated in Section 4.3.3. A graph of the predicted ankle moment plotted against dorsiflexion angle was also approximately linear, showing no reduction in stiffness to indicate the onset of buckling. An apparent reason for this discrepancy with experimental evidence was that the constraints at the heel region of the model were applied over too many nodes, effectively restricting the malleoli region from bulging out during dorsiflexion. As the experimental test rigs described in the literature [Condie & Meadows, 1977; Leone *et al.*, 1988] did not include any form of constraint at the heel, the published results cannot be directly compared with the results from the present analyses.

It was noted that the medial/lateral displacements of the distal trimline predicted under rotation in either direction were *both* in a lateral direction and were accompanied by external rotation of the AFO about the tibial axis (see Table 5.7). This behaviour was different from that reported in previous sections, where the directions were opposite for plantar flexion and dorsiflexion. Although the

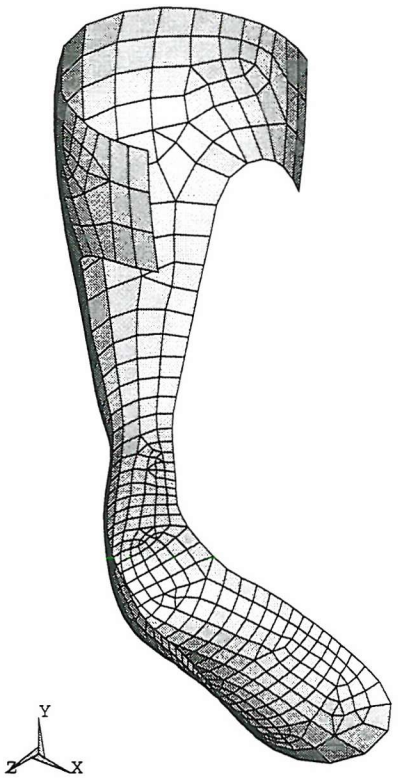

Figure 5.2. Element mesh of prefabricated AFO showing revised trimline

magnitude of this medial/lateral displacement was similar for both directions, the magnitude of the external rotation appeared greater under dorsiflexion (see Figure 5.3). By re-defining the radial constraint at the heel region relative to a cylindrical, rather than spherical, coordinate system, this external rotation during dorsiflexion was accompanied by a large and unrealistic medial displacement of the complete foot and heel region, causing the calf region to undergo a twisting deformation. This change in coordinate system therefore had a stronger effect under this large rotation than in the earlier linear analysis, indicating the importance of modelling the constraint at the heel in the global Z direction.

In a further attempt at simulating the experimentally observed behaviour, the non-linear analyses were repeated with the constraint at the heel region removed and additional translation constraints applied at the calfband in the remaining

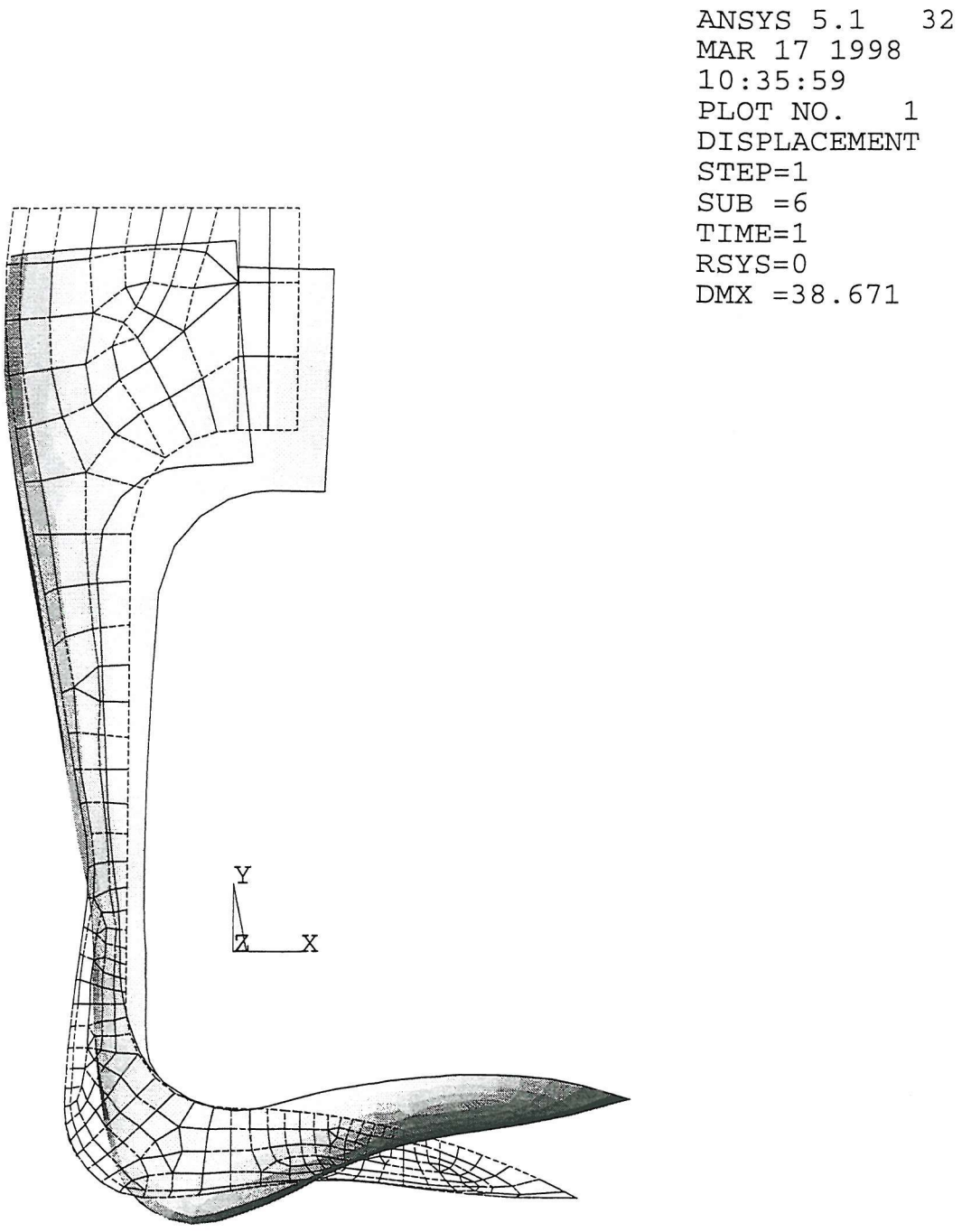

Figure 5.3. Lateral view of 15 ° dorsiflexed prefabricated AFO showing external rotation

Heel Constraint	Direction of Rotation	δ_{max} (mm)	δ_z (mm)	θ_f (°)	M (Nm)	Max σ_{eqv} (MPa)	
						Inner	Outer
Reduced	Plantar Flexion	38.2	9.1	−14.8	−9.7	19.5	18.5
	Dorsiflexion	38.7	9.8	15.2	13.5	21.6	19.4
None	Plantar Flexion	37.6	6.1	−14.5	−3.9	15.9	14.3
	Dorsiflexion	38.4	−4.1	15.6	3.6	15.3	13.8

Table 5.7. Effect of heel constraint on prefabricated AFO under 15 ° rotation

directions. This form of constraint was considered more representative of the experiments where buckling behaviour had been reported. The number of substeps was also increased for improved accuracy with this large angle of rotation. The results showed that, as with the previous analysis lacking heel constraint detailed in Section 4.1.12, the maximum equivalent stresses were reduced considerably. The ankle moments were also found to have reduced by 60 % and 73 % during plantar flexion and dorsiflexion respectively, but, more importantly, the resistance to plantar flexion (calculated from the quotient of moment and rotation) was 17 % greater than that to dorsiflexion. A graph of ankle moment versus ankle angle during dorsiflexion also showed a slight non-linearity above 8 ° rotation such that the stiffness of the AFO reduced with increasing angle (see Figure 5.4). In conclusion, the manner of heel constraint can affect the non-linear behaviour of an AFO and, as shown in Table 5.7, the direction of medial/lateral displacement of the distal trimline.

5.4 Simulation of Experiments by Sumiya *et al.*

As stated in Section 2.5, the device developed by Sumiya *et al.* [1996a] consisted of an artificial foot attached to a metal pipe representing the tibia with a hinged ankle joint. The joint axis was at lateral malleolus height, perpendicular to the sagittal plane at the intersection of the midline of the foot with the anatomical ankle axis. The pipe formed a sliding joint through the centre of an artificial calf

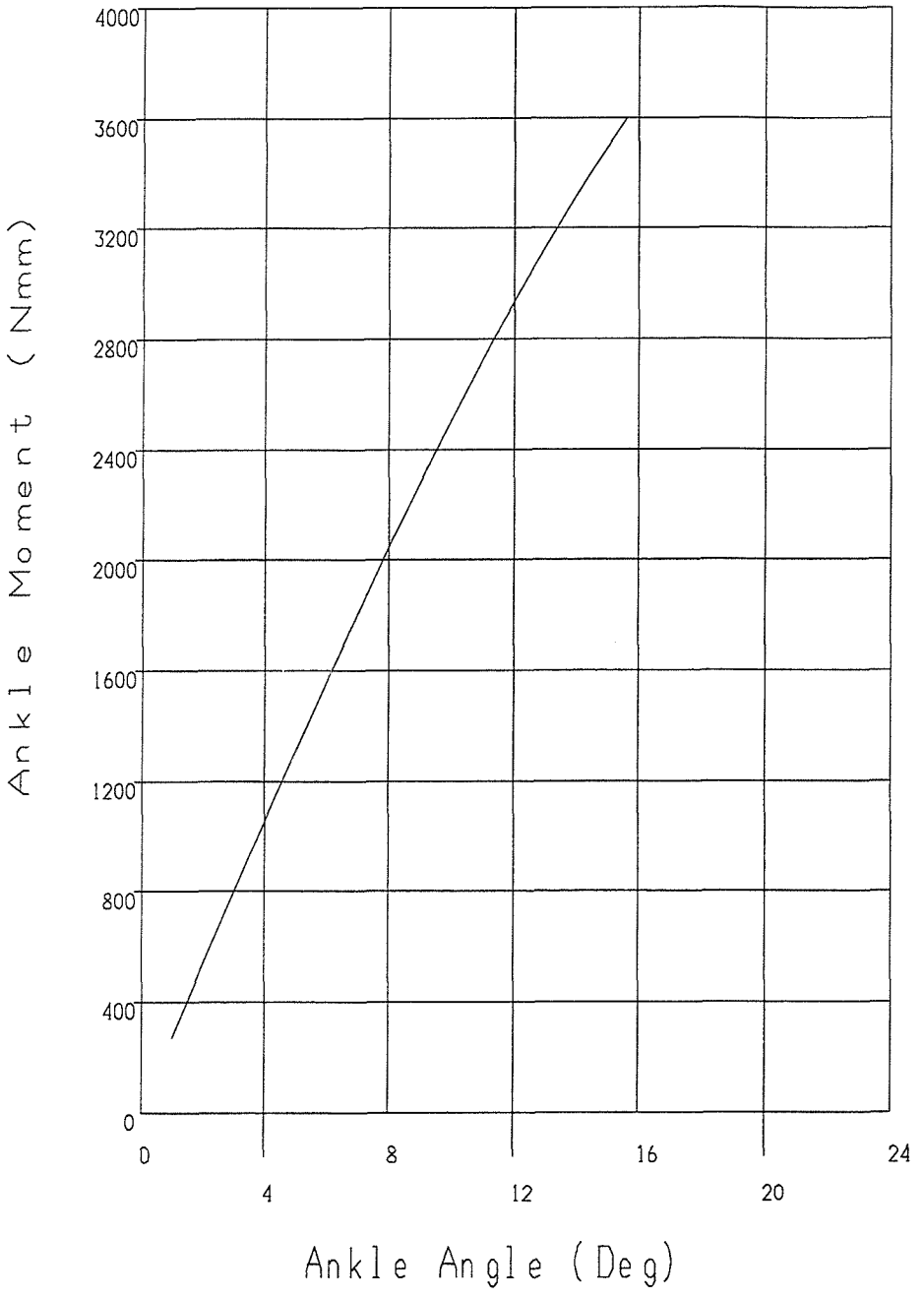

Figure 5.4. Ankle moment versus angle of rotation of prefabricated AFO during dorsiflexion

and was clamped at its free end. Each AFO was secured to the artificial calf by its calf strap, and its sole was bolted to the artificial foot anterior to the heel. A tensiometer was attached perpendicular to a lever arm, which was hinged at the ankle joint and coupled to the artificial foot. A moment was applied to the AFO by manually pulling the tensiometer, whilst rotation was measured using a protractor centred at the ankle axis. Experiments were performed on a number of AFOs whose ankle trimline, consisting of a circular arc centred at the ankle axis, varied in radius from 20 % to 60 % of the lateral malleolus height. The ankle moment in both directions was found to be roughly inversely proportional to the ankle trimline radius.

5.4.1 Model Development

As a preliminary validation exercise, and to investigate the effect of ankle trimline variation on the stiffness of plastic AFOs, a number of analyses were performed to simulate the experiments carried out by Sumiya *et al.* [1996b]. The initial finite element model was modified during these analyses in stages, in order to better simulate the test conditions, by duplicating more exactly the AFO specimen geometry and mode of imposed displacement. The trimline dimensions were defined to duplicate, as close as possible, data on mean measurements of the geometry of the 30 AFOs tested, which was obtained directly from the investigators (see Figure 5.5 and Table 5.8). As no data was available on the surface geometry of these specimens, the data described in Section 3.3.1 was used. It may be noted that the flat sole region that extended to the distal trimline at the end of the toes in the AFOs tested was not included in the model.

The initial model developed was based on the dimensions for the 40 % trimline stage, where the ankle trimline arc radius was set to 40 % of the lateral malleolus height, so the behaviour would be between the two extremes (20 % and 60 % trimlines). Due to the fact that the definition of the vertical position of the ankle joint axis in these experiments was at lateral malleolus height, which was different

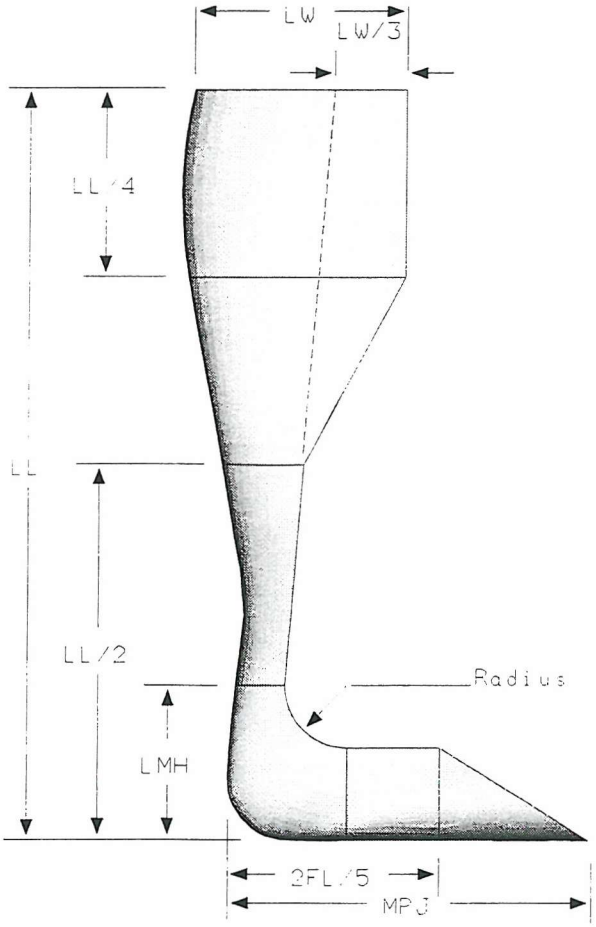

Figure 5.5. Trimline dimensions of the AFOs tested by Sumiya *et al.*

from that used in previous sections, a correction had to be incorporated into the model. The distance of the metatarsophalangeal joint (MPJ) from the heel in the model was calculated from the average of the tabulated distances to the 1st (medial) and 5th (lateral) MPJ. As the flat region of the AFO extending to the toes was not modelled, the MPJ location became the distal trimline. The material thickness was assumed a constant 3 mm to match the reported thickness of the polypropylene sheet used to manufacture the specimens tested. Non-linear elasticity and large deformation effects were both incorporated into the model

To accurately model the test rig detailed by Sumiya *et al.* [1996a], the constraints were applied in a more representative manner. Displacement was imposed over a patch of nodes on the two distal foot areas, similar to the previous chapter, to represent the rigid rotation of the foot region about the ankle joint axis provided

Dimension			Magnitude (mm)
Leg	Length (LL)		350
	Width	Max (LW)	97.5
		Min	67
	Height of Min Width		132.3
Malleoli	Height	Lateral	72.1
		Medial	79.3
	Inter-malleolar Distance		79.6
	Distance from Heel	Lateral	50
		Medial	59.7
Foot	Length (FL)		244.3
	Distance from Heel	1st MPJ	172.2
		5th MPJ	159.8
	Max Width		92.3

Table 5.8. Data on the AFOs tested by Sumiya *et al.*

by the plaster foot part of the apparatus. The posterior foot region of the AFO in the rig was bolted to the underside of the plaster foot directly below the ankle joint axis to provide the radial constraint in this region. This was modelled by constraining a patch of nodes in this region close to the global Cartesian X-Y plane. However, rather than constraining these nodes radially with respect to a spherical coordinate system, they were constrained radially with respect to a cylindrical coordinate system, whose origin was located on the ankle joint axis, in a similar manner to Section 4.1.12. Additionally, these nodes were also constrained in the global Z (medial/lateral) direction to correctly simulate the hinged ankle joint. The calf constraint was identical to that used previously.

As shown in Table 5.9, the discrepancy between measured and predicted moments for 5 ° plantar flexion and dorsiflexion was found at this stage to be considerable, since the experimental moments were reported as -3.3 Nm and 2.4 Nm respectively, while the predicted moment, M, in plantar flexion was greater than in

Modification Stage	Direction of Rotation	M (Nm)	Discrepancy (%)
Initial Model	Plantar Flexion	−6.8	+106
	Dorsiflexion	5.7	+138
Flattened Foot Geometry	Plantar Flexion	−6.8	+106
	Dorsiflexion	5.7	+138
Scaled Leg Geometry	Plantar Flexion	−5.7	+73
	Dorsiflexion	4.7	+96
Variable Thickness	Plantar Flexion	−4.4	+33
	Dorsiflexion	2.8	+17
Imposed Heel Rotation	Plantar Flexion	−4.5	+36
	Dorsiflexion	3.0	+25
Improved Rotation Modelling	Plantar Flexion	−3.7	+12
	Dorsiflexion	2.2	−8

Table 5.9. Effect of model development on moment prediction for 5 ° rotation: 40 % trimline

dorsiflexion. Therefore, further improvements to the model were deemed necessary. The geometry of the model was brought closer to that of the specimen by straightening the arch of the foot in the sagittal plane and incorporating a flat region into the foot tapering back to the heel. As Table 5.9 shows, these alterations were found to have no effect on the calculated moments. The leg geometry before trimming was modified for the next analyses to more closely match that of the AFOs tested. This involved scaling the width of each cross-section spline by factors ranging from 0.8 at the proximal cross-section to 1.2 at the ankle region and back to 1.0 at the distal cross-section. These modifications were found to have a considerable effect on results, reducing the moments in plantar flexion and dorsiflexion considerably, but the discrepancies were still large at 73 % and 96 % respectively.

Another crucial step towards a more representative geometry was then taken. The thickness of the AFO was modified from being constant over the whole AFO to

variable. Although no information was available on the thickness variation of the AFOs tested, by assuming the reduction in thickness over different regions was similar to that observed in the custom-made AFO modelled in Section 5.2, a variation based on the nominal sheet material thickness could be calculated. The effect of the variable thickness was found to be more pronounced on this model than that analysed in the previous section. Indeed, this modification to the model had the greatest effect out of all those described above, reducing the discrepancy in the predicted moments for plantar flexion and dorsiflexion to 33 % and 17 % respectively. Although the dorsiflexion moment was considered acceptable, the plantar flexion discrepancy was too great.

As the AFO was bolted to the plaster foot of the testing apparatus directly below the ankle joint, near the heel, rotation would be applied to this region about the ankle axis, as well as at the foot. For the following analyses, displacements were therefore imposed at the nodes below the ankle joint in the circumferential direction (rotated nodal y direction) of the existing cylindrical coordinate system representing the ankle joint of magnitude $R\theta$, as per the foot, in addition to the radial and longitudinal constraint at these nodes. It may be noted that the moment calculation macro had to be modified to include the contribution of additional reaction forces generated at these nodes. This modification was found necessary to overcome convergence problems during an analysis of a revised model, having a 20 % trimline stage. Although additional modifications were incorporated into these analyses, as described below, these measures did not help convergence.

The region of constraint near the heel was reduced to include only those nodes near the global Cartesian X-Y plane (see Figure 5.6). The patch of nodes at the foot where the imposed displacements were applied was also reduced in size because, during dorsiflexion, the test rig only applied loading over a small region of the foot. The region of radial constraint at the calf was modified such that, under dorsiflexion motion, a patch of nodes were constrained at the anterior calf region where the calf strap was riveted to the AFO. Moreover, under plantar flexion, only a patch of nodes located on the posterior calf region were constrained. The mesh

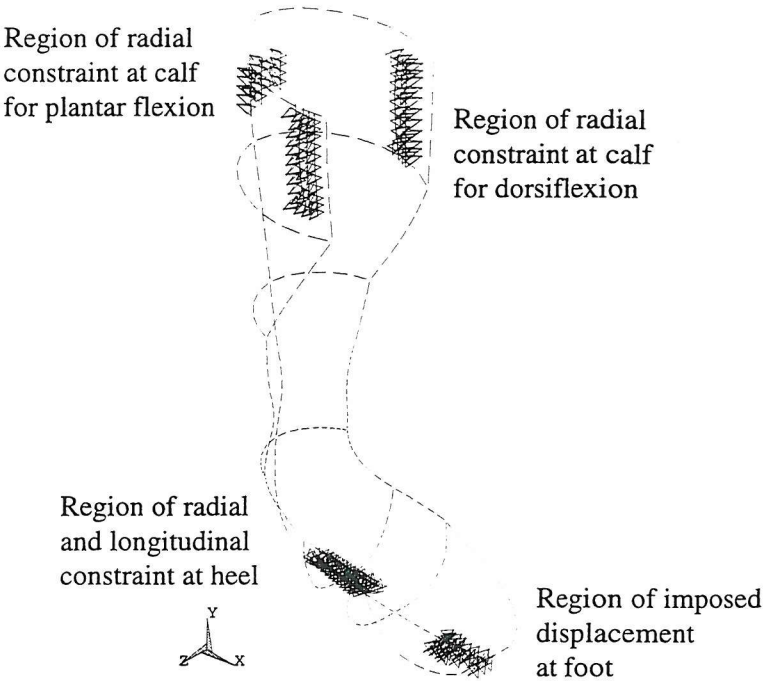

Figure 5.6. Distribution of imposed displacement and constraint used during simulation of experiments by Sumiya *et al.*

was refined at the foot and heel regions, where the imposed displacements had been applied, to distribute peak reaction forces causing stress concentrations. The non-linear elasticity curve was also extended assuming constant curvature to a maximum stress of 24 MPa. The results showed that, as the predicted moment reactions had increased for both plantar flexion and dorsiflexion to -4.5 Nm and 3.0 Nm, respectively, these modifications had caused a more rigid rotation of the foot region of the AFO about the ankle axis.

Finally, a revised method of aligning the nodal coordinate system of each node at the foot region having displacement imposed was devised (see Figure 5.7). This approach involved an additional procedure to those described on page 111 whereby, after initially rotating the nodal coordinate system at each selected node about its z axis, a further rotation equal to the magnitude of the desired rotation of the foot, θ, was applied about this same axis (+ve dorsiflexion, $-$ve plantar flexion). The magnitude of the imposed displacement in the nodal y direction was also more accurately defined as $R\sin\theta$, as opposed to $R\theta$, due to the large angles

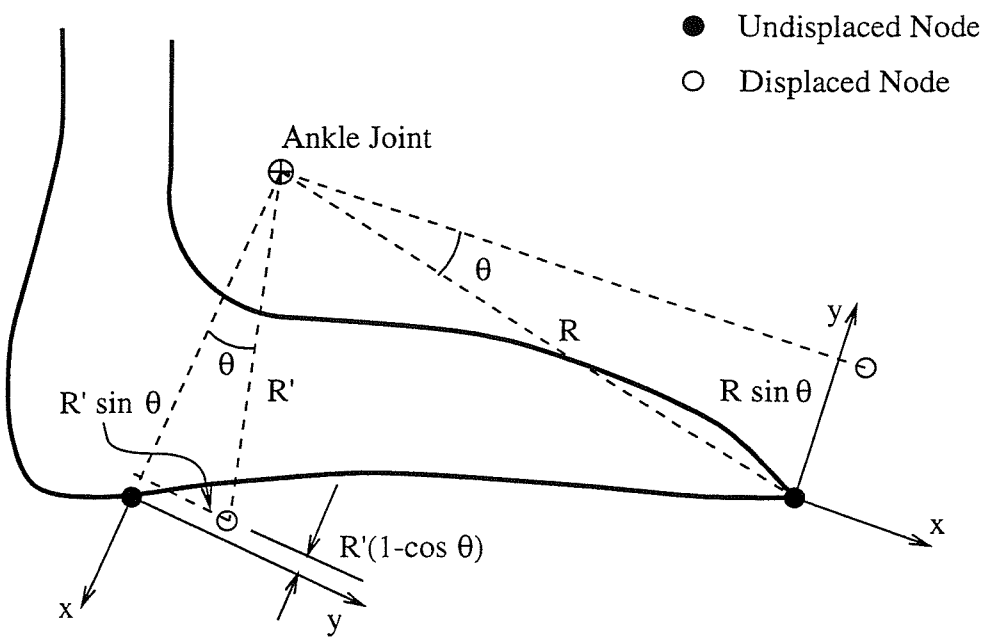

Figure 5.7. Revised nodal coordinate system orientation showing imposed displacement magnitudes

of rotation envisaged for future analyses. This approach allowed the exact desirable rotation of each node about the ankle axis to be achieved, irrespective of its displacement in the nodal x direction. The moment calculation macro was also modified to account for the change in the moment arm of each node at the foot region, in its undeformed configuration, from R to $R\cos\theta$. The moment contribution at the foot was therefore obtained from the following equation, where F_y is the nodal reaction force in the rotated nodal y direction:

$$M_{foot} = \sum_{nodes} F_y(R\cos\theta + \delta_x) \tag{5.1}$$

This additional rotation was not applied to the nodal coordinate systems of those nodes below the ankle axis having displacement imposed, as it was considered unnecessary, but the magnitude of the imposed displacements in the nodal y direction at those nodes was redefined as described above. As the previous analyses did not ensure that the angle of rotation imposed at these nodes was consistent with that applied by the experimental test rig, the radial constraint

below the ankle axis was replaced with displacements imposed in the rotated nodal x directions of magnitude $R'(1 - \cos\theta)$ to more accurately simulate a finite rigid body rotation. Therefore, the exact location of each node after deformation and hence the angle were better controlled. The moment contribution near the heel was hence calculated using Equation (5.2) below.

$$M_{heel} = \sum_{nodes} F_y(R' + \delta_x) = \sum_{nodes} F_y \times R' \cos\theta \tag{5.2}$$

As Table 5.9 shows, this final step brought analytical results considerably close to experimental measurements, with discrepancies of 12 % and −8 % for plantar flexion and dorsiflexion, respectively, and thus established a reliable loading/constraint pattern.

5.4.2 Sensitivity to Ankle Trimline Radius

The imposed displacement technique described above was subsequently applied to AFOs with the ankle trimline arc radius and hence the trimline stage varying from 20 % to 60 % of the lateral malleolus height, to assess its effect on AFO stiffness. It may be noted that the number of nodes and elements decreased irregularly from 2851 and 912, respectively, for the 20 % trimline stage, to 2480 and 787, respectively, for the 60 % trimline stage. The results from these analyses are shown in Table 5.10. Comparing the moments calculated from these analyses, M, and those obtained from the experiments, M_e, it was clear that the discrepancy in the analytical results was small except for the plantar flexion results for both the 50 % and 60 % trimline stages. These discrepancies did not necessarily indicate inaccurate results, as the experimental moments retrieved from a graph in the published work for these two trimline stages were small and therefore not clearly identified. The analytical results also consistently showed the AFO to have a greater stiffness in plantar flexion, whereas experimental results indicated a greater stiffness in dorsiflexion for these two trimlines only.

Trim (%)	Direction of Rotation	M (Nm)	M_e (Nm)	Discrepancy (%)	Max σ_{eqv} (MPa)	
					Inner	Outer
20	Plantar Flexion	−7.4	−7.2	+3	17.6	16.6
	Dorsiflexion	4.2	4.5	−7	16.5	11.8
30	Plantar Flexion	−5.3	−5.0	+6	15.7	15.0
	Dorsiflexion	3.1	3.4	−9	14.4	10.6
40	Plantar Flexion	−3.7	−3.3	+12	13.8	10.3
	Dorsiflexion	2.2	2.4	−8	12.5	9.0
50	Plantar Flexion	−2.2	−1.3	+69	11.8	9.5
	Dorsiflexion	1.5	1.5	0	11.0	8.8
60	Plantar Flexion	−0.9	−0.4	+125	9.5	8.0
	Dorsiflexion	0.7	0.8	−13	9.2	7.5

Table 5.10. Sensitivity of results to ankle trimline radius for 5 ° rotation

A graph of ankle moment calculated from these analyses versus trimline stage showed a smooth and almost linear variation (see Figure 5.8), indicating that the moment was roughly inversely proportional to the radius of the ankle trimline. This agreed with the published results of the experimental work, also shown on this graph. Although the focus of these analyses was on the predicted moment, equivalent stress contours revealed that stress concentrations were located at the ankle trimline on both medial and lateral edges as before, but significant stress concentrations were also evident at the region of imposed displacements at the foot and below the ankle joint (see Figure 5.9).

A slight medial/lateral bulging of the ankle trimlines was noted during dorsiflexion for analyses with a more anterior trimline. It is clear from Table 5.10 that there also exists an inverse relationship between the maximum equivalent stress and the ankle trimline radius. Graphs of moment versus angle of rotation of the foot region for each trimline stage indicated smooth convergence using 10 substeps. The graphs for plantar flexion motion revealed increasing stiffness with an increase in rotation. For dorsiflexion motion, the graph for the 20 % trimline stage showed

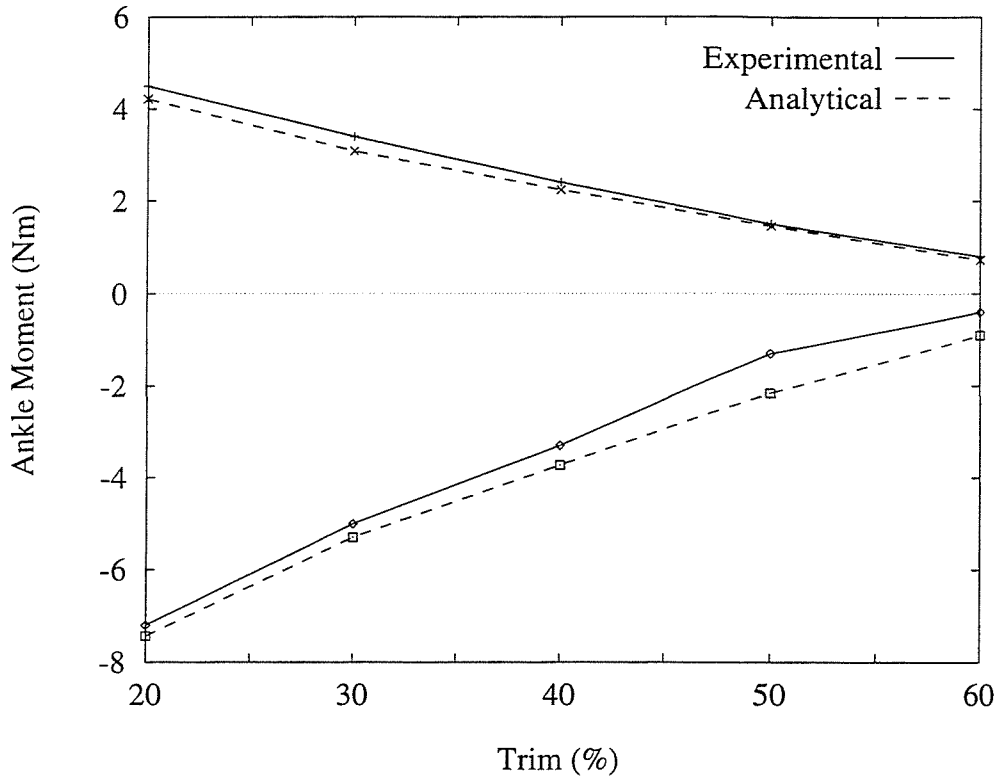

Figure 5.8. Comparison of analytical and experimental ankle moment versus trimline stage for 5 ° rotation

decreasing stiffness as expected, but as the ankle trimline radius became greater, the behaviour changed to increasing stiffness.

Until now, the additional moment generated by the reaction forces at the nodes below the ankle joint axis in the nodal x direction, F_x, had been disregarded, as these reactions had been assumed to act through this axis. To assess their effect on results, the previous analyses for the 40 % trimline stage were repeated. Although the moments were found to be only 1 % and -3 % different for 5 ° plantar flexion and dorsiflexion, respectively, at 2.5 ° rotation the difference was 7 % for both analyses. This change also affected the shape of the moment versus angle of rotation curves, correcting those for dorsiflexion. The reason for this minimal effect on results was the small moment arm of these reaction forces during small angles of rotation, which was equal to $R \sin \theta$, so the moment contribution near the heel was given by Equation (5.3) below.

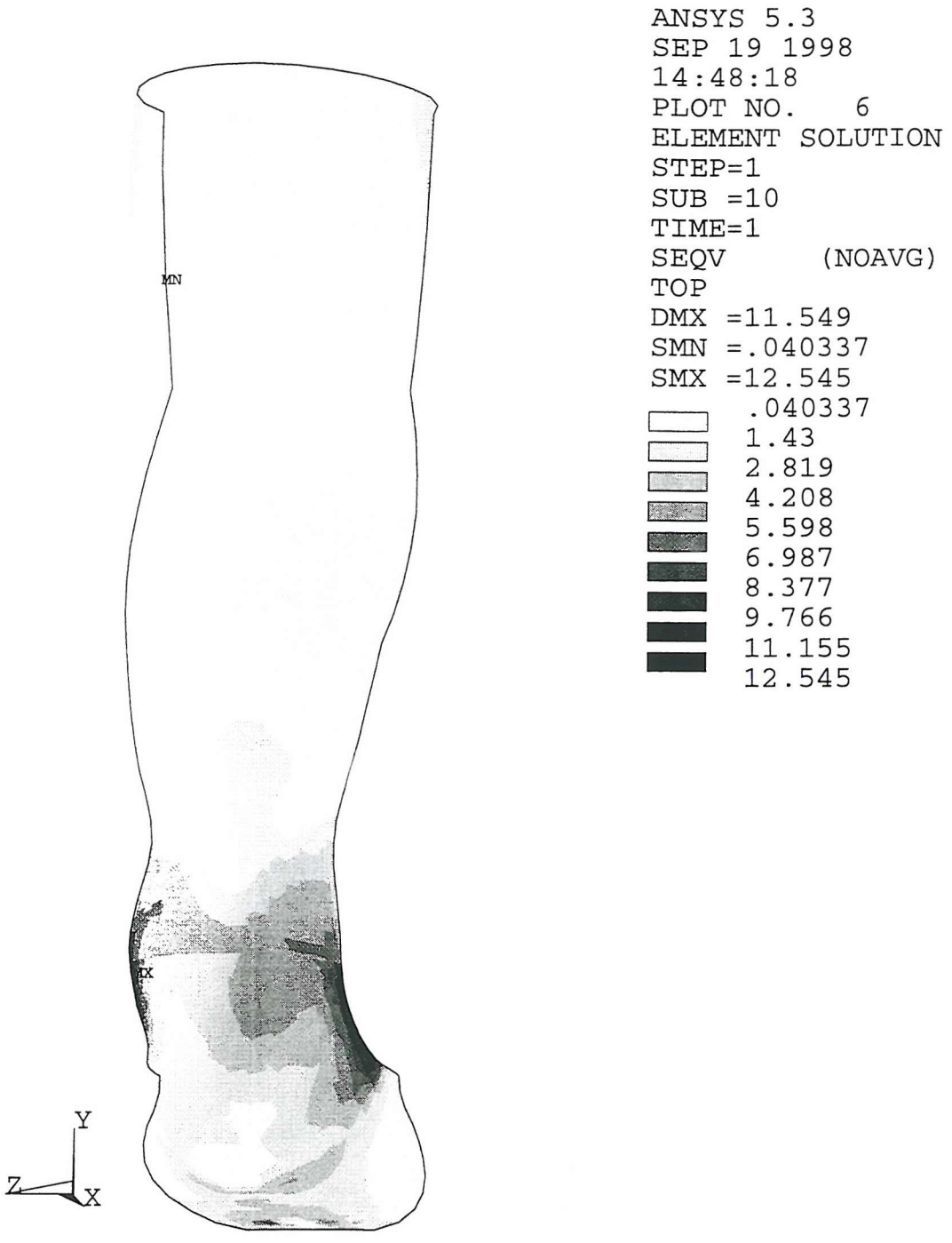

Figure 5.9. Equivalent stress at inner surface of 5 ° dorsiflexed AFO with 40 % trimline

Direction of Rotation	M (Nm)	M_e (Nm)	Discrepancy (%)	Max σ_{eqv} (MPa)	
				Inner	Outer
Plantar Flexion	−2.9	−3.2	−9	18.5	17.8
Dorsiflexion	1.7	1.5	+13	18.0	16.5

Table 5.11. Results for 15 ° rotation with 60 % trimline

$$M_{heel} = \sum_{nodes} F_y \times R' \cos\theta - \sum_{nodes} F_x \times R' \sin\theta \tag{5.3}$$

Under larger rotations, however, these forces may have a greater effect on the total moment acting about the ankle joint axis. In conclusion, the model has been shown to provide accurate results and to be sensitive to ankle trimline radius.

5.4.3 Large Ankle Rotations

On increasing the angle of rotation from 5 ° to 15 ° and the number of substeps from 10 to 30, convergence failures were encountered with the stiffer geometries due to divergence in the solution, although the 60 % trimline converged to accurate results for both directions of motion (see Table 5.11). It may be noted that these predicted moments did not include the contribution from reaction forces F_x near the heel, as described above, but acceptable results were still obtained. Convergence failure occurs when the limit on the number of iterations per substep is reached before convergence is achieved *and* the minimum substep size for automatic time stepping is reached. For example, this may be due to a physical instability in the structure which results in a zero stiffness. It may be noted that hardening structures can exhibit divergence when solved using a *modified* Newton-Raphson iteration method, where the stiffness matrix is updated less frequently, although the standard Newton-Raphson iteration method was used throughout this work.

During a non-linear analysis, the solution is considered satisfactory at each substep

when the specified or default *convergence criteria* have been satisfied. For multi-degree-of-freedom problems within ANSYS, by default the square root of the sum of the squares (SRSS) of the current load imbalances (applied loads minus Newton-Raphson restoring forces) for all degrees of freedom must be less than, or equal to, the product of the *convergence tolerance* (defaults to 0.1 %) and the SRSS of the applied loads at all DOF (or restoring forces for applied displacements). As moments can have significantly different orders of magnitude to forces, moment convergence is performed separately to force convergence for elements with rotational degrees of freedom. If no concentrated forces or moments have been applied at nodes, a default minimum reference value of 1.0 is used for the SRSS of the applied forces or moments, respectively. This value was found to be inappropriate in earlier analyses, where it delayed moment convergence, so the default moment convergence criterion was deactivated for all analyses from Section 5.4.1 onwards.

The graph of moment versus angle of rotation obtained from the converged dorsiflexion analysis showed unrealistic behaviour, as the curve exhibited a 'snap through' condition between two rotations when a limit point (moment) was reached such that the moment temporarily changed sign, although the final moment value obtained was acceptable. This conclusion was justified because the moment predicted at 5 ° rotation was of incorrect sign and magnitude compared to that correctly calculated in the previous section. The reason for this behaviour was thought to be the consequence of each nodal coordinate system having fixed orientation with respect to the global Cartesian coordinate system during these large deformation analyses. Although the convergence behaviour of conservative (path independent) systems can sometimes be improved by applying the load gradually to minimize the number of equilibrium iterations required, this snap through was not caused by an insufficient number of substeps because identical results were obtained using only 10 substeps. It may be noted that a snap through structure, although unstable when force-loaded, may be solved past the limit point when displacement-loaded, the method used for these analyses.

The first solution considered to overcome convergence failure was to apply the 15 ° rotation over a number of load steps, S, such that the nodal coordinate systems at the foot were incrementally rotated at the start of *each* step by θ/S, as opposed to a single rotation of magnitude θ at the first load step. This involved restarting the analysis for each load step after the first such that the displacement imposed at each node was ramped from its previous value, rather than from zero. Analyses were first performed for the 60 % trimline stage, each with a different number of load steps, although the total number of substeps remained constant. With 3 load steps, the moment versus rotation curve obtained for dorsiflexion was found to oscillate such that the correct moment was predicted at the peaks, which corresponded to the last substep of each load step. With 15 load steps, this oscillation in moment was minor and the curve was considered satisfactory. Upon further increasing the number of load steps to 30, a smooth curve was obtained. In all analyses, the moment corresponding to 15 ° rotation agreed with that listed in Table 5.11, as did the maximum equivalent stress results and also results obtained from analyses for plantar flexion.

The graphs obtained using 30 load steps indicated a significant reduction in stiffness with increasing rotation during dorsiflexion, whereas a slight increase in stiffness was noted during plantar flexion. For both analyses, the stress concentrations were located at the ankle trimlines on the lateral and medial edges at inner and outer surfaces, respectively. This technique was considered an improvement on the previous approach of using nodal coordinate systems having fixed orientation and resolved the problem with the incorrect moment history. However, a similar analysis using 30 load steps with the 40 % trimline stage failed to converge under dorsiflexion motion above a rotation of 10.3 ° . It may be noted that rotating the nodal coordinate systems during solution was discouraged in the ANSYS documentation, as it could cause problems when postprocessing if their orientation was inconsistent with that of the results being interpreted. Even when correctly orientated, distortions in the deformed geometry were still evident at the distal trimline. There was also some concern about ramping imposed displacements between values having different orientations, although this proved unfounded.

Convergence Tolerance (%)	Direction of Rotation	M (Nm)	Discrepancy (%)	Max σ_{eqv} (MPa)	
				Inner	Outer
0.1	Plantar Flexion	−2.9	−9	18.5	17.8
	Dorsiflexion	1.7	+13	18.0	16.4
1	Plantar Flexion	−2.9	−9	18.5	17.8
	Dorsiflexion	1.7	+13	18.0	16.4
10	Plantar Flexion	−2.9	−9	18.5	17.8
	Dorsiflexion	2.0	+33	18.0	16.3
50	Plantar Flexion	−2.9	−9	18.5	17.8
	Dorsiflexion	2.0	+33	18.0	16.3

Table 5.12. Sensitivity of results to convergence tolerance for 15 ° rotation with 60 % trimline

5.4.4 Influence of Convergence Tolerance

Although the accuracy of a solution is reduced by using a 'looser' convergence tolerance, this would require less iterations and therefore a shorter solution time. To assess the sensitivity of the results to the convergence tolerance used with the force convergence criterion, the previous analyses with 30 load steps and a 60 % trimline stage were repeated using relaxed tolerances of 1 %, 10 % and 50 %, respectively. The results, which are summarised in Table 5.12, appeared to show that the model was insensitive to changes in convergence tolerance except for the calculated moment under dorsiflexion, which increased significantly as the tolerance increased. However, graphs of moment versus rotation became irregular and less accurate as the tolerance increased to 10 % or above. The cumulative number of equilibrium iterations reduced from 115 for the 0.1 % tolerance to 62 for the 10 % tolerance, but there was an insignificant decrease in the number of iterations when altering the tolerance from 10 % to 50 %. In conclusion, a convergence tolerance of 1 %, which required 89 iterations, would seem to offer the best compromise between accuracy and solution time. It may be noted that, in analyses with fewer load steps, the value of convergence tolerance may be more critical.

An analysis for 15 ° dorsiflexion was then performed with the 40 % trimline model using the preferred convergence tolerance of 1 %, to see if this would overcome the convergence failure reported in the previous section, but the solution failed to converge above a rotation of 11.5 °. The moment predicted at 5 ° dorsiflexion was equal to the value listed in Table 5.10 for the same trimline stage. No experimental results were available for the moment at 10 ° rotation, so the analytical result was compared to the average of the measured experimental moments at 5 ° and 15 ° rotation, which assumes a linear relationship between moment and rotation. Good agreement was observed between the analytical and experimental moments, which were 3.6 Nm and 4.0 Nm respectively, resulting in a discrepancy of −10 %.

As a means of overcoming the problem of divergence, the direction of constraint at nodes in the calfband region was modified from the current radial constraint. For dorsiflexion, two patches of nodes located where the calf strap would be riveted to either side of the AFO were constrained in the global X direction, whereas for plantar flexion the patch was located at the posterior calfband region. Additionally, for both directions, two patches of nodes located at the calf strap rivets were constrained in the global Z direction. The analysis for the 40 % trimline stage again failed to converge for dorsiflexion, although the predicted moments had increased from the previous analysis indicating a more rigid AFO response to the rotation of the foot. The reaction forces generated in the global X direction at the calfband constraint varied from a positive force at the upper node to a negative force of similar magnitude at the lower node. This was considered unrealistic as a flexible calf strap cannot withstand compressive loads, due to being a membrane and lacking bending stiffness. Hence, the reaction forces would all have the same sign.

5.4.5 Simulating Contact with Link Elements

To realistically simulate the interaction between the AFO and the plaster foot of the rig, the preferred approach ensuring correct application of loading would be to

additionally model the plaster foot and use non-linear contact (gap) elements between the two bodies. These elements can transmit compressive but not tensile loads, allowing separation between the contacting bodies but not penetration, will permit slip after friction is overcome, and can calculate the contacting region(s), which may be unknown beforehand. This approach was not possible because the contacting body had not been modelled. One of the disadvantages of modelling contact problems using nodal constraints, that is, of the method adopted in previous sections, is that displacement is prohibited in both directions along a particular coordinate axis. For example, at the nodes in the posterior calf band region, motion in the negative global X direction would not be directly constrained as modelled. Also, the extent of contact can be difficult to determine and model without including the contacting body.

A feasible alternative to using contact elements but providing acceptable result is to model the contacting body using stiff, pin-jointed link elements connecting the nodes of the AFO to a point representing the interior of the contacting body [Fagan, 1992]. One advantage over nodal constraints, which are perfectly rigid, is that the stiffness of the links could be adjusted allowing the elasticity provided by the limb and shoe to be modelled to some extent. It may be noted that link elements will not buckle under compression because they cannot sustain bending moments due to their assumed displacement shapes. To try and solve the convergence difficulties described above, a number of link arrangements were developed, each with varying degrees of success, but the following elaborate approach was considered the most appropriate.

The radial constraint at each of the nodes below the ankle joint axis was replaced with a link element connecting it to an artificial node located at the intersection of this axis and the global Cartesian X-Y plane (point 'A' in Figure 5.10). This node was fixed by constraining its translational degrees of freedom. The global X direction constraint applied previously at each node in the calf band region was replaced with a link element parallel to the global X axis and connecting it to an artificial node constrained in all directions. With dorsiflexion motion these links

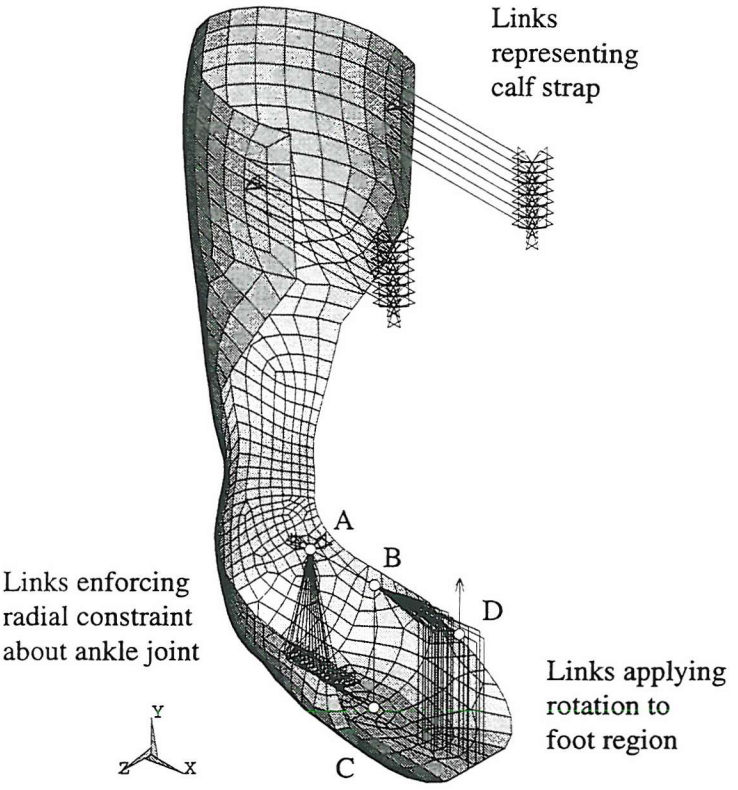

Figure 5.10. Beam and link elements simulating testing apparatus

represented the calf strap (shown in Figure 5.10), whereas under plantar flexion they represented the plaster calf (not shown).

The displacements were imposed at nodes in the foot region, simulating rotation about the ankle joint axis, through link elements. These links were defined parallel to the global Y axis and connected each node to a rigid structure consisting of a horizontal beam (AD) with additional horizontal beam elements radiating out from the node at its mid-span (point 'B'). This beam structure was constrained at one end to allow rotation about the ankle joint axis only. The displacements were imposed at nodes below the ankle axis also through horizontal link elements connecting them to the end (point 'C') of a vertical beam element rigidly connected to the mid-span of the horizontal beam. The global Z constraint remained. The load could then simply be applied to the node at the free end of the

horizontal beam (point 'D') and transferred to the AFO through the links, rather than directly to a patch of nodes on the AFO. The advantage with this approach over the analyses described in the previous section was that it gives the model freedom to comply to a less rigid, more natural deformation pattern.

An analysis was performed for the 40 % trimline model with a vertical force applied to the beam whose magnitude was calculated from the estimated moment required to achieve the desired dorsiflexion rotation about the ankle joint axis. A stiffness of 1000 N/mm was initially chosen for all link elements such that under a reaction force of 100 N, an approximation of the maximum value predicted in previous analyses, the extension of the link would be 0.1 mm. The solution failed to converge above 10.5 ° dorsiflexion, although some useful results were obtained. The moment calculated at 5 ° rotation of the distal trimline was slightly greater than the experimental value and that predicted at 10 ° was nearly identical to the estimated experimental value, so the non-linear behaviour was considered more accurate than that obtained by the previous analysis (see Table 5.13). On reducing the stiffness of all link elements to 10 N/mm, the solution failed above 11.9 ° dorsiflexion. The moments calculated at 5 ° and 10 ° were found to decrease from the values obtained with a stiffness of 1000 N/mm. The reaction force distribution at the links in the calfband region varied from positive to negative, which was again considered unrealistic, although the tensile forces dominated. It may be noted that the maximum elongation of the link elements was −0.8 mm and occurred below the ankle axis.

In a further attempt to improve convergence, the stiffness of all the link elements were reduced to 1 N/mm so that a more realistic distribution of reaction forces at the calfband could be obtained. The loading was changed from a force to a displacement imposed at the node at the free end of the beam to provide better control in the likelihood of buckling behaviour. The medial/lateral constraint at the heel was also reduced to only a single node to eliminate the oscillating direction of reaction forces previously noted in this area, while an additional constraint was applied to a single node at the middle of the distal foot trimline in

Link Stiffness (N/mm)	θ_f ($^\circ$)	M (Nm)	Discrepancy (%)
1000	5	2.6	8
	10	4.1	3
10	5	2	−17
	10	3.3	−18

Table 5.13. Sensitivity of results to link stiffness for 40 % trimline under dorsiflexion moment

this direction. The predictor was not utilised, as the effect of non-linearity was becoming significant and so this feature would not aid convergence rates. The maximum number of substeps was also increased from 100 to 200.

Convergence of a non-linear solution can also be based on displacements, in which case the SRSS of the displacement increments is compared to the SRSS of the current displacements. As force and moment-based convergence criteria both provide an absolute measure of convergence, whereas displacement and rotation-based convergence only provide a relative measure, the latter should not generally be used in isolation. Since these analyses included only imposed displacements, force convergence could only be based on the restoring forces, which are also relative. It was thus considered acceptable to use displacement convergence criteria in isolation for the following analyses, with a tolerance of 0.1 %.

An analysis was performed on the 40 % trimline model with a rotation of 15 $^\circ$ dorsiflexion applied to the beam using the approach described on page 171. The solution was found to converge to a moment of 3.3 Nm, considerably less than the experimental result of 5.5 Nm. The moments predicted under 5 $^\circ$ and 10 $^\circ$ rotation were found to be significantly less than the respective values from previous analyses, with discrepancies of −38 % and −35 % respectively. The calculated angle of rotation was found to vary from 14.6 $^\circ$ at the foot region to 15.7 $^\circ$ towards the heel, indicating that some bending occurred along the length of the foot region due to the compliance of the links. Indeed, the extension varied from −4.6 mm in

the radial links below the ankle axis to 1.9 mm at the foot links. It may be noted that during an earlier analysis with all links having a stiffness of 100 N/mm, the rotation was uniform over the whole foot region. The forces in the link elements at the calfband region were mostly tensile, an improvement on previous analyses. A further analysis with the stiffness of the links at the foot and below the ankle increased to 10 N/mm revealed that the solution was sensitive to the link stiffness, as it failed to converge. Although this indicated that convergence could ultimately be achieved by simply reducing this parameter, the accuracy of the results would be reduced due to the increasing elongation of the link elements.

A further refinement involved widening the region of imposed displacement to nodes below the ankle axis, which required the beam structure to be slightly altered. To better distribute the loading at the foot, the number of links in this region was also increased posteriorly. Analyses were performed for 16 ° dorsiflexion and plantar flexion, the angle being over-specified to ensure the desired rotation of the foot was achieved with the compliant links, and both converged. The moments calculated at 5 ° and approximately 15 ° are shown in Table 5.14 and indicate significant underestimate of the stiffness of the AFO. This was due to the link elements providing a less rigid rotation than enforced by the experimental rig. The moment versus rotation history for plantar flexion showed a slightly non-linear relationship with increasing stiffness, whereas that for dorsiflexion showed a stronger non-linearity with decreasing stiffness and the onset of buckling (see Figure 5.11). Plots of equivalent stress showed similar trends to corresponding results from previous analyses, with the maximum occurring at a stress concentration zone at the ankle trimline on the lateral edge. The maximum extension in the link elements was considerable, being 5.6 mm in the radial links below the ankle axis during plantar flexion and −2.7 mm in the same location during dorsiflexion.

It was concluded that the large deformation formulation of the ANSYS shell element selected was not sufficiently robust to deal with very large deformations, and a model incorporating both interacting bodies and also contact elements may

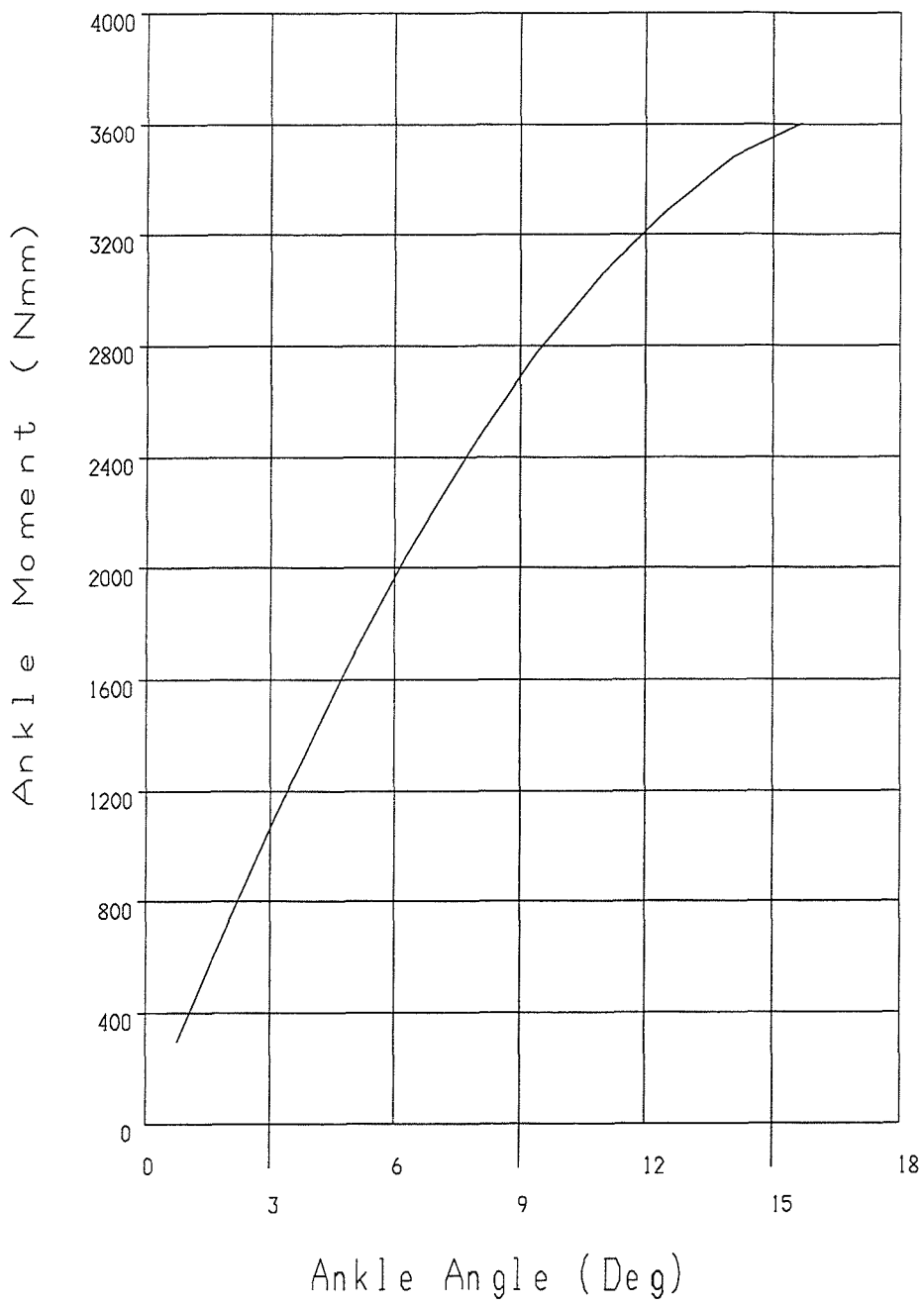

Figure 5.11. Ankle moment versus angle of rotation obtained for 40 % trimline using link elements

Direction of Rotation	θ_f (°)	M (Nm)	M_e (Nm)	Discrepancy (%)	Max σ_{eqv} (MPa)	
					Inner	Outer
Plantar Flexion	−5	−2.2	−3.3	−33	N/A	N/A
	−15.0	−7.3	−13.3	−45	17.9	15.3
Dorsiflexion	5	1.7	2.4	−29	N/A	N/A
	15.7	3.6	5.5	−35	18.8	16.7

Table 5.14. Results for 16 ° rotation with 40 % trimline obtained using link elements

not have such convergence difficulties. The results were shown to be sensitive to link stiffness, with a reduction in accuracy for a corresponding decrease in link stiffness, and convergence failures occurred if this stiffness was too high. Although a solution was obtained with the 40 % trimline for both directions of rotation, the plantar flexion analysis required 377 iterations and 29 substeps compared to only 80 iterations and 11 substeps for dorsiflexion. It was therefore expected that an analysis for plantar flexion with the more rigid 20 % trimline would not successfully converge.

5.5 Further Model Validation

5.5.1 Experiments

Experiments were performed on the custom-made AFO obtained from St. Mary's Hospital (see Section 5.2), which was manufactured from the same grade of polypropylene tested in Section 3.7.2. The main objective for the exercise was to experimentally validate the method of loading and constraint used in the modelling routine. This was considered more useful than performing an exact foot/shoe/AFO simulation, which could only be approximately modelled. Previous experimental rigs appeared to simplify the loading conditions an actual AFO would be subjected to during gait, due to the difficulties involved in their

simulation. For example, the apparatus used by Condie & Meadows [1977] and Chowaniec *et al.* [1979] appeared to provide no constraint at the heel region, while those used by Golay *et al.* [1989] and Lunsford *et al.* [1994] provided some heel constraint. Sumiya *et al.* [1996a] provided rigid radial constraint below the ankle axis which was simpler to simulate analytically than modelling a strap. When comparing the various modes of constraint provided at the calfband region, Condie & Meadows [1977] rigidly constrained this region, Golay *et al.* [1989] and Lunsford *et al.* [1994] provided some resistance to internal/external rotation and vertical translation, while Chowaniec *et al.* [1979] and Sumiya *et al.* [1996a] provided no resistance to these movements to simulate slip between the AFO and calf. All rigs restricted slippage between the AFO, foot and shoe.

The present rig design consisted of a vertical, stainless steel tube of circular cross-section (25 mm Ø) representing the leg's axis and which was grounded at its upper end (see Figure 5.12). A plaster calf region with an acrylic inner bush was free to slide vertically along this tube. This provided radial constraint at the calf band region of the AFO with respect to the centre-line of the vertical tube, positioned during assembly at the approximate centre of the calfband region, while allowing internal/external rotation about this axis and translation upwards and downwards. Although the Velcro calf strap could have been used to secure the AFO to the plaster calf, an attachment using screws was adopted to provide a more rigid constraint for easier simulation. At the lower end of the leg axis there was a hinged, single axis mechanism representing the ankle joint, whose axis was assumed normal to the leg and positioned at the estimated ankle joint location of the AFO during assembly. This mechanism comprised three members, the leg axis, moment arm and heel support (described below), each of which could rotate about the hinge pin (stainless steel, 15 mm Ø) independently or be locked to it by pins.

The heel region of the AFO was clamped at a constant radial distance from the ankle joint by means of the *heel support*, which pivoted about the ankle joint axis. This comprised plaster clamps moulded to fit the inner and outer surfaces of the AFO and fitted on a threaded shaft, which passed through a small hole in the

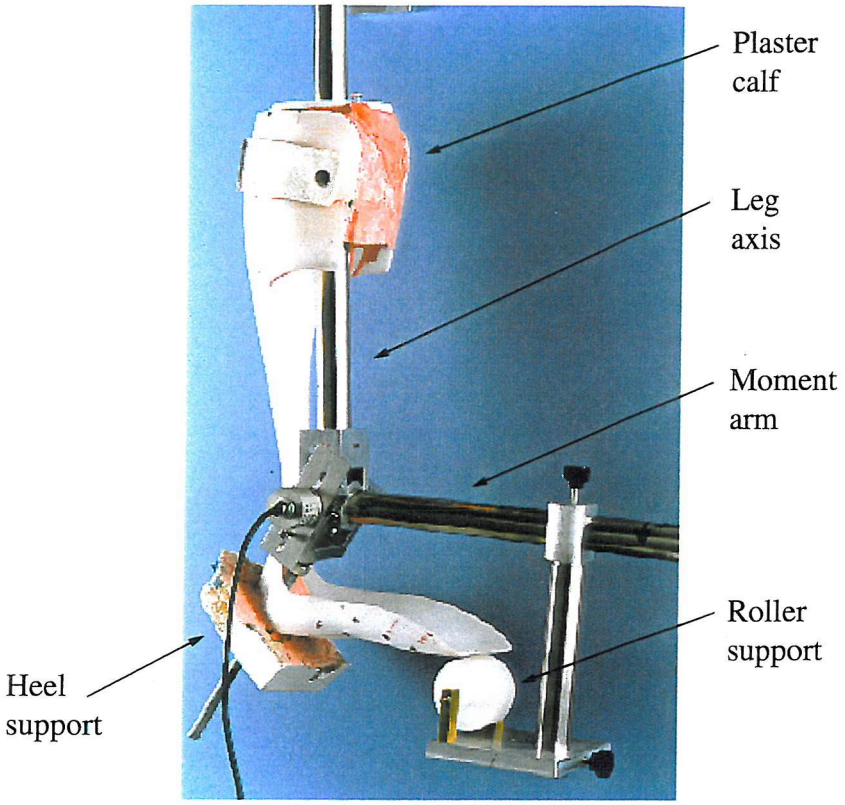

Figure 5.12. Experimental rig with AFO assembled indicating components

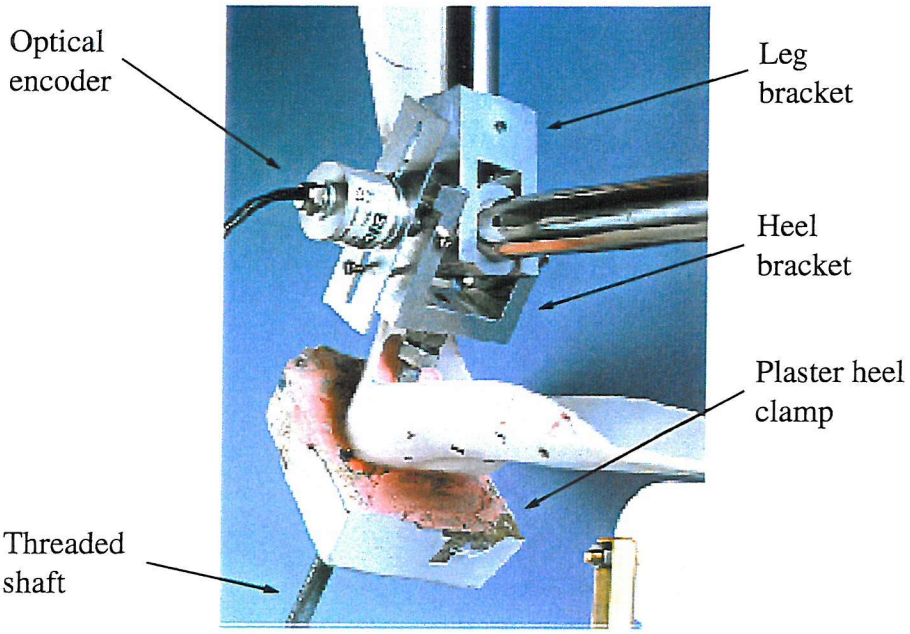

Figure 5.13. Detail of experimental rig ankle joint mechanism and heel support

AFO's heel and was fixed to an aluminium heel bracket (see Figure 5.13). The hole through the heel was not thought to have weakened the AFO as it was very rigid in that region. This clamping assembly therefore provided both medial/lateral and radial constraint at the heel. An alternative to clamping the AFO in this region that was considered was a strapping arrangement, but this would elongate during testing and pure rotation of the AFO about the ankle axis would not occur. This strap may also interfere with buckling of the ankle trimlines.

The foot region was loaded towards the distal trimline region using a *moment arm* (stainless steel tube) pivoted about the ankle joint axis and loaded at its free end. Positioned along and below this moment arm was an adjustable aluminium platform, and mounted on this platform was a cylindrical, acrylic roller whose axis was parallel to the ankle joint axis. This roller contacted a small patch on either the inner or outer surface of the AFO foot region to force it into plantar flexion and dorsiflexion, respectively. Therefore, as the moment arm was rotated about the ankle joint, the roller transferred the rotation to this region while allowing the AFO to deform longitudinally to simulate slip between the AFO and foot. As some of the loading on an AFO is applied at the heel region, it was also considered necessary to couple the heel support to rotate with the roller support about the ankle joint axis. This forced rotation at the heel was achieved by locking (pinning) both the heel bracket to the hinge pin, and the hinge pin to the moment arm. It may be noted that, as the leg axis was grounded for these experiments, it was not coupled to the hinge pin but remained free.

The moment was applied to the AFO by linearly ramping the mass at the free end of the moment arm using a reservoir of water. Alternatives considered were firstly to attach a force transducer to the moment arm, but as the loading must be maintained parallel to its axis, a more complicated linkage would be required. Another alternative involved measuring the load directly where it was applied at the foot using a force transducer or pressure transducer mounted in place of the roller support on the same platform, but this approach would only record the proportion of loading applied at the foot and ignore the proportion applied at the

Test	Plantar Flexion		Dorsiflexion	
	θ_f ($^\circ$)	M (Nm)	θ_f ($^\circ$)	M (Nm)
1	−22	−9.6	24	6.6
2	−24	−10.0	28	6.9
3	−24	−9.8	30	6.8

Table 5.15. Moment and rotation data obtained from validation experiments

heel. Also, if the gauge was mounted on a sliding platform to allow slip, this would have to be measured with a linear position sensor to allow the moment to be accurately calculated. An optical encoder (0.5 $^\circ$ resolution) was used to measure the ankle joint rotation during testing, which was recorded at intervals using a PC data acquisition system. To achieve this, the body of the encoder was anchored to the aluminium leg bracket at the lower end of the leg axis and the shaft of the encoder was mounted colinear to the hinge pin.

Time constraints only allowed three tests to be performed for both dorsiflexion and plantar flexion. Sufficient time was allowed for recovery between tests. Before testing, the custom-made AFO was modified from its original, rigid trimline to a more flexible trimline to allow a large rotation to be easily achieved. This trimline was set to be symmetric when viewed in the sagittal plane and was constructed through the data points used for digitising the geometry, as explained in the next section, allowing easy replication during modelling. As shown in Table 5.15, the results indicated that the AFO had a greater stiffness to plantar flexion motion than dorsiflexion, as previously reported, and good repeatability in the moment versus angle of rotation data was obtained.

The moment was calculated from the summation of the moments generated by the mass of the water and the weight of the test rig's moment arm. The latter component required the position of the moment arm's centre of gravity to be calculated, and its contribution to the total moment was significant, accounting for approximately 50 % in the case of dorsiflexion. A graph of moment versus rotation for the second plantar flexion experiment showed that, except for the first segment

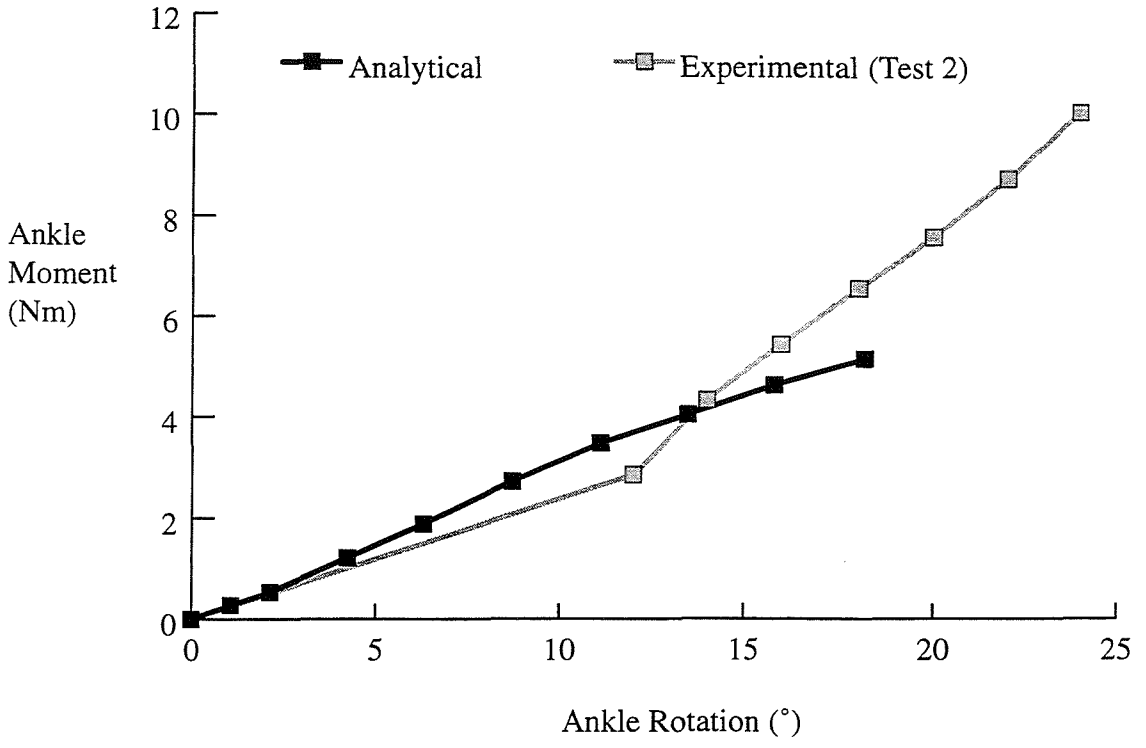

Figure 5.14. Comparison of analytical and experimental ankle moment versus rotation for plantar flexion

where the mass of the moment arm was applied, an approximately linear relationship was obtained (see Figure 5.14). It was noted that deformation of the distal trimline in the medial/lateral direction was constrained by the roller support due to friction.

5.5.2 Analysis

To enable an accurate geometric model of the custom-made AFO to be developed, its outer surface was digitised prior to final trimming using a computer-controlled, three axis coordinate measurement machine at the Advanced Manufacturing Technology Laboratory, Southampton Institute. A number of features were firstly digitised to locate the global Cartesian coordinate system origin at the intersection of the midsagittal plane of the leg and a line connecting the medial and lateral malleoli, as with previous models. The Y axis was aligned perpendicular to the

sagittal plane, although the orientation of the X and Z axes was not explicitly defined. A total of 98 data points positioned around the circumference of 15 imaginary cross-sections through the AFO were then digitised with respect to this global coordinate system. The coordinate measurement machine provided automatic output of the coordinate data to a text data file, which would be less time consuming than the manual entry used with the previous models and reduce the possibility of numerical errors in the data. Software was then written in the C programming language [Kernighan & Ritchie, 1988] to convert the format of this data into that suitable for input into ANSYS (see Section 3.3.1)

Unlike the previous models, these cross-sections deviated from being planar to allow the curvature to be more accurately captured. For this same reason, the number of data points around each cross-section varied from 5 at the proximal trimline to 9 at the heel/ankle region and then back to 3 at the distal trimline. These data points were also not equally spaced around the circumference of each cross-section, but were more concentrated where the curvature changed abruptly. It may be noted that the limited adaptability of the current modelling routine, which was due to the limitations with the preprocessor, prevented its use with this more complicated data set. However, improvements with ANSYS Revision 5.3 allowed a more sophisticated modelling routine to be developed (see Section C.1).

The solid model of the untrimmed AFO was again constructed by inputting coordinate data, defining keypoints, fitting splines through these points and finally skinning an area through these lines (see Figure 1.1 on page 19). This model was then trimmed within ANSYS to match the flexible AFO tested by dividing it at its intersection with a number of areas, which were defined perpendicular to the sagittal plane and passed through a number of the digitised data points on its surface. To facilitate mesh refinement and the application of boundary conditions, the area remaining after the trimming operation was subdivided into areas of simpler shape. It may be noted that the global Cartesian coordinate system was rotated about its Y axis prior to this subdivision process such that its X axis passed through the midpoint of the proximal trimline.

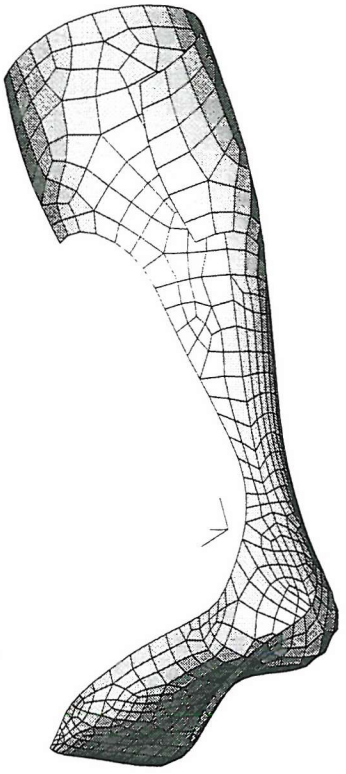

Figure 5.15. Element mesh for trimmed experimental AFO

The mesh density was specified using the 'SmartSizing' element sizing feature introduced in the later ANSYS Revision 5.3. This algorithm calculates initial element sizes on all lines of the areas being meshed, then automatically refines these edge lengths for curvature and small geometric features. The advantage with this approach is that, as the element sizes are calculated before meshing begins, the mesh generated is thus independent of the order in which the areas are meshed. The resulting mesh consisted of 1869 nodes and 584 elements (see Figure 5.15), a similar density to the initial model developed in Section 3.5.2. The variation in thickness over the AFO's surface was from 2.9 mm to 4.1 mm and was modelled as in Section 5.2.

An analysis involving both geometric and material non-linearities was performed for 24 ° plantar flexion to allow comparisons to be made between the experimental

and analytical moments and hence validate the model. Due to the difficulty in mounting the AFO onto the experimental test rig, it was not possible to align the axis of rotation of the hinged mechanism exactly where the ankle joint axis was positioned. For the same reason, the centre line of the leg axis could not be aligned to pass through the exact midpoint of the proximal trimline. These offsets were therefore measured and used within the model to define a local Cartesian coordinate system representing the axis of rotation of the experimental rig's hinge mechanism.

Displacements were imposed over a patch of nodes on the distal foot region to simulate contact with the roller using the same technique introduced on page 171. Although the contact region between the roller and AFO would have been a line during the experiments, a patch of nodes having a width equal to that of the roller was selected for the analysis to reduce stress concentrations and account for the slight change in contact during rotation due to slip. Radial and medial/lateral constraint was provided over a patch of nodes at the heel of similar dimensions to the region clamped in the experimental test rig. All nodes in the calfband region were constrained in a radial direction relative to the leg axis of the test rig but allowed to translate vertically and rotate about this axis to simulate the attachment to the sliding plaster calf.

For this initial analysis, the strategy adopted was a force convergence tolerance of 0.1 % and a maximum number of substeps of 100. The solution failed to converge after 18.2 ° and, although resources prohibited a detailed investigation and further analyses, postprocessing was performed on the available results up to the maximum angle of rotation achieved by this numerical simulation. Lateral and anterior views of the deformation for the last converged substep appeared to be realistic. The moments at each substep were calculated as before, including the contribution from the radial reaction forces at the heel, and the magnitude for the final converged substep was −5.1 Nm. A graph of the predicted moment versus rotation showed slight non-linear behaviour (see Figure 5.14). For comparison with this analytical result, an experimental moment of −6.6 Nm was obtained under

18.2 ° plantar flexion, so the discrepancy was −23 %. Although this was significant, it was concluded that further analysis using incremental rotation of the nodal coordinate systems, as described in Section 5.4.3, may provide more reliable results. Also, based on analyses in previous sections, an analysis of dorsiflexion rotation might converge successfully.

Chapter 6

Conclusions

6.1 Discussion

This work has succeeded in satisfying all of the objectives outlined in Chapter 1 and provided a foundation upon which further investigations into the stiffness characteristics of plastic AFOs can be based. Computational simulation using the finite element method is regarded as a more versatile and economical alternative to experimentation, but its reliability must be carefully examined as unrealistic loading or constraints, a coarse mesh or ignored physical phenomena such as creep and buckling can lead to inaccurate results. It should be noted that, although the use of commercial software packages such as ANSYS appears straightforward, many problems may arise in practice that can only be overcome through accumulated experience.

6.1.1 Customising AFO Geometry

The currently popular manufacturing method adequately captures the geometry of the patient's leg in the final AFO. This can be measured using a digitiser so that a

detailed geometric model could be generated for analysis purposes. A versatile modelling routine was developed in Chapter 3 whereby a 3D solid model of a custom-made or prefabricated AFO could be generated prior to manufacture. This process used the CAD techniques available within a general-purpose FEA package and resulted in a realistic geometric representation of an asymmetric AFO with the additional advantage of allowing subsequent trimline variation.

Rather than digitising and modelling a trimmed AFO directly, a process for trimming an AFO within the software was demonstrated. This involved sculpturing the digitised surface of an untrimmed AFO using Boolean subtraction operations. The disadvantage with the former approach was that the AFO would have to be partially re-digitised if the trimline was modified and, if the trimline was required to move anteriorly, a new AFO would have to be manufactured and digitised. If the AFO's surface is to be generated by skinning a surface through a series of cross-section splined lines that interpolated the digitised points, the trimline would also be limited to a smooth curve if no further trimming was performed within the software.

Although it was found possible to generate within ANSYS some form of AFO asymmetry from a symmetric trimline, this and any resulting medial/lateral deformation of the distal trimline can be directly attributed to the asymmetry in leg geometry. Alternative schemes or software packages may offer greater versatility in defining a more realistic trimline. A more natural plane for dimensioning the calf trimlines would be the frontal plane, as the width of the posterior calf region is critical and this dimension is difficult to define exactly from the sagittal plane. For example, an alternative preprocessor, tried towards the end of this programme, allowed a trimline to be generated from digitised points on the surface of a positive cast. It was possible to firstly project these digitised points onto the surface representation of the leg, generate lines through these points such that they also lay on the surface and finally cut this surface to obtain the AFO.

The feasibility of using shell elements to accurately model an AFO, which may be classified as a thin shell-type solid, was shown. These elements are more efficient

than solid elements, reducing solution time, and allow abstraction of the geometry from a volume to an area, simplifying the modelling process. Also, quadratic elements having mid-sided nodes proved to be more efficient than linear elements for this work by allowing a coarser mesh. Although mapped meshing does offer advantages over meshes consisting of mixed element shapes because it avoids the less accurate triangular shaped elements, it was found to be too restrictive in this work when combined with local mesh refinement. However, with recent improvements in meshing algorithms, this approach may prove to be a more efficient alternative.

Finally, using automatic mesh generation, rather than direct generation of nodes and elements from digitised points on an AFO's surface, made possible an iterative process of rational mesh refinement through re-analysis. The process was based on energy errors to investigate the sensitivity of the model to discretisation error. Although the initial, uniform mesh was found adequate for assessing the deformed shape of the AFO, it was shown that a finer mesh was required at locations having high stress gradients to accurately calculate the maximum stresses at these critical regions. These regions of high stress gradient were found near discontinuities in geometry at the ankle trimline. To avoid unnecessarily refining the mesh at artificial stress concentrations arising from concentrated loading or constraint, these analyses were performed using a distributed loading. Although grading the density of the mesh was found to produce a more efficient model, mesh density may become less important as computers become more powerful and solution times reduced unless offset by more demanding analyses.

6.1.2 Prediction of AFO Stiffness

An analytical procedure has been documented in Chapter 4 for evaluating AFO designs under static loading. The analysis was focused at that stage on identifying those aspects of modelling which may influence the accuracy of the results obtained and therefore require careful definition. For simplicity, the decision was

made to model an isolated AFO. Thus, the parametric studies were concerned with the modelling of support and applied loading, although mesh density, geometry and material were later included. This was deemed necessary because of the difficulty in accurately representing the interaction between the AFO, lower limb and shoe without resorting to modelling contact as well as the latter two bodies. Although the range of parameters used was not exhaustive, these analyses gave a clear indication of variable model behaviour under modified conditions.

Linear static analyses were first performed to obtain an initial assessment of the stiffness characteristics of the device under moderate loading and to develop a versatile solution strategy. Due to the lack of data on the pressure distribution over the foot region of an AFO, the most rational alternative attempted in this work was to examine an AFO's response to a known rotation of the foot region about its ankle joint axis. A three point system of loading, consisting of displacements imposed at the distal foot region and constraints distributed at the posterior calf enclosure and heel of the AFO, was used. This approach allowed simulation of dorsiflexion and plantar flexion of the AFO. It was found that the way the loading and constraint are applied at the foot and heel, respectively, can affect the predicted stiffness of an AFO.

Analyses were performed using different deformation strategies, each with varying degrees of imposed rigidity at the foot, with the aim of inducing 5 $^{\circ}$ plantar flexion rotation of the AFO. By imposing displacement at a single node located at the centre of the distal trimline, roughly where the 2nd and 3rd toes locate, rotation of the foot region about the ankle joint axis was not uniform. Instead, the predicted rotation at the heel was less than that applied at the distal trimline. A high stress concentration at this node was also caused by the inadequate distribution of reaction forces, which was considered artificial because the contact forces between the AFO and the foot or shoe would be applied over a finite region and hence the stress variation over this region would be smooth.

Distributing the imposed displacements over a line of nodes extending posteriorly towards the heel reduced this unrealistic stress concentration at the distal trimline,

but caused higher maximum equivalent stresses to develop at the medial ankle trimline and a greater moment. This was due to a more rigid rotation of the foot and heel about ankle joint axis, that is, the rotation at the heel was similar to that applied at the foot. A concentrated loading, in this case an imposed displacement at a single node, was thus shown to produce both local and global inaccuracies in results and should thus be avoided. Further distributing the imposed displacements over an area had less significant effects. These analyses therefore gave an insight into the effect of shoe rigidity, as compliant shoes might allow some local deformation in the foot region, whereas firm shoes would transfer the rotation from the heel to the foot and vice versa. In retrospect, it was considered more realistic to additionally apply rotation at the heel.

The calf region was predicted to translate in a proximal direction during plantar flexion rotation and in the opposite direction during dorsiflexion, which would occur during use due to the high compliance of the leg tissue. The foot region of the AFO was found to have displaced medially when subjected to plantar flexion through displacement imposed at a point, over a line or a patch, and was accompanied by an internal rotation of the calf region about the leg. This coupled motion was eliminated when the analysis was applied to a model symmetric relative to the midsagittal plane; it could thus be attributed to the asymmetry of the original model. Coupled motion was also eliminated in an analysis of the asymmetric model with displacements imposed at all nodes in the distal half of the foot region. This mode of kinematic loading minimised the distortion of the foot region and twisting about its longitudinal axis.

These findings therefore suggest that it is important to ensure the finite element model captures the asymmetry of the AFO and the rigidity imposed by the shoe if correct results are to be obtained. The medial/lateral displacements predicted from these analyses gave a visual indication of the type of correction the AFO could provide to a varus or valgus deformity, although no data on the AFO's internal/external restoring moment was predicted from these analyses due to the lack of medial/lateral constraint and therefore reaction forces at the foot. An

alternative approach would be to apply medial/lateral constraint to a set of nodes at the foot region, which would then allow the moment to be calculated. If data of the forces required to correct a patient's deformity were available, design optimisation could arrive at a suitable AFO providing analysis was obtained under the same conditions.

Applying a uniform pressure over the distal half of the foot region was found to be a possible alternative to the imposed area displacement, although it did not provide as rigid a rotation of the AFO. The medial/lateral displacement of the distal trimline was also found to be greater due to the pressure acting on the sides of the foot region and causing a net force in that direction. Sensitivity to imposed rigidity at the heel was investigated by reducing the constraint in this region. This was found to cause a significant reduction in the magnitude of the maximum equivalent stresses and moment; completely eliminating this heel constraint was found to have an even greater effect. The reason was that deformation was not concentrated around the ankle trimline, so the stresses were more widely distributed. This could explain the effect that reduced tension in the shoe laces would have on AFO behaviour. The influence of the loading and constraints on results highlights the importance of understanding such parameters, particularly their in-vivo measurement under dynamic conditions. It further emphasises the importance of reporting the exact nature of a model and its parameters so that results of different simulations may be compared.

Static analyses were performed with both geometric and material non-linearities. The latter were based on uniaxial stress-strain data for copolymer polypropylene. These two types of non-linearity were initially considered independently to assess their individual contribution to the AFO behaviour, but the results obtained were echoed in the combined non-linear analyses. These showed that a linear analysis would fail to predict the difference in AFO behaviour during dorsiflexion and plantar flexion by ignoring the geometric non-linearity, which becomes important during large rotations of the foot. Linear elasticity was found to overestimate the magnitude of the maximum equivalent stresses due to ignoring the material

non-linearity, which results in a reduced stiffness at high stress regions due to the strain-dependent behaviour of the material. Time-dependent material properties were also considered due to the sensitivity of the material to strain rate. A creep model was developed based on reported empirical results, but was found to significantly underestimate the creep strain rate over the initial period of creep.

From linear sensitivity analyses in Chapter 5, the deformations and maximum equivalent stresses of an AFO were found to be virtually insensitive to variations in Poisson's ratio, although deformation was inversely proportional to Young's modulus. This indicated that, when defining the properties for a particular type of material, an exact value of Poisson's ratio may not be necessary but the accuracy of Young's modulus is critical. By incorporating alternative materials having different elastic properties into the finite element model, it would be possible to easily assess any improvements in AFO behaviour without having to manufacture it. In view of the limited range of suitable materials, a more flexible approach to adjusting characteristics would be to vary the trimline or material thickness, as discussed below.

The variation in material thickness over the surface of a custom-made AFO was measured and found to have reduced to a minimum of 54 % of its maximum value. This deviation is due to manual draw of the material during vacuum forming, which is required because of the non-developable and asymmetric geometry of the positive cast. Linear and non-linear analyses performed on a model incorporating the same thickness variation over the surface predicted slight increases in rotation and equivalent stresses compared to those obtained from analyses with a constant thickness. These changes in stiffness were minor due to the fact that the large reductions in thickness occurred where the stresses were small. This is not an adverse factor as a lighter design can be obtained whilst maintaining the required stiffness. Further reductions in thickness at the highly stressed ankle trimlines was found to cause a considerable reduction in the stiffness, increasing the deformations and equivalent stresses by about a factor of two.

These results are of practical importance as the characteristics of an AFO could be

modified by altering its thickness. For example, by reducing the material thickness at low stress regions, an AFO with a significant weight reduction and uniform stress distribution could be developed. However, the vacuum forming process currently used for the manufacture of custom-made AFOs would not provide either the required accuracy in thickness or repeatability, due to the manual application of force when stretching the material. A more objective approach would be to use a milling machine to reduce the thickness after vacuum forming, although this may not be practical for high production rates. Therefore, the easiest method for changing the stiffness of an AFO would be during the trimming stage of manufacture.

A variable thickness model approximating a prefabricated AFO was found during non-linear analysis to exhibit different behaviour depending on the existence of constraint at the heel. With the heel constrained the resistance to dorsiflexion rotation was greater than that to plantar flexion due to restriction of bulging at the malleoli region, but with the heel constraint removed the resistance to plantar flexion was greater. The moment versus rotation history, which was considered as the most suitable method for presenting AFO characteristics, also exhibited a slight non-linearity for dorsiflexion indicating the onset of buckling. Therefore, as was found with the earlier linear analyses, the region of constraint at the heel has a significant influence on AFO behaviour. Also, the medial/lateral displacement of the distal trimline predicted with the heel constraint was in a lateral direction for both plantar flexion and dorsiflexion, but in opposite directions without the heel constraint. This indicates there is no relationship between the direction of rotation about the ankle joint axis and the direction of medial/lateral displacement.

6.1.3 Model Validation

The analyses simulating the experiments performed by Sumiya *et al.* [1996b] initially provided the opportunity to assess the sensitivity of the AFO model to parameters not previously investigated, as well as proving reliability of the model.

For example, flattening the curvature of the foot region was found to have no effect on the predicted moment for either 5 ° plantar flexion or dorsiflexion due to the high stiffness of this region, although adjusting the width of the elliptical cross-sections before trimming was found to have a significant effect on the AFO's stiffness. This highlighted that adjustments to the positive cast before vacuum forming to incorporate additional support or relieve pressure at sensitive areas, which may incur the expense of manufacturing several AFOs until a satisfactory stiffness is achieved, can instead be verified analytically prior to manufacture. It may be noted that as the surface geometry of an AFO must match that of the patient's limb, there would be more scope for adjusting its stiffness by altering the material thickness or location of the trimlines, rather than through minor cast modifications.

With rotation additionally imposed at the nodes near the heel to better simulate the AFO bolted to the plaster foot in this region, a more rigid rotation of the foot region about the ankle joint axis occurred resulting in a slightly greater moment. This observation is of importance when simulating an AFO during gait because it is not obvious whether the foot would be forced to rotate about the ankle joint axis as a rigid body. An improved method of aligning the nodal coordinate system of each displaced node at the foot region allowed more accurate control over rotation of the distal trimline about the ankle axis. This approach also brought the analytical moments considerably close to experimental measurements for both directions of rotation, showing that an apparently minor approximation in defining the direction and magnitude of imposed displacements can have a major affect on results.

This model was subsequently utilised to assess the sensitivity to ankle trimline radius, which has previously been reported as being the most important factor affecting AFO rigidity. The model was found to predict accurate results for all trimlines analysed, with a greater stiffness in plantar flexion than dorsiflexion rotation. The moment was also found to be roughly inversely proportional to the radius of the ankle trimline, which agreed with published experimental results.

Under larger rotations of 15 °, convergence failures were encountered for the stiffer trimlines and an unrealistic moment versus rotation history was obtained for the converged trimline under dorsiflexion. The reason for the latter inaccuracy was shown to be a consequence of the nodal coordinate systems of those nodes at the foot with imposed displacement having fixed orientation during the analysis. By incrementally rotating these nodal coordinate systems during the analysis to remain in a radial direction an accurate curve could be obtained, although this did not overcome the convergence failures.

Alternative software packages providing more sophisticated analysis capabilities may not experience such convergence difficulties. The convergence failures were overcome for one of the stiffer trimlines by replacing the rigid constraints with compliant link elements and the imposed displacements with a mechanism comprising further compliant links and stiff beam elements. The objective of this was to simulate elasticity in the calf strap and provide a less rigid deformation pattern. Due to the compliance of the link elements, the rotation of the model was not applied in as rigid a manner as during the experiment and hence the predicted moments were less than those obtained experimentally.

The experiments documented in Chapter 5 can be considered a good representation of the loading conditions an AFO is subjected to during gait. Good repeatability of measurements was obtained with the experimental apparatus. A typical plantar flexion test was simulated with the finite element modelling routines developed. The analysis predicted the specimen response up to a certain angle of rotation at which convergence failure occurred. Although this analysis is incomplete, it nonetheless indicates a realistic approach for validation of a finite element model and the ability to predict deformation well within the range the AFO is expected to experience in service.

6.1.4 Originality of Work

An effective and reliable finite element model was developed and used to study AFO deformation under various conditions. This took advantage of solid modelling and automatic mesh generation capabilities of the software, forming the basis of an innovative, integrated procedure for customising an AFO prior to manufacture. A detailed examination of the effect key modelling parameters have on prediction of AFO stiffness was performed. This included the distribution and magnitude of loading, orientation and location of constraint, symmetric and asymmetric geometry, elastic material properties, material thickness and trimline location. Coupled rotation of the AFO and foot about the ankle joint axis was simulated using a novel arrangement of imposed displacement and constraint. This consolidated the differences in strategy between previously reported experimental and analytical work.

Mesh refinement was carried out to investigate the significance of discretisation error and obtain a more efficient mesh. A non-linear analysis procedure, incorporating both large deformation effects and non-linear elasticity, was developed to predict an AFO's behaviour over the whole range of potential deformations during gait. A novel test rig was designed and utilised for the experimental verification of non-linear analytical predictions. The main point demonstrated throughout this work was the sensitivity and unpredictability of an AFO's response due to its complex shape. Apart from the predominant sagittal plane rotation, other possible AFO deformations were identified which may have a significant effect on AFO performance as supporting devices.

6.1.5 Implications for Patient Care

Having established the validity of features essential to a finite element model of an AFO, it can be used with greater confidence in the design process. The performance of different designs of AFO can be assessed before manufacture using

the proposed modelling approach by simply modifying the trimline within the software. Combined with computer aided manufacture, this technology could replace the current trial-and-error approach to customising an AFO, which is necessary due to the difficulty in predicting the relationship between its geometry and stiffness. This would ultimately lead to improved patient care, customisation and production efficiency.

Improved designs of AFO could be developed which better aid daily function, are easier to put on, offer enhanced comfort due to better fit and lightweight construction, and are cosmetically more pleasing due to reduced thickness or slender design. As well as their improved stiffness and reduced weight, the use of materials such as carbon fibre may also provide cosmetic advantages over thermoplastic materials due to their high tech appearance. There is a potential for predicting the pressure distribution over the sole of the foot from reaction forces and then customising an AFO to better reduce foot ulcerations. An improved matching of the AFO's rigidity in different planes to a patient's condition may allow the abnormality to be more successfully corrected, without interfering with normal function.

6.2 Recommendations for Future Work

6.2.1 Solid Modelling

There were numerous issues that were identified during this work as requiring further investigation. Firstly, a comprehensive assessment of the effects of varying the surface geometry of the leg on AFO behaviour should be undertaken. This would best be performed by modifying the modelling routine to incorporate a method of interactively manipulating the keypoints through which the splines and hence the area are interpolated. Although this functionality is not currently available in finite element preprocessors, it is available in most 3D modelling

packages, so the geometry could be exchanged between software as required. Alternatively, bespoke software incorporating interactive surface manipulation and trimline adjustment could be written specifically for modelling AFOs. As the thickness variation in some of these analyses was stepped between areas of the model, a smooth variation may be required for more accurate assessment of behaviour. The error in approximating the leg surface and hence the inner surface of the AFO as the mid-surface of the shell elements needs to be assessed, as the areas are out of position by half the shell thickness and this may be critical. The solution to this problem also becomes more complicated when modelling a variable thickness AFO.

It is sometimes desirable to alter the orientation of an AFO's foot enclosure relative to its posterior calf enclosure, for example vacuum forming the AFO over a positive cast set in dorsiflexion has been found to provide additional lift during the swing phase of gait. This type of adjustment could be made whilst defining the cross-sections through the leg's surface, by allowing the user to rotate about the ankle joint axis the splined lines through the foot relative to those through the calf. As the leg surface is then skinned through these cross-sections, any small movement at the boundary of these two regions could be tolerated. An AFO with different medial and lateral trimlines when viewed in the sagittal plane was not successfully modelled in this work. As an actual AFO may have a higher degree of asymmetry in the trimline and also geometry than modelled in this work, further analyses are needed to investigate the affects of such asymmetry.

Throughout this work the ankle joint axis was simplified as being perpendicular to a plane passing through the midplane of the foot and also the approximate centre of the calf band region, and was positioned at the intersection of this plane and a line connecting the medial and lateral malleoli. Although this offered the advantage that any medial/lateral displacement of the foot during plantar flexion or dorsiflexion could be attributed to the asymmetric geometry, rather than an asymmetric loading, a more realistic orientation would provide better moment versus rotation characteristics. This data could then be complemented by motion

about other axes, for example the moment versus rotation characteristics about the subtalar joint axis would provide information on an AFO's stiffness under inversion and eversion.

6.2.2 AFO/Limb/Shoe Interaction

Variations in the predicted moments and stresses with changes in the distribution of both imposed displacement and constraint at the heel indicate the necessity of developing a model including the AFO, lower limb and the shoe. The complex interaction between these components could then be more accurately modelled using contact non-linearity whilst applying loading to the combined model, and the compliance of both the lower limb (deformation of soft tissue) and shoe should allow the prediction of more accurate AFO behaviour.

6.2.3 Viscoelasticity

Although creep or viscoelastic behaviour was not modelled in this work, it was considered to be the most important issue for further investigation because stiffness degradation of an AFO could cause failure due to insufficient support of the limb. A static analysis adopting a creep material model concentrating on the primary creep phase would be a suitable initial step to obtain a relationship between the magnitude of creep strain and the loading applied. Under intermittent loading, an AFO would recover during periods of zero stress where the patient is at rest such that the creep strain would be less than that under continuous load [Turner, 1974]. A non-zero mean stress will nonetheless result in an accumulation of creep strain with time [Gotham, 1974]. Therefore, static analyses should be followed by dynamic analyses to investigate creep behaviour under cyclic loading. As plastics exhibit a high mechanical hysteresis, cyclic loading can also cause rises in temperature and failure due to thermal softening. Sensitivity of an AFO's behaviour to variations in temperature should be investigated, as creep can be

affected by thermal stresses.

6.2.4 Material Anisotropy

Composite materials consist of reinforcement, usually fibres of glass or carbon, and a continuous matrix capable of transferring loads to the fibres, usually a thermosetting plastic [Datoo, 1991]. These are increasingly being used in industry due to their improved properties over other materials. For example, the specific modulus of a high modulus carbon epoxy composite in the direction of reinforcement is over 4 times greater than that of either mild steel or aluminium alloy, and about 100 times greater than that of polypropylene. The raw materials are available in either separate fibre and matrix, or alternatively pre-impregnated unidirectional or woven sheets. The latter offer the advantage of reproducibility and, as the manufacturing process involves laying sheets onto a mould and vacuum forming, is similar to current practice for AFO manufacture. The individual layers of fibre-reinforced composites can be laminated together, each with the fibres orientated in a particular direction, to achieve the desired stiffness in different directions. Therefore, a thorough understanding of the stresses and strains would be required to gain maximum benefits from such materials for AFO design, which necessitates an analytical approach. Composites can be modelled with finite element software using layered elements, whereby the orthotropic material properties and orientation of each layer must be defined.

6.2.5 Dynamic Loading

The static analyses reported in this work assumed that the loading and the AFO's response varied slowly with respect to time so that inertia and damping effects can be ignored. The cyclic loading conditions during gait may cause additional loading on the AFO in the form of inertia and damping forces if the frequency of excitation is higher than one-third of the AFO's lowest natural frequency.

Therefore, modal analyses should be performed to calculate the natural frequencies of the AFO. If necessary, dynamic analyses should complement the static analyses to determine the AFO's response to transient loading. These analyses should incorporate all forms of non-linearities that were introduced in the static analyses, and the load history should be defined such that it is consistent with the typical loading pattern encountered during gait.

6.2.6 Modelling and Manufacture

The manufacturing process of an AFO will also require improvement with respect to accuracy if the advantages gained through finite element analysis are to be realised. For example, a device similar to a digitiser could be developed to transfer the trimline, designed through finite element analysis, onto the vacuum formed material prior to trimming. Rapid prototyping systems such as stereolithography could currently be of benefit for the assessment of the fit, but not function, of an AFO. In future, it may be possible to use such systems to actually manufacture a functional AFO for a patient directly from a computer model. Large strain analyses of the current vacuum forming process may allow the prediction of the thickness variation throughout an AFO, results which could be utilised during the design process itself. Modelling the orthotropic material properties of an AFO induced by vacuum forming would also allow more accurate prediction of its characteristics.

Appendix A

Assessment of Element Accuracy

A.1 Square Plate Problems

One approach that was adopted to validate the model was to solve a number of test problems to assess the accuracy of the selected shell element in certain situations, rather than relying on the supplied ANSYS verification problems. The first problem considered was that of a uniformly loaded square plate with all edges simply supported. The solution for the maximum deflection, w_{max}, at the centre of a rectangular plate under such conditions can be obtained from the following equation [Timoshenko & Woinowsky-Krieger, 1959].

$$w_{max} = \alpha \frac{qa^4}{D} \qquad \text{where} \qquad D = \frac{Eh^3}{12(1-\nu^2)} \tag{A.1}$$

In the above equation, α is a numerical factor depending on the ratio b/a of the plate, a is the plate dimension parallel to the x axis, b is the dimension parallel to the y axis, q is the applied pressure, and D is the flexural rigidity, which is dependent of the Young's modulus, E, Poisson's ratio, ν, and thickness, h. Similarly, the magnitude of the bending stresses at the outer surfaces of the plate,

σ_x and σ_y, can be calculated from the maximum bending moments per unit length at the middle of the plate, $(M_y)_{max}$ and $(M_y)_{max}$, using the equations below. In the case of a square plate, α equals 0.00406 and the numerical factors β and β_1, which are also dependent on the ratio of the sides of the plate, are both equal to 0.0479.

$$\sigma_x = \frac{6M_x}{h^2} \qquad \text{where} \qquad (M_x)_{max} = \beta q a^2 \tag{A.2}$$

$$\sigma_y = \frac{6M_y}{h^2} \qquad \text{where} \qquad (M_y)_{max} = \beta_1 q a^2 \tag{A.3}$$

Considering the simplest case of a square plate, a and b were both defined as 100 mm, q was 5×10^{-4} MPa, E was 1000 MPa, ν was 0.3, and h was 2 mm. This problem was analysed within ANSYS using a symmetry model for different mesh densities, and the results are summarised in Table A.1. The solutions for the maximum displacement and bending stresses have been normalised against the solutions obtained using the equations above, which were calculated as 0.277 mm and $\pm$0.359 MPa respectively. Clearly, with coarse meshes the displacements were more accurate than stresses, however, as the mesh was refined, the stresses converged to within the same percentage error as the displacements. Note that the percent energy error, η, for each mesh is much greater than the actual error in the two results, so this measure of discretisation error should not be considered as conclusive.

These analyses were repeated for a similar problem with all edges built-in (clamped), while all other parameters remained the same. For a rectangular plate with clamped edges, the maximum displacement is again at the middle of the plate and can be calculated from the equation above. The maximum bending moments in this case are located at the middle of the clamped edges of the plate, although the above equations are still valid. In the case of a square plate, the numerical factor α is equal to 0.00126, and the factors β and β_1 are both equal to -0.0513. For comparison purposes, the value of the bending moment at the middle of the

Mesh	w_{max}	$(\sigma_x)_{max} = (\sigma_y)_{max}$	η (%)
1×1	1.092	1.340	N/A
2×2	1.038	1.107	28.2
3×3	1.025	1.049	20.4
4×4	1.021	1.032	17.7
5×5	1.020	1.025	16.3
6×6	1.020	1.021	15.0
12×12	1.020	1.015	9.5
24×24	1.020	1.014	4.1

Table A.1. Summary of results for simply supported plate

plate may be obtained from the same equation but with β and β_1 both equal to 0.0231.

The results for a number of analyses performed with different mesh densities are summarised in Table A.2. The solutions for the maximum displacement, the maximum bending stresses and the bending stresses at the centre have been normalised against the solutions obtained using the equations above, which were calculated as 0.086 mm, ±0.385 MPa and ±0.173 MPa respectively. These results show that a built-in plate is significantly stiffer than one with simply supported edges. Although the results again converged to within a few percent of the correct solutions, the percent errors for the initial mesh were far greater than those obtained for the simply supported plate, indicating that the constraints have a significant effect on the accuracy of the results for a given mesh density.

The above problems assumed that the plate was bent by the application of only lateral loads. However, additional forces acting in the middle plane of the plate can have a considerable effect on bending. In the case of tensile forces the deflection of the plate is diminished, however, if the load in the plane of the plate is compressive, the deflections become larger than those of a plate with lateral loads only. Also, if this compressive force reaches a critical value, the plate will buckle without any lateral loading. Therefore, to study element accuracy under

Mesh	w_{max}	$(\sigma_x)_{max} = (\sigma_y)_{max}$	$(\sigma_x)_{centre} = (\sigma_y)_{centre}$	η (%)
1×1	1.270	0.731	2.110	N/A
2×2	0.927	0.903	1.095	36.8
3×3	1.006	0.946	1.059	15.7
4×4	1.012	0.971	1.030	7.9
5×5	1.012	0.981	1.016	4.4
6×6	1.012	0.986	1.009	2.6
12×12	1.012	0.996	0.996	0.7
24×24	1.012	0.998	0.993	0.3

Table A.2. Summary of results for built-in plate

bending due to the combined actions of both lateral loads and forces in the middle plane of the plate, the first problem consisting of a simply supported plate under uniform pressure was modified to incorporate a uniform edge tension.

In this case, the equations for the maximum displacement and maximum bending moments at the centre are similar to those above, although they are expressed in a slightly different form as below.

$$w_{max} = \alpha \frac{qb^4}{Eh^3} \qquad (M_x)_{max} = \beta q b^2 \qquad (M_y)_{max} = \beta_1 q b^2 \tag{A.4}$$

Similarly, the constants α, β and β_1 depend on the ratio a/b and also on the parameter γ evaluated from the following equation, where N_x is the magnitude of the lateral load per unit length.

$$\gamma = \frac{N_x b^2}{4\pi^2 D} \tag{A.5}$$

The problem parameters were unchanged to allow comparisons to be made with the results above, however N_x was additionally defined as 5 N/mm. The values for the constants α, β and β_1 were obtained from plots against the parameter a/b for

Mesh	w_{max}	$(\sigma_x)_{max}$	$(\sigma_y)_{max}$
1×1	1.107	1.024	1.337
2×2	1.088	1.012	1.239
3×3	1.082	1.009	1.075
4×4	1.081	1.009	1.042
5×5	1.080	1.009	1.037
6×6	1.080	1.009	1.033
12×12	1.080	1.008	1.026
24×24	1.080	1.008	1.025

Table A.3. Summary of results for combined loading of plate

different values of γ. In this case, they were found to be approximately 0.0173, 0.015 and 0.0175 respectively for a calculated γ of 1.728. This allowed the theoretical solutions for the maximum displacement and the maximum bending stresses in the x and y directions to be calculated as 0.106 mm, $\pm$0.113 MPa and $\pm$0.131 MPa respectively. The membrane stress in the x direction was calculated as 2.5 MPa, giving a total maximum stress in the x direction of 2.613 MPa.

The results from a number of analyses performed are summarised in Table A.3, normalised against the solutions above. The results for the maximum displacements do not appear as accurate as with previous problems, however this was found to be a result of using too few substeps, and increasing this number from 5 to 10 decreased the error to less than 1 %. Note that, although the results for the total maximum stress in the x direction appear more accurate than the results for the maximum bending stress in the y direction, if the maximum bending stress in the x direction had instead been tabulated, the errors would have been about 20 %. Also, these analyses must incorporate stress stiffening because the membrane stresses affect the out-of-plane stiffness of the plate. By ignoring this geometric non-linearity, the results are identical to those obtained for the simply supported plate above with the exception of the maximum stress in the x direction, which would additionally include membrane stresses.

As the bending characteristics of plates have a greater dependency on the thickness than the in-plane dimensions, plate problems are usually classified as either thin or thick [Boresi *et al.*, 1993]. However, problems are also classified according to the magnitude of the out-of-plane deflections compared to the thickness. Small deflection theory is generally applicable when the deflections are less than half the thickness, and this approach was used for the above analyses. Although this ignores second order effects, these are considered negligible and so accurate results can be obtained. However, when the deflections are greater than half the thickness, these second order effects become significant and develop membrane stresses that stiffen the plate. Therefore, ignoring these large deflection effects will result in over-estimates of displacements and stresses.

To test the accuracy of the element under large deflections, the second problem consisting of a clamped plate under uniform pressure was modified to incorporate this geometric non-linearity. The results from the second set of analyses show that the maximum deflection at the centre of the plate was significantly less than half the plate thickness so, to ensure that these effects would be developed, the magnitude of the applied pressure was increased by a factor of 100 to 5×10^{-2} MPa. Under such conditions, linear theory predicts solutions for the maximum displacement at the centre and maximum bending stresses at the middle of the clamped edges of 8.6 mm and ± 38.5 MPa respectively.

The results obtained from a series of analyses with different mesh densities are summarised in Table A.4. These results have been normalised against approximate solutions for the maximum displacement and maximum stress of 3.3 mm and 25.8 MPa respectively, which were obtained from plots in Timoshenko & Woinowsky-Krieger [1959]. The convergence of the results obtained for the maximum stress to the final solution appears to be slower than in the second problem, although this could be a consequence of the number of substeps used. Note that, compared to the results obtained from large deflection theory, those obtained from linear theory gave an overestimate of the maximum displacement by a factor of 2.6, although this error would ultimately reduce with a reduction in

Mesh	w_{max}	$(\sigma_x)_{max} = (\sigma_y)_{max}$
1×1	1.253	0.543
2×2	1.009	0.816
3×3	1.025	0.870
4×4	1.025	0.912
5×5	1.025	0.934
6×6	1.019	0.947
12×12	1.019	0.974

Table A.4. Summary of results for large deflection of built-in plate load (see Figure A.1).

A.2 Problems Proposed by MacNeal & Harder

A comprehensive set of problems for verifying element accuracy have been proposed by MacNeal & Harder [1985] to demonstrate frequently encountered element failure modes and take into account parameters affecting accuracy. These problems were then tested on a number of solid and shell elements available within an alternative FEA package named NASTRAN. The problems suitable for testing shell elements were a twisted beam, a Scordelis-Lo roof and a spherical shell, and sufficient information was given to permit the construction of the models, along with theoretical results. Therefore, to enable more thorough testing on the selected element within ANSYS, these tests were performed within ANSYS.

The *twisted beam* problem consisted of a cantilever beam initially twisted 90 ° from root to tip with unit forces individually applied to the middle of the free end in two perpendicular directions, to simulate both in-plane and out-of-plane bending responses independently (see Figure A.2). For the problem, the length was defined as 12.0, the width was 1.1, the depth was 0.32, Young's modulus was 29.0×10^6, Poisson's ratio was 0.22, and a 12 × 2 mesh was used. This problem

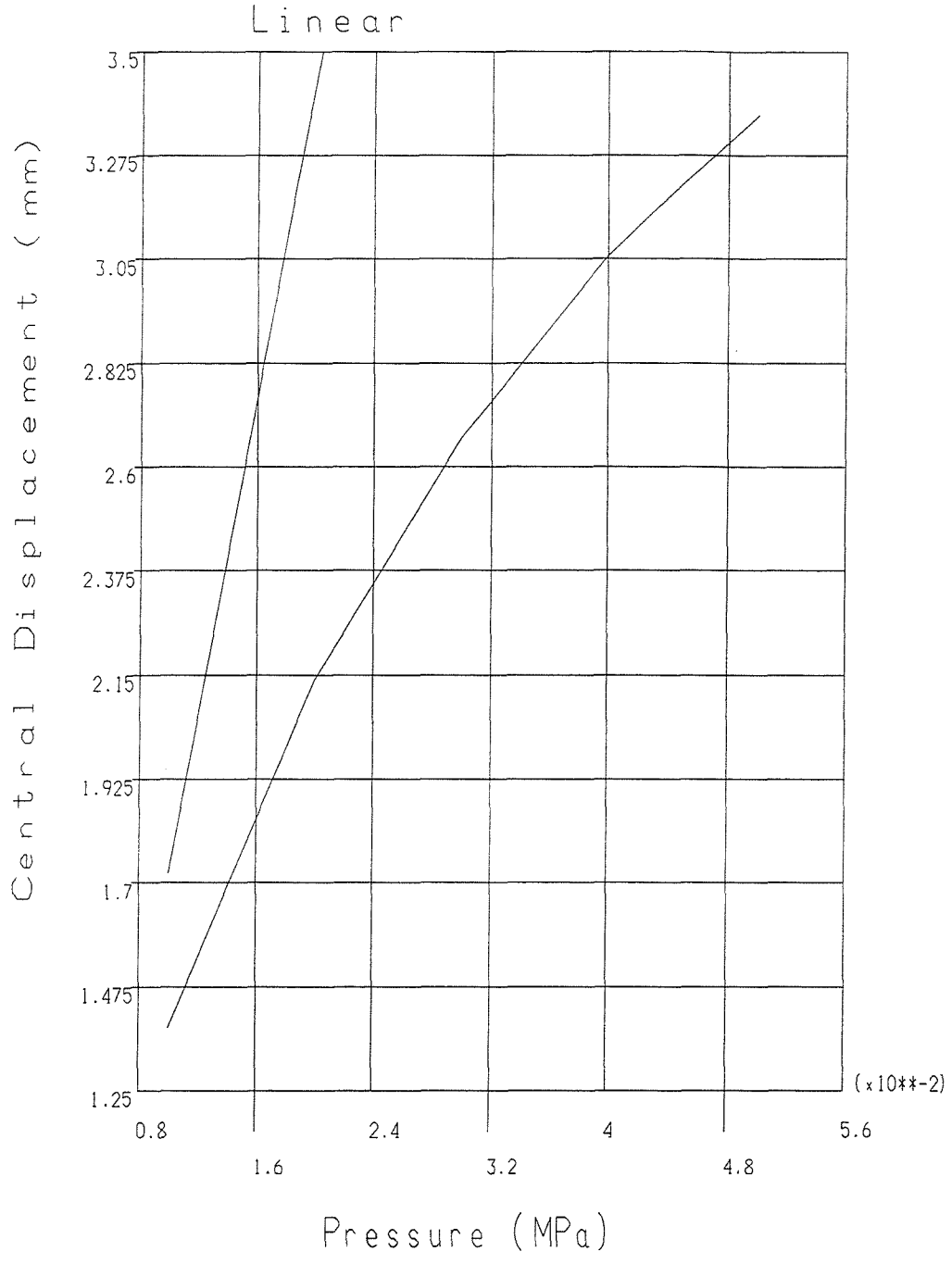

Figure A.1. Effects of large deflection on a plate

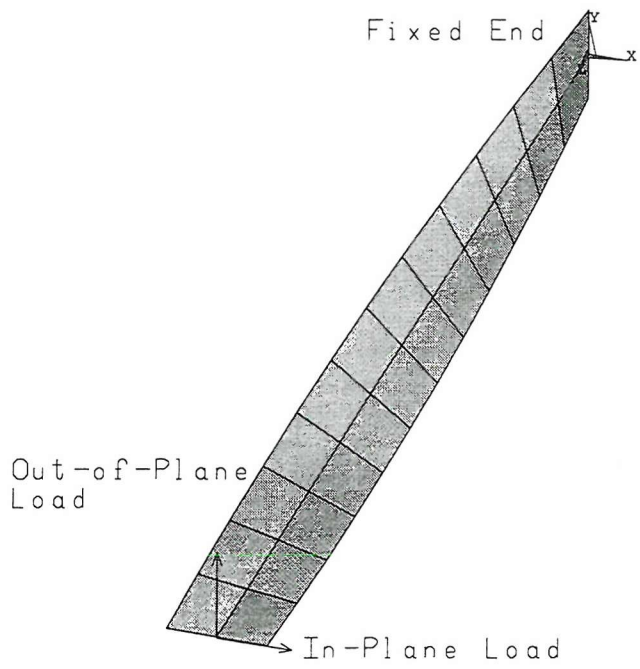

Figure A.2. Twisted beam problem

was the only one proposed to test the effect of warp on shell elements. Other geometric parameters affecting accuracy that were tested by this problem included aspect ratio, double curvature and slenderness, the final parameter affecting the conditioning of the stiffness matrix.

The results for displacement in the direction of the load for both in-plane and out-of-plane loading are summarised in Table A.5. Each has been normalised against the given theoretical solutions for the displacements under in-plane and out-of-plane loads, which were 0.005424 and 0.001754 respectively. Although not proposed, a number of analyses were performed with different mesh densities to study the sensitivity of the results to the magnitude of element warping. The errors were found to be less than 1 % in most cases, only becoming significant when a single element was used. These results agreed with those obtained by MacNeal & Harder [1985] for a similar element type, which gave an error of less than 1 % when a 12 $\times$ 2 mesh was used.

Mesh	Normalised Tip Displacement in Direction of Load	
	In-Plane Load	Out-of-Plane Load
1×1	0.927	0.751
2×1	0.971	0.958
4×1	0.990	0.991
6×1	0.995	0.995
12×2	0.998	0.998
24×2	0.999	0.999

Table A.5. Summary of results for twisted beam problem

The *Scordelis-Lo roof* problem consisted of a cylindrical roof, simply supported at two ends, with a uniform pressure applied in the vertical direction (see Figure A.3). For the problem, the radius was set to 25.0, the length was 50.0, the arc angle was 80 °, the thickness was 0.25, Young's modulus was 4.32×10^8, Poisson's ratio was 0.0, the loading was 90.0 per unit area in the negative Y direction, the nodes on the curved edges were constrained in both X and Y directions, and a number of mesh densities were used. This problem was the only singly-curved shell problem proposed, however, as some elements that behave well with single curvature will behave poorly with double curvature, this test alone is not sufficient. Both membrane and bending deformations contribute significantly to the deformation behaviour.

As the problem was actually symmetric with respect to the geometry, material and loading, it was modelled using two perpendicular planes of symmetry for efficiency. The results obtained for the vertical displacement at the midpoint of the free edge are summarised in Table A.6 for different mesh densities. These have again been normalised against the theoretical solution, which was given as 0.3086, and show that the displacements are generally not that sensitive to mesh density. These results agreed with those obtained by [MacNeal & Harder, 1985], where the error in displacement for a 2 × 2 mesh was found to be about 2 %, although they had

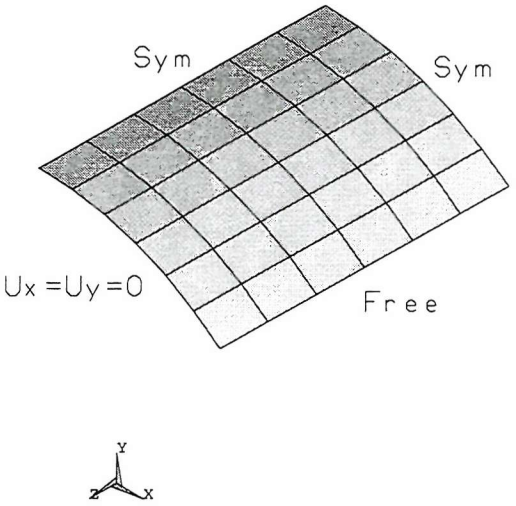

Figure A.3. Scordelis-Lo roof problem

normalised their results against a slightly smaller value because most elements converge to a result slightly lower than the theoretical solution.

The *spherical shell* problem represented a hemisphere with four point loads alternating in sign at 90 ° intervals around the circumference (see Figure A.4). More specifically, the radius was defined as 10.0, the thickness was 0.04, Young's modulus was 6.825×10^7, Poisson's ratio was 0.3, the concentrated forces were as shown, and a number of mesh densities were used. However, to avoid having to use triangular shaped elements with sharp corner angles, a hole was introduced at the top of the model. This doubly-curved problem develops both membrane and bending strains, as with the previous shell problem, which both contribute to the radial displacement at the point of application of the load. Again, due to the symmetric nature of the problem, only a quarter of the problem was modelled. This was the only shell problem to utilise tapered elements.

The results obtained for the radial displacement under the load are summarised in

Mesh	Normalised Vertical Displacement at Midpoint of Free Edge
1×1	1.329
2×2	1.024
3×3	1.007
4×4	0.994
5×5	0.988
6×6	0.985
8×8	0.982
10×10	0.981

Table A.6. Summary of results for Scordelis-Lo roof problem

Table A.7. As the given theoretical solution for the displacement of 0.0924 corresponded to the physical problem, which had no hole at the centre, a slightly higher value has been used for normalisation of the results, which was again given in the reference as 0.0940. These results show that the elements behaved poorly when the mesh was reasonably coarse, although convergence to the exact solution was obtained with repeated mesh refinement. The results obtained by MacNeal & Harder [1985] also had an error of about 18 % for a 4 × 4 mesh of similar elements although, rather surprisingly, they obtained results with two different 4-noded elements that were more consistent and had errors of only a few percent. The description of this problem was found to be misleading in the literature, however Cook [1995] provided a better description.

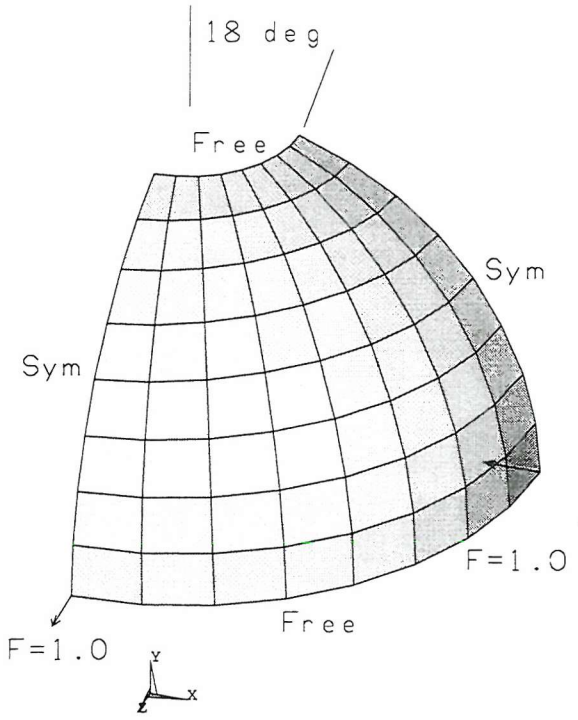

Figure A.4. Spherical shell problem

Mesh	Normalised Radial Displacement at Point of Application of Load
1×1	1.068
2×2	0.178
3×3	0.525
4×4	0.817
5×5	0.948
6×6	0.985
8×8	0.998
10×10	1.000
12×12	1.000

Table A.7. Summary of results for spherical shell problem

Appendix B

Additional Figures

Included here are a number of figures referenced in the text but considered of secondary importance to the reader. Figure B.1 and Figure B.2 are referenced in Section 4.1.7. Figure B.3 and Figure B.4 are referenced in Section 4.1.8. Figure B.5 to Figure B.7 are referenced in Section 4.1.12. Figure B.8 and Figure B.9 are referenced in Section 4.2.2. Lastly, Figure B.10 to Figure B.12 are referenced in Section 4.3.3.

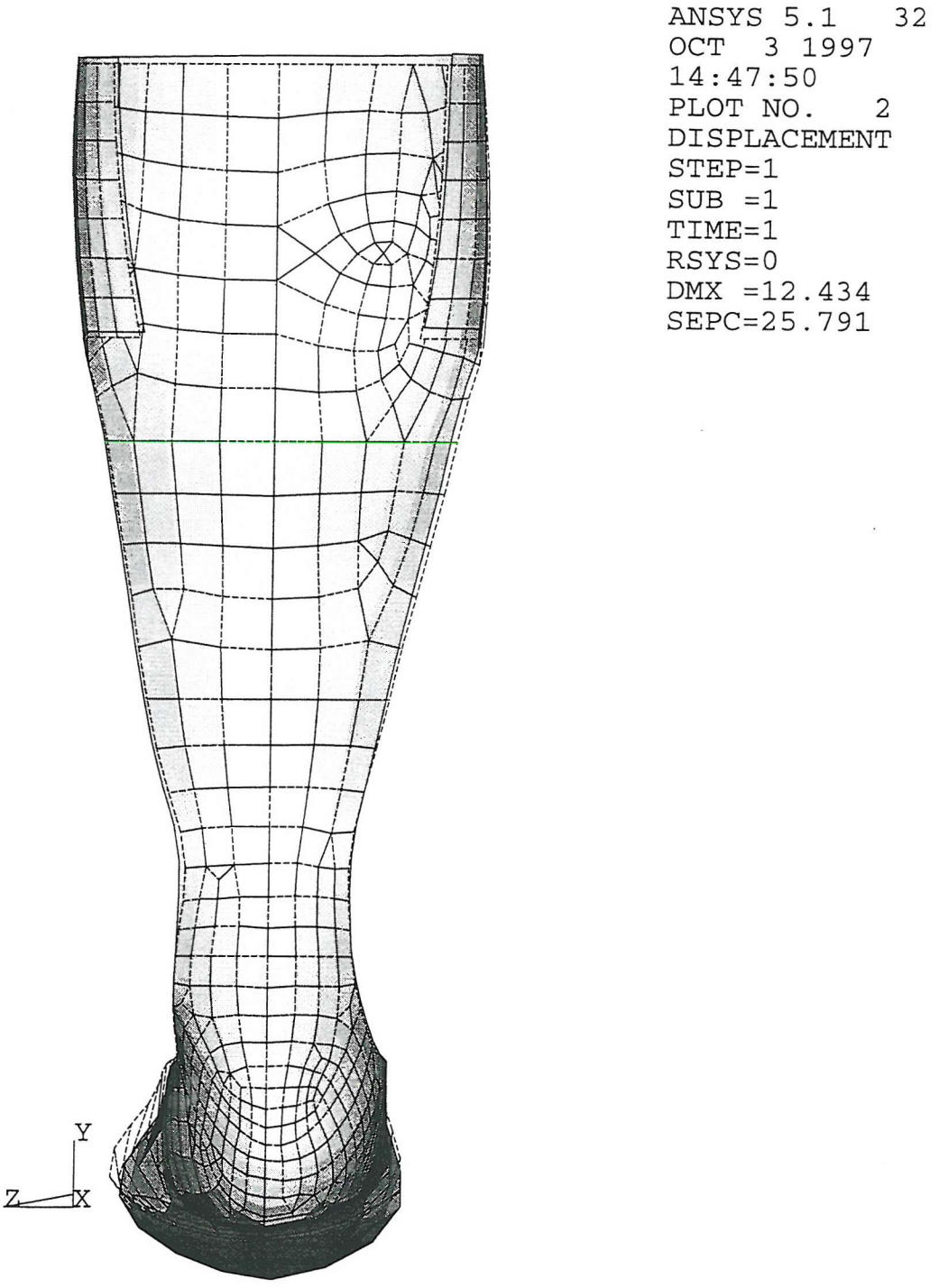

Figure B.1. Anterior view of 5 ° plantar flexed AFO due to single node displacement

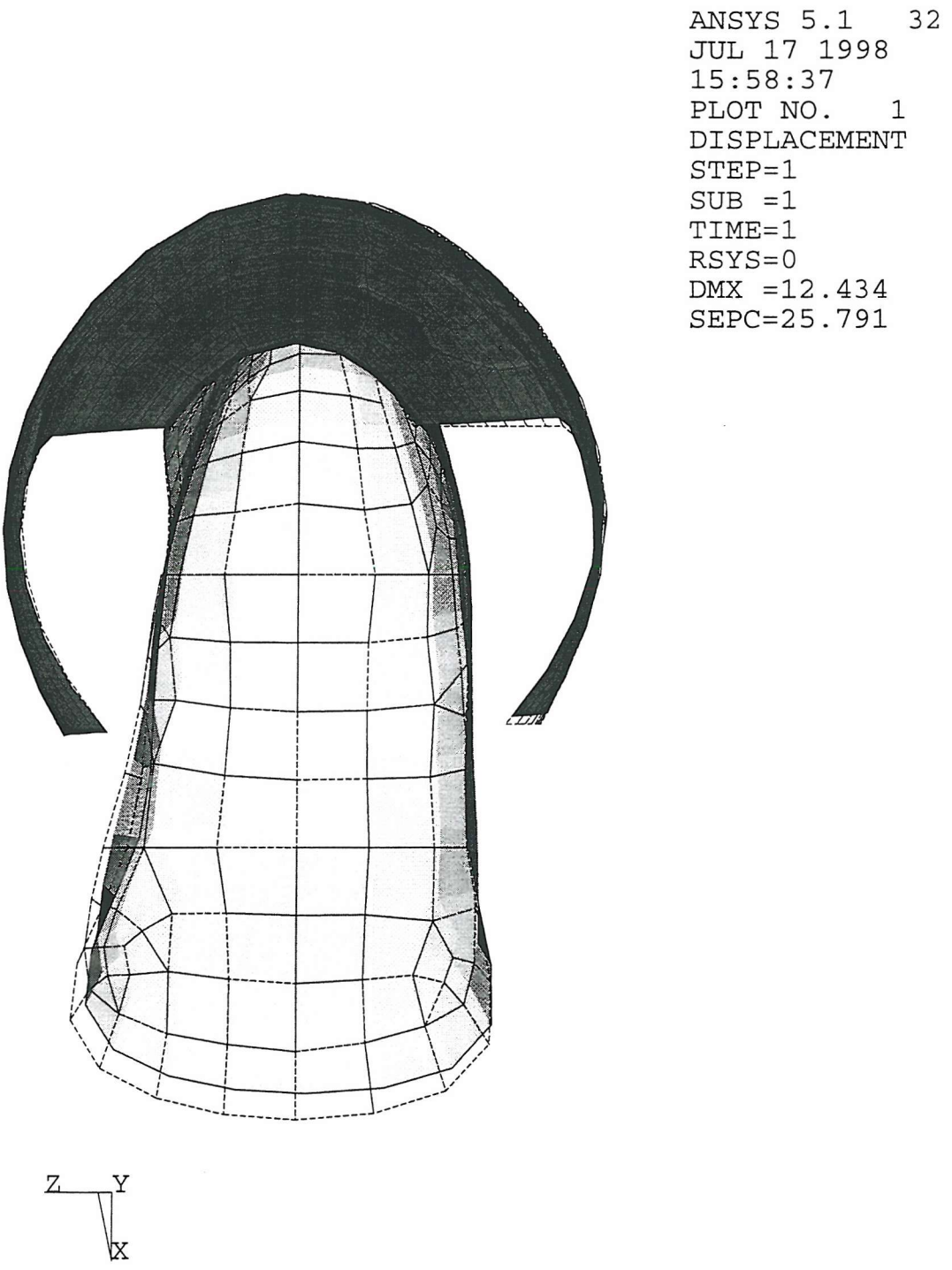

Figure B.2. Superior view of 5 ° plantar flexed AFO due to single node displacement

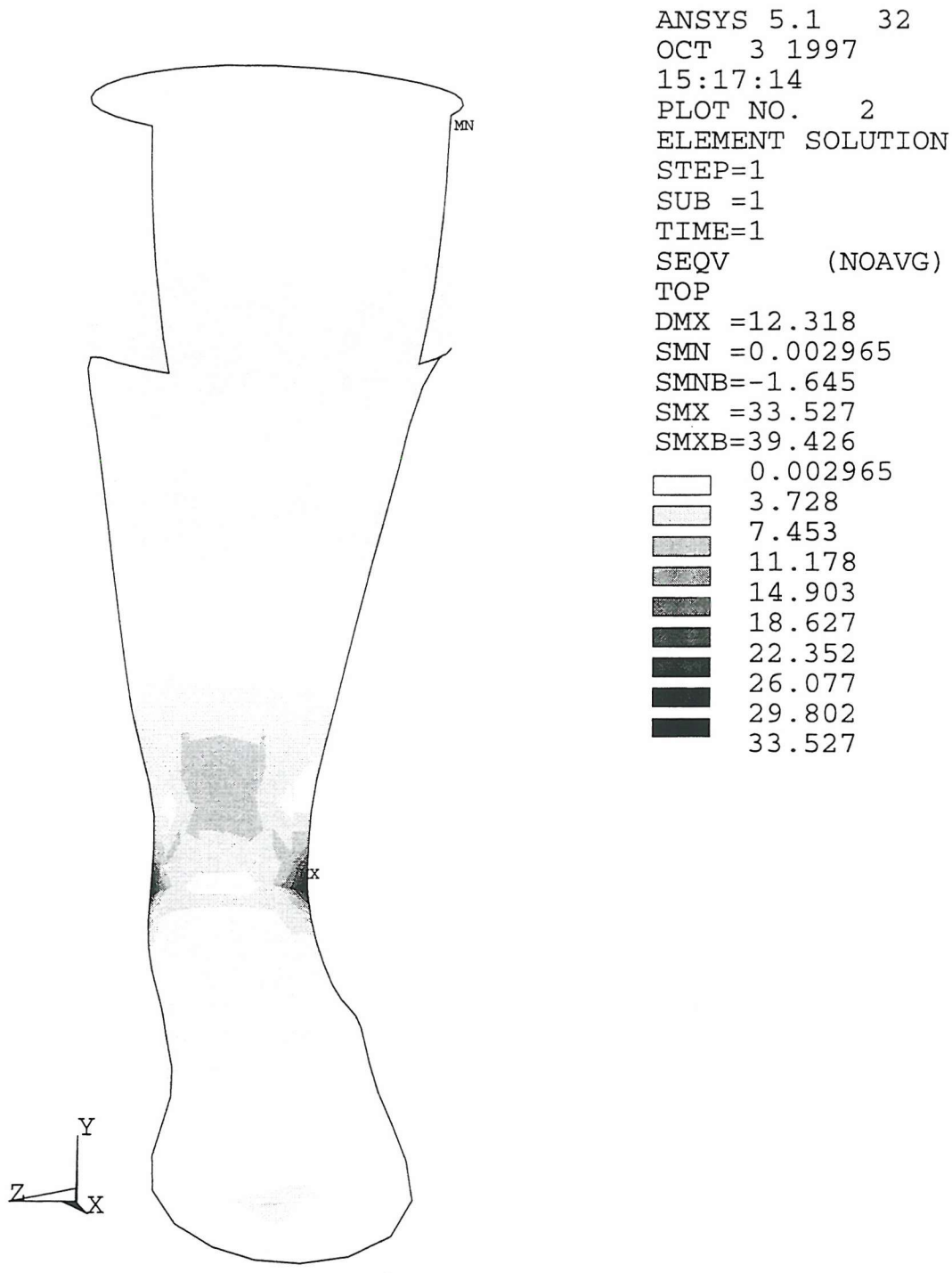

Figure B.3. Equivalent stress at inner surface of 5 ° plantar flexed AFO due to line displacement

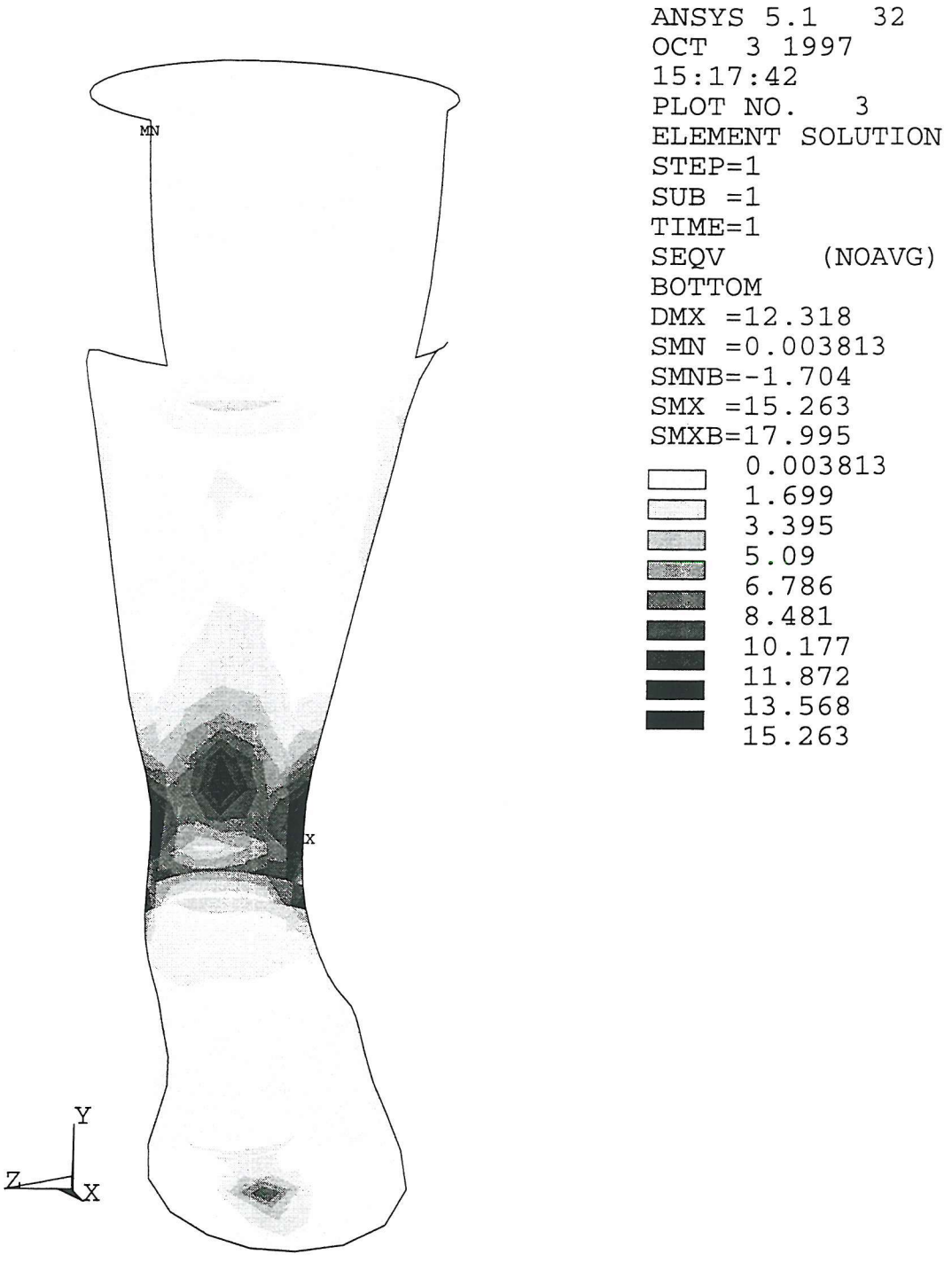

Figure B.4. Equivalent stress at outer surface of 5 ° plantar flexed AFO due to line displacement

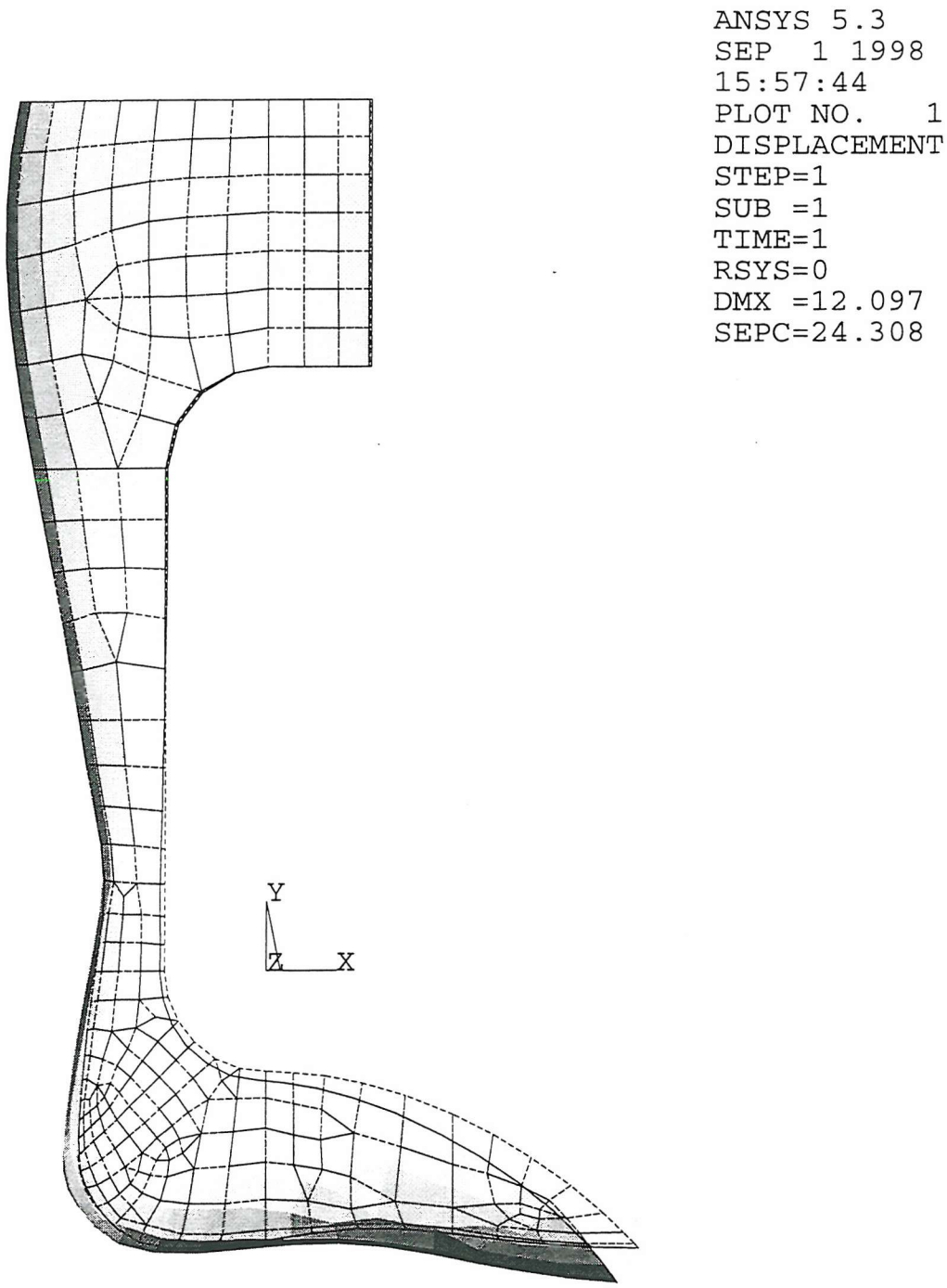

Figure B.5. Lateral view of plantar flexed AFO in the absence of heel constraints

Figure B.6. Equivalent stress at inner surface of plantar flexed AFO in the absence of heel constraints

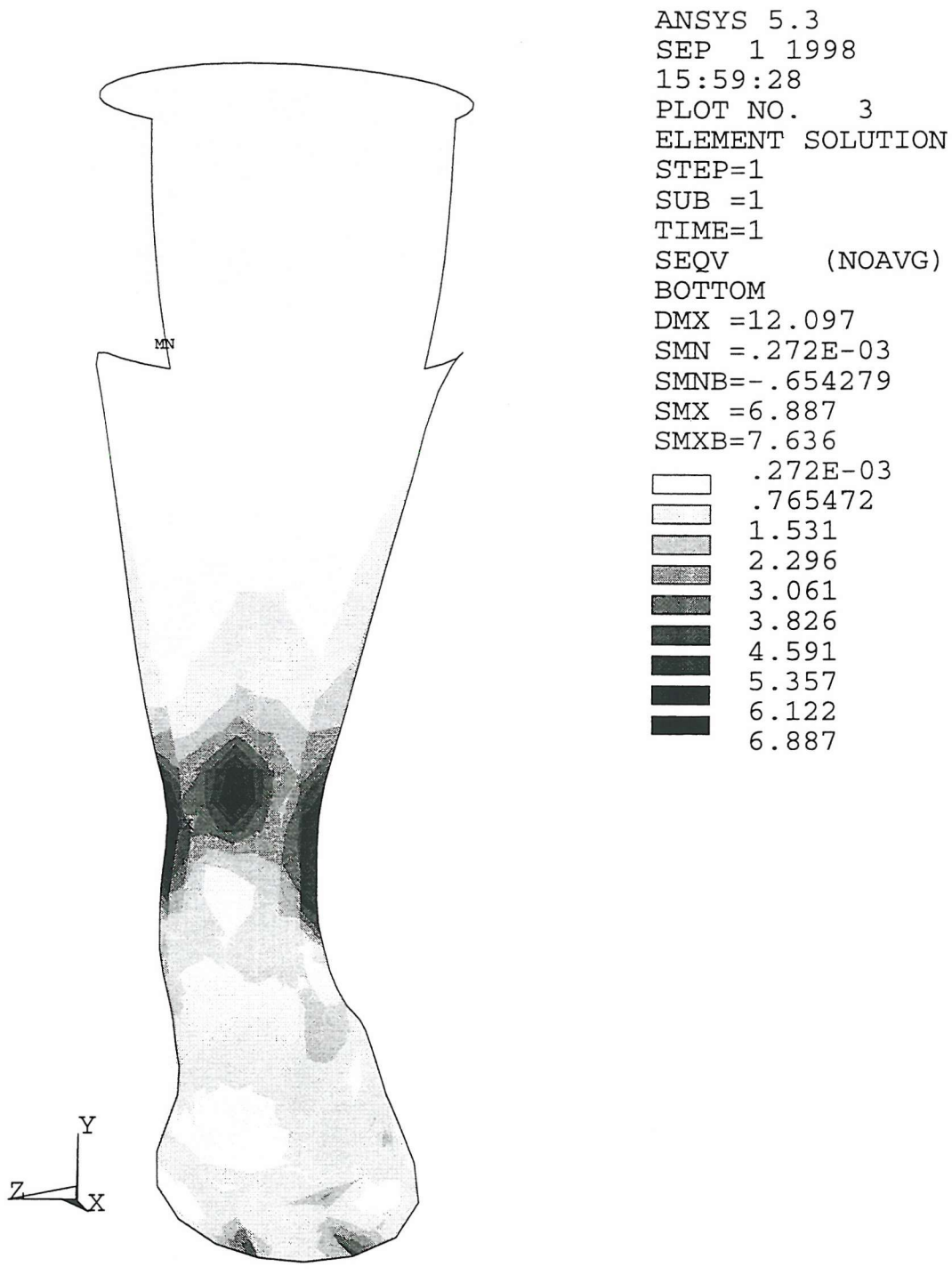

Figure B.7. Equivalent stress at outer surface of plantar flexed AFO in the absence of heel constraints

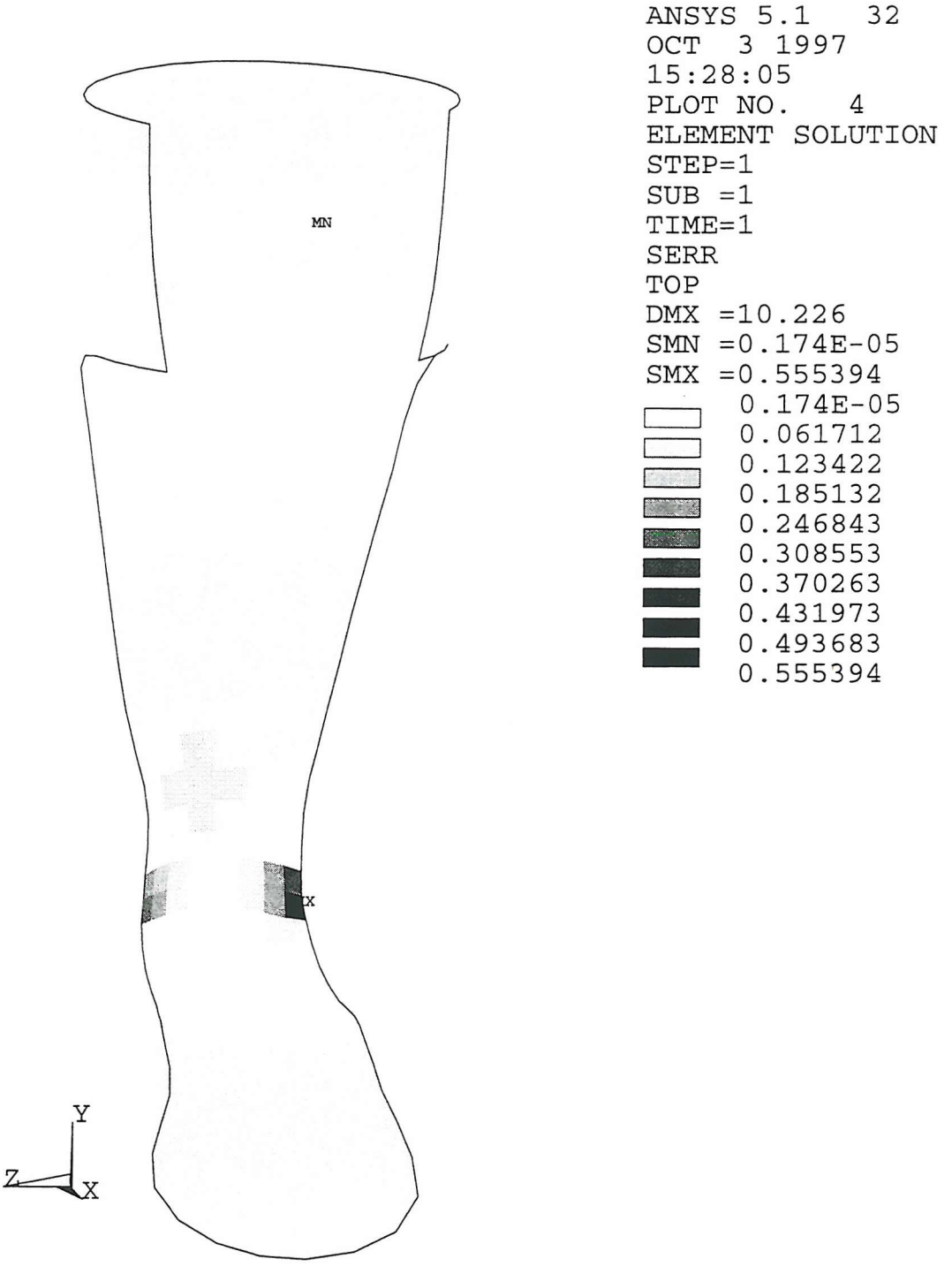

Figure B.8. Energy error for initial mesh due to uniform pressure

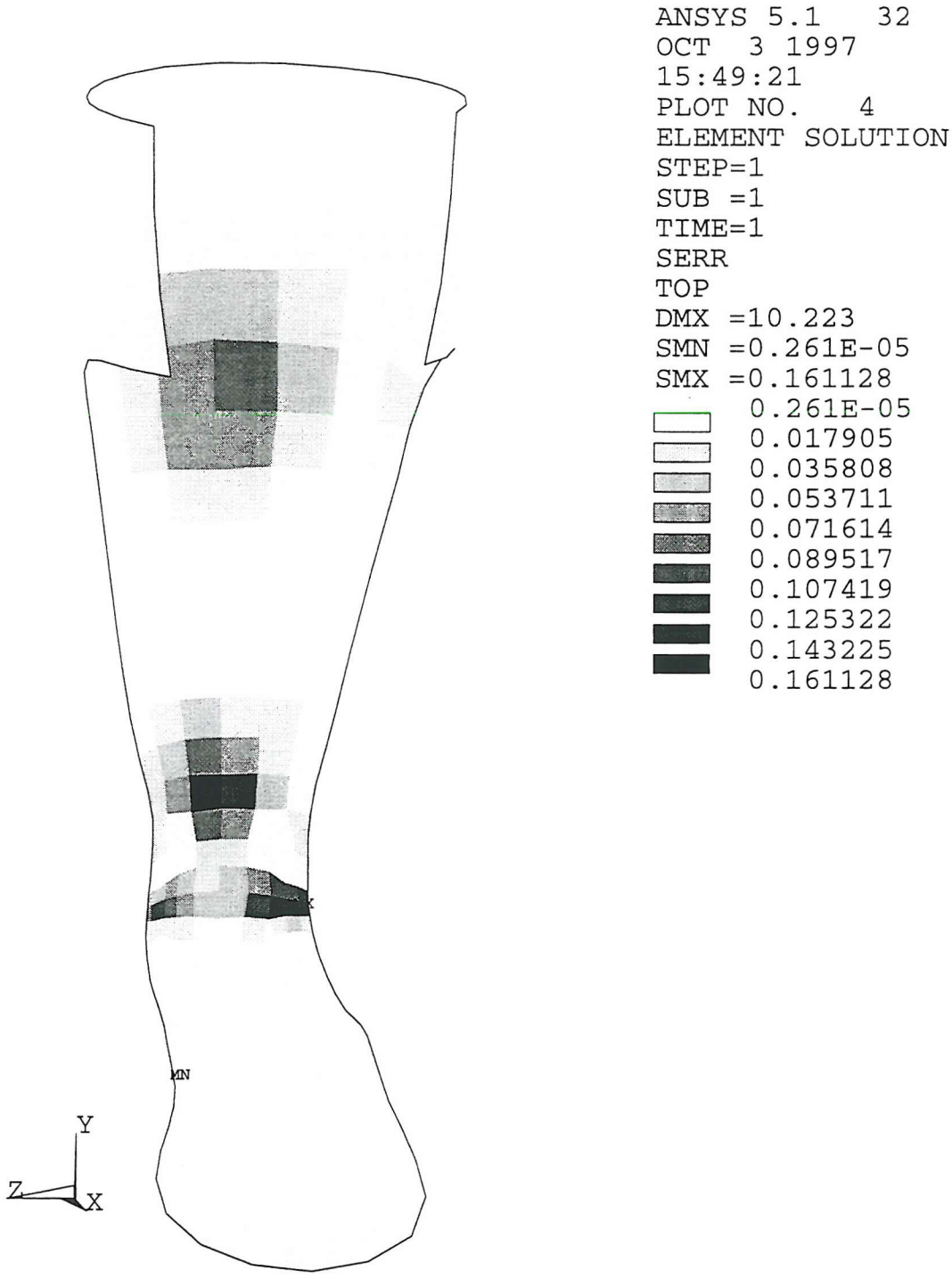

Figure B.9. Energy error for second mesh due to uniform pressure

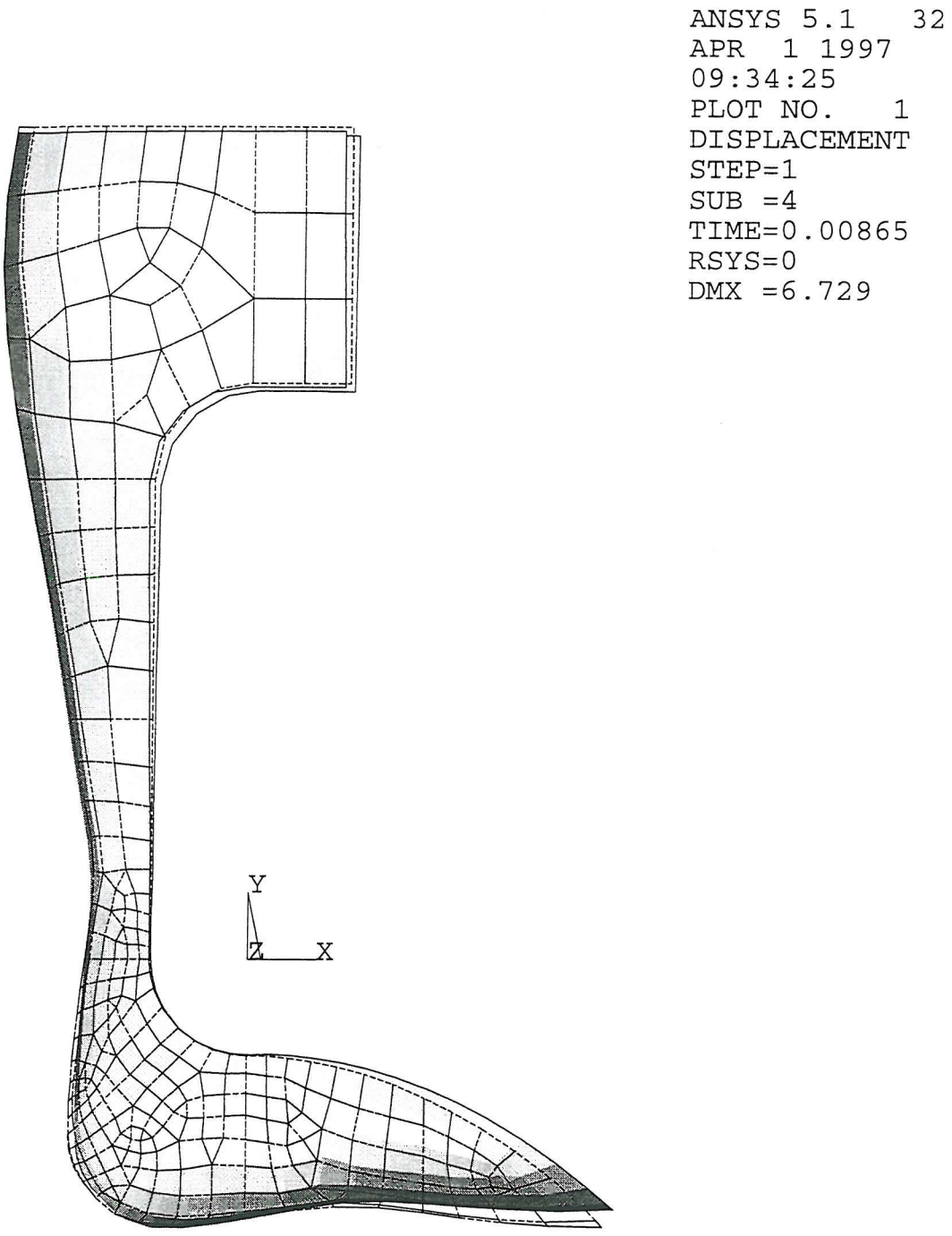

Figure B.10. Lateral view of dorsiflexed AFO due to uniform pressure: combined non-linearities

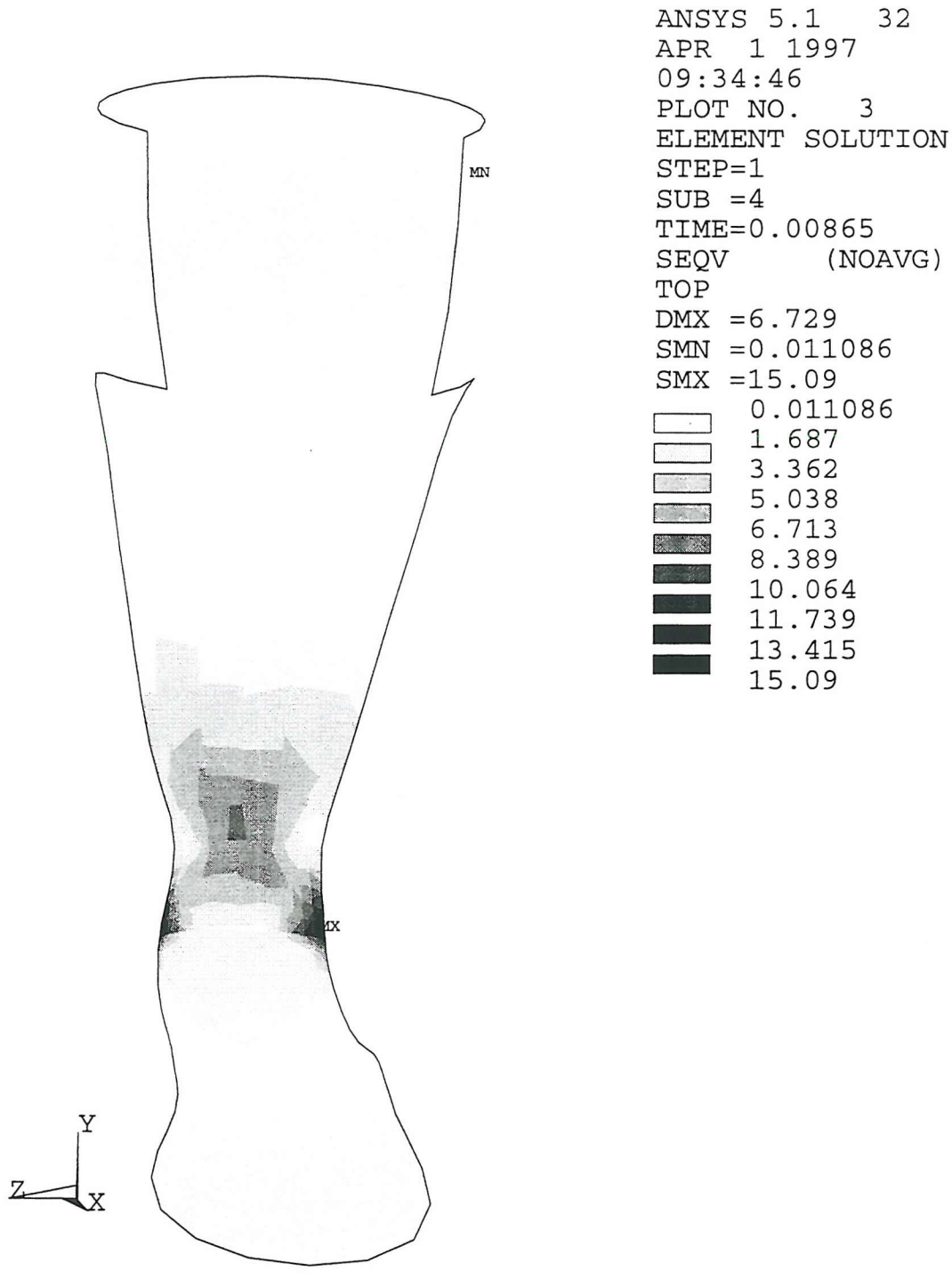

Figure B.11. Equivalent stress at inner surface of dorsiflexed AFO due to uniform pressure: combined non-linearities

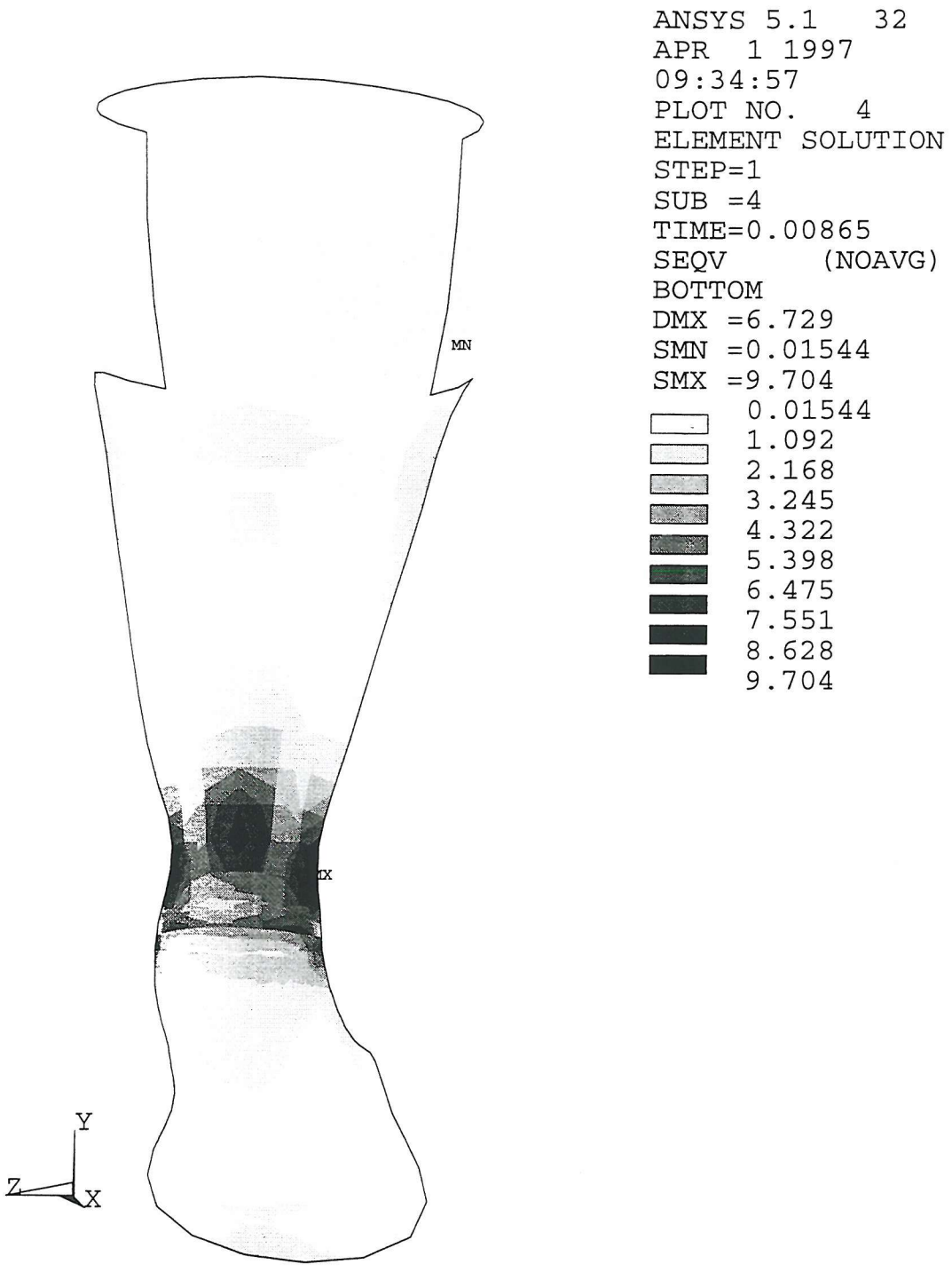

Figure B.12. Equivalent stress at outer surface of dorsiflexed AFO due to uniform pressure: combined non-linearities

Appendix C

ANSYS Specifics

C.1 ANSYS Parametric Design Language

The *ANSYS Parametric Design Language (APDL)* is a set of instructions that extend the ANSYS command language to allow such features as looping and branching, as well as user-defined parameters, abbreviations and macros. For example, values representing the number of cross-sections and the number of data points per section were assigned to user-defined scalar parameters, allowing the input file to be modified at a later date to accommodate a different set of data. The coordinate data was to be read into the preprocessor and stored within a two-dimensional array parameter, also referred to as a matrix, in an identical format to that of the data file. As ANSYS could only read data into a vector, the data had to be read into the two-dimensional array a column at a time, as a column was also a vector.

These commands proved to be beneficial to this research as they allowed the modelling routine to be written so that it would automatically adapt to an arbitrary number of lines from which to generate the leg area. It should be noted that the maximum number of keypoints that a splined line could be fitted through

with ANSYS Revision 5.1 was restricted to six, limiting the number of data points that could be used to represent each cross-section. Also, if the spline command was used within a loop, the number of keypoints for each spline had to remain constant. Therefore, because of these limitations, it was not possible to write the routine so that it would adapt automatically to any number of keypoints for constructing each line. One useful advantage with ANSYS Revision 5.3 was that the restriction on the number of keypoints through which a splined line could be fitted was removed. The spline command could therefore be used within a do-loop to fit a line through a variable number of keypoints for each cross-section, although this required additional information to be incorporated into the data file on the number of data points for each line.

The commands used to define the keypoints for each cross-section were included within a do-loop, which conveniently allows the repeated use of a block of commands with the loop counter held in a scalar parameter. The do-loop was executed from an initial value of one to a final value equal to the number of data points, although the increment was set to four so that the loop would point to the row of the array parameter holding the coordinate data for the first point of each cross-section. After generating a splined line through the keypoints representing the first cross-section, the remaining lines were generated using a repeat command. This simply incremented the values entered in each of the numerical fields of the previous command by a specified amount. It was a more limited command than a do-loop, as it could only be used to repeat certain single commands, but it was considered more suitable in that situation.

C.2 Selecting and Numbering Controls

After each splined line had been generated only the two end keypoints were attached to it, so the internal guiding keypoints had become redundant. Also, after generating the leg area by using the skinning operation, only the four boundary lines were attached to it and so the internal guiding lines and associated

keypoints were also redundant. Therefore, to reduce the storage size of the problem and clarify any subsequent displays, the unwanted construction lines and keypoints used during modelling were deleted. This operation was achieved by firstly selecting only those lines and keypoints that were associated with the generated leg area. Those lines and keypoints not associated with the leg area were then selected by simply inverting the current selected sets of lines and keypoints (selected becomes unselected and vice versa).

The selected construction lines and keypoints were then deleted using the relevant commands and all remaining areas, lines and keypoints were then reselected. The completed solid model of the leg then comprised of only 4 keypoints, 4 lines and 1 area. It may be noted that, after the construction lines and keypoints had been deleted, the numbering sequence of both these entities contained unused numbers. Therefore, the numbering of all entities was compressed, that is, renumbered to take advantage of these unused numbers. Although this operation is not essential, unless memory space is limited, it was considered useful in this situation to keep the model database tidy.

C.3 Primitives and the Working Plane

There are two different approaches to solid modelling using ANSYS which can, if necessary, be combined when building a model. The first approach is to build the solid model 'from the bottom up', where the user firstly defines keypoints, followed by lines, areas and then volumes. Alternatively, when building a solid model 'from the top down', geometric primitives (predefined lines, areas and volumes) can be defined directly without first having to define the lower order entities, which are created automatically by ANSYS. Any primitive area is defined on the active *working plane*, which is an imaginary plane that has an origin and a two-dimensional coordinate system. By default, this infinite plane is coincident to the global Cartesian coordinate system X-Y plane with its X and Y axes colinear with the global Cartesian X and Y axes.

These features were used to obtain the Y coordinate of keypoint 'J' before constructing the trimlines. A primitive rectangular area was firstly defined parallel to the Y-Z plane at an X coordinate corresponding to the distal trimline location. As this area would not lie on the default working plane, the working plane origin had to be moved to the required location and rotated about its Y axis by 90 ° relative to the original orientation prior to generating this area. The common region of intersection of the rectangular area and the leg surface area was then found using a Boolean intersect operation. In this situation the region of intersection was a line, hence a new line was generated at this intersection.

The rectangular area and its associated lower order entities were then deleted, as they were used for construction purposes only. Having obtained a line representing the cross-section of the leg at the distal trimline location, a point on this line with the minimum Y coordinate was then found by firstly defining a straight line parallel to the Y axis, and then constructing another straight line perpendicular to this line at one end and tangent to the cross-section line at the opposite end. Keypoint 'J' was then defined using the Y coordinate of the tangent point, and the auxiliary lines and keypoints were then deleted.

C.4 Boolean Operations

The ANSYS Boolean operations were found to be essential to the development of the finite element model. For example, the Boolean subtract command was used to divide the leg area at the dragged trimline areas to give the trimmed AFO. This operation generates new areas by subtracting regions of area intersection, although in this situation the regions of intersection of the leg area and the dragged trimline areas were lines. Therefore, the leg area was effectively divided in two at these lines such that the new areas were connected, sharing common lines at their intersection. After deleting the unwanted region of the leg area, along with the keypoints and lines attached to this area but not shared by the required AFO area, the model consisted of only one area with 4 keypoints and 4 lines located around

its boundary. The Boolean subtract operation was also used to divide the solid model of the AFO into smaller areas, after which it consisted of 28 keypoints, 43 lines and 16 areas.

Sometimes, ANSYS will encounter difficulties with certain Boolean operations, in which case it might be possible to work around the problem using a number of techniques. For example, if the Boolean operation includes more than two input entities, breaking the single operation into a series of operations involving fewer input entities might be successful. If failure occurs during a series of Boolean operations, changing the order that these operations are performed may sometimes work. Boolean operations can also be more efficient when performed using lower order entities. One problem that the user has to be aware of is that if solid modelling entities are not connected together correctly, which might be the case following a Boolean operation, problems will arise during mesh generation as the nodes along the boundaries will not be connected.

C.5 Meshing Controls

The element sizes in ANSYS can be specified in a variety of ways, including both local and global control of the element mesh. At a minimum the user only has to specify the allowable element shapes and midside node placement options, in which case ANSYS will generate the mesh using the default global element size specifications for every line. If this mesh is not adequate, the user can change the default values used by ANSYS before remeshing. This allows global control over such things as the maximum and minimum number of elements attached to a line, the maximum and minimum element edge lengths, the maximum spanned angle per element for curved lines, and the target aspect ratio, all using a single command [SASI, 1994b]. These defaults are used only when no other element size specification exists for a particular line. It is also possible to preview the default element sizes by transferring the divisions to the lines of the solid model, however before meshing these should be removed or they would take precedent over any

sizes defined at keypoints (see below) [SASI, 1994a].

The use of the default element sizes alone may not produce a satisfactory mesh in some cases, in which case the user must specify more controls over meshing. For example, the user can specify the number of element divisions (or element edge length) to be generated on all lines that have not had divisions defined directly using either of the methods discussed below. A more direct approach is to specify the edge length of elements nearest a particular keypoint, however this affects only the divisions adjacent to that keypoint for lines that have not been forced to have a specific number of divisions (see below). The element division at the other end of a particular line is determined from any other specifications that exist. It is also possible to specify a scale factor to apply to a previously defined element size at a keypoint, which is useful when performing mesh refinement manually.

Finally, the user can force a certain number of divisions on specified lines by specifying either the element edge length, the division arc (in degrees) spanned by element edges (except for straight lines, which always result in one division), or the number of element divisions along a line. When the element edge length or the division arc is specified, the number of divisions is automatically calculated from the line length and rounded upward to the next integer. The user may also specify the nominal spacing ratio for that line, which is simply the ratio of the last to first division sizes, although if assigned a negative value it represents the ratio of the centre division(s) to the end division sizes. All of these commands can be used together for total control over the mesh density, although if conflicting element sizes are specified with different commands a hierarchy is observed.

C.6 Loading

In ANSYS, the term *loads* is used to mean both boundary conditions and applied loading, and these loads are also classified as either nodal or element loads [SASI, 1994a]. *Nodal* loads, which include the DOF constraints and forces, are associated

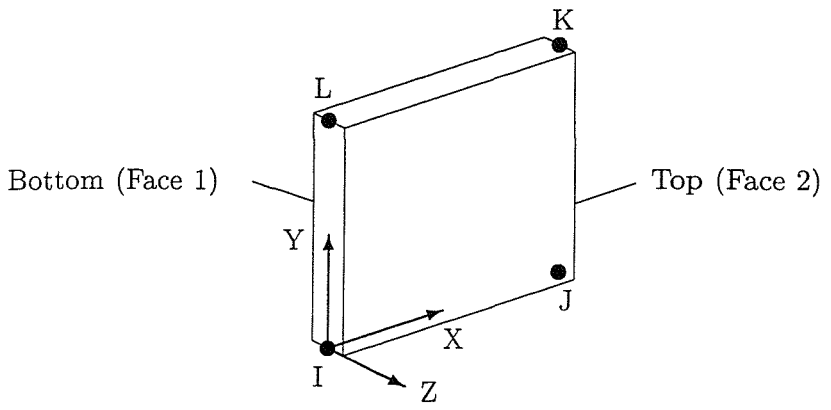

Figure C.1. Orientation of element coordinate system and surfaces

with a particular node and are defined relative to their nodal coordinate system. *Element* loads, which include surface loads, body loads and inertia loads, are associated with a particular element and are defined in terms of its element coordinate system. It should be noted that material properties are also defined with respect to the element coordinate system directions along which each property is measured. The procedure for carrying out an analysis using ANSYS differs slightly from that outlined in Section 3.1.2, as loads are applied to the finite element model in the *solution phase*, where the solution is obtained, although they may be specified in the preprocessing phase if preferred.

Surface loads can be applied to different faces of an element. The bottom surface of an element (face 1) is orientated so that a positive pressure applied to this face, that is, a pressure acting into the element, will be directed in the positive Z direction of the element coordinate system, which is also termed the positive normal direction [SASI, 1994c]. For shells, the default orientation of this coordinate system for each element is such that the X axis is directed from node 'I' toward node 'J', with the Z axis normal to the element surface at node 'I' such that the positive direction is determined by the right-hand rule around the element from node 'I' to 'J' to 'K' (see Figure C.1).

The top surface (face 2) is orientated such that a positive pressure applied to this face will be directed in the negative Z direction. The easiest method of

ascertaining the direction of the element coordinate system Z directions is to use an ANSYS feature that allows only those shell elements whose positive normals are directed toward (or alternatively away from) the viewing point to be displayed. If adjacent shell elements have inconsistent positive normal directions the stresses averaged at the nodes will be incorrect, although if the elements are generated by meshing an area the normal direction of all elements will be consistent [SASI, 1994a]. In this model, the top and bottom faces of every element were found to correspond to the inner and outer surfaces of the AFO respectively.

As the quantity of data that can be generated during solution for each substep of a non-linear analysis will be similar to that produced during a linear analysis, it may be necessary to restrict the amount before performing such an analysis. Therefore, after anticipating the data that will be of interest, controls may be used before solving to specify the frequency and type of results data to be written to the results file. For these analyses the nodal degree-of-freedom solution was requested for all substeps, although the default option to write all solution items for the last substep remained. Although this limited the type of results that could be viewed during postprocessing, it kept the size of the results file to an acceptable level.

C.7 Solution

ANSYS includes alternatives to the frontal solver which are more suitable for certain types of problem. The *Jacobi Conjugate Gradient (JCG) solver* differs from the frontal solver in that it assembles the full global stiffness matrix and obtains the nodal DOF by an iterative method. This approach is best suited to solving 3D scalar field problems involving large, sparse matrices. The *Preconditioned Conjugate Gradient (PCG) solver* is similar to the JCG solver but is well suited to many problems having sparse matrices, for example shell structures. It has the advantage of being 4 to 10 times faster than the JCG solver for structural solid and shell elements, but requires approximately twice as much memory during solution.

Comparing it to the frontal solver, it requires less than 1/4 of the disk space, with savings increasing with the size of the problem, but it can only be used for solving static and transient analyses and is only faster than the frontal solver for large models where the wavefront is greater than 1000. During the solution phase of a non-linear analysis, as well as specifying the analysis type and the equation solver to be used as in a linear analysis, additional *analysis options* must be specified. Large deformation and stress stiffening effects may be activated if appropriate, and the Newton-Raphson option can be specified if necessary to override the default setting.

C.8 Postprocessing

The results output calculated by ANSYS during the solution phase are categorised into two groups. The *primary data* consists of the degree-of-freedom solution calculated at each node, which, in a structural analysis, is the nodal displacements in each direction, and this data is also known as nodal solution data. The *Derived data* consists of the results derived at the integration points for each element from the primary data associated with that element. In a structural analysis this includes element stresses and strains, and this data is also known as element solution data, except when averaged at the nodes when it becomes nodal solution data. When plotted, the contours within each element are determined by linear interpolation from the nodal values, which are themselves extrapolated from the values at the element's integration points where they are usually most accurate [Cook, 1995].

During the solution process, primary data is stored relative to the nodal coordinate system, but the derived data is stored relative to the element coordinate system directions. It should be noted that, for postprocessing, these results are transformed into the active *results coordinate system* which is, by default, the global Cartesian coordinate system. It is possible to change the active results coordinate system to any existing local or global coordinate systems, or

alternatively the coordinate system used during the solution. This can be advantageous for models using shell elements, where the stresses make more sense when expressed in directions tangential and normal to the shell surface.

The ANSYS program contains two postprocessors, although the choice of which to use depends on the type of analysis performed. The most commonly used processor is the *general postprocessor*, where the results can be viewed over the entire model at a specific time, and this postprocessor may be used to review the results from a typical analysis in the form of stress contour plots, plots of deformed shape and tabular listings. If the value of time does not correspond to a substep, ANSYS will calculate the results by linear interpolation and they will therefore be less accurate. By default, ANSYS will automatically scale the displacements in all plots such that the maximum displacement displays as 5 % of the graphics window, which is useful when the deformation is small and the deformed and undeformed shapes are hard to differentiate. It is also possible to specify a user defined multiplication factor, however, with large displacement analyses, they are best scaled true to the model geometry.

For a dynamic or non-linear static analysis, the *time history postprocessor* may be used to review results at specific points in the model as a function of time in the form of graphs or tabular listings of one type of results data, or *variable*, against another. These variables must firstly be defined and assigned an arbitrary reference number, however time is defined by default. *Time* is a parameter used by ANSYS in both static and transient analyses for tracking purposes. In a transient analysis (or a rate-dependent static analysis) time represents actual chronological time, however in a rate-independent static analysis it simply represents a counter which can be used as an alternative method for identifying load steps and substeps. The term *time step* is used to represent the difference in time between two successive substeps. Once defined, a number of variables can be easily plotted against a single variable on the X axis, which defaults to time, although if the time at the end of the load step had been set equal to the magnitude of the applied loading, this axis would represent load.

Appendix D

ANSYS Files

D.1 Modelling the AFO

The following listing generates the solid model of the leg from the coordinate data. Comments are included in this, and subsequent, listings and are preceded by a comment character, which in ANSYS is an exclamation mark.

```
! Filename 'leg1.log' by Mark Arnold on 28/01/97
! Enter preprocessor
/PREP7
! Assign number of cross-sections to scalar parameter
numsect=17
! Assign number of points per section to scalar parameter
numpoint=4
! Dimension array parameter for coordinate data
*DIM,legdata,,numsect*numpoint,3
! Read in X coordinates into column of array parameter
! Note: a FORTRAN format specification follows the command
*VREAD,legdata(1,1),leg1,dat,/home/maa92me/ansys/logfiles/
(F7.1)
! Read in Y coordinates into column of array parameter
*VREAD,legdata(1,2),leg1,dat,/home/maa92me/ansys/logfiles/
(7X,F7.1)
! Read in Z coordinates into column of array parameter
*VREAD,legdata(1,3),leg1,dat,/home/maa92me/ansys/logfiles/
```

```
(14X,F7.1)
! Start of do-loop marking first row of data for each cross-section
*DO,loop,1,numsect*numpoint,4
! Define all keypoints on cross-section from coordinate data
K,,legdata(loop,1),legdata(loop,2),legdata(loop,3)+1
K,,legdata(loop+1,1),legdata(loop+1,2),legdata(loop+1,3)
K,,legdata(loop+2,1),legdata(loop+2,2),legdata(loop+2,3)
K,,legdata(loop+3,1),legdata(loop+3,2),legdata(loop+3,3)
K,,legdata(loop,1),legdata(loop,2),legdata(loop,3)-1
! End of do-loop
*ENDDO
! Define line from spline fit of keypoints
BSPLIN,1,2,3,4,5,,0,0,-1,0,0,1
! Repeat previous command and increment fields by specified values
*REPEAT,numsect,5,5,5,5,5
! Generate area by skinning surface through picked lines
FLST,2,numsect,4,ORDER,2
FITEM,2,1
FITEM,2,-numsect
ASKIN,P51X
! Select only lower order entities attached to selected area
ALLSEL,BELOW,AREA
! Invert currently selected set of lines
LSEL,INVE
! Invert currently selected set of keypoints
KSEL,INVE
! Delete selected construction lines
LDELE,ALL
! Delete selected construction keypoints
KDELE,ALL
! Reselect all entities
ALLSEL
! Compress numbering of all entities
NUMCMP,ALL
! Exit preprocessor
FINISH
```

The following is a listing of the three-dimensional coordinates of the data points representing the leg surface.

```
  64.0  300.0    0.0
   1.5  300.0   53.5
 -61.0  300.0   -2.0
   1.5  300.0  -57.0
  60.0  250.0    0.0
  -7.5  250.0   58.5
 -75.0  250.0   -1.0
```

```
 -7.5  250.0  -60.0
 53.5  200.0    0.0
-11.5  200.0   57.5
-76.5  200.0   -2.0
-11.5  200.0  -61.5
 44.0  150.0    0.0
-12.5  150.0   51.5
-69.0  150.0   -2.0
-12.5  150.0  -56.0
 36.5  100.0    0.0
-11.5  100.0   44.0
-59.5  100.0    0.0
-11.5  100.0  -44.5
 33.0   50.0    0.0
 -9.0   50.0   35.5
-51.0   50.0    1.0
 -9.0   50.0  -33.5
 35.0   28.0    0.0
 -6.5   25.0   30.5
-48.0   21.5    0.5
 -6.5   25.0  -29.5
 40.0   15.0    0.0
 -6.0    1.0   32.5
-52.0  -13.5    1.0
 -6.0    1.0  -31.0
 47.5    6.0    0.0
 -4.0  -21.0   27.5
-55.0  -48.5   -2.0
 -4.0  -21.0  -32.0
 57.0   -2.0    0.0
  2.0  -34.0   27.0
-52.5  -66.5   -3.5
  2.0  -34.0  -34.0
 67.0   -8.5    0.0
 13.0  -44.0   29.5
-40.5  -79.5   -2.0
 13.0  -44.0  -34.0
 77.5  -15.5    0.0
 27.5  -49.0   31.5
-22.5  -83.0   -1.5
 27.5  -49.0  -34.5
 87.5  -22.5    0.0
 44.0  -51.5   35.0
  0.0  -80.5    0.0
 44.0  -51.5  -35.0
 99.5  -30.0    0.0
 66.0  -53.5   40.5
 32.5  -77.0    2.0
 66.0  -53.5  -37.0
112.5  -37.0    0.0
 91.0  -59.0   45.5
```

```
  69.0  -80.5    3.0
  91.0  -59.0  -40.0
 126.0  -44.5    0.0
 116.0  -64.0   43.5
 105.5  -83.0    0.0
 116.0  -64.0  -43.0
 147.0  -51.0    0.0
 145.0  -65.0   35.0
 143.5  -79.5   -4.0
 145.0  -65.0  -43.0
```

The following listing generates the solid model of the AFO from the solid model of the leg.

```
! Filename 'trim1.log' by Mark Arnold on 15/11/96
! Enter preprocessor
/PREP7
! Assign distal trimline location to scalar parameter
distal=110
! Assign proximal trimline height to scalar parameter
proximal=260
! Assign calfband trimline length to scalar parameter
calfband=80
! Assign calfband trimline overlap to scalar parameter
overlap=30
! Assign ankle trimline arc radius to scalar parameter
radius=30
! Assign ankle joint clearance to scalar parameter
ankle=30
! Define keypoint 'A' from parameters
K,,-100,proximal,100
! Define keypoint 'B' from parameters
K,,overlap,proximal,100
! Define keypoint 'C' from parameters
K,,overlap,proximal-calfband,100
! Define keypoint 'D' from parameters
K,,0,proximal-calfband,100
! Define keypoint 'E' from parameters
K,,0,proximal-calfband-radius,100
! Define keypoint 'F' from parameters
K,,-radius,proximal-calfband-radius,100
! Define keypoint 'G' from parameters
K,,-radius,radius-ankle,100
! Define keypoint 'H' from parameters
K,,0,radius-ankle,100
! Define keypoint 'I' from parameters
K,,0,-ankle,100
```

```
! Move working plane origin to distal trimline location
WPAVE,distal,0,0
! Rotate working plane 90 degrees about its Y axis
WPROTA,0,0,-90
! Create rectangular area on working plane
RECTNG,100,-100,KY(13),-100
! Reset working plane to default location
WPSTYL,DEFA
! Specify boolean operation option to keep input entities
BOPTN,KEEP,YES
! Find common intersection of leg area and rectangle (a line)
AINA,1,2
! Delete rectangular area and associated lower order entities
ADELE,2,,,1
! Define keypoints for straight line
K,,distal,KY(13),-100
K,,distal,-100,-100
! Define straight line parallel to Y axis
LSTR,14,15
! Generate line at specified angles to two existing lines
L2ANG,9,5,0,90
! Define keypoint 'J' from coordinates of tangent point
K,,KX(16),KY(16),100
! Delete construction lines and associated keypoints
LDELE,5,9,,1
! Compress numbering of all entities
NUMCMP,ALL
! Define straight line representing proximal trimline
LSTR,5,6
! Define straight line representing calfband trimline
LSTR,6,7
! Define circular arc and straight lines representing
! calf trimline
LSTR,7,8
LARC,8,10,9,radius
LSTR,10,11
! Define circular arc representing ankle trimline
LARC,11,13,12,radius
! Define line tangent to end of ankle trimline to represent
! foot/distal trimline
LTAN,10,14
! Extend above line at keypoint 'J'
LEXTND,11,14,10,0
! Define keypoints and straight line for drag path
K,9,0,radius-ankle,-100
LSTR,9,12
! Combine adjacent lines into one line
LCOMB,7,8,0
! Drag picked trimlines parallel to drag path to generate areas
FLST,2,6,4,ORDE,4
FITEM,2,5
```

```
FITEM,2,-7
FITEM,2,9
FITEM,2,-11
ADRAG,P51X,,,,,,12
! Delete drag path and associated keypoints
LDELE,12,,,1
! Specify Boolean operation option to delete input entities
BOPTN,KEEP,NO
! Subtract picked trimline areas from solid model of leg
FLST,3,6,5,ORDE,2
FITEM,3,2
FITEM,3,-7
ASBA,1,P51X
! Delete excess part of solid model of leg and associated
! lower order entities
ADELE,9,,,1
! Compress numbering of all entities
NUMCMP,ALL
! Create rectangular dividing areas on working plane whilst
! rotating it and moving its origin to various locations
RECTNG,-100,distal+10,-100,proximal+10
WPROTA,0,0,-90
RECTNG,100,-100,0,-100
RECTNG,100,-100,proximal+10,proximal-calfband-10
WPAVE,distal/2,0,0
RECTNG,100,-100,0,-100
WPAVE,0,radius-ankle,0
WPROTA,0,-45,0
RECTNG,100,-100,-200,10-radius
WPROTA,0,-45,0
RECTNG,100,-100,-100,10-radius
WPAVE,0,(proximal-calfband-ankle)/2,0
RECTNG,100,-100,-100,10-radius
WPAVE,0,proximal-calfband-radius,0
RECTNG,100,-100,-100,10-radius
! Reset working plane to default location
WPSTYL,DEFA
! Subtract picked dividing areas from solid model of AFO
FLST,3,8,5,ORDE,2
FITEM,3,2
FITEM,3,-9
ASBA,1,P51X
! Compress numbering of all entities
NUMCMP,ALL
! Exit preprocessor
FINISH
```

The following listing generates the first mesh of the AFO consisting of 1848 nodes and 597 elements.

```
! Filename 'mesh1.log' by Mark Arnold on 18/11/96
! Enter preprocessor
/PREP7
! Define element type from element library
ET,1,SHELL93
! Define set of element real constants (element thickness)
R,1,2
! Define set of constant, linear, isotropic material properties
! Young's modulus
MP,EX,1,1000
! Poisson's ratio
MP,NUXY,1,0.35
! Specify controls on default element sizes
DESIZE,,3,15,,30,,15,1,4
! Generate mesh of nodes and elements within areas
AMESH,ALL
! Exit preprocessor
FINISH
```

D.2 Static Analyses

D.2.1 Linear Static Analyses

The following listing performs the linear static analysis with the AFO subjected to a single imposed nodal displacement.

```
! Filename 'linear1.log' by Mark Arnold on 15/11/96
! Enter preprocessor
/PREP7
! Activate global cylindrical coordinate system
CSYS,1
! Assign node number at keypoint where nodal
! displacement is to be applied to scalar parameter
nodenumb=NODE(KX(5),KY(5),KZ(5))
! Rotate nodal coordinate system of above node
! into active coordinate system
NROTAT,nodenumb
! Activate global spherical coordinate system
CSYS,2
! Select 4 areas at heel region of model
FLST,5,4,5,ORDE,2
FITEM,5,9
```

```
FITEM,5,-12
ASEL,S, , ,P51X
! Select nodes associated with selected areas
NSLA,,1
! Group selected nodes at heel region into a component
CM,heel,NODE
! Rotate nodal coordinate system of selected
! nodes into active coordinate system
NROTAT,ALL
! Reselect all entities
ALLSEL
! Rotate working plane 90 degrees about its X axis
WPROTA,0,90,0
! Define new local cylindrical coordinate system
! at the working plane origin
CSWPLA,11,1
! Select 2 areas at posterior calfband region of model
FLST,5,2,5,ORDE,2
FITEM,5,15
FITEM,5,-16
ASEL,S, , ,P51X
! Select nodes associated with selected areas
NSLA,,1
! Group selected nodes at calfband region into a component
CM,calfband,NODE
! Rotate nodal coordinate system of selected
! nodes into active coordinate system
NROTAT,ALL
! Reselect all entities
ALLSEL
! Restore global Cartesian coordinate system
CSYS,0
! Reset working plane to default location
WPSTYLE,DEFA
! Exit preprocessor
FINISH
! Enter solution phase
/SOLU
! Specify a new, static analysis
ANTYPE,STATIC,NEW
! Select components of nodes in calfband and heel
! regions where radial constraints are to be applied
CMSEL,S,calfband
CMSEL,A,heel
! Apply constraints at all selected nodes in
! nodal X coordinate directions
D,ALL,UX,0
! Reselect all entities
ALLSEL
! Assign imposed angular displacement about
! ankle joint axis to scalar parameter
```

```
! (-ve plantar flexion/ +ve dorsiflexion)
degrees=-5
! Assign distance of node from global
! origin to scalar parameter
distance=SQRT(NX(nodenumb)**2+NY(nodenumb)**2)
! Apply imposed displacement to node in
! nodal Y coordinate direction
D,nodenumb,UY,distance*degrees*2*PI/360
! Initiate solution procedure
SOLVE
! Exit solution phase
FINISH
! Save database to a file
SAVE
```

The following listing performs the linear static analysis with the AFO subjected to a constant pressure applied to two areas.

```
! Filename 'linear3.log' by Mark Arnold on 19/11/96
! Enter preprocessor
/PREP7
! Calculate geometry statistics for all areas
ASUM
! Activate global spherical coordinate system
CSYS,2
! Select 4 areas at heel region of model
FLST,5,4,5,ORDE,2
FITEM,5,9
FITEM,5,-12
ASEL,S, , ,P51X
! Select nodes associated with selected areas
NSLA,,1
! Group selected nodes at heel region into a component
CM,heel,NODE
! Rotate nodal coordinate system of selected
! nodes into active coordinate system
NROTAT,ALL
! Reselect all entities
ALLSEL
! Rotate working plane 90 degrees about its X axis
WPROTA,0,90,0
! Define new local cylindrical coordinate system
! at the working plane origin
CSWPLA,11,1
! Select 2 areas at posterior calfband region of model
FLST,5,2,5,ORDE,2
FITEM,5,15
```

```
FITEM,5,-16
ASEL,S, , ,P51X
! Select nodes associated with selected areas
NSLA,,1
! Group selected nodes at calfband region into a component
CM,calfband,NODE
! Rotate nodal coordinate system of selected
! nodes into active coordinate system
NROTAT,ALL
! Reselect all entities
ALLSEL
! Restore global Cartesian coordinate system
CSYS,0
! Reset working plane to default location
WPSTYLE,DEFA
! Exit preprocessor
FINISH
! Enter solution phase
/SOLU
! Specify a new, static analysis
ANTYPE,STATIC,NEW
! Select components of nodes in calfband and heel
! regions where radial constraints are to be applied
CMSEL,S,calfband
CMSEL,A,heel
! Apply constraints at all selected nodes in
! nodal X coordinate directions
D,ALL,UX,0
! Reselect all entities
ALLSEL
! Apply constraint to an arbitrary node in
! nodal Z coordinate direction
D,NODE(KX(23),KY(23),KZ(23)),UZ,0
! Retrieve surface areas of two distal
! foot areas and store in scalar parameter
*GET,area1,AREA,1,AREA
*GET,area2,AREA,2,AREA
! Assign sum of surface areas to scalar parameter
areatotl=area1+area2
! Assign previously calculated total nodal reaction force
! to scalar parameter
reaction=46.556
! Assign pressure magnitude to scalar parameter
pressure=reaction/areatotl
! Apply surface pressure on face of two distal foot areas
! (face 1 = outer/ face 2 = inner)
SFA,1,2,PRES,pressure
SFA,2,2,PRES,pressure
! Initiate solution procedure
SOLVE
! Exit solution phase
```

```
FINISH
! Save database to a file
SAVE
```

The following listing performs the linear static analysis with the AFO subjected to imposed displacements over a patch of nodes and revised heel constraints.

```
! Filename 'linear7.log' by Mark Arnold on 21/10/97
! Enter preprocessor
/PREP7
! Select two distal foot areas and associated
! lines, keypoints, nodes and elements
ASEL,S,AREA,,1,2,(2-1),1
! Reselect from these nodes only those within a
! specified distance from the X-Y plane
NSEL,R,LOC,Z,KZ(8)/2,KZ(6)/2
! Group selected nodes at foot region into a component
CM,foot,NODE
! Activate global cylindrical coordinate system
CSYS,1
! Rotate nodal coordinate system of selected
! nodes into active coordinate system
NROTAT,ALL
! Reselect all entities
ALLSEL
! Define local Cartesian coordinate system at ankle
! trimline centre rotated 45 degrees about Z axis
LOCAL,21,0,,radius-ankle,,45,0,0
! Select nodes at heel region that are further than a
! specified distance away from ankle trimline
NSEL,S,LOC,X,(KX(23)-radius)/2,-300
! Group selected nodes at heel region into a component
CM,heel,NODE
! Activate global spherical coordinate system
CSYS,2
! Rotate nodal coordinate system of selected
! nodes into active coordinate system
NROTAT,ALL
! Reselect all entities
ALLSEL
! Rotate working plane 90 degrees about its X axis
WPROTA,0,90,0
! Define new local cylindrical coordinate system
! at the working plane origin
CSWPLA,11,1
! Select 2 areas at posterior calfband region of model
FLST,5,2,5,ORDE,2
```

```
FITEM,5,15
FITEM,5,-16
ASEL,S, , ,P51X
! Select nodes associated with selected areas
NSLA,,1
! Group selected nodes at calfband region into a component
CM,calfband,NODE
! Rotate nodal coordinate system of selected
! nodes into active coordinate system
NROTAT,ALL
! Reselect all entities
ALLSEL
! Restore global Cartesian coordinate system
CSYS,0
! Reset working plane to default location
WPSTYLE,DEFA
! Exit preprocessor
FINISH
! Enter solution phase
/SOLU
! Specify a new, static analysis
ANTYPE,STATIC,NEW
! Select components of nodes in calfband and heel
! regions where radial constraints are to be applied
CMSEL,S,calfband
CMSEL,A,heel
! Apply constraints at all selected nodes in
! nodal X coordinate directions
D,ALL,UX,0
! Reselect all entities
ALLSEL
! Assign imposed angular displacement about
! ankle joint axis to scalar parameter
! (-ve plantar flexion/ +ve dorsiflexion)
degrees=-5
! Select component of nodes in foot region
CMSEL,S,foot
! Retrieve number of selected nodes and store in
! scalar parameter
*GET,numnodes,NODE,,COUNT
! Retrieve lowest selected node number and store
! in scalar parameter
*GET,lownode,NODE,,NUM,MIN
! Set starting node number
nodenumb=lownode
! Start of do-loop to apply constraints
*DO,loop,1,numnodes
! Assign distance of node from global
! origin to scalar parameter
distance=SQRT(NX(nodenumb)**2+NY(nodenumb)**2)
! Apply imposed displacement to node in
```

```
! nodal Y coordinate direction
D,nodenumb,UY,distance*degrees*2*PI/360
! Increment node number to that of next selected node
nodenumb=NDNEXT(nodenumb)
! End of do-loop
*ENDDO
! Reselect all entities
ALLSEL
! Initiate solution procedure
SOLVE
! Exit solution phase
FINISH
! Save database to a file
SAVE
```

D.2.2 Mesh Refinement

The following listing generates the second mesh of the AFO consisting of 1708 nodes and 549 elements.

```
! Filename 'mesh2.log' by Mark Arnold on 21/11/96
! Enter preprocessor
/PREP7
! Define element type from element library
ET,1,SHELL93
! Define set of element real constants (element thickness)
R,1,2
! Define set of constant, linear, isotropic material properties
! Young's modulus
MP,EX,1,1000
! Poisson's ratio
MP,NUXY,1,0.35
! Specify controls on default element sizes
DESIZE,,3,15,,30,,,1,4
! Transfer default element divisions to lines
LESIZE,ALL
! Scale existing element sizes at keypoints by factors
KESIZE,19,,,0.5
KESIZE,21,,,0.5
KESIZE,25,,,0.75
KESIZE,26,,,0.75
KESIZE,6,,,0.5
KESIZE,7,,,0.7
KESIZE,8,,,0.7
! Remove element divisions from all lines
```

```
LESIZE,ALL,,,-1,,1
! Force specified number of element divisions on lines
LESIZE,10,,,3
LESIZE,1,,,3
LESIZE,13,,,3
LESIZE,2,,,3
LESIZE,8,,,2
LESIZE,9,,,2
LESIZE,11,,,2
LESIZE,12,,,2
! Generate mesh of nodes and elements within areas
AMESH,9,14
AMESH,1,2
AMESH,7,8
AMESH,5,6
AMESH,15,16
AMESH,3,4
! Exit preprocessor
FINISH
```

The following listing generates the fifth mesh of the AFO consisting of 5028 nodes and 1667 elements.

```
! Filename 'mesh5.log' by Mark Arnold on 27/11/96
! Enter preprocessor
/PREP7
! Define element type from element library
ET,1,SHELL93
! Define set of element real constants (element thickness)
R,1,2
! Define set of constant, linear, isotropic material properties
! Young's modulus
MP,EX,1,1000
! Poisson's ratio
MP,NUXY,1,0.35
! Specify controls on default element sizes
DESIZE,,3,15,,30,,,1,4
! Transfer default element divisions to lines
LESIZE,ALL
! Scale existing element sizes at keypoints by factors
KESIZE,14,,,0.6
KESIZE,15,,,0.175
KESIZE,17,,,0.6
KESIZE,13,,,0.675
KESIZE,16,,,0.7
KESIZE,18,,,0.675
KESIZE,19,,,0.094
```

```
KESIZE,20,,,0.263
KESIZE,21,,,0.094
KESIZE,25,,,0.7
KESIZE,26,,,0.55
KESIZE,27,,,0.7
KESIZE,6,,,0.4
KESIZE,7,,,0.65
KESIZE,8,,,0.4
KESIZE,5,,,0.8
! Remove element divisions from all lines
LESIZE,ALL,,,-1,,1
! Force specified number of element divisions on lines
LESIZE,10,,,3
LESIZE,1,,,3
LESIZE,13,,,3
LESIZE,2,,,3
LESIZE,8,,,2
LESIZE,9,,,2
LESIZE,11,,,2
LESIZE,12,,,2
! Generate mesh of nodes and elements within areas
AMESH,9,14
AMESH,1,2
AMESH,7,8
AMESH,5,6
AMESH,15,16
AMESH,3,4
! Exit preprocessor
FINISH
```

D.2.3 Non-linear Static Analyses

The following listing performs the static analysis incorporating combined geometric and material non-linearities with the AFO subjected to a constant pressure applied to two areas.

```
! Filename 'comb3.log' by Mark Arnold on 04/12/96
! Enter preprocessor
/PREP7
! Calculate geometry statistics for all areas
ASUM
! Activate global spherical coordinate system
CSYS,2
! Select 4 areas at heel region of model
FLST,5,4,5,ORDE,2
```

```
FITEM,5,9
FITEM,5,-12
ASEL,S, , ,P51X
! Select nodes associated with selected areas
NSLA,,1
! Group selected nodes at heel region into a component
CM,heel,NODE
! Rotate nodal coordinate system of selected
! nodes into active coordinate system
NROTAT,ALL
! Reselect all entities
ALLSEL
! Rotate working plane 90 degrees about its X axis
WPROTA,0,90,0
! Define new local cylindrical coordinate system
! at the working plane origin
CSWPLA,11,1
! Select 2 areas at posterior calfband region of model
FLST,5,2,5,ORDE,2
FITEM,5,15
FITEM,5,-16
ASEL,S, , ,P51X
! Select nodes associated with selected areas
NSLA,,1
! Group selected nodes at calfband region into a component
CM,calfband,NODE
! Rotate nodal coordinate system of selected
! nodes into active coordinate system
NROTAT,ALL
! Reselect all entities
ALLSEL
! Restore global Cartesian coordinate system
CSYS,0
! Reset working plane to default location
WPSTYLE,DEFA
! Exit preprocessor
FINISH
! Enter solution phase
/SOLU
! Specify a new, static analysis
ANTYPE,STATIC,NEW
! Select components of nodes in calfband and heel
! regions where radial constraints are to be applied
CMSEL,S,calfband
CMSEL,A,heel
! Apply constraints at  all selected nodes in
! nodal X coordinate directions
D,ALL,UX,0
! Reselect all entities
ALLSEL
! Apply constraint to an arbitrary node in
```

```
! nodal Z coordinate direction
D,NODE(KX(23),KY(23),KZ(23)),UZ,0
! Retrieve surface areas of two distal
! foot areas and store in scalar parameter
*GET,area1,AREA,1,AREA
*GET,area2,AREA,2,AREA
! Assign sum of surface areas to scalar parameter
areatotl=area1+area2
! Assign previously calculated total nodal reaction force
! to scalar parameter
reaction=46.556
! Assign pressure magnitude to scalar parameter
pressure=reaction/areatotl
! Apply surface pressure on face of two distal foot areas
! (face 1 = outer/ face 2 = inner)
SFA,1,2,PRES,pressure
SFA,2,2,PRES,pressure
! Material non-linearity
! Re-define Young's modulus
MP,EX,1,1390
! Activate data table for multilinear elasticity
TB,MELAS,1,,8,0
! Define data points for stress-strain curve
TBPT,,48e-4,6.67
TBPT,,72E-4,9.23
TBPT,,100E-4,11.4
TBPT,,140E-4,13.62
TBPT,,200E-4,15.85
TBPT,,268E-4,17.80
TBPT,,360E-4,19.80
TBPT,,468E-4,21.58
! Geometric non-linearity
! Include large deformation effects
NLGEOM,ON
! Set time at end of load step equal to pressure magnitude
TIME,pressure
! Specify initial, maximum and minimum number of substeps
NSUBST,5,10,3
! Use automatic time stepping
AUTOTS,ON
! Activate predictor for initial equilibrium iteration
! of each substep after the first
PRED,ON
! Write nodal DOF solution to results file for every substep
OUTRES,NSOL,ALL
! Initiate solution procedure
SOLVE
! Exit solution phase
FINISH
! Save database to a file
SAVE
```

D.3 Postprocessing Macros

The following macro listing calculates the rotation about the global Z axis of the node at the middle of the distal trimline. It is valid for all the analyses outlined in Chapter 4.

```
! Macro for calculating rotation about ankle joint axis
! Set results coordinate system to Global Cartesian
RSYS,0
! Assign node number at centre of distal foot
! trimline to scalar parameter
node=NODE(KX(5),KY(5),KZ(5))
! Define one dimensional array parameters for vectors
*DIM,vectorA,,2
*DIM,vectorB,,2
*DIM,vectorU,,2
! Prompt user to input number of result substeps
*ASK,steps,NUMBER OF STEPS,1
! Define one dimensional array parameter for angles
*DIM,vectorT,,steps
! Assign undeformed coordinates of node to vector
vectorA(1)=NX(node),NY(node)
! Calculate magnitude of undeformed position vector
magA=SQRT(vectorA(1)**2+vectorA(2)**2)
! Set units for angular functions to degrees
*AFUN,DEG
! Start of do-loop to calculate angle at each substep
*DO,loop,1,steps
! Read data set from results file for substep
SET, , , , , , ,loop
! Assign nodal displacement components to vector
vectorU(1)=UX(node),UY(node)
! Add vectors to give deformed coordinates of node
*VOPER,vectorB(1),vectorA(1),ADD,vectorU(1)
! Calculate magnitude of deformed position vector
magB=SQRT(vectorB(1)**2+vectorB(2)**2)
! Calculate angle of rotation for this substep
cross=vectorA(1)*vectorB(2)-vectorA(2)*vectorB(1)
vectorT(loop)=ASIN(cross/(magA*magB))
! End of do-loop
*ENDDO
! List angles held in array parameter
*STATUS,vectorT
```

The following macro listing calculates the moment generated about the global Z

axis by the nodal reaction forces at the displaced nodes. It is valid for most of the linear analyses outlined in Chapter 4.1.

```
! Macro for calculating moment about ankle joint axis
! Select component of nodes in foot region
CMSEL,S,foot
! Retrieve number of selected nodes and store in
! scalar parameter
*GET,numnodes,NODE,,COUNT
! Retrieve lowest selected node number and store
! in scalar parameter
*GET,lownode,NODE,,NUM,MIN
! Set starting node number
node=lownode
! Define array parameters
*DIM,distance,,numnodes
*DIM,reaction,,steps,numnodes
*DIM,reac2,,numnodes,steps
*DIM,displace,,steps,numnodes
*DIM,disp2,,numnodes,steps
*DIM,mom_arm,,numnodes,steps
*DIM,moment,,numnodes,steps
*DIM,moment2,,steps
! Start of do-loop for each node
*DO,loop,1,numnodes
! Assign distance of node from global
! origin to scalar parameter
distance(loop)=SQRT(NX(node)**2+NY(node)**2)
! Store reaction force for node in variable
RFORCE,2,node,F,Y
! Move reaction data into array parameter vector
VGET,reaction(1,loop),2
! Store nodal displacement in variable
NSOL,3,node,U,X
! Move displacement data into array parameter matrix
VGET,displace(1,loop),3
! Increment node number to that of next selected node
node=NDNEXT(node)
! End of do-loop
*ENDDO
! Transpose array parameter matrices
*MFUN,reac2(1,1),TRAN,reaction(1,1)
*MFUN,disp2(1,1),TRAN,displace(1,1)
! Start of do-loop for each step
*DO,loop,1,steps
! Add array parameter elements to give moment arm
*VOPER,mom_arm(1,loop),distance(1),ADD,disp2(1,loop)
! Multiply array parameter elements to give moment
*VOPER,moment(1,loop),mom_arm(1,loop),MULT,reac2(1,loop)
```

```
! Sum nodal moments in array to give total moment
*VSCFUN,moment2(loop),SUM,moment(1,loop)
! End of do-loop
*ENDDO
! Reselect all entities
ALLSEL
! List moments held in array parameter
*STATUS,moment2
```

Glossary

Below is an explanation of the directional terms used to explain the location of various body structures relative to each other, terms used to discuss the structural plan of the human body with respect to the planes that pass through it, and terms used to describe movement at synovial (freely movable) joints [Tortora & Grabowski, 1993]. The anatomical position is where the subject is standing erect and facing the observer, the upper extremities are placed at the sides, and the palms of the hands are turned forward. Terms describing types of deformity and other miscellaneous terms used in the text are also explained [World Book Inc., 1988].

Abduction	Movement of a bone away from the midline.
Adduction	Movement of a bone toward the midline.
Anterior	Nearer to or at the front of the body.
Distal	Farther from the attachment of an extremity to the trunk or a structure.
Dorsiflexion	Bending of the foot in the direction of the upper surface (dorsum).
Eversion	Movement of the sole of the foot outward so that the soles face away from each other.

Extension	Involves an increase in the angle between the surfaces of articulating bones.
Flexion	Involves a decrease in the angle between the surfaces of articulating bones.
Frontal	A vertical plane that divides the body into anterior and posterior portions.
Hyperextension	Continuation of extension beyond the anatomical position.
Inferior	Away from the head or toward the lower part of a structure.
Inversion	Movement of the sole of the foot inward so that the soles face toward each other.
Lateral	Farther from the midline of the body or a structure.
Ligament	Tough, fibrous tissue restricting movement in joints and connecting bones.
Malleolus	Bony protrusion at the distal end of the tibia and fibula.
Medial	Nearer to the midline of the body or a structure.
Midsagittal	A vertical plane passing through the midline of the body and dividing it into equal right and left sides.
Oblique	A plane passing through the body at an angle between the transverse plane and either of the other planes.
Plantar flexion	Bending of the foot in the direction of the sole (plantar surface).
Posterior	Nearer to or at the back of the body.
Proximal	Nearer to the attachment of an extremity to the trunk or a structure.
Sagittal	A plane parallel to the midsagittal plane that divides the body into unequal left and right portions.

Superior	Toward the head or the upper part of a structure.
Tendon	Tough tissue attaching a muscle to a bone.
Transverse	A plane parallel to the ground (horizontal) that divides the body into superior and inferior portions.
Valgus	A deformity where part of the body bends outwards from the midline.
Varus	A deformity where part of the body bends inwards from the midline.

Bibliography

ABU-HASABALLAH K.S., NOWAK M.D. & COOPER P.D., 1997. Enhanced Solid Ankle-Foot Orthosis Design: Real-Time Contact Pressures Evaluation and Finite Element Analysis. *ASME Bioengineering Division (Publication)*, 36, 285–286.

ANDERSON D.M. & MEADOWS C.B., 1979. Some Influences on the Design and Production of Polypropylene Ankle-Foot Orthoses for the Young Cerebral Palsied Child. *In:* R.M. KENEDI, J.P. PAUL & J. HUGHES, eds. *Disability.* London: Macmillan, 462–470.

ANSYS, INC., 1995. *ANSYS Structural Nonlinearities User's Guide for Revision 5.1 — Volume II.* Houston.

ARNOLD M.A., 1995. *Investigation into the Design and Function of the Ankle Foot Orthosis (AFO).* Report No. SP33 94/95. Department of Mechanical Engineering, University of Southampton, UK.

BENHAM P.P. & CRAWFORD R.J., 1987. *Mechanics of Engineering Materials.* England: Longman Scientific & Technical.

BIRLEY A.W. & SCOTT M.J., 1982. *Plastic Materials: Properties and Applications.* Glasgow: Leonard Hill.

BOONE D.A., HARLAN J.S. & BURGESS E.M., 1994. Automated fabrication of mobility aids: Review of the AFMA process and VA/Seattle ShapeMaker software design. *Journal of Rehabilitation Research and Development*, 31(1), 42–49.

BORESI A.P., SCHMIDT R.J. & SIDEBOTTOM O.M., 1993. *Advanced Mechanics of Materials*, Fifth Edition. New York: John Wiley & Sons, Inc.

BOWKER J.H. & HALL C.B., 1975. Normal Human Gait. *In:* AMERICAN ACADEMY OF ORTHOPAEDIC SURGEONS. *Atlas of Orthotics: Biomechanical Principles and Applications.* Saint Louis: The C.V. Mosby Company.

BRITISH STANDARDS INSTITUTION, 1980. *BS 5848: 1980 — Numbering of Divisions and Subdivisions in Written Documents (point-numbering).* London.

BRITISH STANDARDS INSTITUTION, 1989. *BS 1629: 1989 — British Standard Recommendations for References to Published Material.* London.

BRITISH STANDARDS INSTITUTION, 1990. *BS 4821: 1990 — Recommendations for the Presentation of Theses and Dissertations.* London.

BUCKNALL C.B. & PAGE C.J., 1982. Rubber-toughening of Plastics, Part 6: Effects of Rubber Particles on the Kinetics of Creep in Polypropylene. *Journal of Materials Science*, 17(3), 808–816.

CALLISTER W.D., 1991. *Materials Science and Engineering: An Introduction*, Second Edition. Chichester: John Wiley & Sons, Inc.

CHOWANIEC Z., ANDERSON W.F., THOMSON A., JACOBS N., NICOL A.C. & BERME N., 1979. Use of Plastic Ankle-Foot Orthoses in the Rehabilitation of the Elderly Hemiplegic. *In:* R.M. KENEDI, J.P. PAUL & J. HUGHES, eds. *Disability.* London: Macmillan, 450–461.

CHU T.M., REDDY N.P., & PADOVAN J., 1995. Three-Dimensional Finite Element Stress Analysis of the Polypropylene, Ankle-Foot Orthosis: Static Analysis. *Medical Engineering and Physics*, 17(5), 372–379.

CHU T., 1995. Experimental Validation on Finite Element Stress Analysis of a Polymeric Orthotic Device. *Proceedings of the Annual International Conference of the IEEE, Engineering in Medicine and Biology, Montreal, September 1995*, 1259–1260.

CONDIE D.N. & MEADOWS C.B., 1977. Some Biomechanical Considerations in the Design of Ankle-Foot Orthoses. *Orthotics and Prosthetics*, 31(3), 45–52.

COOK R.D., MALKUS D.S. & PLESHA M.E., 1989. *Concepts and Applications of Finite Element Analysis*, Third Edition. Chichester: John Wiley & Sons.

COOK R.D., 1995. *Finite Element Modeling for Stress Analysis.* Chichester: John Wiley & Sons, Inc.

CZERNIECKI J.M., 1988. Foot and Ankle Biomechanics in Walking and Running: A Review. *American Journal of Physical Medicine and Rehabilitation*, 67, 246–252.

DATOO M.H., 1991. *Mechanics of Fibrous Composites.* London: Elsevier Applied Science.

DIXON-STUBBS P.J., 1981. Creep Behaviour of Polyethylene and Polypropylene. *Journal of Materials Science*, 16(2), 389–396.

ENGEN T.J., 1972. The TIRR Polypropylene Orthoses. *Orthotics and Prosthetics*, 26, 1–15.

FAGAN M.J., 1992. *Finite Element Analysis: Theory and Practice.* England: Longman Scientific & Technical.

FOLEY J.D., VAN DAM A., FEINER S.K. & HUGHES J.F., 1990. *Computer Graphics: Principles and Practice*, Second Edition. Wokingham: Addison-Wesley Publishing Company.

GOLAY W., LUNSFORD T., LUNSFORD B.R. & GREENFIELD J., 1989. The Effect of Malleolar Prominence on Polypropylene AFO Rigidity and Buckling. *Journal of Prosthetics and Orthotics*, 1(4), 231–241.

GOTHAM K.V., 1974. Long-Term Durability. *In:* R.M. OGORKIEWICZ, ed. *Thermoplastics: Properties and Design.* London: John Wiley & Sons.

HALAR E. & CARDENAS D.D., 1987. Ankle-Foot Orthoses: Clinical Implications. *Physical Medicine and Rehabilitation: State of the Art Reviews*, 1(1), 45–66.

HARTMANN B., 1980. Ultrasonic Measurements. *In:* R.A. FAVA, ed. *Methods of Experimental Physics, Volume 16: Polymers — Part C: Physical Properties*, 59–90. London: Academic Press.

HKS (HIBBIT, KARLSSON & SORENSEN, INC.), 1994. *ABAQUS/Pre User's Manual, Version 5.4 — Volume I*, Second Edition. USA.

HKS (HIBBIT, KARLSSON & SORENSEN, INC.), 1996. *Getting Started with ABAQUS/Standard.* USA.

HICKS J.E., LEONARD J.A., NELSON V.S., FISHER S.T. & ESQUENAZI A., 1989. Prosthetics, Orthotics, and Assistive Devices. 4. Orthotic Management of Selected Disorders. *Archives of Physical Medicine and Rehabilitation*, 70(5), S210–S217.

ICI (IMPERIAL CHEMICAL INDUSTRIES), 1980. *Plastics — Presentation & Use of Data on the Mechanical Properties of Thermoplastics: Technical service note G123*, Third Edition. Hertfordshire: ICI Petrochemicals and Plastics Division.

ICI (IMPERIAL CHEMICAL INDUSTRIES). *Propathene Polypropylene P1/1 — Properties of 'Propathene'.* ICI Chemicals and Polymers.

ITALIANO K., MACEDO C., VERANIS S. & CALLAHAN K., 1986. Techniques of Weight Reduction of Polypropylene Ankle Foot Orthosis. *Proceedings of the Ninth Annual Conference on Rehabilitation Technology, Minneapolis, USA, 23–26 June 1986*, 126–128.

JEBSEN R.H., SIMONS B.C. & CORCORAN P.J., 1968. Experimental Plastic Short Leg Brace. *Archives of Physical Medicine and Rehabilitation*, 49, 108–109.

KERNIGHAN B.W. & RITCHIE D.M., 1988. *The C Programming Language*, Second Edition. New Jersey: Prentice Hall.

KLASSON B., CONVERY P. & RASCHKE S., 1998. Test apparatus for the measurement of the flexibility of ankle-foot orthoses in planes other than the loaded plane. *Prosthetics and Orthotics International*, 22(1), 45–53.

LAM P.C., REDDY N.P. & DOWNING M., 1986a. Effects of Heel and Toe Forces on Ankle-Foot Orthoses Design using Finite Element Analysis. *American Society of Mechanical Engineers, Design Engineering Division (Publication)*, 1, 49–52.

LAM P.C., REDDY N.P. & DOWNING M., 1986b. Dynamic Responses of Ankle-Foot Orthoses. *American Society of Mechanical Engineers, Bioengineering Division (Publication)*, 2, 130–131.

LeBLANC M.A., 1972. A Clinical Evaluation of Four Lower-Limb Orthoses. *Orthotics and Prosthetics*, 26(1), 27–41.

LEHMANN J.F., 1979. Biomechanics of Ankle-Foot Orthoses: Prescription and Design. *Archives of Physical Medicine and Rehabilitation*, 60, 200–207.

LEHMANN J.F., ESSELMAN P.C., KO M.J., SMITH J.C., deLATEUR B.J. & DRALLE A.J., 1983. Plastic Ankle-Foot Orthoses: Evaluation of Function. *Archives of Physical Medicine and Rehabilitation*, 64, 402–407.

LEHMANN J.F., CONDON S.M., PRICE R. & deLATEUR B.J., 1987. Gait Abnormalities in Hemiplegia: Their Correction by Ankle-Foot Orthoses. *Archives of Physical Medicine and Rehabilitation*, 68, 763–771.

LEHNEIS H.R., 1974. Plastic Spiral Ankle-Foot Orthoses. *Orthotics and Prosthetics*, 28(2), 3–13.

LEONARD J.A., ESQUENAZI A., FISHER S.V., HICKS J.E., MEIER R.H. & NELSON V.S., 1989. Prosthetics, Orthotics, and Assistive Devices. 1. General Concepts. *Archives of Physical Medicine and Rehabilitation*, 70(5), S195–S201.

LEONE D.J., 1987. A Structural Model for Molded Thermoplastic Ankle-Foot Orthoses. *Transactions of the ASME — Journal of Biomechanical Engineering*, 109, 305–310.

LEONE D., DIEMENTE S., GUSTAVE S. & LOPEZ-ISA M., 1988. Structural Analysis of Solid Ankle-Foot Orthoses. *Proceedings of the 14th Annual Northeast Bioengineering Conference, Durham, USA, March 1988*, 26–28.

LEONE D., DIEMENTE S. & LOPEZ-ISA M., 1991. Structural Stability Prediction for Thermoplastic Ankle-Foot Orthoses. *Proceedings of the 17th Annual Northeast Bioengineering Conference, Hartford, USA, April 1991*, 231–232.

LORD M. & JONES D., 1988. Issues and themes in computer aided design for external prosthetics and orthotics. *Journal of Biomedical Engineering*, 10(6), 491–498.

LORD M., FOULSTON J. & SMITH P.J., 1991. Technical Evaluation of a CAD System for Orthopaedic Shoe-Upper Design. *Proceedings of the Institution of Mechanical Engineers — Part H: Journal of Engineering in Medicine*, 205, 109–115.

LUNSFORD T.R., RAMM T. & MILLER J.A., 1994. Viscoelastic Properties of Plastic Pediatric AFOs. *Journal of Prosthetics and Orthotics*, 6(1), 3–9.

MACNEAL R.H. & HARDER R.L., 1985. A Proposed Standard Set of Problems to Test Finite Element Accuracy. *Finite Elements in Analysis and Design*, 1(1), 3–20.

MANN R.A., 1975. Biomechanics of the Foot. *In:* AMERICAN ACADEMY OF ORTHOPAEDIC SURGEONS. *Atlas of Orthotics: Biomechanical Principles and Applications.* Saint Louis: The C.V. Mosby Company.

McCOLLOUGH N.C., 1975. Biomechanical Analysis Systems. *In:* AMERICAN ACADEMY OF ORTHOPAEDIC SURGEONS. *Atlas of Orthotics: Biomechanical Principles and Applications.* Saint Louis: The C.V. Mosby Company.

MIDDLETON E.A., HURLEY G.R.B. & McILWAIN J.S., 1988. The role of rigid and hinged polypropylene ankle-foot-orthoses in the management of cerebral palsy: a case study. *Prosthetics and Orthotics International*, 12, 129–135.

MURRAY W.T. & GREENFIELD J.E., 1970. The Cosmetic Below-Knee Brace. *Orthotics and Prosthetics*, 24, 27–30.

NAGAYA M., 1997. Shoehorn-Type Ankle-Foot Orthoses: Prediction of Flexibility. *Archives of Physical Medicine and Rehabilitation*, 78, 82–84.

NSP (NORTH SEA PLASTICS LTD.), 1995. *Data Sheets on the Physical, Mechanical and Thermal Properties of Various Polymers — Issue 1.* Glasgow.

OGORKIEWICZ R.M., 1977. *Engineering Design Guides 17 — The Engineering Properties of Plastics.* Oxford: Oxford University Press.

PAUL J.P., 1996. Letter to the Editor. *Medical Engineering and Physics*, 18(7), 607.

PEIZER E. & WRIGHT D.W., 1969. Human Locomotion. *In:* G. MURDOCH, ed. *Prosthetic and Orthotic Practice.* London: Edward Arnold (Publishers) Ltd., 15–35.

PERRY J., 1975. Pathologic Gait. *In:* AMERICAN ACADEMY OF ORTHOPAEDIC SURGEONS. *Atlas of Orthotics: Biomechanical Principles and Applications.* Saint Louis: The C.V. Mosby Company.

RUBIN G. & DIXON M., 1973. The Modern Ankle-Foot Orthoses (AFOs). *Bulletin of Prosthetics Research*, 10, 20–41.

ROSENTHAL R.K., 1984. The Use of Orthotics in Foot and Ankle Problems in Cerebral Palsy. *Foot & Ankle*, 4(4), 195–200.

SHOWERS D.C. & STRUNCK M.L., 1985. Sheet Plastics and their Applications in Orthotics and Prosthetics. *Orthotics and Prosthetics*, 38(4), 41–48.

STAROS A. & LeBLANC M., 1975. Orthotic Components and Systems. *In:* AMERICAN ACADEMY OF ORTHOPAEDIC SURGEONS. *Atlas of Orthotics: Biomechanical Principles and Applications.* Saint Louis: The C.V. Mosby Company.

STILLS M., 1975. Thermoformed Ankle-Foot Orthoses. *Orthotics and Prosthetics*, 29(4), 41–51.

SUMIYA T., SUZUKI Y. & KASAHARA T., 1996a. Stiffness Control in Posterior-Type Plastic Ankle-Foot Orthoses: Effect of Ankle Trimline, Part 1: A Device for Measuring Ankle Moment. *Prosthetics and Orthotics International*, 20(2), 129–131.

SUMIYA T., SUZUKI Y. & KASAHARA T., 1996b. Stiffness Control in Posterior-Type Plastic Ankle-Foot Orthoses: Effect of Ankle Trimline, Part 2: Orthosis Characteristics and Orthosis/Patient Matching. *Prosthetics and Orthotics International*, 20(2), 132–137.

SASI (SWANSON ANALYSIS SYSTEMS, INC.), 1994a. *ANSYS User's Manual for Revision 5.1 — Volume I: Procedures.* Houston.

SASI (SWANSON ANALYSIS SYSTEMS, INC.), 1994b. *ANSYS User's Manual for Revision 5.1 — Volume II: Commands.* Houston.

SASI (SWANSON ANALYSIS SYSTEMS, INC.), 1994c. *ANSYS User's Manual for Revision 5.1 — Volume III: Elements.* Houston.

SASI (SWANSON ANALYSIS SYSTEMS, INC.), 1994d. *ANSYS User's Manual for Revision 5.1 — Volume IV: Theory.* Houston.

TIMOSHENKO S.P. & WOINOWSKY-KRIEGER S., 1959. *Theory of Plates and Shells*, Second Edition. London: McGraw-Hill.

TORTORA G.J. & GRABOWSKI S.R., 1993. *Principles of Anatomy and Physiology*, Seventh Edition. New York: HarperCollins College Publishers.

TURNER S., 1974. Deformation Behaviour. *In:* R.M. OGORKIEWICZ, ed. *Thermoplastics: Properties and Design.* London: John Wiley & Sons.

VAN KREVELEN D.W. & HOFTYZER P.J., 1976. *Properties of Polymers: Their Estimation and Correlation with Chemical Structure*, Second Edition. Oxford: Elsevier Scientific Publishing Company.

WILLIAMS J.G., 1973. *Stress Analysis of Polymers.* London: Longman.

WONG A.M.K., TANG F-T., WU S-H., & CHEN C-M., 1992. Clinical Trial of a Low Temperature Plastic Anterior Ankle Foot Orthosis. *American Journal of Physical Medicine and Rehabilitation*, 71(1), 41–43.

WORLD BOOK INC., 1988. *The World Book Medical Encyclopedia: Your Guide to Good Health*, Revised 1988 Edition. London.

WU G., 1994. Kinematics Theory. *In:* R.L. CRAIK & C.A. OATIS, eds. *Gait Analysis: Theory and Application.* London: Mosby.

YAMAMOTO S., EBINA M., IWASAKI M., KUBO S., KAWAI H. & HAYASHI T., 1993a. Comparative Study of Mechanical Characteristics of Plastic AFOs. *Journal of Prosthetics and Orthotics*, 5(2), 59–64.

YAMAMOTO S., EBINA M., KUBO S., KAWAI H., HAYASHI T., IWASAKI M., KUBOTA T. & MIYAZAKI S., 1993b. Quantification of the Effect of Dorsi-/Plantarflexibility of Ankle-Foot Orthoses on Hemiplegic Gait: A Preliminary Report. *Journal of Prosthetics and Orthotics*, 5(3), 88–94.